

## NATIONAL & INTERNATIONAL SCIENTIFIC EVENTS

39th IEEE International Conference on Consumer Electronics (ICCE 2021)

Venue: Virtual  
Location: Las Vegas, USA

Begins: January 10, 2021  
Ends: January 12, 2021

8th International Conference on Geological and Civil Engineering (ICGCE 2021)

Location: Tokyo, Japan

Begins: January 28, 2021  
Ends: January 30, 2021

33rd International Symposium on Power Semiconductor Devices and ICs (ISPSD)

Venue: Nagoya Congress Center  
Location: Nagoya, Japan

Begins: May 30, 2021  
Ends: June 3, 2021

35th IAS Meeting of Sedimentology

Venue: Conference Centre of the Vienna House Diplomat Hotel  
Location: Prague, Czech Republic

Begins: June 22, 2021  
Ends: June 24, 2021

39th IAHR World Congress

Venue: Palacio de Congresos de Granada  
Location: Granada, Spain

Begins: July 4, 2021  
Ends: July 9, 2021

50th International Congress and Exposition on Noise Control Engineering

Venue: Marriott Wardman Park  
Location: Washington, USA

Begins: August 1, 2021  
Ends: August 4, 2021

25th International Congress of Theoretical and Applied Mechanics

Venue: MiCo Congress Centre  
Location: Milano, Italy

Begins: August 22, 2021  
Ends: August 27, 2021

20th International Conference on Soil Mechanics and Geotechnical Engineering 2021

Venue: International Convention Centre  
Location: Sydney, Australia

Begins: September 12, 2021  
Ends: September 17, 2021

17th International Symposium on Biopolymers (ISBP 2021)

Venue: Congress Center Le Regent  
Location: Crans-Montana, Switzerland

Begins: September 14, 2021  
Ends: September 17, 2021

14th Mediterranean Congress of Chemical Engineering

Venue: Gran Via Venue, Pavillion 3  
Location: Barcelona, Spain

Begins: September 14, 2021  
Ends: September 17, 2021

2021 International Conference on Smart Transportation and Future Mobility (CSTFM 2021)

Location: Frankfurt, Germany

Begins: September 17, 2021  
Ends: September 19, 2021

8th World Congress on Engineering and Technology (CET 2021)

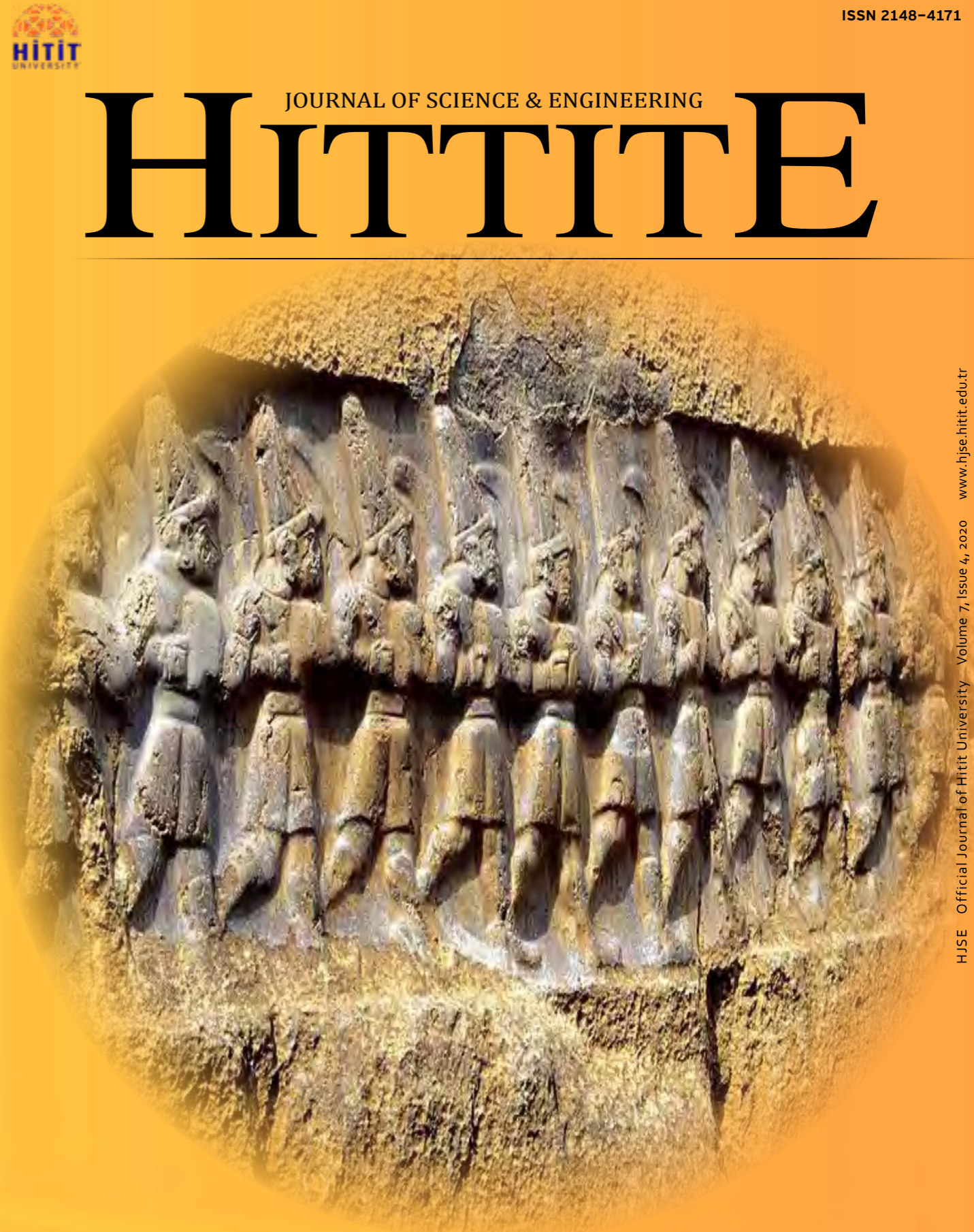
Venue: The Grand Dynasty Culture Hotel  
Location: Xi'an, China

Begins: October 22, 2021  
Ends: October 24, 2021

# HITTITE

JOURNAL OF SCIENCE & ENGINEERING

HJSE Official Journal of Hitit University Volume 7, Issue 4, 2020 www.hjse.hitit.edu.tr



HJSE Official Journal of Hitit University Volume 7, Issue 4, 2020 www.hjse.hitit.edu.tr



Abstracted & Indexed in:

TR Dizin Mühendislik ve Temel Bilimler Veri Tabanı | CrossRef | Google Scholar | MIP Database | StuartxChange | ResearchBib | Scientific Indexing Services (SIS)

HITTITE

Volume 7, Issue 4, 2020

www.hjse.hitit.edu.tr





*A Case Study in Ergonomics by Using REBA, RULA and NIOSH Methods: Logistics Warehouse Sector in Turkey* 257-264

Besim Kaan Kirci, Muge Ensari Ozay and Rustu Ucan

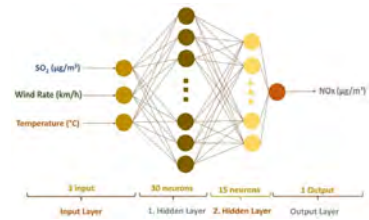
The aim of this study is to investigate ergonomic risk assessment of a logistic warehouse in the Kocaeli province, located in the Marmara Region.



*Prediction of NOx Emissions with A Novel ANN Model in Adana* 265-270

Senem Sezer, Halime Yakisik, Furkan Kartal, N. Nur Futucu, Yagmur Dalbudak, Sevi Yasar and Ugur Ozveren

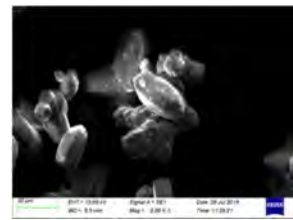
In this study, artificial neural network (ANN), which is a biological mimicked computer algorithm that simulates the functions of neurons using artificial neurons, has been used to present a quantitative determination of the NO<sub>x</sub> emission in Adana through the influences of temperature (°C), wind rate (km/h), and SO<sub>2</sub> (µg/m<sup>3</sup>) on NO<sub>x</sub> emissions.



*In Vitro Study on the Influence of Proline on Struvite Crystals* 271-277

Sevgi Polat and Perviz Sayan

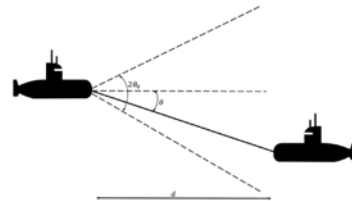
This study investigated the effect of amino acid proline, as crystal modifier, on the struvite crystallization in vitro conditions.



*Investigation of Underwater Wireless Optical Communication Channel Capacity for Different Environment and System Parameters* 279-285

Yigit Mahmutoglu, Kadir Turk and Cenk Albayrak

In this study, the signal to noise ratio (SNR) and channel capacity for UWOC systems are presented according to the divergence angle of the beam and the change in the aperture diameter of the receiver, which are the important parameters for UWOC systems.



*Mineral Chemistry-thermobarometry and Petrography of Metamorphic Sole Rocks of Kömürhan Ophiolite (SE Turkey): Constraints to Evolution and Emplacement* 287-296

Nusret Nurlu

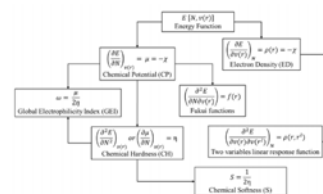
This paper presents the generation of metamorphic sole rocks through the detailed geochemical and petrographical analysis of field work carried out on the Kömürhan ophiolite.



*The Quantum Mechanics Calculation of Molybdenum and Tungsten Influence on the CrM-oxide Catalyst Acidity* 297-311

Toyese Oyegoke, Fadimatu N. Dabai, Adamu Uzairu and Baba El-Yakubu Jibril

In this study, the Lewis acidity of the catalyst was examined using Lewis acidity parameters (Ac), including ammonia and pyridine adsorption energy.



*Performance Evaluation of Empirical Path Loss Models for a Linear Wireless Sensor Network Deployment in Suburban and Rural Environments* 313-320

Yaser Dalveren and Ali Kara

This article presents a preliminary propagation study on the accuracy of empirical path loss models for efficient planning and deployment of a linear wireless sensor network (LWSN) based on long range (LoRa) enabled sensor nodes in suburban and rural environments.



*Investigation of Bond Strength Between GFRP Wrapped Steel Reinforcement and Concrete with Pullout Test* 321-327

Bogachan Basaran and Erkan Turkmen Donmez

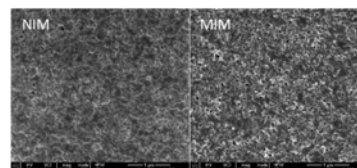
In this study, resin-impregnated glass fibers were wrapped on deformed steel reinforcements and new composite re-inforcements of three diameters were produced, and these composite reinforcements bond with concrete were examined by pullout test.



*Selective Removal of Penicillin G from Environmental Water Samples by Using Molecularly Imprinted Membranes* 329-337

Meshude Akbulut Soylemez

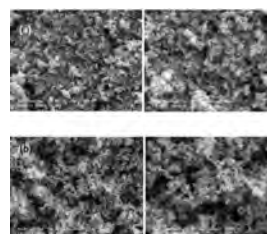
Penicillin G imprinted membranes were prepared by utilizing UV induced in-situ polymerization.



*Boron Doped TiO<sub>2</sub> For The Photodegradation of 4-nitrophenol: Optimization of The Doping Parameters* 339-344

Nazli Turkten and Dila Kaya

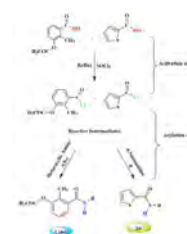
In this work we prepared boron doped TiO<sub>2</sub> ( B-TiO<sub>2</sub>) photocatalysts and evaluated their photocatalytic activity for the degradation of our model organic pollutant, 4-nitrophenol (4-NP).



*Preparation, Characterization and Evaluation of Some New Amides as Antimicrobial Agents* 345-351

Sukriye Cakmak and Aysel Veyisoglu

The some new amide derivatives 1(a-c) and, 2d were synthesized by the two-step N-acylation of 4-nitroaniline or heterocyclic amine derivatives with acyl chlorides.



*Wintering Bird Diversity and Population Sizes at Obruk Dam Lake (Corum) in Turkey* 353-358

Kadir Ulusoy and Safak Bulut

In this study, species diversity of waterbirds, which are the indicator species of wetland quality were investigated at Obruk Dam Lake in Turkey, which was built in 1996 and started to operate in 2009.



**Owner**

Prof. Dr. Ali Osman ÖZTÜRK on  
behalf of Hitit University

**Editor-in-chief**

Prof. Dr. Ali KILIÇARSLAN

**Section Editors**

Prof. Dr. D. Ali KÖSE  
Assoc. Prof. Dr. Öncü AKYILDIZ

**Production**

Assoc. Prof. Dr. Kazım KÖSE  
Res. Asst. Dr. Erhan ÇETİN  
Res. Asst. Mustafa Reşit HABOĞLU  
Res. Asst. Harun Emre KIRAN  
Res. Asst. Ömer Faruk TOZLU  
Lect. Tugrul YILDIRIM

**Editor's Office**

Tel: +90 364 227 45 33 / 12 36

Fax: +90 364 227 45 35

Email: alikilicarslan@hitit.edu.tr

**Subscription Service:**

Tel: +90 364 227 45 33 / 12 82

Fax: +90 364 227 45 35

Email: hjse@hitit.edu.tr

**EDITORIAL BOARD**

Prof. Dr. İftikhar AHMAD

Prof. Dr. Mike BECKETT

Prof. Dr. İbrahim DİNÇER

Prof. Dr. Ali ELKAMEL

Prof. Dr. Mohamad S QATU

Prof. Dr. Saffa RIFFAT

Prof. Dr. Thanos SALIFOGLU

Assoc. Prof. Dr. Yuehong SU

Dr. Wojciech NOGALA

Prof. Dr. Yusuf AYVAZ

Prof. Dr. Adil DENİZLİ

Prof. Dr. Ali GENÇER

Prof. Dr. Metin GÜRÜ

Prof. Dr. Murat HOŞÖZ

Prof. Dr. Sadık KAKAÇ

Prof. Dr. Tarık Ömer OĞURTANI

Prof. Dr. Ender SUVACI

Assoc. Prof. Dr. Ali TOPÇU

Prof. Dr. Kazım Savaş BAĞÇECİ

Assoc. Prof. Dr. Cengiz BAYKASOĞLU

Prof. Dr. Naki ÇOLAK

Prof. Dr. Vedat DENİZ

Prof. Dr. Hakan GÜNGÜNEŞ

Prof. Dr. Bülent KABAK

Prof. Dr. Ali KILIÇARSLAN

Prof. Dr. Dursun Ali KÖSE

Prof. Dr. İrfan KURTBAŞ

Prof. Dr. İbrahim SÖNMEZ

Assoc. Prof. Dr. Seyfi ŞEVİK

Prof. Dr. Dilber Esra YILDIZ

University of Malakand, Chakdara, Pakistan

Bangor University, Bangor, United Kingdom

Uoit Ontario University, Ontario, Canada

University of Waterloo, Ontario, Canada

Central Michigan University, Michigan, United States

The University of Nottingham, United Kingdom

Aristotle University of Thessaloniki, Thessaloniki, Greece

The University of Nottingham, United Kingdom

Polish Academy of Sciences, Poland

Suleyman Demirel University, Turkey

Hacettepe University, Turkey

Ankara University, Turkey

Gazi University, Turkey

Kocaeli University, Turkey

TOBB University, Turkey

Middle East Technical University, Turkey

Anadolu University, Turkey

Hacettepe University, Turkey

Hitit University, Turkey

Hitit University, Turkey

Hitit University, Turkey

Hitit University, Turkey

Hitit University, Turkey

Hitit University, Turkey

Hitit University, Turkey

Hitit University, Turkey

Hitit University, Turkey

Hitit University, Turkey

Hitit University, Turkey

Hitit University, Turkey

Journal Name	: HITTITE JOURNAL OF SCIENCE AND ENGINEERING
Year	: 2020
Managing Editor	: Prof. Dr. Ali KILIÇARSLAN
Managing Office	: Hitit University Faculty of Engineering
Managing Office Tel	: +90 364 227 45 33 / 12 36
Publication Language	: English
Publication Type	: Peer Reviewed, Open Access, International Journal
Delivery Format	: 4 times a year (quarterly)
Print ISSN	: 2149-2123
Online ISSN	: 2148-4171
Publisher Address	: Hitit Üniversitesi Kuzey Kampüsü Çevre Yolu Bulvarı 19030 Çorum / TÜRKİYE
Publisher Tel	: +90 364 227 45 33/1236



*This new issue of Hittite Journal of Science and Engineering contains twelve manuscripts from the disciplines of chemistry, molecular biology and genetics, chemical engineering, civil engineering, electrical and electronics engineering, geological engineering. These manuscripts were first screened by Section Editors using plagiarism prevention software and then reviewed and corrected according to the reviewer's comments. I would like to express my gratitude to all our authors and contributing reviewers of this issue.*

*I would like to thank to the new President of Hitit University, Prof. Dr. Ali Osman Öztürk, for his support and interest in HJSE and also to*

*the Section Editors of HJSE, namely Prof. Dr. Dursun Ali Kose and Assoc. Prof. Dr. Oncu Akyıldız, as well as our Production Editors Assoc. Prof. Dr. Kazım Kose, Mustafa Reşit Haboğlu, Dr. Erhan Çetin, Tugrul Yildirim, Harun Emre Kiran and Ömer Faruk Tozlu for their invaluable efforts in making of the journal.*

*It's my pleasure to invite the researchers and scientists from all branches of science and engineering to join us by sending their best papers for publication in Hittite Journal of Science and Engineering.*

*Prof. Dr. Ali Kiliçarslan*

*Editor-in-Chief*





# A Case Study in Ergonomics by Using REBA, RULA and NIOSH Methods: Logistics Warehouse Sector in Turkey

Besim Kaan Kirci<sup>1b</sup> Muge Ensari Ozay<sup>1b</sup> and Rustu Ucan<sup>1b</sup>

Uskudar University, Department of Occupational Health and Safety, Istanbul, Turkey

## ABSTRACT

Employees in the warehouse processes of the logistics sector are engaged in activities such as pushing, pulling and lifting during a day. Intense work tempo, power requirement, working in unsuitable positions and physical factors of working environment adversely affect employees. The aim of this study is to investigate ergonomic risk assessment of a logistic warehouse in the Kocaeli province, located in the Marmara Region. This study was conducted over a sample area where 57 people work in, 5 work processes in a warehouse with a closed area of 8000 m<sup>2</sup> and all processes were examined during 4 months. Employees' working postures in daily routine were studied by using REBA, RULA and NIOSH as ergonomic risk assessment methods. Furthermore, ambient noise, personal noise, ambient dust, personal dust, vibration, chemical and thermal comfort values were measured with accredited devices.

### Keywords:

Ergonomics; Occupational health and safety; REBA; RULA; NIOSH.

## INTRODUCTION

The field of ergonomics science comprises planning to carry out works in accordance with human abilities and capacities while occupational health of employee and minimizing occupational accidents [1]. The aim of ergonomics is to reduce or eliminate situations that may cause musculoskeletal disorders, to prevent incidents and occupational accidents occurring in the workplace [1, 2, 3, 4]. The task of management is to ensure the continuity of a safe work environment and employee safety. These include following the principles of occupational safety in workplace design, equipment selection, providing protective equipment and mechanisms, planning employee training and preparing clear and understandable occupational safety rules [5]. Protecting the health and comfort of the employee is one of the pioneers of work health and safety during the warehousing processes, which is one of the important service areas of the logistics sector. The logistics sector has some processes in working environment of warehousing, such as handling, storage, material handling, packing and stacking. [6].

Intense working tempo and improper working postures may cause musculoskeletal diseases [7]. There exist several ergonomics risk evaluation methods to prevent musculoskeletal diseases [8, 9]. These methods are divided into two as observational and measurement-

based techniques [8]. Observational methods such as REBA, RULA, OWAS, BAUA, NIOSH etc. are the most common methods used in evaluation [10, 11, 12, 13, 14, 15 16].

Within the scope of this study, logistics sector is undoubtedly one of the most important areas for storage activities [5, 6]. The main aim of the occupational health and safety is to establish a healthy and safe environment for employees and to prevent occupational accidents that may occur due to operational reasons [17, 18, 19]. The objective of this research is to evaluate ergonomics risk assessment by using REBA (Rapid Entire Body Assessment), RULA (Rapid Upper Limb Assessment) and using revised NIOSH (The National Institute for Occupational Safety and Health) lifting equation methods in a logistics company located within the boundaries of Marmara Region, Kocaeli province. Beside the ergonomics risk assessment methods, environmental conditions were measured with calibrated instruments by an accredited laboratory to evaluate personal noise, ambient dust, respirable dust, vibration, chemical and thermal comfort measurements.

## MATERIAL AND METHODS

The duration of the study was limited to four months. Before, one month of observation and data collection

### Article History:

Received: 2019/12/13

Accepted: 2020/09/17

Online: 2020/12/31

**Correspondence to:** Muge Ensari Ozay,  
Uskudar University, Occupational Health  
and Safety, 34662, Istanbul/Turkey.  
E-Mail: muge.ensariozay@uskudar.edu.tr  
Phone: +90 216 400 2222  
Fax: +90 216 474 1256

were carried out. The study was divided into three stages. The first stage consists of understanding and recording working conditions and work processes. The second stage is the decision stage on the risk assessment methodology that is appropriate for ongoing works. Calculations were made by selecting the appropriate risk assessment methodology according to their working postures. The third stage is where the work environment measurements were made by accredited instruments.

### First Stage

This study was carried out on 5 work processes in a warehouse with a closed area of 8000 m<sup>2</sup>, on a sample area where 57 employees. At this stage, the barcode system and reading devices connected to the system are used. Products are taken to the workplace from the goods receiving area. The goods are read by handheld terminal device and placed on next to the products in the warehouse. The products are prepared to be placed on the shelves determined by the system. The products are read back with the handheld terminal device to determine which shelf to place and move to the specified shelf. Before placing, the number of the product and the shelf are read again with hand held terminal device. The shipping products, determined according to customer requests, are prepared from the products that already placed on the shelves. During the preparation process, the product barcodes are read with handheld terminal device and their locations are determined. The products are collected from certain places and brought to the product preparation yard for shipment. Products are stacked by handling in this area. Labeling is done after the products are stretched. To ensure the order and safety of the products, it is caged with boards. Prepared products are read with handheld terminal device in order to be able to exit the system and they are transported to the loading area for shipment by forklift trucks. Products are shipped after being loaded on the vehicle. Fig. 1 shows the sequence of workflow.

### Second Stage

The work of the employees in a logistics warehouse has been identified and photographed. Observed persons and observation time were randomly selected. For risk assessment, as ergonomic risk assessment methods, REBA [20], RULA [21] and NIOSH [22] tools were used and observation was made during working hours. 18 REBA examinations, 9 RULA examinations and 6 NIOSH examinations were conducted during the workflow.

### Third Stage

The work environment was measured with calibrated instruments in an accredited laboratory to eliminate

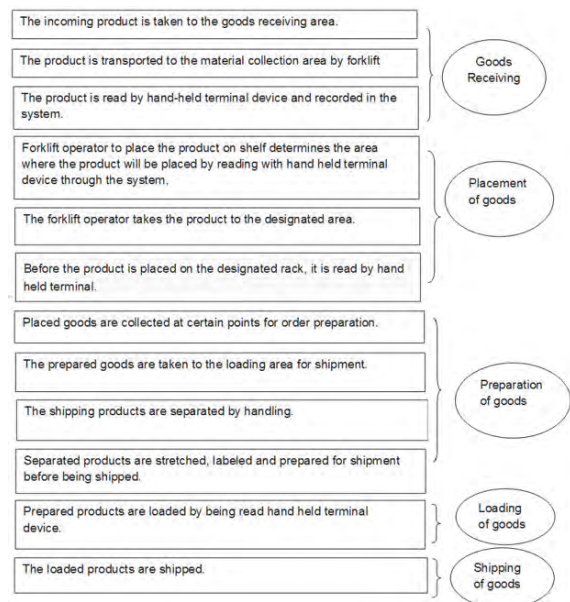


Figure 1. Workflow in logistics warehouse

environmental factors that could affect it. Ambient measurements include ambient noise, personal noise, ambient dust, personal dust, vibration, chemical and thermal comfort measurements. Measurements were carried out for two days, during day and night, together with measurement test personnel. During measurements of daytime, the work done by the employees was also observed in the study.

Thermal comfort measurement was performed according to TS EN ISO 7730 [23]. LASTEM thermal comfort meter was used for the measurements of thermal comfort. Thermal comfort measurements were carried out at 14 points in the working environment.

Ambient noise measurement was performed in accordance with TS EN ISO 11202:2020 [24]. In ambient noise measurements; CASELLA CEL 63X and CASELLA CEL ACOUSTIC CAL devices were used for verification. The measurements were applied in workplaces where compressor and air staple gun are used.

Personal noise measurement was performed according to TS 2607 ISO 1999 [25]. CASELLA CEL 35 and CASELLA CEL Acoustic calibrator were used for personal noise measurements. Personal noise measurements were made at 4 points, including 3 forklift operators and 1 loading personnel.

Vibration measurement was carried out in accordance with the TS EN 1032 + A1 .standard [26]. Measurements were performed with transducers using OKTABTA AP-TECH meter for hand-arm and whole-body vibration measurement. . Vibration measurements were made at 3 points,

including 2 forklift operators and 1 picker (electric pallet truck) operator.

Measurements of ambient and breathable dust were realized in accordance with TS EN 689 standard [27]. CA-SELLA CEL TUFF sampling pump was used for the measurements. The system consists of air sampling pump and filter with sampling heads. The system consists of air sampling pump, sampling heads and filter. The sampling pump flow rate was set at 2.2 l/min. Measurements were made for ambient dust measurement at 15 points. Personal dust exposure measurement was carried out on 5 personnel in the workplace.

Chemical substance measurement was performed according to ASTM 1 4490-96 standard [28]. Kitagawa Gas detector tube system AP-20 was used for measurements. Hydrogen, Ethyl Benzene and Xylene gas measurements were made at 3 points in the workplace.

## RESULTS AND DISCUSSION

### REBA Analyses

After the observations and ergonomic risk assessments made by REBA method in the relevant working area, the studies are presented in Table 1 as follows.

One of the very risky postures (Fig. 2) is selected as an example of the calculations with REBA method (Table 2).

According to the posture of the worker in Fig. 2, trunk is 3 points since it is flexed between 0° – 20° and slightly side flexed (2+1). Neck is 2 points due to the flexion more than 60°. Legs are 3 points since there is unilateral weight bearing and knees between 30° and 60° flexion (2+1). Since the load is greater than 10 kg, the Load/Force score is 2 and the Load/Force score is added to Table A score. Upper arm is 2 points due to the flexion between 20° and 45°. Lower arm 2 points due to flexed less than 60°. Wrist 2 points due to the flexion greater than 15°. The total REBA score is 11, this refers to a REBA action level of 4 indicating a very high risk of injury.

During the preparing product phase, removing the product from the shelf (1), palletizing the product (1), handling for packaging of products (1) procedures (Table 1) are at a high risk level and require immediate action. When removing the product from the shelf, the score can be reduced by improving the posture of the neck, upper arm, lower arm and wrist, primarily the body and leg. When palletizing the product (2), the risk can be reduced by reducing the score with improvements in order of priority; in body, leg, neck and upper arm postures. When handling for packaging of products, the score can be reduced by improving the neck,

**Table 1.** REBA results.

NO	JOB DESCRIPTION	REBA SCORE	REBA RESULT
1	Read-out with handheld terminal device	2	Low risk
2	Using Picker Forklift (forward)	4	Medium risk
3	Using Picker Forklift (backward)	4	Medium risk
4	Pallet Handling Process	9	High risk
5	Removing the Product from the Shelf 1	11	Very high risk
6	Removing the Product from the Shelf 2	9	High risk
7	Palletizing the Product 1	8	High risk
8	Palletizing the Product 2	11	Very high risk
9	Handling for Packaging of Products 1	9	High risk
10	Handling for Packaging of Products 2	11	Very high risk
11	Cage process 1	5	Medium risk
12	Cage process 2	9	High risk
13	Stretch film packaging processes	9	High risk
14	Labeling process	5	Medium risk
15	Handling process	13	Very high risk
16	Pallet Truck Handling (Towing) Process	9	High risk
17	Pallet Truck Operation (Push) Operation	12	Very high risk
18	Battery charge water filling process	2	Low risk



**Figure 2.** Removing the product from the shelf 1

**Table 2.** REBA evaluation of removing the product from the shelf 1.

	SCORES
Trunk	3
Neck	2
Legs	3
<b>Table A</b>	<b>6</b>
Load Force	2
<b>SCORE A</b>	<b>8</b>
Upper Arm	2
Lower Arm	2
Wrist	2
<b>Table B</b>	<b>3</b>
Coupling	2
<b>SCORE B</b>	<b>5</b>
<b>SCORE C</b>	<b>10</b>
Activity Score	1
<b>REBA SCORE</b>	<b>11</b>

upper arm, lower arm and wrist postures, primarily with the body and leg. In order to reduce the scores, the workers could use equipment such as a high platform or lifting vehicle.

### RULA Analyses

Results of RULA method are shown in Table 3 for all working positions.

Reading of the product with the hand held terminal on forklift (Fig. 3) is selected as an example of the calculations with RULA method (Table 4).

According to the scores given to this posture (Fig. 3), upper arm is 2 points, lower arm 3 is points, wrist score is 2 points, wrist rotation is 1 point, neck and trunk postures have 4 points, legs score is 1 point, muscle use is 1 point, force is 0 point. The RULA score was calculated as 7. In order to decrease the scores of the unloading of the vehicle, the use of forklifts is one of the processes, precautions should be taken as soon as possible. The forklift seat should be adjustable and ergonomic. Vehicle seats can be adjusted until reaching the correct position.

The use of Reach Truck (forward) in the product placement process and the re-reading of the product with the hand held terminal in the product placement on the shelf had a very high risk. The values can be decrease by improvements in product placements on the shelf, especially in the lower arm, neck and body postures and in the process of re-reading the product by hand held terminal.

**Table 3.** RULA results

NO	JOB DESCRIPTION	REBA SCORE	REBA RESULT
1	Vehicle Unloading (forklift operations)	6	Medium risk
2	Reach-Truck Operation (forward)	7	Very high risk
3	Reach-Truck Operation (backward)	5	Medium risk
4	Product reading process with hand held terminal	3	Low risk
5	Reading of the product with the hand held terminal on forklift	7	Very high risk
6	Product Rack Placement Process	6	Medium risk
7	Forklift Operation	3	Low risk
8	Driver's Seating Process	5	Medium risk
9	Cleaning Automat Using Process	6	Medium risk

**Figure 3.** Reading the product with the hand held terminal on the forklift.

Precautions are also required for the use of Reach-Truck (back) and for placing product on the shelf identified as medium risk. If the neck and trunk postures can be improved at an angle suitable for ergonomic conditions; resulting values can be reduced.

### NIOSH Results

Results of the NIOSH method are shown in Table 5 for all working positions.

**Table 4.** RULA analysis of the reading of the product with the hand held terminal on the forklift

	SCORES
Upper Arm	2
Lower Arm	3
Wrist	2
<b>Wrist rotation</b>	<b>2</b>
SCORE A	4
<b>Muscle use</b>	<b>1</b>
Force	0
SCORE C	5
Trunk	4
<b>Neck</b>	<b>4</b>
Legs	1
<b>SCORE B</b>	<b>7</b>
<b>Muscle use</b>	<b>1</b>
Force	0
<b>SCORE D</b>	<b>8</b>
<b>RULA SCORE</b>	<b>7</b>

One of the very risky postures is selected as an example of the calculations with NIOSH method as in Fig. 4 and Table 6.

In the NIOSH calculations, the lifting index is less than 1.0, indicates that there is no risk during lifting. Therefore, the lifting work should be planned with a lifting index below 1.0. The lift index between 1.0 and 3.0 indicates that the job is risky and requires ergonomic regulation, and above 3.0 point indicates that the lifting has very high risk and also requires ergonomic regulation. According to NIOSH calculations for the “product preparation process”, product preparation 1, preparation of products 2 and preparation of products 4 are very risky and should be taken immediate precautions to ensure employee ergonomics. Product preparation 3, preparation of products 5 and preparation of products 6 are risky and necessary precautions should be taken to protect the musculoskeletal. In order to decrease the lifting index values, load must be brought closer to the employee's body. As the load is closer to the employee's body, the horizontal (H) distance value will decrease, thus the horizontal multiplier (HM) value will increase. The height of the place where the product will be placed should be increased. Vertical multiplier (VM) value will decrease as the vertical height increases. When these arrangements are made, the origin and destination lifting index values will be reduced to below 1 and the work will be safer. In addition to that, it is recommended to use mechanical device for the transportation.

**Table 5.** NIOSH results

NO	JOB DESCRIPTION	Position	Lifting Index (LI) Value	Assessment
1	Product Preparation position 1	Origin	5.49	Very risky
		Destination	7.46	
2	Product Preparation position 2	Origin	7.17	Very risky
		Destination	5.24	
3	Product Preparation position 3	Origin	1.66	Risky
		Destination	2.11	
4	Product Preparation position 4	Origin	3.50	Very risky
		Destination	4.09	
5	Product Preparation position 5	Origin	1.74	Risky
		Destination	1.49	
6	Product Preparation position 6	Origin	2.45	Risky
		Destination	2.12	

### Ambient Measurements

**Thermal Comfort Measurement:** Thermal comfort measurements were performed at 14 points in the work environment. When the calculated PMV and PPD values are compared with the values given in TS EN ISO 7730 standards [23]; 9 points were warm (slightly warm) and 5 points were in the thermal comfort range for employees. As a result of thermal comfort measurements, the highest PPD value of 9 points measured as slightly warm was 48.2 PPD and the highest PPD value of 5 points in the thermal comfort range was 8.12. Taking into consideration the warehouse structure, a ventilation system can be constructed to ensure that all results are within the range of thermal comfort.

**Noise Measurement:** The compressor and air staple gun were selected for the noise measurement. During routine operations, the noise sound of the work area with the compressor was measured as 83.2 dB and the noise of the area with the air staple gun was measured as 90.8 dB. Personal noise measurements were carried out at 4 different points, including 3 forklift operators and 1 personnel working in loading operation. In the warehouse, first forklift operator measurement result was 86.5 dB, second forklift operator measurement result was 84.4 dB and the third forklift operator measurement result was 77.9 dB. The measured values of compressor and air staple gun exceed the values recommended by the legislation [29]. In order to eliminate the noise in the environment, the working place of the compressor and air staple gun should be changed and placed in an area where nobody works. The existing noise will be reduced by removing it from the work environment. If this cannot be done, the equipment will be placed in the

**Table 6.** Revised NIOSH calculation of product preparation position 1

STEP 1 . Measure and record task variables											
	LC (Load Constant) (kg)	Hand Location (cm)				Vertical Distance (cm)	Aymetric angle (degree)		Frequency rate Lifts/min	Duration (Hour)	Object Coupling
		Orijin	Destination		Orijin		Destination				
3L (Object Weight) (kg)	20	H	V	H	V	D	A	A	F	2-8	C
10	20	45	35	60	35	0	45	45	8	2-8	Good

STEP 2 . Determination of the multipliers and compute the Recomeded Weiight Limists (RWL)		
RWL=LC·HM·VM·DM·AM·FM·CM		
Orijin	RWL=23*0.57*0.90*1*0.86*0.18*1	=1.82 kg
Destination	RWL=23*0.42*0.90*1*0.86*0.18*1	=1.34 kg

STEP 3 . Computation of the Lifting Index (LI)		
Orijin	Removal % = $\left(\frac{C_0 - C}{C_0}\right) \times 100$	10/1.82 = 5.49
Destination	Removal % = $\left(\frac{C_0 - C}{C_0}\right) \times 100$	10/1.34 = 7.46



**Figure 4.** RThe product preparation position 1 (a) origin position, (b) destination position.

cabin that absorbs the noise. Even though all the measures are taken and the noise level cannot be reduced below the legal legislative limit, employees should use personal protector equipment.

According to the results of personal noise measurement, high results were obtained in two forklift operators respecting to legal regulations. The measurement results of the other two personnel are below the legally approved values [29]. As a precaution for forklift operators, noise-absorbing apparatus should be used in forklift cabins. In case the noise level cannot be reduced, employees working in places that exceed the noise limit should wear earplugs during operations.

**Vibration Measurement:** Three points were selected for vibration measurement and the measurement was made on 2 forklift operators and 1 picker operator. First forklift operator's vibration measurement result was  $405 \times 10^{-3}$  m/s<sup>2</sup>, second forklift operator's vibration measurement result was  $593 \times 10^{-3}$  m/s<sup>2</sup>, and the result of the operator using the crane was  $621 \times 10^{-3}$  m/s<sup>2</sup>. The vibration value of first truck operator is below the value recommended by the legislation [30], while the vibration value of other vehicles' operator is higher than legal values. Factors such as the defects on the ground in the warehouse, the working time and the duration of the work, the type and weight of transported product may cause these alterations in the value of the vibration measurements. Necessary precautions should be taken for the exposure above the action limit.. Damaged floors should be amended. Vibration absorbance materials should be used such as sponge, cover, cushion, etc.

**Dust Measurement:** 15 Points were determined in the work area for ambient dust measurement. Results are as follows: 2.833 mg/m<sup>3</sup>, 2.347 mg/m<sup>3</sup>, 1.856 mg/m<sup>3</sup>, 1.356 mg/m<sup>3</sup>, 1.025 mg/m<sup>3</sup>, 0.865 mg/m<sup>3</sup>, 0.791 mg/m<sup>3</sup>, 0.754 mg/m<sup>3</sup>, 0.674 mg/m<sup>3</sup>, 0.583 mg/m<sup>3</sup>, 0.577 mg/m<sup>3</sup>, 0.567 mg/m<sup>3</sup>, 0.522 mg/m<sup>3</sup>, 0.496 mg/m<sup>3</sup>, 0.386 mg/m<sup>3</sup>. 5 personnel were assigned for individual dust exposure measurement. The results are as follows: 1.867 mg/m<sup>3</sup>, 1.546 mg/m<sup>3</sup>, 1.071 mg/m<sup>3</sup>, 1.049 mg/m<sup>3</sup>, 0.862 mg/m<sup>3</sup>. The values were below the legal limits [27]. The work environment

should be cleaned regularly with a cleaning machine.

**Chemical Substance Measurement:** Hydrogen, Ethyl Benzene and Xylene measurements were made by selecting 3 different points. Hydrogen was measured in trace amounts, Ethyl Benzene was 1 ppm and Xylene was 25 ppm. Although the results are below the legal limits [31], the standard masks should be used and ventilation are recommended.

## CONCLUSION

In this study, REBA, RULA and NIOSH methods were used as ergonomic risk assessment tools. As a result of these analyses, it was identified that there are risky working postures in the work processes. There is a lot of pushing, pulling, lifting and carrying work in the logistics sector. This study was carried out in order to be an example for detecting and correcting awkward postures in the sector. It is aimed to show the ergonomics science and occupational health and safety discipline must be handled in the logistics' sector in work processes against repeated and inappropriate working postures. In this way, safe working environments can be established with simple-preventive measures for both employers and employees.

Considering the human factor, changes may occur in the consequences of hazards and risks due to the effects such as employee's knowledge, safety culture approach and experience. The measures should be taken at the source of the hazard and the use of human factor will be minimized by making technological improvements such as automation and arranging the products by using machine power. If precautions cannot be taken at the source, the risks should be reduced with engineering measures to be carried out in the environment. Improvements can be made with engineering applications such as safe high platforms, mechanical arms used to take materials.

A collaborative work with the management system is recommended to prevent inappropriate positions and to raise awareness in logistics' sector. In very dangerous workplaces, the training period of an employee is 16 hours according to the legislations [32] in Turkey. Additional ergonomics training is recommended for employees at regular intervals. Training should be prepared by examining inappropriate work experiences and hazards as well as the reason and prevention methods of occupational musculoskeletal disorders. The posture suggestions presented in relation to the activities such as lifting, pushing and pulling movements are valid also to ensure the quality of daily life. Special efforts should be made by occupational physicians and job analysts in order to eliminate or reduce backbone problems. Special work,

training, nutrition, rest periods, exercise movements and personalized work plans could be prepared for employees.

Ergonomics science and occupational health and safety discipline must be handled in the logistics' sector in work processes against unwittingly repeated and habitual dangerous behaviors and against inappropriate working postures. In this way, safe working environments can be established with simple and preventive measures for both employers and employees.

## ACKNOWLEDGEMENT

The authors would like to thank Assist. Prof. Dr. Esin Tümer Kurnaz for her valuable advice on this project. This article is derived from the Master thesis of Kaan Kırıcı at Üsküdar University, Institute of Health Sciences.

## References

1. Dul J, Weerdmeester B. Ergonomics for Beginners: A Quick Reference Guide, third ed. CRC Press, 2008.
2. Alan W, Salmoni AP. Case studies in whole-body vibration assessment in the transportation industry challenges in the field. *International Journal of Industrial Ergonomics* 38 (2008) 783-791.
3. Merlino LA, Rosecrance JC, Anton D, Cook TM. Symptoms of musculoskeletal disorders among apprentice construction workers. *Applied Occupational and Environmental Hygiene* 18(1) (2003) 57-64.
4. Morken T, Riise T, Moen B, Hauge Hvs, Holien S, Langedrag A, Pedersen S, Saue L, Seljeb M, Thoppil V. Low back pain and widespread pain predict sickness absence among industrial workers. *BMC Musculoskeletal Disorders* 21(4) (2003) 1-8.
5. Kırımtayyif D. Occupational Health and Safety Practices in Logistics Sector. Yeni Yüzyıl University. Istanbul, 2014.
6. Anderson VP. Ergonomic solutions for retailers: prevention of material handling injuries in the grocery sector. Cincinnati, OH: U.S. Department of Health and Human Services, Centers for Disease Control and Prevention, National Institute for Occupational Safety and Health, DHHS (NIOSH) Publication No: 2015-100, 2015.
7. Çırpan M, Kahraman F, Çırpan R. Temizlik İşlerinde Çalışanların Kas İskelet Sistemi Hastalıklarının Değerlendirilmesi. 8. İş Sağlığı ve Güvenliği Konferansı Bildiri Tam Metinleri Kitabı 1 608-616.
8. Kee D, Karwowski W. A comparison of three observational techniques for assessing postural loads in industry. *International Journal of Occupational Safety and Ergonomics* 13(1) (2007) 3-14.
9. Akay D, Dağdeviren M, Kurt M. Çalışma duruşlarının ergonomik analizi. *Gazi Üniversitesi Mühendislik Mimarlık Fakültesi Dergisi* 18(3) (2003) 73-84.
10. Takala EP, Pehkonen I, Forsman M, Hansson GA, Mathiassen SE, Neumann, WP, Sjøgaard G, Veiersted KB, Westgaard RH, Winkel J. Systematic evaluation of observational methods assessing biomechanical exposures at work. *Scandinavian Journal Work Environmental Health* 36(1) (2010) 3-24.
11. Özay ME, Doğanbatır ÇŞ. Ergonomic risk analysis case study using REBA, NIOSH and Snook table methods in a supermarket in the retail industry. *Journal of Engineering Sciences and Design* 6 (3) (2018) 448 - 459.
12. Atıcı H, Gönen D, Oral A. Çalışanlarda zorlanmaya neden olan

- duruşların REBA yöntemi ile ergonomik analizi. Süleyman Demirel Üniversitesi Mühendislik Bilimleri ve Tasarım Dergisi 3(3) (2015) 239-244.
13. Enez K, Nalbantoğlu SS. REBA yönteminin ormançılık faaliyetleri açısından değerlendirilmesi. Süleyman Demirel Üniversitesi Mühendislik Bilimleri ve Tasarım Dergisi 3(3) (2015) 127-131.
  14. Erdemir F, Eldem C. Bir döküm atölyesindeki çalışma duruşlarının dijital insan modelleme tabanlı REBA yöntemi ile ergonomik analizi. Gazi Üniversitesi Politeknik Dergisi 22(3) (2019) 1-10.
  15. Sağıroğlu H, Coşkun MB, Erginel N. REBA ile bir üretim hattındaki iş istasyonlarının ergonomik risk analizi. Süleyman Demirel Üniversitesi Mühendislik Bilimleri ve Tasarım Dergisi 3(3) (2015) 341.
  16. Sevimli M, Atıcı H, Gündüz T. Pirinç paketleme işinde çalışanların çalışma koşullarının ergonomik risk analizleri ile geliştirilmesi.
  17. Zunjic A, Yue X. Application of ergonomics in supply chains IETI Transactions on Ergonomics and Safety 2 (2018) 1-4.
  18. Mocan A, Draghici A, Mocan M. A way of gaining competitive advantage through ergonomics improvements in warehouse logistics. Research and Science Today 2 (2017).
  19. Dul J, Neuman WP. Ergonomics contributions to company strategies. Applied Ergonomics 40 (2009) 745-752.
  20. Hignett S, McAtamney L. Rapid entire body assessment (REBA). Applied Ergonomics 31 (2000) 201-205.
  21. McAtamney L, Corlett EN. RULA: a survey method for the investigation of world-related upper limb disorders. Applied Ergonomics 24 (1993) 91-99.
  22. Waters TR, Putz-Anderson V, Garg A. Applications Manual for the Revised NIOSH Lifting Equation. Cincinnati, 1994.
  23. TS EN ISO 7730- Standard for Medium Temperature Thermal Environments - Determination of PMV and PPD Indices for Evaluation of Conditions for Thermal Comfort.
  24. TS EN ISO 11202: 2020 - Acoustics — Noise emitted by machinery and equipment — Determination of emission sound pressure levels at a work station and at other specified positions applying approximate environmental corrections.
  25. TS 2607 ISO 1999 Standard for Acoustics - Determination of occupational noise exposure and estimation of noise-induced hearing impairment.
  26. TS EN 1032 + A1 Standard for Mechanical Vibration -Testing of Mobile Machinery in Order to Determine the Vibration Emission Value.
  27. TS EN 689 GuidanceStandard for the Assessment of Exposure by Inhalation to Chemical Agents for Comparison with Limit Values and Measurement Strategy.
  28. ASTM D4490 - 96 Standard Practice for Measuring the Concentration of Toxic Gases or Vapors Using Detector Tubes.
  29. Regulations of the Ministry of Labour and Social Security on protection of workers from risks related to noise. Official Gazette of the Republic of Turkey No: 28721.
  30. Regulations on the protection of workers from risks of vibration. Official Gazette of the Republic of Turkey No: 28743.
  31. Regulations on safety and health in working with carcinogenic or mutagenic substances. Official Gazette of the Republic of Turkey No: 28730.
  32. Regulations of the Ministry of Labour and Social Security on the Principles and Regulations for Occupational Health and Safety Training of Employees. <https://www.bilgit.com/yonetmelikler.html>. [Date accessed:07.08.2018].



# Prediction of NO<sub>x</sub> Emissions with A Novel ANN Model in Adana

Senem Sezer  Halime Yakisik  Furkan Kartal  N. Nur Fucucu  Yagmur Dalbudak  Sevi Yasar   
Ugur Ozveren 

Marmara University, Department of Chemical Engineering, Istanbul, Turkey

## ABSTRACT

NO<sub>x</sub> emissions are one of the typical air pollutants that has drawn worldwide attention. NO<sub>x</sub> emissions from air cause detrimental effects on the environment and human health such as lung cancer, asthma, allergic rhinitis, and mental diseases. Therefore, real-time NO<sub>x</sub> monitoring has been very popular research topics in atmospheric and environmental science. However, the spatial coverage of monitoring stations within Adana is limited and thus often insufficient for exposure. Moreover, NO<sub>x</sub> monitoring stations are also lacking to reveal the influences of meteorological and air pollutant effects. In this study, artificial neural network (ANN), which is a biological mimicked computer algorithm that simulates the functions of neurons using artificial neurons, has been used to present a quantitative determination of the NO<sub>x</sub> emission in Adana through the influences of temperature (°C), wind rate (km/h), and SO<sub>2</sub> (µg/m<sup>3</sup>) on NO<sub>x</sub> emissions. The high R<sup>2</sup> values in testing dataset lead to the conclusion that the artificial neural network model provides predictions. The developed model in study is a useful tool for the design and planning of air pollution control policies as well as reducing economic cost. The developed model in study is a useful tool for the design and planning of air pollution control policies as well as reducing economic cost.

### Keywords:

Adana, Air Pollution, NO<sub>x</sub> Emissions, Artificial Neural Networks, Prediction

## INTRODUCTION

Air quality is becoming an essential environmental issue in nowadays [1-3]. Researchers have been interested in air quality due to severe health problems caused by air pollution as it is one of the factors that effects the nature of human beings [1, 4]. Air pollution have been considered as one of the most important environmental concern especially for urban areas due to their high population and industries [4, 5].

There are a number of pollutants that are also known ground-level air pollutants, namely PM<sub>10</sub>, O<sub>3</sub>, CO, NO<sub>x</sub>, NO, NO<sub>2</sub>, H<sub>2</sub>S and SO<sub>2</sub> [6]. Nitrogen oxide, generally known as NO<sub>x</sub>, is a common term for compounds include oxygen and nitrogen such as NO<sub>3</sub>, NO, N<sub>2</sub>O, N<sub>2</sub>O<sub>3</sub>, NO<sub>2</sub>, N<sub>2</sub>O<sub>4</sub>, and N<sub>2</sub>O<sub>5</sub> [7, 8]. Combustion emissions and vehicle exhaust are the main source of NO<sub>x</sub> [9, 10]. NO<sub>x</sub> emissions can cause acid rains and photochemical smog that has an effect on human health (such as infection, cancer, etc.) and air quality [9]. Inhaling NO<sub>x</sub> is associated with increased health problems including respiratory disease, difficulty in breathing, and premature death [11]. Moreover, accumulation of NO<sub>x</sub> that is come from the air into water, lowering the

oxygen concentration in the water, causes acidification and eutrophication of lakes, which can damage the survival of aquatic plants and other organisms [8].

Prediction of NO<sub>x</sub> has great importance for these environmental and health concerns. Current air quality monitoring systems provide a great amount of dataset and therefore, loss of data is occurred commonly due to instrument break down, failure of data transmission and maintenance, etc. Therefore, these monitoring techniques have failed to measure the NO<sub>x</sub> concentration for monitoring air quality and exhibited low precision in long-term predictions according to industrial and meteorological changes [2].

In recent years, artificial neural network structures (ANNs) have been widely used as a well-known technique of capturing nonlinear relations for air pollutants prediction and air quality monitoring [6]. ANN modeling is a proper mathematical approach for demonstrating highly complex relationships and can be generalized accurately when new input parameter was presented [5]. Compared to the traditional modeling

### Article History:

Received: 2020/02/21

Accepted: 2020/11/14

Online: 2020/12/31

**Correspondence to:** Uğur Özveren,  
Department of Chemical Engineering,  
Marmara University, Istanbul, Turkey  
Tel: +90 5358837701  
Fax: +90 2163480293  
E-Mail: ugur.ozveren@marmara.edu.tr

techniques, ANN is a data driven, self-adaptive, black-box method, which learns from examples.

There are several studies on prediction of ground-level air pollutants have been conducted with an ANN model. Sofuoglu et al. [12]. utilized an ANN model that examines meteorological parameters (wind speed and temperature) and measured particulate matter concentrations as input variables, to forecast  $\text{SO}_2$  concentrations in Izmir. Baawain and AS Al-Serhi [6] proposed a rigorous method of preparing air quality data to achieve more accurate air pollution prediction models which based on an artificial neural network (ANN). Lal Benjamin et al. [5] developed two air quality prediction models using feed-forward neural network to predict  $\text{NO}_x$  concentrations in Ujjain city that belongs to India. However, there aren't any study for the air quality prediction in Adana.

The main aim of the present study is to reveal the impact of meteorological and air pollutant influence for  $\text{NO}_x$  prediction in Adana. Therefore, a method based on artificial neural networks (ANNs) model generation is presented to forecast monthly  $\text{NO}_x$  concentrations in Adana province. Meteorological influencing factors including wind rate (km/h), temperature ( $^{\circ}\text{C}$ ), and  $\text{SO}_2$  concentrations ( $\mu\text{g}/\text{m}^3$ ) which is related traffic and industrial effect were selected as input variables to develop neural network model that is capable of estimating  $\text{NO}_x$  concentrations ( $\mu\text{g}/\text{m}^3$ ) as output parameter.

## MATERIAL AND METHODS

### Material

Adana is the sixth largest city of Turkey with 1,854,270 inhabitants in 2017 [13]. The city of Adana is also localized in the interface of developed and relatively underdeveloped cities in Turkey. Therefore, high unusual urbanization rate (75%) is occurred due to migration from rural areas and the lack of resources and it can cause urban problems. As conclusion, the  $\text{NO}_x$  yearly average for Adana is supposed as the higher levels compared to the other locations of Turkey. The monthly variations of average  $\text{NO}_x$  and  $\text{SO}_2$  emissions in Adana between 2014 and 2018, which was obtained from Republic of Turkey Ministry of Environment and Urbanization, "Air Quality Monitoring Stations" website [14] have been presented in Table 1. The monthly average of wind rate and temperature values in Table 1. have been acquired by using World Weather Online website [15]. The dataset was selected by randomly by using MATLAB SOFTWARE and was divided into three parts: training, validation, and testing.

**Table 1.** The monthly variations of average  $\text{NO}_x$  emissions.

Year	Month	$\text{SO}_2$ ( $\mu\text{g}/\text{m}^3$ )	Wind Rate (km/h)	Temperature ( $^{\circ}\text{C}$ )	$\text{NO}_x$ ( $\mu\text{g}/\text{m}^3$ )
2018	January	5.214576	8.4	9	34.87
	February	3.762245	7.7	12	20.45
	March	3.762245	7.5	15	20.45
	April	3.781792	7.8	18	21.88
	May	1.761529	8.4	24	7.87
	June	9.736235	9.3	26	10.67
	July	7.713672	10.1	28	9.68
	August	3.622233	9.6	28	8.67
	September	10.90257	8.2	27	15.83
	October	10.40373	7.6	27	5.80
	November	11.93729	8.4	19	5.89
	December	11.40444	9.2	13	47.97
2018	January	6.260445	8.4	9	24.61
	February	7.510149	7.7	12	20.02
	March	8.140121	7.5	15	16.22
	April	10.08224	7.8	18	12.96
	May	8.284132	8.4	24	15.83
	June	12.01866	9.3	26	13.43
	July	6.105595	10.1	28	3.43
	August	4.848124	9.6	28	4.32
	September	6.035191	8.2	27	9.75
	October	7.267949	7.6	27	21.57
	November	4.333663	8.4	19	24.14
	December	10.53031	9.2	13	34.90
2017	January	1.535483	9.7	6	30.88
	February	1.707932	8	8	27.10
	March	3.868253	7.9	12	22.96
	April	6.838653	8.4	17	20.92
	May	5.529328	7.8	21	17.10
	June	6.997	8	26	12.17
	July	4.274731	9.4	30	11.75
	August	2.379242	9.5	29	12.84
	September	5.648059	8.2	27	18.59
	October	5.347702	7.8	21	26.04
	November	3.267917	8.4	15	36.67
	December	5.146672	7.7	12	56.06
2016	January	12.18788	9.4	7	33.45
	February	14.43249	7.6	12	33.21
	March	9.846644	9.1	14	21.49
	April	11.53489	7.8	19	17.36
	May	10.24737	8.5	21	13.36
	June	8.026418	8.6	26	14.27
	July	8.55995	8.9	29	9.26
	October	60.60736	7.2	22	30.41
	November	37.57438	7.7	15	44.48
	December	13.45699	9.8	7	36.70

**Table 1 (cont).** The monthly variations of average NO<sub>x</sub> emissions.

Year	Month	SO <sub>2</sub> (μg/m <sup>3</sup> )	Wind Rate (km/h)	Temperature (°C)	NO <sub>x</sub> (μg/m <sup>3</sup> )
Air Quality Monitoring Station: Meteoroloji 2015	January	8.707439	9.7	8	21.19
	February	6.15348	10.2	10	16.43
	March	8.704655	9.1	13	11.42
	April	11.22918	8.4	16	5.53
	May	7.167712	8.7	22	9.83
	June	4.619178	11.1	24	5.49
	July	4.435859	10.6	28	3.82
	August	6.281179	10	29	3.03
	September	8.634721	7.9	27	5.85
	October	8.059739	7.7	23	10.56
	November	8.29913	8.3	17	12.66
	December	9.163185	8.2	11	13.50
Air Quality Monitoring Station: Vallik 2014	January	22.57541	7.8	10	66.68
	February	6.273418	7.9	11	58.34
	March	4.833347	9.5	13	45.08
	April	2.458409	7.6	17	24.94
	May	4.003284	7.4	21	17.92
	June	4.180194	8	25	14.65
	July	3.801008	9.9	27	10.78
	August	4.205149	8.5	28	12.70
	September	3.965452	8.3	25	20.83
	October	4.155049	7.5	21	39.53
Air Quality Monitoring Station: Meteoroloji 2014	January	11.08059	7.8	10	52.07
	February	9.447555	7.9	11	37.00
	March	3.383083	9.5	13	32.24
	April	2.053013	7.6	17	20.16
	May	2.468017	7.4	21	22.68
	June	2.852342	8	25	21.32
	July	3.486149	9.9	27	23.54
	August	3.21794	8.5	28	38.03
	September	3.877626	8.3	25	59.84
	October	4.591569	7.5	21	48.37

## Material

### Artificial neural network

ANN is a set of algorithms includes the functions of neurons that simulates massively parallel-distributed information processing system, inspired by neuroscience. The most commonly used ANN is multi-layer perceptron (MLP) based feed-forward back propagation model. MLP is a layered neural network structure (Fig. 1) with more than a single layer including one or several neuron(s). In this structure, the input of a layer is the output of the previous layer which is achieved through the activation function. As a result, the equation to determine the output of an artificial node *j* is given by:

$$h_k = f\left(\sum_{i=1}^n x_i \cdot w_{ki} + b_k\right) \quad (1)$$

where *h<sub>k</sub>* is the calculated value called output from the *i*<sup>th</sup> node at the previous layer, *w<sub>ki</sub>* is the weight of the artificial node between *i*<sup>th</sup> and *k*<sup>th</sup> node, and *b<sub>k</sub>* is the bias value. The net weights *w<sub>ki</sub>* and biases *b<sub>k</sub>* are calculated based on training algorithm. Along training procedure, training algorithm is updated the weights and deviations to reduce the error between predicted and actual values of the model. In this study we used back propagation algorithm as a training algorithm, which is accomplished through adjusting the gradient weights to minimizing the difference between target output and network output respectively.

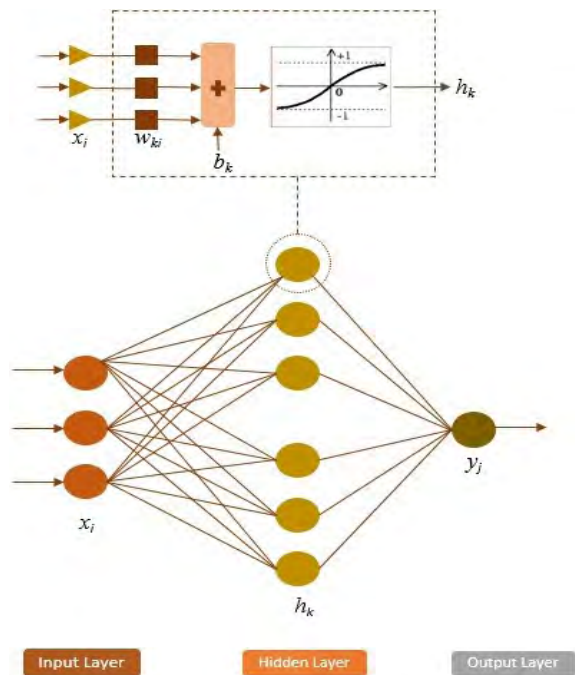


**Figure 1.** The structure of a multilayer perceptron neural network.

Backpropagation algorithm is probably the most popular learning algorithm for supervised learning of artificial neural networks using gradient descent based on generalizing the Widrow-Hoff learning rule. In this study, backpropagation algorithm, which is widely applied in a variety of engineering applications, was applied as the learning algorithm of ANN model.

### Levenberg-Marquardt Algorithm

The Levenberg-Marquardt (LM) is the most used regularization algorithm for backpropagation algorithm to minimize the Mean Squared Error (MSE) of proposed neural network structure. This optimization algorithm is a kind of pseudo second order method and determines the best direction to move the weights with minimization methods accurately when model network topology has

small size. Additionally, the Levenberg–Marquardt algorithm is an iterative process to implement second-order training methods apply the Hessian matrix to determine weight values. The model validation criteria of the proposed ANN model are required to predict NO<sub>x</sub> concentration according to other published correlations on the base of the determination coefficient (R<sup>2</sup>) examination.

### Validation of the model

There are several types of correlation validation criteria exist with their own range of usability to examine the developed model efficiency. These parameters represent prediction accuracy of a statistical estimating method, which expresses generalization performance. Three statistical parameters are employed to make correlation for prediction of NO<sub>x</sub> concentration, which are computed as follows:

Correlation Coefficient (R<sup>2</sup>):

$$R^2 = 1 - \frac{\sum_{i=1}^n (y_{est} - y_{exp})^2}{\sum_{i=1}^n (y_{est} - \bar{y}_{exp})^2} \cdot 100\% \quad (2)$$

Mean absolute percentage error (MAPE):

$$MAPE = \frac{100}{n} \sum_{i=1}^n \left| \frac{Y_{actual} - Y_{predicted}}{Y_{actual}} \right| \quad (3)$$

Root mean squared error (RMSE):

$$RMSE = \sqrt{\frac{1}{n} \sum_{i=1}^n (Y_{predicted} - Y_{actual})^2} \quad (4)$$

## RESULTS AND DISCUSSION

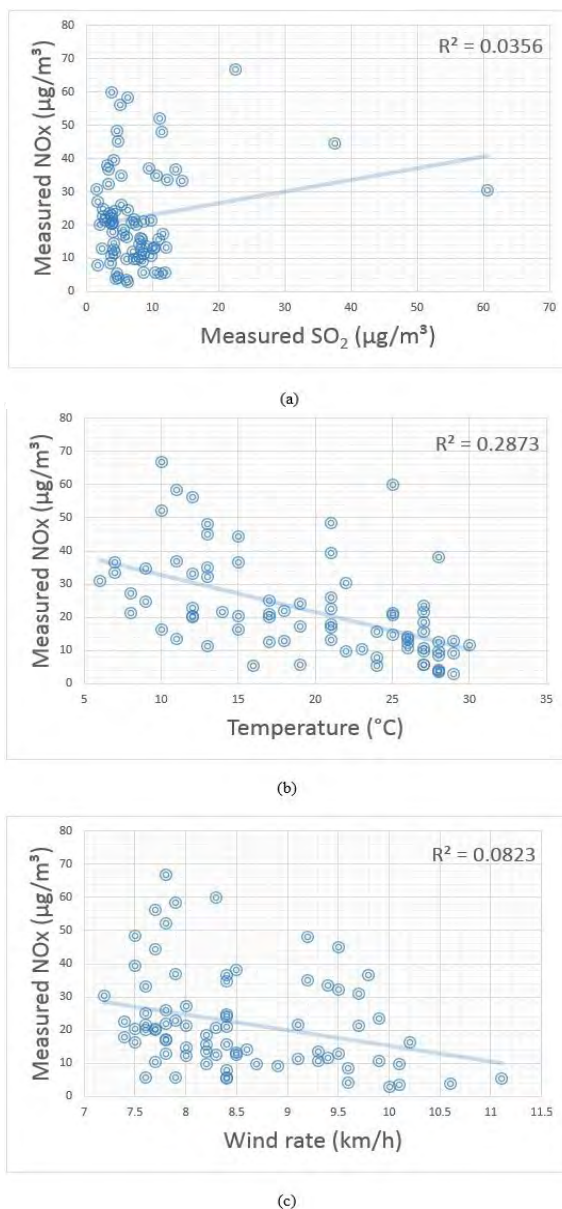
### The Impact of Input Parameters

Fig. 2 were generated by plotting the individual input parameters that are SO<sub>2</sub> (µg/m<sup>3</sup>), temperature (°C) and wind rate (km/h) of the air quality prediction against the corresponding measured NO<sub>x</sub> values.

It is concluded that linear models for individual parameters may not represent the most proper solution to precisely estimate measured NO<sub>x</sub> emissions. This complexity due to the nonlinearity can be handle using artificial intelligence based on data-driven modeling in the form of ANNs.

### Neural Network Model

In this study, the feed-forward multi-layer neural network is used due to its ability to model very effectively any measurable input-output relationship to any desired degree of accuracy. The ANN model consists of three input variables: i) SO<sub>2</sub> (µg/m<sup>3</sup>), ii) wind rate (km/h), iii) temperature (°C). The input data was split into test, training and validation sets.



**Figure 2.** Graphics of the measured NO<sub>x</sub> values against input values that are (a) SO<sub>2</sub> (µg/m<sup>3</sup>), (b) wind rate (km/h) and (c) temperature (°C).

In the absence of any accurate theory to calculate the number of artificial neurons and hidden layers, the network structure related model parameters were calculated heuristically by using trial and error methods. Therefore, the applicability of 350 different ANN models was examined with various activation functions and topology including different number of hidden layers. As seen on Fig. 3, the developed ANN model includes four layers that are input layer, output layer, and two hidden layers.

The first hidden layer has thirty neurons and the second hidden layer consists of four neurons. The tangent sigmoid (tansig) functions were used for the neurons input layer, first and second hidden layers respectively, and line-

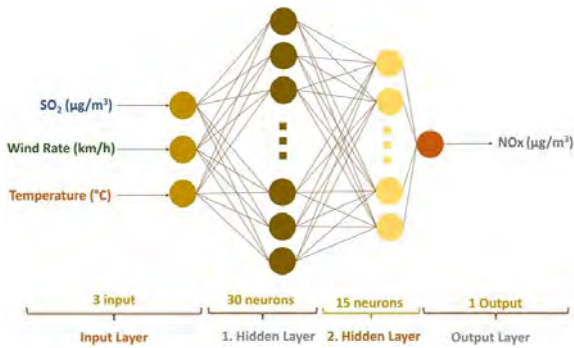


**Figure 3.** Artificial Neural Network Model.

ar function was utilized for output layer. In order to use an artificial neural network model, one needs first to train the proposed model with training dataset. Fig. 4 shows the values obtained training datasets which reached an overall score of 0.8927 when using the Levenberg-Marquardt regularization method. According to this figure, the correlation between the predicted and measured values was high enough to assert that the developed ANN model demonstrates a good agreement with the training datasets.

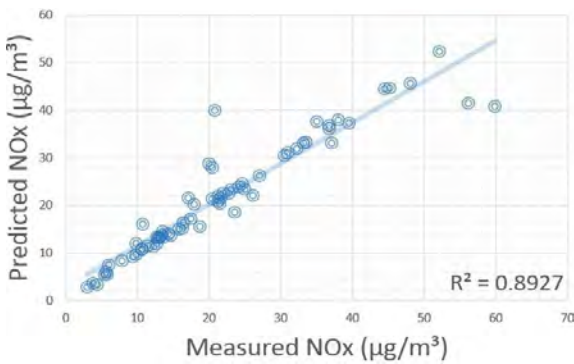


**Figure 4.** Comparing the predicted and measured NOx values that obtained training data sets.

The validation dataset was used to stop training early if the model performance fails. As seen on Fig. 5,  $R^2$  is higher than 0.90 for the validation set. The network structure is capable to generalize the prediction of  $\text{NO}_x$  emissions.

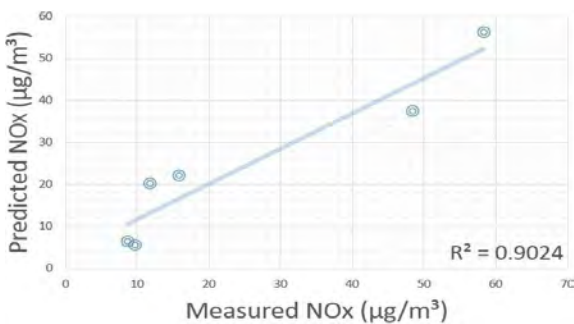


**Figure 5.** Comparing the predicted and measured NOx values that obtained validation data sets.

Fig. 6 indicated that the prediction performance of the

**Table 2.** MAPE and RMSE results for the prediction of  $\text{NO}_x$  emissions in the training, validation and test dataset.

	Root mean squared error (RMSE)	
Training	Root mean squared error (RMSE)	4.32
	Mean absolute percentage error (MAPE)	8.96
Validation	Root mean squared error (RMSE)	6.46
	Mean absolute percentage error (MAPE)	33.99
Test	Root mean squared error (RMSE)	4.38
	Mean absolute percentage error (MAPE)	28.81

ANN model with testing datasets is better than against its training performance. The test data result indicates that the predicted value of  $\text{NO}_x$  concentration is fitted to the measured value, the correlation coefficient can meet the requirements for the estimation. Beyond that, the MAPE and RMSE results for each target were also examined. Table 2 lists the MAPE and RMSE values for the training, validation and test dataset.

## CONCLUSION

In this study, a new correlation based on ANN model approach was used for prediction of  $\text{NO}_x$  concentration ( $\mu\text{g}/\text{m}^3$ ) in Adana, which is rely on  $\text{SO}_2$  concentration ( $\mu\text{g}/\text{m}^3$ ) as an air pollutant and meteorological effecting parameters (wind rate (km/h), temperature ( $^{\circ}\text{C}$ )). The performance of the developed model ( $R^2 > 0.9568$ ) has been evaluated using measurements collected from weather stations in Adana. At the moment of writing this paper, we are not aware of other techniques for  $\text{NO}_x$  prediction in Adana.

The key merit of the proposed model in this study is an easy method to predict  $\text{NO}_x$  concentration when air monitoring station is not available. Therefore, the model could be utilized to provide air monitoring data at currently unmonitored locations in Adana, which obviate the necessity of a relatively high number of monitoring stations for describing the  $\text{NO}_x$  concentration.

## REFERENCES

1. Wang, J. and G. Song, A deep spatial-temporal ensemble model for air quality prediction. *Neurocomputing*, 314 (2018) 198-206.
2. Wen, C., et al., A novel spatiotemporal convolutional long short-term neural network for air pollution prediction. *Science of The Total Environment*, 654 (2019) 1091-1099.
3. Wang, X.-C., et al., Air pollution terrain nexus: A review considering energy generation and consumption. *Renewable and Sustainable Energy Reviews*, 105 (2019) 71-85.
4. Azid, A., et al., Prediction of the level of air pollution using principal component analysis and artificial neural network techniques: A case study in Malaysia. *Water, Air, & Soil Pollution*, 225(8) (2014) 2063.
5. Lal Benjamin, N., et al., Air quality prediction using artificial neural network. *IJCS*, 2(4) (2014) 07-09.
6. Baawain, M.S. and A.S. Al-Serihi, Systematic approach for the prediction of ground-level air pollution (around an industrial port)

- using an artificial neural network. *Aerosol and air quality research*, 14(1) (2014) 124-134.
7. Shakil, M., et al., Soft sensor for NO<sub>x</sub> and O<sub>2</sub> using dynamic neural networks. *Computers & Electrical Engineering*, 35(4) (2009) 578-586.
  8. Park, J.-H., et al., Historic and futuristic review of electron beam technology for the treatment of SO<sub>2</sub> and NO<sub>x</sub> in flue gas. *Chemical Engineering Journal*, 2018.
  9. Hoffman, S., Short-time forecasting of atmospheric NO<sub>x</sub> concentration by neural networks. *Environmental Engineering Science*, 23(4) (2006) 603-609.
  10. Shi, J.P. and R.M. Harrison, Regression modelling of hourly NO<sub>x</sub> and NO<sub>2</sub> concentrations in urban air in London. *Atmospheric Environment*, 31(24) (1997) 4081-4094.
  11. Carbajal-Hernandez, J.J., et al., Assessment and prediction of air quality using fuzzy logic and autoregressive models. *Atmospheric Environment*, 60 (2012) 37-50.
  12. Sofuoglu, S.C., et al., Forecasting ambient air SO<sub>2</sub> concentrations using artificial neural networks. *Energy Sources, Part B*, 1(2) (2006) 127-136.
  13. Unsal, F., Globalization and the mid-rank city: The case of Adana, Turkey. *Cities* 21(5) (2004) 439-449.
  14. <https://www.havaizleme.gov.tr/>, 2019
  15. <https://www.worldweatheronline.com/adana-weather-averages/adana/tr.aspx>, 2019

# In Vitro Study on the Influence of Proline on Struvite Crystals

Sevgi Polat  Perviz Sayan 

Marmara University, Department of Chemical Engineering, Istanbul, Turkey

## ABSTRACT

This study investigated the effect of amino acid proline, as crystal modifier, on the struvite crystallization in vitro conditions. The struvite crystals were evaluated experimentally through XRD, SEM, and FTIR to determine the structure, morphology, and chemical composition, respectively. XRD analysis pointed out that struvite crystals belonged to the orthorhombic  $Pmn2_1$  space group. SEM analysis depicted that proline had a significant influence on the morphology as well as the particle size of the struvite. Moreover, the length and width of struvite crystals varied with different concentrations of proline. The length of struvite crystals decreased, and their width thickened in the presence of the crystal modifier. The negativity of the zeta potential value became less negative in the presence of proline and the values were determined to be  $-6.10$  mV and  $-4.00$  mV for 25 and 100 ppm, respectively. According to BET analysis results, the surface area of the struvite decreased in the proline media when compared with the crystals formed without the crystal modifier. In addition, the thermal degradation of the formed crystals was examined. Regarding the results of the thermodynamic analysis, the average  $\Delta H$ ,  $\Delta G$ , and  $\Delta S$  were 92.17 kJ/mol, 197.85 kJ/mol, and  $-254.63$  J/mol K, respectively. As a result, this study could provide a potential crystal modifier for the inhibition of struvite stones.

### Keywords:

Struvite, Crystal Morphology, Crystallization, Characterization, Proline.

### Article History:

Received: 2020/05/03

Accepted: 2020/11/28

Online: 2020/12/31

Correspondence to: Sevgi Polat,  
Marmara University, Department of  
Chemical Engineering, Istanbul, Turkey  
E-Mail: sevgi.polat@marmara.edu.tr

## INTRODUCTION

In urolithiasis, stones are formed in the urethra, kidney, or bladder. Kidney stones cause severe pain in the abdomen and flank [1]. Supersaturation of urine leads to the formation of kidney stones, and their formation is dependent on the pH, ionic strength, specific gravity, and solute concentration of urine [2]. Five types of urinary stones are primarily encountered: calcium oxalate, calcium phosphate, urates, cysteines, and magnesium ammonium phosphate hexahydrate ( $MgNH_4PO_4 \cdot 6H_2O$ , struvite) [3,4]. Of these types of stone, struvite is unique owing to its association with the presence of infection in the urinary tract and thus struvite stones are also called infection stones [1,4]. The main cause of the infection is urease-producing organisms, such as *Proteus* spp., *Klebsiella pneumoniae* spp., and *Providencia* spp [5,6]. Urease is a characteristic bacterial enzyme that hydrolyzes the urea ( $H_2N-CO-NH_2$ ) in urine to form ammonia [1,5]. As a result of this hydrolysis reaction, the pH of the urine and then the concentration of ammonia ( $NH_4^+$ ) and phosphate ( $PO_4^{3-}$ ) in the urine increases

[5]. These urea ions combine with the  $Mg^{2+}$  that is normally present in urine under alkaline conditions, leading to the formation of struvite [7,8]. Naturally formed struvite crystals usually exhibit coffin-like morphology, but when they grow rapidly dendrites can also occur [7,9]. The dendrite form of struvite crystals is particularly dangerous because they damage the epithelium of the urinary tract as they move through it [7]. If the problems related to struvite stones are not treated appropriately, kidney loss may be seen. Moreover, the high rate (up to 50%) of recurrence of infection stones leads to serious medical problems [9]. Thus, the precipitation of struvite is an important medical research topic that needs to be addressed. Currently, urinary stones are usually treated using drug therapy for pain relief and inflammation reduction, whilst surgery is applied in extreme cases. Acetohydroxamic acid is prevalently used for treatment of patient suffering from struvite stones. However, the potential side effect of acetohydroxamic acid cannot be ignored. Thus, alternative ways to

eliminate health problem related to struvite stones have gained a great importance [1]. For these reasons, many studies have been conducted on the struvite precipitation in urine to eliminate these problems with an alternative way. Li et al. proved the inhibitory effects of polyaspartic acid with different concentrations on the struvite crystallization [10]. Olszynski et al. revealed that nanosilver particles having different size and shape had a distinctive impact on the growth process of struvite in artificial urine in the presence of *Proteus mirabilis* [11]. They showed that nanosilver particles had an inhibitory effect on struvite formation depending on their size and shape and also observed that smaller particles exhibited greater negative effect on the growth of struvite. Moreover, Manzoor et al. performed a study to understand the role of vitamin C on struvite precipitation. They revealed that vitamin C or ascorbic acid modulated the formation of struvite crystals in the presence of uropathogenic bacteria [12]. The growth rate of the struvite crystals decreased depending on the increasing vitamin C concentration. Sayan et al. [13] researched the influence of different amino acids such as lysine, proline, alanine and tryptophane with different concentrations on struvite crystals at 37 °C and pH 8. Adding these additives in studied concentrations did not lead to any changes in crystal morphology and structure. Although several studies are reported in the literature regarding struvite urinary stone formation, more research on struvite crystallization is still needed to find a viable method of removing struvite stones to give a suitable treatment alternative. Thus, studying the influence of crystal modifiers, especially biocompatible modifiers, on the precipitation of struvite is a highly attractive and promising research area to solve this problem. Proline, a type of nonessential amino acid, was studied in vitro as a crystal modifier to struvite crystallization media and found to be a potent inhibitor of struvite crystallization.

## MATERIAL AND METHODS

Magnesium chloride hexahydrate ( $\text{MgCl}_2 \cdot 6\text{H}_2\text{O}$ ), ammonium dihydrogen phosphate ( $\text{NH}_4\text{H}_2\text{PO}_4$ ), L-proline ( $\text{C}_5\text{H}_9\text{NO}_2$ ), and sodium hydroxide (NaOH) were of reagent grade and purchased from Merck Company. Distilled water was utilized when preparing the solutions. All experiments were performed at least in triplicate.

The crystallization experiment was conducted in batch mode at 37 °C in a double-jacketed crystallizer.  $\text{MgCl}_2 \cdot 6\text{H}_2\text{O}$  and  $\text{NH}_4\text{H}_2\text{PO}_4$  were used as the reactants for struvite crystallization. The procedure was as follow: Firstly, 1M  $\text{MgCl}_2 \cdot 6\text{H}_2\text{O}$  and 1M  $\text{NH}_4\text{H}_2\text{PO}_4$  solutions were prepared. 300 ml of  $\text{MgCl}_2 \cdot 6\text{H}_2\text{O}$  solution was put into the crystallizer. The solution was maintained at a constant temperature of  $37 \pm 0.5$  °C using a thermostat. The stirring rate was 500 rpm. When the solution reached its target temperature and

equilibrium, the  $\text{NH}_4\text{H}_2\text{PO}_4$  solution was placed into the crystallizer via a peristaltic pump at a flow rate of 5 ml/min. During the crystallization process, the pH of the solution was continuously followed and kept at pH 7.4 using dilute sodium hydroxide.

The effect of proline and its concentration on the crystallization of struvite was examined in this study. Proline solution was added to the crystallizer via an infusion pump to provide the desired concentrations of 25 and 100 ppm in the crystallizer. At the end of the experiments, all suspension was taken from the crystallizer, filtered and collected the solid and liquid separately. Finally, the upper solid phase washed thoroughly with distilled water. The prepared crystals were dried at room temperature and the samples are kept for further analysis.

X-ray diffraction (XRD; Bruker D2 Phaser benchtop) was used to identify the phase structure of the struvite crystals. The functional groups of samples were confirmed by ATR method on a Fourier Transform-Infrared Spectrometer (FTIR; Shimadzu). The crystal size and morphology of the struvite were investigated by particle size analyzer (Malvern) and scanning electron microscopy (SEM, Zeiss EVO LS 10), respectively. The length and width of the struvite crystals were determined using Data Translation Image-Pro Plus image analysis software. BET analysis was performed by a Quantachrome Autosorb SI instrument to investigate the surface area of the products. Moreover, zeta potential of the samples was analyzed using a Malvern Zetasizer Nano ZS to detect the surface charge of the struvite. The thermal property of the struvite formed was determined using a Setaram LABSYS Evo thermogravimetric analyzer in a  $\text{N}_2$  atmosphere between 30 °C and 500 °C with a heating rate of 10 °C/min.

## RESULTS AND DISCUSSION

### XRD Analysis

The structure analysis of the struvite crystals formed in the absence and presence of proline was performed and the XRD diffraction patterns are shown in Fig. 1. In pure media, the main diffraction peaks were distributed at 14.9°, 20.8°, 27.0°, and 33.2°, corresponding to crystal lattice planes (101), (111), (103), and (022) of struvite, indicative of high crystallinity of struvite. The relevant results were consistent with the literature reports [14,15]. The crystal obtained belonged to the orthorhombic  $Pmn2_1$  space group. The diffraction peaks of the (101), (111), (103), and (022) crystal planes were observed among all the samples prepared under different conditions, which confirmed that the prepared crystals with and without proline were in the struvite form, indicating that no intermediate phase was occurred.



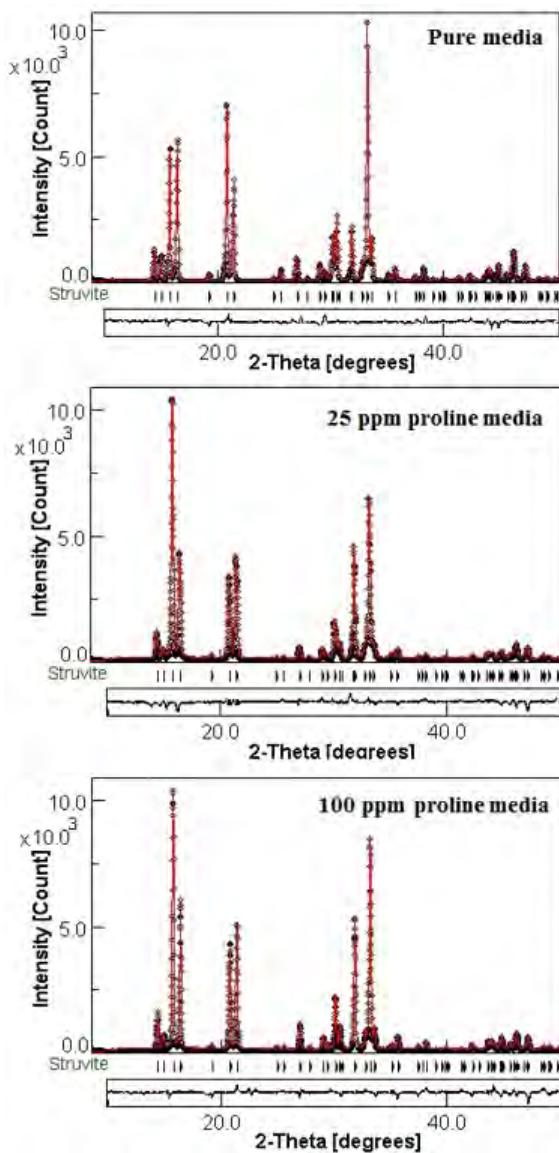


**Figure 1.** XRD results for struvite crystals obtained with and without proline

The addition of proline caused to change the intensity of the diffraction peaks. The *a*, *b* and *c* unit cell parameters were 6.957 Å, 6.138 Å, and 11.220 Å for pure media, and these parameters were 6.970 Å, 6.147 Å, and 11.224 Å; 6.967 Å, 6.146 Å, and 11.225 Å for the struvite crystals formed in the presence of 25 and 100 ppm media, respectively.

### FTIR Analysis

The struvite samples prepared were characterized by FTIR spectrometer to identify the functional groups on the surface of the samples. FTIR was also used to analyze the adsorption of the proline modifier on the surface of

struvite. Fig. 2 illustrates the spectra of struvite obtained in the absence and presence of proline. The FTIR result of the crystal obtained in pure media showed the specific peaks of struvite at  $\sim 2900\text{ cm}^{-1}$  (N-H stretching),  $\sim 2350\text{ cm}^{-1}$  (O-H stretching),  $\sim 1430\text{ cm}^{-1}$  (N-H stretching), and  $\sim 980\text{ cm}^{-1}$  (PO<sub>4</sub><sup>3-</sup> stretching) which was consistent with the literature [16-18]. Furthermore, the peaks at  $\sim 880\text{ cm}^{-1}$  and  $\sim 760\text{ cm}^{-1}$  were associated with the hydrogen bond in the absorption peaks of weak water-water and ammonium-water bonds, respectively.

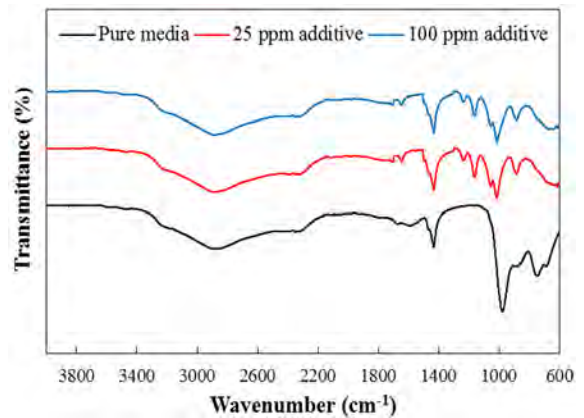


**Figure 2.** FTIR results for struvite crystals obtained with and without proline

Compared with the FTIR spectrum of struvite without crystal modifier, the new absorption bands between  $1250$  and  $1100\text{ cm}^{-1}$  were observed for the struvite obtained with proline. Another important difference was the intensity of the peaks. These changes suggested that the proline interacted with the surface of the struvite.

### Zeta Potential Analysis

To further reveal the adsorption characteristics of proline on struvite crystals, the surface charges of the crystals were measured, and the zeta potential analysis results are given in Fig. 3.

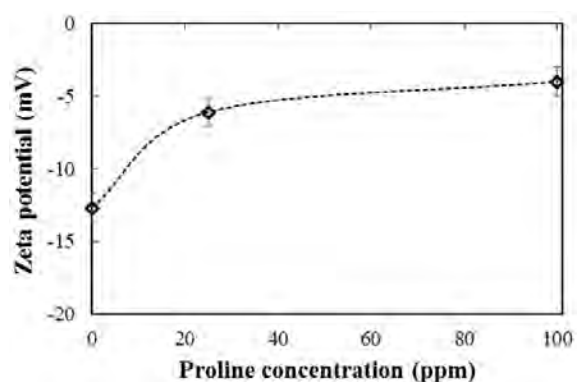


**Figure 3.** The variation of zeta potential with proline concentration

The surface charge of the struvite crystals formed in pure media was  $-12.70$  mV. It can be seen in Fig. 3, the zeta potential value reached  $-4.00$  mV at 100 ppm crystal modifier concentration, compared with the value of  $-6.10$  mV at 25 ppm concentration. These results clearly illustrated that less negative surface charge value was obtained at higher proline concentration, which might result in more electrostatic repulsion between struvite surface and the positively charged proline species. Thus, crystal modifier concentra-

tion increase can strengthen the proline adsorption, and finally increase in the inhibitory effect.

### Morphology Analysis

To clarify the size and morphological changes of the crystals obtained under different proline concentrations, the SEM analysis were performed. The SEM images taken at different magnifications and the particle size distributions are shown in Fig. 4 and 5, respectively.

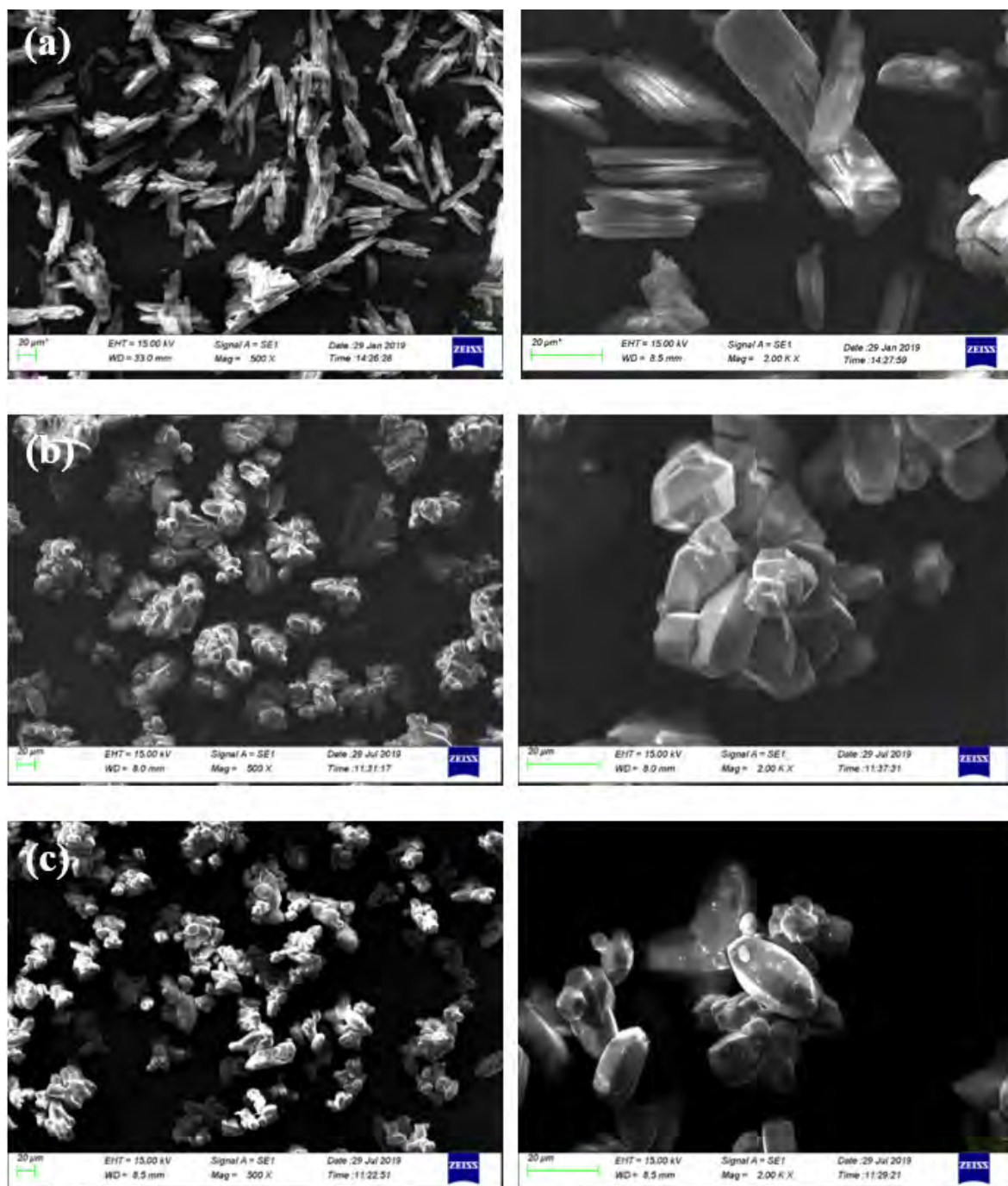


**Figure 4.** SEM photos of struvite crystals obtained in pure media (a), in the presence of 25 ppm (b) and 100 ppm (c) proline media

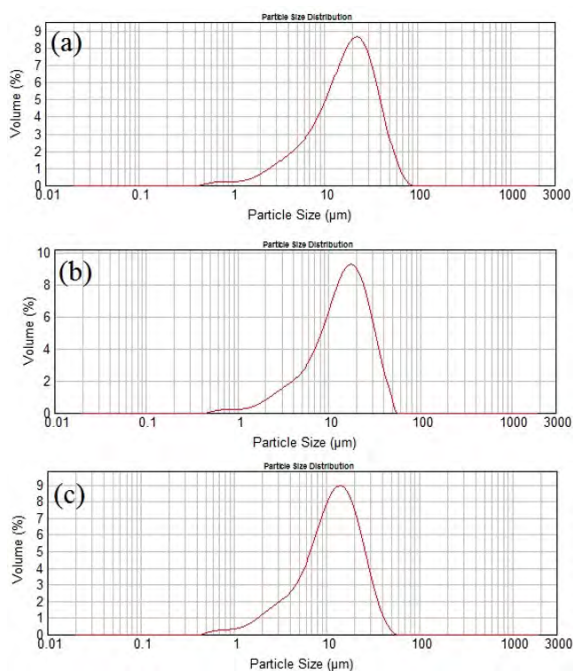


**Figure 5.** Particle size distributions of struvite obtained in pure media (a) and in the presence of 25 ppm (b) and 100 ppm (c) proline media

The rod-like struvite crystals with a mean size of  $18.0 \pm 1.8 \mu\text{m}$  were synthesized in pure media. The struvite obtained in pure media had homogenous-looking and regular form. Meanwhile, they had the tendency of growing on each other and the surface of the rod-like crystals were porous.

The BET surface area of struvite obtained in pure media was determined to be  $241.93 \text{ m}^2/\text{g}$ . The length, width and aspect ratio of products are displayed in Fig. 6. The length and width of struvite crystals varied with different concentrations of proline. The rod-like struvite crystals had an aspect ratio of  $0.363 \pm 0.19$  and a mean length of  $40.10 \pm 2.1 \mu\text{m}$ . According to SEM images, the crystal morphology of the struvite can be significantly changed with addition of the proline to crystallization media. Therefore, it is inferred that proline has ability to control the crystal morphology of struvite. The surface properties and morphology of struvite crystals were connected to the concentration of proline. By increasing the proline concentration to 25 ppm, the mean width reached to  $20.0 \pm 2.9 \mu\text{m}$  and the mean length dramatically decreased to  $23.15 \pm 2.4 \mu\text{m}$ . The particle size of the samples obtained in the solutions with proline were reduced due to the surface adsorption of proline. As seen in Fig. 5, the mean particle size of the struvite crystals obtained in media supplemented with 25 and 100 ppm proline were  $14.6 \pm 2.2 \mu\text{m}$  and  $10.4 \pm 1.4 \mu\text{m}$ , respectively. The morphology results for the crystals obtained with varying concentrations of modifier are consistent with the particle size results.

At 100 ppm proline concentration, the surface of the struvite crystals was smooth, non-porous and smaller

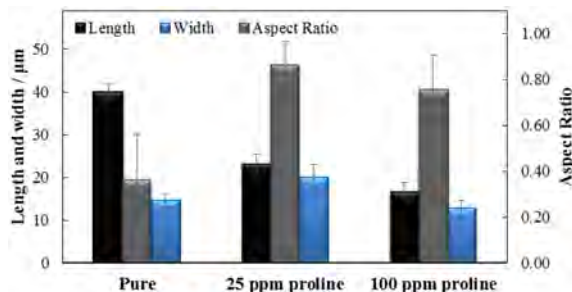


**Figure 6.** Effects of proline on the length, width, and aspect ratio of struvite crystals

crystals were precipitated. The BET surface area of the struvite crystals decreased  $0.034 \text{ m}^2/\text{g}$  at 100 ppm, compared with the value of  $9.30 \text{ m}^2/\text{g}$  at 25 ppm modifier concentration. For specific surface area aspect, a higher proline concentration value led to a lower BET surface area. Fig. 6 shows that mean width and mean length of struvite crystals obtained with proline were determined to be  $12.67 \pm 1.8 \mu\text{m}$  and  $16.75 \pm 1.9 \mu\text{m}$ , respectively. The quantitative variations in crystal morphology showed that with the increase of the proline concentration, the struvite crystals were shortened in length and enlarged in width, resulting in the increase of aspect ratio. The morphology results indicated that the presence of proline can effectively hindered the crystal nucleation and growth of struvite, and the magnitude of the effect depended on the proline concentration. Thus, it can be concluded that proline is an effective crystal modifier to control the crystal habit of struvite. The morphological transformation can be performed, short rod crystals with smaller particle size can be obtained in the presence of proline. This change could be explained by an adsorption mechanism. The adsorption of proline accounted for its interaction with struvite. Proline can bound on the active growth surface by chemical, physical forces and electrostatic interaction between proline and struvite; it could slow the growth rate on the crystal faces and thus lead to a modification of the habit of crystals grown in its presence of the crystal modifier.

### Thermal Analysis

Thermogravimetric analysis was utilized for the evaluation of the thermal degradation behavior of struvite crystals obtained with and without crystal modifier. The TG and DTG curves are illustrated in Fig. 7. As observed in Fig. 7, the thermal degradation of struvite crystals obtained with and without proline included one main step, which corresponded to the ammonium degradation and the loss of water simultaneously in the temperature range of approximately  $70\text{--}200 \text{ }^\circ\text{C}$  [19]. In accordance with the literature [20], the total weight loss of the struvite obtained without crystal modifier was  $\sim 51.0\%$ . Unlike the crystals from the pure media, the increment of  $1.8\%$  was observed for the struvite obtained in media supplemented with 100 ppm proline. Moreover, the addition of

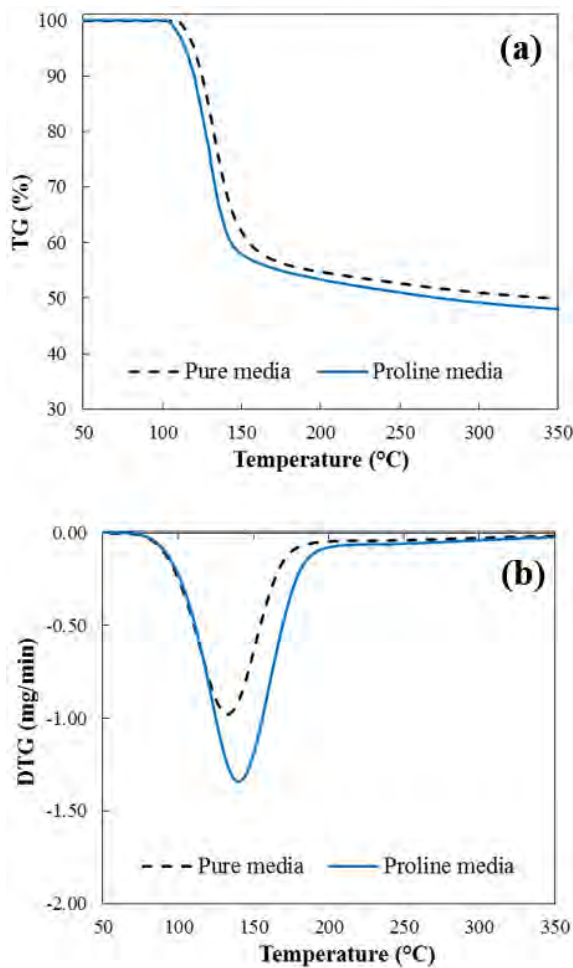


**Figure 7.** TG (a) and DTG (b) results of the struvite obtained with and without proline

the crystal modifier was found to shift the degradation temperature higher. The increased weight loss and shifting behavior of the peak temperature indicated that the proline adsorbed onto and interacted with the surface of the struvite.

In order to determine the activation energy during the thermal degradation of struvite, the Horowitz–Metzger equation was used for a first-order ( $n=1$ ) kinetic process as shown in Eq. (1) [21].

$$\lg \left[ \lg \left( \frac{w_\alpha}{w_\gamma} \right) \right] = \frac{E_a \theta}{2.303RT_{peak}^2} - \lg 2.303 \quad (1)$$

Where  $w_\gamma = w_\alpha - w$ ,  $\theta = T - T_{peak}$ ,  $E_a$  is the activation energy (kJ/mol),  $T_{peak}$  is the peak temperature of DTG curve,  $R$  is the ideal gas constant (8.314 J/mol K),  $w_\alpha$  is the final sample weight, and  $w$  is the sample weight at time  $t$ . According to the Eq. (1), when plotting of  $\lg[\lg(w_\alpha/w_\gamma)]$  versus  $\theta$ , the value of  $E_a/2.303RT_{peak}^2$  is obtained from the slope of the graph and the activation energy is calculated by using this

relation. Moreover, the thermodynamic parameters such as the enthalpy ( $\Delta H$ ), entropy ( $\Delta S$ ), and Gibbs free energy ( $\Delta G$ ) were also calculated.

The thermodynamic parameters such as enthalpy change ( $\Delta H$ ), Gibbs free energy change ( $\Delta G$ ), and entropy change ( $\Delta S$ ), were calculated using Eyring equations [22].

$$\Delta H = E_\alpha - RT \quad (2)$$

$$\Delta G = E_\alpha + RT_{peak} \ln \left( \frac{K_B T_{peak}}{hA} \right) \quad (3)$$

$$\Delta S = \frac{\Delta H - T_{peak} \Delta G}{T_{peak}} \quad (4)$$

Where  $K_B$  is the Boltzmann constant, and  $h$  is the Planck constant.

The activation energy was 95.6 kJ/mol for the struvite crystals obtained without crystal modifier. The values of  $\Delta H$ ,  $\Delta G$  and  $\Delta S$  were determined to be 92.17 kJ/mol, 197.85 kJ/mol, and -254.63 J/mol.K, respectively. The positive value of  $\Delta H$  calculated for the crystals attributed to the endothermic nature of thermal degradation process. The negative  $\Delta S$  entropy value revealed the decrease in randomness during the degradation process. The positive  $\Delta G$  showed that the degradation process of the struvite was nonspontaneous.

## CONCLUSION

In this study, the proline used as the crystal modifier with different concentration was studied to modify the crystal size and morphology of the struvite. XRD results showed that the crystals obtained were in orthorhombic structure. SEM images showed that proline had a significant modification effect on struvite morphology. With the increase of the proline concentration, the struvite crystals were shortened in length and enlarged in width, resulting in the increase of aspect ratio. In the presence of 100 ppm proline, the aspect ratio of struvite was  $0.756 \pm 0.15 \mu\text{m}$  with the mean length of  $16.75 \pm 1.9 \mu\text{m}$ . Zeta potential measurements showed that proline played a significant role in controlling the crystal surface charge during the crystal growth process. The value of zeta potential decreased along with the increase of crystal modifier concentration. The surface of the crystals became less negative in the presence of proline. From the characterization results, it is possible to conclude that proline has the ability to change the crystal size and morphology and it can be used a potential crystal modifier for the inhibition of struvite stones. In addition to characterization analysis, thermal degradation of the struvite crystals was investigated in this study. According to the kinetic analysis performed by Horowitz–Metzger model, the calculated activation energy value was 95.6 kJ/mol.

---


## References

---

1. Das P, Gupta G, Velu V, Awasthi R, Dua K. Formation of struvite urinary stones and approaches towards the inhibition—A review. *Biomed. Pharmacother.* 96 (2017) 361–370.
2. Manzoor MAP, Mujeeburahiman M, Ram Duwal S, Rekha P.D. Investigation on growth and morphology of in vitro generated struvite crystals. *Biocatal. Agric. Biotechnol.* 17 (2019) 566–570.
3. Griffith DP. Struvite stones. *Kidney International.* 13 (1978) 372–382.
4. Clapham L, Mclean RJC, Nickel JC, Downey J, Costerton, JW. The influence of bacteria on struvite crystal habit and its importance in urinary stone formation. *J. Cryst. Growth.* 104 (1990) 475–484.
5. Prwyer J, Olszynski M. Influence of disodium EDTA on the nucleation and growth of struvite and carbonate apatite. *J. Cryst. Growth.* 375 (2013) 108–114.
6. Siener R, Struwe F, Hesse A. Effect of L-methionine on the risk of phosphate formation. *Urology.* 98 (2016) 39–43.
7. Olszynski M, Prwyer J, Mielniczek-Brzoska E. Inhibition of struvite crystallization by tetrasodium pyrophosphate in artificial urine: Chemical and physical aspects of nucleation and growth. *Cryst. Growth Des.* 16 (2016) 3519–3529.
8. Olszynski M, Prwyer J, Torzewska A. Effects of size and shape of nanosilver particles on struvite and carbonate apatite precipitation. *Cryst. Growth Des.* 15 (2015) 3307–3320.
9. Abbona F, Boistelle R. Growth morphology and crystal habit of struvite crystal ( $MgNH_4PO_4 \cdot 6H_2O$ ). *J. Cryst. Growth.* 46 (1979) 339–354.
10. Li H, Yao QZ, Wang YY, Li YL, Zhou GT. Biomimetic synthesis of struvite with biogenic morphology and implication for pathological biomineralization. *Sci. Rep.* 5 (2018) 7718.
11. Olszynski M, Prwyer J, Torzewska A. Effect of size and shape of nanosilver particles on struvite and carbonate apatite precipitation. *Cryst. Growth Des.* 15 (2015) 3307–3320.
12. Manzoor MAP, Duwal SR, Mujeeburahiman M, Rekha PD. Vitamin C inhibits crystallization of struvite from artificial urine in the presence of *Pseudomonas aeruginosa*. *Int. Braz. J. Urol.* 44 (2018) 1234–1242.
13. Titiz-Sargut S, Sayan P, Masum A, Kiran B. Effect of Amino Acids on Magnesium Ammonium Phosphate Hexahydrate (Struvite) Crystallization. *Iranian Journal of Chemical Engineering.* 11 (2014) 3–18.
14. Kumari S, Jose S, Tyagi M, Jagadevan S. A holistic and sustainable approach for recovery of phosphorus via struvite crystallization from synthetic distillery wastewater. *J. Clean. Prod.* 254 (2020) 120037.
15. Prywer J, Torzewska A. Biomineralization of struvite crystals by *Proteus mirabilis* from artificial urine and their mesoscopic structure. *Cryst. Res. Technol.* 45 (2012) 1283–1289.
16. Chauhan CK, Joshi MJ. In vitro crystallization, characterization and growth-inhibition study of urinary type struvite crystals. *J. Cryst. Growth.* 362 (2013) 330–337.
17. Bindhu B, Thambi TA. Formation and Microanalysis of Struvite Urinary Calculi. *International Journal of Engineering Research and Applications.* 2 (2012) 1480–1485.
18. Polat S, Sayan P. Application of response surface methodology with a Box-Behnken design for struvite precipitation. *Adv. Powder Technol.* 30 (2019) 2396–2407.
19. Tansel B, Lunn G, Monje O. Review: struvite formation and decomposition characteristics for ammonia and phosphorus recovery: a review of magnesium-ammonia phosphate interactions. *Chemosphere.* 194 (2018) 504–514.
20. Frost RL, Weier ML, Erickson KL. Thermal Decomposition of Struvite— Implications for the decomposition of kidney stones. *J. Therm. Anal. Calorim.* 76 (2004) 1025–1033.
21. Horowitz HH, Metzger G. A new analysis of thermogravimetric traces. *Anal. Chem.* 35 (1963) 1464–1468.
22. Fernandez A, Mazza G, Rodriguez, R. Thermal decomposition under oxidative atmosphere of lignocellulosic wastes: different kinetic model application. *J. Environ. Chem. Eng.* 6 (2018) 404–415.



# Investigation of Underwater Wireless Optical Communication Channel Capacity for Different Environment and System Parameters

Yigit Mahmutoglu<sup>1</sup>  Cenk Albayrak<sup>2</sup>  Kadir Turk<sup>3</sup> 

<sup>1</sup>Recep Tayyip Erdogan University, Department of Electrical and Electronics Engineering, Rize, Turkey

<sup>2</sup>Karadeniz Technical University, Department of Energy Systems Engineering, Trabzon, Turkey

<sup>3</sup>Karadeniz Technical University, Department of Electrical-Electronics Engineering, Trabzon, Turkey

## ABSTRACT

Underwater wireless optical communication (UWOC) systems using the blue / green bands of the visible light spectrum stand out as an important solution in underwater applications that require high data communication rate such as remote sensing and navigation, real-time video transmission and imaging. The main factor that limits the data communication distance and determines the data rate in UWOC systems is the disruptive (absorption and scattering) effects of the underwater environment on optical waves. In this study, the signal to noise ratio (SNR) and channel capacity for UWOC systems are presented according to the divergence angle of the beam and the change in the aperture diameter of the receiver, which are the important parameters for UWOC systems. These examinations were repeated for pure sea water, clean ocean water, coastal ocean water and harbor water environments commonly used in the literature, and the obtained results were compared. With the presented results, the current limits for UWOC systems have been revealed and provide predictions about the applications that can be realized with UWOC systems for different environments..

### Keywords:

Underwater wireless optical communication, Channel capacity, Underwater wireless optical channel, Underwater optical noise, Underwater environments

## INTRODUCTION

Wireless data communication in the underwater environment started with the measurement of the sound velocity underwater in 1826. After that, it gained a strong acceleration with the submarine technology developed during the 1st and 2nd World Wars [1]. Today, high-speed real-time underwater wireless data communication is in huge demand in many commercial and military applications such as ocean exploration, offshore oil industry, remote controlled unmanned underwater vehicles, port security and control [2,3].

In underwater environment, data can be transmitted wirelessly by three types of waves: electromagnetic, acoustic and optical [4]. Since the electromagnetic waves attenuate rapidly in the underwater environment, the data communication distance and speed can be achieved at 10 m and Mbps levels, respectively [4,5]. Low frequencies are used in these systems because electromagnetic waves are attenuated less at lower frequen-

cies in the underwater environment. For this reason, the antenna lengths of the mentioned systems are getting larger. Moreover, high-power transmitters are needed for these systems [5].

Another alternative for wireless communication in underwater is acoustic communication systems [5]. It is possible to transmit data to kilometers away using acoustic waves. However, since the bandwidth of acoustic waves, that can be used for communication at these distances is quite narrow, data transmission can only be achieved at kbps levels [4]. Acoustic systems are costly because they need high power transmitters [5]. In addition, these systems cause high delay and have negative effects on marine life [6].

On the other hand, using the optical waves in the blue / green bands of the visible light spectrum, data transmission at Gbps data rate levels can be achieved at distances between 10 and 100 m [3,5]. In [7], using

### Article History:

Received: 2020/05/16

Accepted: 2020/09/28

Online: 2020/12/31

**Correspondence to:** Yigit Mahmutoglu,  
Department of Electrical and Electronics  
Engineering, Recep Tayyip Erdogan  
University, Rize, Turkey  
Tel: +90 4642237518  
Fax: +90 4642237514  
E-Mail: yigit.mahmutoglu@erdogan.  
edu.tr

a laser source with 15 mW power, a data transmission of 12.4 Gbps up to 6 m was achieved. In [8], using a laser source with a power of 2000-3000 mW, data rate ranging from Mbps to Gbps up to 80 was achieved. In [9], data communication was provided at a speed of 5 Gbps up to 64 m using a LED source with 3000 mW power. In [10], using a LED source with a power of 1000 mW, data transmission speeds of 1 Gbps up to 30-50 m distance were achieved. In [11], data transmission was provided at a speed of 1 Gbps up to 31 m distance by using a 100 mW LED source. Compared to electromagnetic and acoustic systems, in the underwater environment, UWOC systems are the only alternative for applications requiring high-speed data communication at short and medium range. In addition, UWOC systems need much lower transmit power to allow data communication in underwater environment.

In the field of wireless underwater communication, where interest has increased in recent years, UWOC systems attract the attention of technological and academic communities as a very important alternative due to the above mentioned features. Data transmission distance, data rate, reliability of transmission and similar features of UWOC systems are limited due to the disruptive (absorption and scattering) effects of the underwater environment on optical waves. In practice, it is important to identify effects of the underwater wireless optical channel in detail in order to determine the usage scenarios of UWOC systems and to design systems. In [12], where the Beer-Lambert channel model is employed, the effects of refractive index of the water and communication distance on SNR for four different water types have been examined. In [13], three different water types are considered and the performance of the UWOC system has been examined for various attenuation coefficients, where Monte Carlo channel model is used. In [14], channel capacity equations are derived for three situations depending on the ratio between the allowed average power and the allowed peak power based on the Beer-Lambert channel model. An examination has been given on the variation of the channel capacity according to the relevant conditions and three different water types. In [15] and [16], the performance of the UWOC system with impacts of air bubbles in the underwater environment and turbulence were examined, respectively. The studies outlined above do not fully provide the performance limits of a typical UWOC system. In this study, we have demonstrated the capacity limits that can be reached by distance in various underwater environments in case of changing important design parameters of the system such as the beam divergence angle and the aperture diameter of the receiver.

In this study, the variation of received powers and channel capacity for a typical UWOC system according to some basic system parameters and different water types was

investigated. With the presented results, the available limits for UWOC systems have been revealed and it is hoped that readers can be given an idea about the applications that can be realized with UWOC systems for various environments.

## ANALYSIS METHOD

In this study, first of all, underwater wireless optical communication channel for UWOC systems and the noise in this channel are introduced in section 2.1. and section 2.2., respectively. The method followed in the rest of the investigation is as follows. The power of the signal received from the transmitter at the receiver side, the signal to noise ratio (SNR) and the resulting channel capacity are examined. Received signal power and channel capacity are presented according to the variation in the divergence angle of the beam and the aperture diameter of the receiver which are important parameters for UWOC transmitter and receiver units. In addition, these examinations were repeated for pure sea water (PSW), clean ocean water (COW), coastal ocean water (CAOW) and harbor water (HW) environments, which are commonly considered in the literature, and the obtained results were compared.

## UNDERWATER WIRELESS OPTICAL COMMUNICATION CHANNEL

In optical wireless communication systems, the most common link used in point to point communication is line of sight (LOS) link. LOS scenario discussed in this study is shown in Fig. 1. In this scenario, the transmitter is assumed to direct the light towards the receiver. The Eq. (1) states the power of the optical signal received by the receiver [17].

$$P_{al} = P_{ve} \eta_{al} \eta_{ve} L_{yk} \left( \lambda, \frac{d}{\cos \theta} \right) \frac{A_{al} \cos \theta}{2\pi d^2 (1 - \cos \theta_0)} \quad (1)$$

Here,  $\eta_{al}$  and  $\eta_{ve}$  are optical efficiencies of receiver and transmitter,  $A_{al}$  is the aperture area of the receiver,  $P_{ve}$  is the average optical power of the transmitter,  $L_{yk} \left( \lambda, \frac{d}{\cos \theta} \right)$  is propagation loss factor,  $\lambda$  is wavelength of the light,  $d$  is the vertical distance between the receiver and the transmitter planes,  $\theta$  is the angle between the transmitter-receiver projection and the perpendicular to the receiver plane and  $\theta_0$  is divergence angle of the beam.

Due to its coaction with dissolved particles and water molecules in water, light is subject to a certain absorption and scattering depending on wavelength and distance [18]. These effects are expressed by the propagation loss factor given in the Eq. (2).



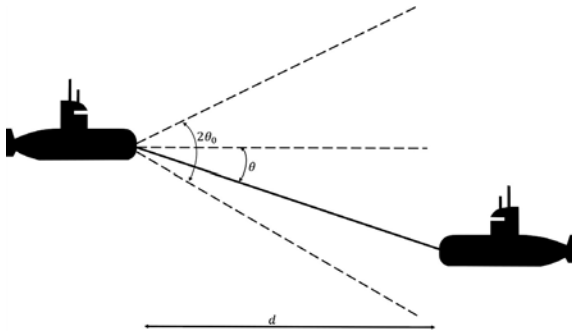


Figure 1. LOS communication scenario.

$$L_{yk} \left( \lambda, \frac{d}{\cos \theta} \right) = \exp \left[ -K(\lambda) \frac{d}{\cos \theta} \right] \quad (2)$$

Here,  $K(\lambda)$ , which can be calculated as in the Eq. (3), is the attenuation coefficient.

$$K(\lambda) = \alpha(\lambda) + \beta(\lambda) \quad (3)$$

Here,  $\alpha(\lambda)$  represents absorption coefficient and  $\beta(\lambda)$  stands for scattering coefficient. Absorption and scattering coefficients are two important factors that define light attenuation in the underwater environment. In absorption process, which is known as an energy transfer process, photons lose their energy and this energy turns into a different form: heat or chemical (photosynthesis). Scattering occurs when light interacts with the water molecules and atoms. While absorption causes the light to attenuate and the data communication distance to limit in a UWOC system, scattering decreases the amount of photons reaching the receivers and the SNR of the received signal [18]. Typical values of  $\alpha(\lambda)$ ,  $\beta(\lambda)$  and  $K(\lambda)$  are given in the literature as in Table 1 for four types of water: PW, COW, CAOW and HW. Attenuation coefficient depends on many parameters such as temperature, pressure, density of chlorophyll, plankton, detritus, colored dissolved organic materials and so on. Turbidity is effected by density of chlorophyll, plankton, detritus and colored dissolved organic materials [18]. Thus, the turbidity is directly proportional to the attenuation coefficient. For this reason, we can list the water types as pure water, clear ocean water, coastal ocean water and harbor water from small to large according to their turbidity levels. These water types (accordingly turbidity) represent the typical performance results for the best and worst cases and other cases between them for underwater wireless optical communication.

## NOISE

In the UWOC system, there are many noise sources that affect the optical signals transmitted wirelessly through

Table 1. Typical values of  $\alpha(\lambda)$ ,  $\beta(\lambda)$  and  $K(\lambda)$  for various water types [18].

Water types	$\alpha(\lambda) (m^{-1})$	$\beta(\lambda) (m^{-1})$	$K(\lambda) (m^{-1})$
PW (Pure Sea Water)	0.053	0.003	0.056
COW (Clean Ocean Water)	0.114	0.037	0.151
CAOW (Coastal Ocean Water)	0.179	0.219	0.398
HW (Harbor Water)	0.295	1.875	2.170

the underwater environment, in the photo-detector of the receiving unit. These noise sources can be listed as thermal noise, ambient light background noise, shot noise and dark current noise [10,19]. In this study, similar to [20], for the ease of operation, the shot noise was neglected and the total noise affecting the received signal by the photo-detector was composed of thermal, dark current and ambient light (solar) background noise components.

The main source of ambient light background noise is sunlight reflected from the surface of the water. The variance of ambient light background noise is calculated as given in the Eq. (4). Here  $q$  is the electronic charge,  $S$  is the sensitivity of the photo-detector and  $B$  is the electrical bandwidth.  $P_{sol}$  represents ambient light background noise power and is calculated as given in the Eq. (5).

$$\sigma_{sol}^2 = 2qSP_{sol}B \quad (4)$$

$$P_{sol} = \frac{\pi^2 D^2 (FOV)^2 \Delta \lambda T_F L_{sol}}{4} \quad (5)$$

Here,  $D$  is the aperture diameter of the photo-detector,  $FOV$  is the field of view of the system in radians,  $\Delta \lambda$  is the bandwidth of the optical filter and  $T_F$  is the optical filter transmissivity.  $L_{sol}$  is upwelling solar radiance and is calculated as given in the Eq. (6).

$$L_{sol} = \frac{ERL_{fac} e^{(-Kh)}}{\pi} \quad (6)$$

Here,  $L_{fac}$  is the factor that describes the directional dependence of the underwater radiance,  $E$  is downwelling irradiance,  $K$  attenuation coefficient,  $R$  is underwater reflectance of the downwelling irradiance and  $h$  is depth of the receiver.

Dark current noise is caused by constant current that occurs when light does not fall on the photo-detector. The variance of this noise is given in the Eq. (7). Here,  $I_{kar}$  denotes the dark current value.

$$\sigma_{kar}^2 = 2qI_{kar}B \quad (7)$$

Thermal noise varies depending on resistance, temperature and bandwidth, and the variance of thermal noise is calculated as given in the Eq. (8). Here  $k$ ,  $R_L$ ,  $T_e$ , and  $F$  are Boltzman constant, load resistance, temperature in Kelvin and noise figure of the system, respectively.

$$\sigma_{ter}^2 = \frac{4kT_eFB}{R_L} \tag{8}$$

The variance of the total noise affecting the signal received in the photo-detector is obtained as given in the Eq. (9).

$$\sigma_{top}^2 = \sigma_{sol}^2 + \sigma_{kar}^2 + \sigma_{ter}^2 \tag{9}$$

The channel capacity of a communication system is calculated as given in the Eq. (10) (the Shannon-Hartley theorem) depending on the signal to noise ratio and bandwidth [21].

$$R_b = B \frac{1}{2} \log_2 (1 + SNR) \tag{10}$$

## NUMERICAL RESULTS AND DISCUSSION

In this section, the effects of aperture diameter of the receiver and beam divergence angle parameters on the UWOC system are examined for various underwater environments. Depending on the parameters handled, variations in the channel capacity and power of the signal at the receiver are given and interpreted. Channel capacity is derived as in Eq. (11) using Eq. (1), Eq. (9) and Eq. (10). In the conducted studies, PSW, COW, CAOW and HW environments, which are widely used in the literature for comparison, have been taken into consideration. For these underwater environments,  $\alpha(\lambda)$ ,  $\beta(\lambda)$  and  $K(\lambda)$  coefficient values, which are given in Table1, are used. As given in Fig. 1, a scenario, where there is LOS link between the transmitter and receiver units (two underwater vehicles) and they communicate with each other via the UWOC system, is discussed. The parameter values for the UWOC system and the transmitter - receiver units are given in Table 2. In addition, it was assumed that the transmitter power is 1 Watt in all the studies.

$$R_b = B \frac{1}{2} \log_2 \left( 1 + \frac{P_{ve} \eta_{at} \eta_{ve} L_{yk} \left( \lambda, \frac{d}{\cos \theta} \right) A_{al} \cos \theta}{\sigma_{top}^2 2\pi d^2 (1 - \cos \theta_0)} \right) \tag{11}$$

For the mentioned water environments, the variations of the signal power at the receiver (photo-detector) accor-

**Table 2.**Parameter values of the mentioned UWOC system [10, 19, 22, 23].

	Parameter	Value
	Electrical bandwidth (B)	100 MHz
	Aperture diameter of receiver (D)	1-50 cm
	Beam divergence angle ( $\theta_0$ )	$1^0 - 30^0$
	Average transmitter optical power ( $P_{ve}$ )	1 W
	Depth of receiver (h)	30 m
	Wavelength ( $\lambda$ )	532 nm
	Angle between the perpendicular to the receiver plane and the transmitter-receiver projection ( $\theta$ )	$0^0$
System parameters	Field of view (FOV)	$40^0$
	Bandwidth of the optical filter ( $\Delta\lambda$ )	10 nm
	Optical efficiency of the transmitter ( $\eta_{ve}$ )	0.9
	Optical efficiency of the receiver ( $\eta_{at}$ )	0.9
	Sensitivity of the receiver (S)	0.35 A/W
	Optical filter transmissivity ( $T_p$ )	0.5
	Load resistance ( $R_L$ )	100 $\Omega$
	Noise figure of the system (F)	4
	Dark current ( $I_{dr}$ )	1.226 nA
		Downwelling irradiance (E)
Ambient parameters	Underwater reflectance of the downwelling irradiance (R)	% 1.25
	Factor describing the directional dependence of the underwater radiance ( $L_{fac}$ )	2.9 (horizontally)
	Temperature ( $T_e$ )	290 K
Constants	Boltzman constant (k)	$1.38 \times 10^{-23}$ J / K
	Electronic charge (q)	$1.6 \times 10^{-19}$ C

ding to the communication distance are given in Fig. 2. These results were obtained for the beam divergence angle of  $5^0$  and aperture diameter of the receiver of 50 cm. When the absorption and scattering coefficients for the underwater environments, which are given in Table 1, are taken into consideration, it is seen that the dominance of the disruptive effects is increasing as PSW, COW, CAOW and HW, respectively. Therefore, as expected, the results in Fig. 2 showed that for the same transmitter power, in the PSW environment data communication can be carried out at the longest distance, while in the HW environment, data communication can be made at the shortest distance. In other words, the greater the distance and the turbidity cause more photons to scatter and the light becomes weaker, so power of the received signal decreases.

The relationships between power of the signal at the receiver and the beam divergence angle are given in Fig. 3.

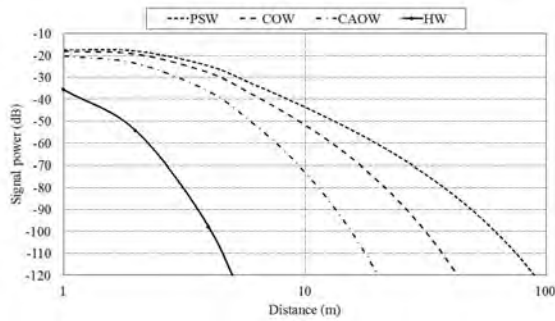


**Figure 2.** Signal power - communication distance relationship for various underwater environments.

For these examinations, distance between the transmitter and receiver units is taken as 10 m and aperture diameter of the receiver is taken as 50 cm. Beam divergence angle is changed from 1° to 30°. It is seen that the power of the signal at the receiver decreases when the divergence angle increases. According to the dominance of the disruptive effects, the power levels of the received signals for various underwater environments are sorted as in Fig. 3. When the divergence angle is increased from 1° to 30°, the power of the signal decreases approximately 50 dB for each underwater environment. Increasing the divergence angle causes the optical beam to spread rather than focus on somewhere. In this case, the power of the optical signal coming to the receiver will be lower than the focused optical signal.

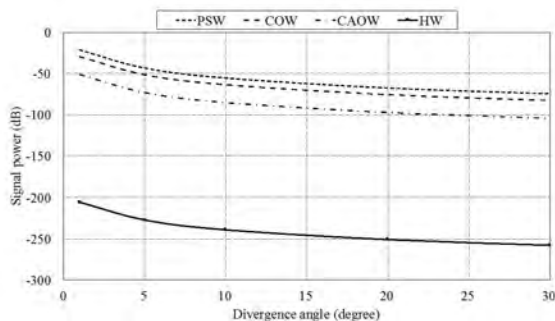


**Figure 3.** Signal power - beam divergence angle relationship for various underwater environments.

Relations between the power of the signal at the receiver and aperture diameter of the receiver are given in Fig. 4. In these examinations, the beam divergence angle is taken as 5° and the distance between the transmitter-receiver units is taken as 10 m. Aperture diameter of the receiver is changed from 1 cm to 50 cm. Results showed that increasing aperture diameter increases the power of the received signal exponentially. For each underwater environment, it is seen that upsizing the aperture diameter from 1 cm to 50 cm, leads to an increase of approximately 75 dB in the power of the signal at the receiver. As the receiving aperture area increases, the number of received photons increases. Thus, if the number of received photons increases, power of the signal at the receiver increases.

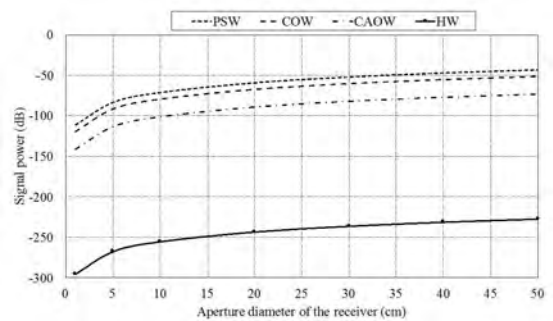


**Figure 4.** Signal power - aperture diameter of the receiver relationship for various underwater environments.

For the aforementioned underwater environments, relations between the channel capacity and the data communication distance are given in Fig. 5. For these examinations, the beam divergence angle is taken as 5° and the aperture diameter of the receiver is taken as 50 cm. As expected, increasing the distance between the transmitter and receiver units decreases the power of the signal at the receiver so channel capacity also decreases with increasing distance. According to the taken parameters, for communication distance of 10 m, it is understood that data transmission can be achieved at data rate levels of Gbps in PSW, COW and CAOW environments, while in the HW environment data communication cannot be done. It is seen that for the communication distance of 100 m, while it is possible to transmit data at the level of approximately 67.9 Mbps data transmission rate in PSW environment, data communication is not possible for the rest of the underwater environments.

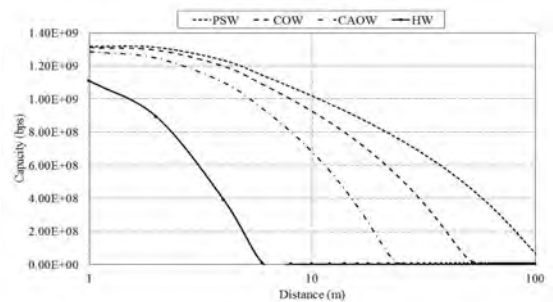


**Figure 5.** Channel capacity - communication distance relationship for various underwater environments.

In the UWOC system, where the distance between the transmitter and receiver units is taken as 10 m and the aperture diameter of the receiver as 50 cm, the variation of the channel capacity according to the beam divergence angle is shown in Fig. 6. The channel capacity decreases exponentially as the divergence angle increases. As it can be seen from Fig. 3, for the HW environment, it is not possible to perform data communication since of power of the signal at the receiver is very low (about -200 dB). Therefore, even if the divergence angle for the HW environment is 1°,

the channel capacity is quite close to zero level (about 2 bps). When the divergence angle is increased from 1° to 30°, data rates for PSW, COW and CAOW environments decreased by rate of %52.2, %48.3 and %34.5, respectively.

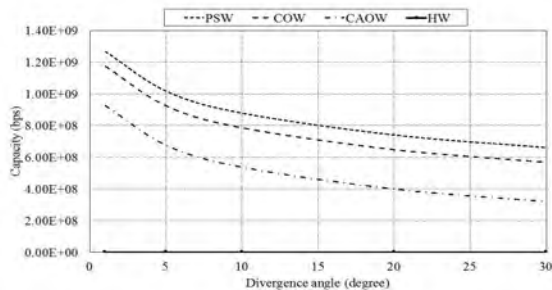


**Figure 6.** Channel capacity – beam divergence angle relationship for various underwater environments.

The variations of the channel capacity according to aperture diameter of the receiver are given in Fig. 7. In these examinations, the beam divergence angle is taken as 5° and the communication distance is taken as 10 m. It is seen that increasing the aperture diameter of the receiver increases the channel capacity exponentially. It is deduced that in the HW environment, in line with the system parameters considered for these results, since the power of the signal at the receiver is too low (below -200 dB), it is not possible to perform data communication at a distance of 10 m even if aperture diameter of the receiver increases. On the other hand, increasing aperture diameter of the receiver from 1 cm to 50 cm increases the data rates approximately 4 times and 6 times in PSW and COW environments, respectively. In the CAOW environment, it is only possible to perform data communication at 5.6 Mbps by using aperture diameter of 1 cm. However, it is possible to transmit data at 676 Mbps data rate level with aperture diameter of 50 cm. As the channel capacity directly depends on power of the received signal, the reasons that cause obtained results are the same as in power of the received signal results.

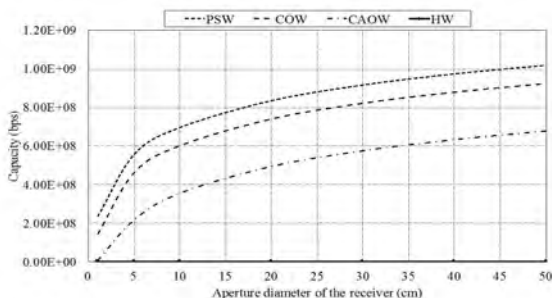


**Figure 7.** Channel capacity – aperture diameter of the receiver relationship for various underwater environments.

The obtained results showed that the performance of UWOC systems differs significantly for various environment and system parameters. Therefore, it is clear that in

marine environments, where system parameters and environment can always change, systems must be designed to operate in a wide SNR range in order to achieve efficient communication. For this reason, it is seen that an adaptive modulation and coding (AMC) algorithm is needed in which the depth of the modulation used in communication and the rate of error correction codes are changed according to the changing SNR value. In addition, energy can be saved by changing the transmitter power according to the SNR value obtained in the receiver. In all results, the transmitter optical power was chosen as 1 W. For different transmitter powers, the results can be easily calculated and used for system designs. It is possible to increase the communication distance and / or capacity by increasing the transmitter power.

## CONCLUSION

In this study, for underwater wireless communication systems the distribution of signal noise ratio and channel capacity for various values of the beam divergence angle and aperture diameter of the receiver in PSW, COW, CAOW and HW environments were examined. The obtained results, revealed that the performance of UWOC systems differs significantly for various environments and system parameters. Therefore, it is clear that in underwater environments, where system parameters and the ambient can always change, systems must be designed to operate in a wide SNR range in order to communicate effectively. In all of the numerical analyses, the transmitter optical power was chosen as 1 W. For different transmitter powers, the results can be easily calculated and used for system designs.

## REFERENCES

1. Quazi AH, Konrad WL. Underwater acoustic communications. *IEEE Communications Magazine* 20 (1982) 24–30.
2. Miramirkhani F, Uysal M. Visible Light Communication Channel Modeling for Underwater Environments with Blocking and Shadowing. *IEEE Access* 6 (2017) 1082-1090.
3. Chen H, Chen X, Lu J, Liu X, Shi J, Zheng L, Liu R, Zhou X., Tian P. Toward Long-Distance Underwater Wireless Optical Communication Based on A High-Sensitivity Single Photon Avalanche Diode. *IEEE Photonics Journal* 12 (2020) 7902510.
4. Shihada B, Amin O, Bainbridge C, Jardak S, Alkhazragi O, Ng TK, Ooi B, Berumen M, Alouini MS. Aqua-Fi: Delivering Internet Underwater Using Wireless Optical Networks. *IEEE Communications Magazine* 58 (2020) 84–89.
5. Kaushal H, Kaddoum G. Underwater Optical Wireless Communication. *IEEE Access* 4 (2016) 1518–1547.
6. Che X, Wells I, Dickers G, Kear P, Gong X. Re-Evaluation of RF Electromagnetic Communication in Underwater Sensor Networks. *IEEE Communications Magazine* 48 (2010) 143–151.
7. Wu TC, Chi YC, Wang HY. Blue laser diode enables underwater communication at 12.4Gbps. *Scientific Reports* 7 (2017) 1–10.
8. Miller JK, Morgan K, Li W, Li Y, Johnson, E. Data Agile Underwater Optical Communication Link using Flexible Data Formats and

- Orbital Angular Momentum Multiplexing. Paper presented at OCEANS 2018 MTS/IEEE, Charleston, SC, USA, 22-25 October, IEEE, pp. 1-4, 2018.
9. Cochenour B, Mullen L, Laux A. Spatial and temporal dispersion in high bandwidth underwater laser communication links. Paper presented at IEEE Military Communications Conference, San Diego, CA, USA, 16-19 November, IEEE, pp. 1-7, 2008.
  10. Jaruwatanadilok S. Underwater wireless optical communication channel modeling and performance evaluation using vector radiative transfer theory. *IEEE Journal on Selected Areas in Communications* 26 (2008) 1620-1627.
  11. Gabriel C, Khalighi A, Bourennane S, Léon R, Rigaud V. Optical communication system for an underwater wireless sensor network. Paper presented at EGU General Assembly, Vienna, Austria, 22-27 April, pp. 2685, 2012.
  12. Ali M. Characteristics of Optical Channel for Underwater Optical Wireless Communication System. *IOSR Journal of Electrical and Electronics Engineering* 10 (2015) 1-9.
  13. Li J, Ma Y, Zhou Q, Wang H. Channel capacity study of underwater wireless optical communications links based on Monte Carlo simulation. *Journal Of Optics A: Pure And Applied Optics* 14 (2012) 015403.
  14. Matta G, Agrawal M, Bahl R. Channel Capacity for Underwater Visible Light Communication Systems. Paper presented at Oceans 2019, Marseille, France, 17-20 June, IEEE, pp. 1-4, 2019.
  15. Shin M, Park K, Alouini M. Statistical Modeling of the Impact of Underwater Bubbles on an Optical Wireless Channel. *IEEE Open Journal of the Communications Society* 1(2020) 808-818.
  16. Zhang S, Zhang L, Wang Z, Quan J, Cheng J, Dong Y. On Performance of Underwater Wireless Optical Communications Under Turbulence, Paper presented at IEEE 17th Annual Consumer Communications & Networking Conference (CCNC), Las Vegas, NV, USA, 10-13 January, IEEE, pp. 1-2, 2020.
  17. Arnon S. Underwater optical wireless communication network. *Optical Engineering* 49 (2010) 015001-1-015001-6.
  18. Zeng Z, Fu S, Zhang H, Dong Y, Cheng J. A Survey of Underwater Optical Wireless Communications. *IEEE Communications Surveys & Tutorials* 19 (2017) 204-238.
  19. Giles JW, Bankman IN. Underwater optical communications systems. Part 2: basic design considerations. Paper presented at IEEE Military Communications Conference, Atlantic City, NJ, USA, 17-20 October, IEEE, pp. 1-6, 2005.
  20. Zhang H, Dong Y, Hui L. On Capacity of Downlink Underwater Wireless Optical MIMO Systems With Random Sea Surface. *IEEE Communications Letters* 19 (2015) 2166-2169.
  21. Sticklus J, Hoehner PA, Röttgers, R. Optical Underwater Communication: The Potential of Using Converted Green LEDs in Coastal Waters. *IEEE Journal Of Oceanic Engineering* 44 (2019) 535-547.
  22. Manor H, Arnon S. Performance of an optical wireless communication system as a function of wavelength. *Applied Optics* 42 (2003) 4285-4294.
  23. Boucouvalas AC. Underwater Optical Wireless Communications With Optical Amplification and Spatial Diversity. *IEEE Photonics Technology Letters* 28 (2016) 2613-2616.



# Mineral Chemistry–thermobarometry and Petrography of Metamorphic Sole Rocks of Kömürhan Ophiolite (SE Turkey): Constraints to Evolution and Emplacement

Nusret Nurlu 

Cukurova University, Department of Geological Engineering, Adana, Turkey

## ABSTRACT

This paper presents the generation of metamorphic sole rocks through the detailed geochemical and petrographical analysis of field work carried out on the Kömürhan ophiolite. The metamorphic sole rocks of Kömürhan ophiolite are defined as amphibolite (Pl+Mg–Hbl+Ttn±Ap) plagioclase–amphibole schist (Pl+Mg–Hbl+Cpx+Ttn±Zrn±Ap), plagioclase–clinopyroxene–amphibole schist (Pl+Di+Mg–Hbl+Ttn±Ap), and epidote–plagioclase amphibole schist (Ep+Pl+Mg–Hbl+Ttn±Ap±Qtz±Zrn). This research mainly reports comprehensive petrography and mineral chemistry analyses of metamorphic sole rocks of Kömürhan ophiolite of SAOB (Southeast Anatolian Orogenic Belt) together with a goal of presenting geothermobarometric examination and unravelling the mineral systematics. The metamorphic sole rocks have been observed as a thin slice and these rocks are seen at the base of the tectonites, metamorphosed in amphibolites facies throughout the intra–oceanic supra–subduction geodynamic environment. The Kömürhan ophiolite includes from the top to bottom volcanics, sheeted dike complex, isotropic gabbros cumulates, and tectonites and shows a complete oceanic lithospheric fragments. Analyses of mineral chemistry and petrography of metamorphic sole rocks have been used to exhibit the metamorphic processes of these rocks. Mineral chemistry analyses of pyroxene phenocrysts in the metamorphic sole rocks of Kömürhan ophiolite present similarities island arc tholeiite (IAT), proposing that protolith of the sole rocks was related to the supra–subduction geodynamic environment. The amphibolites were occurred by metamorphism of island arc tholeiite–type volcanics that separated from the front of the obducted ophiolite (Kömürhan ophiolite) and after that underplated.

### Keywords:

Mineral chemistry; Kömürhan ophiolite; Amphibolites; Petrography; Metamorphic sole; Thermobarometry

## INTRODUCTION

Slim sheets of the metamorphic sole rocks related to ophiolitic bodies were presented by many researchers and numerous ophiolitic bodies hold amphibolite at their sole which includes a clear inverted grade of metamorphism. [e.g. 1, 2, 3, 4]. These mainly amphibolite rocks are believed to have occurred throughout the emplacement and detachment of the ophiolite. The Kömürhan ophiolite holds the amphibolites of metamorphic sole rocks in the SAOB. Many publications have reported the presence of metamorphic sole rocks beneath several ophiolitic complexes of the Tethys, including Baer–Bassit in Syria [5, 11, 12], Mersin in south Turkey [6, 7, 8], and Pozanti–Karsanti in Turkey [13]. One of the best–preserved examples is Semail in Oman [3, 14, 9, 10]. The ophiolitic bodies of the eastern Mediterranean district in southern Turkey comprise two main features: (i) the

SAOB and (ii) the Inner Tauride Suture Zone. The SAOB also includes the Bitlis–Zagros thrust belt and folds that include pristine oceanic lithosphere from the southern branch of Neo–Tethys, especially Troodos, Kızıldağ, İspendere, Guleman and Bear–Bassit in Syria. The Neo–Tethyan duration of the SAOB started in the Triassic (by rifting) and finished in the Miocene, with the collision of the Tauride plate and the Arabian plate [15, 16, 17, 18, 19, 48]. The Southeast Anatolian Orogenic belt includes important examples of unmetamorphosed ophiolites (given from west to east): Göksun, Meydan (Kahramanmaraş), İspendere, Kömürhan (Malatya), and Guleman (Elazığ), observed in the north, and also the Koçali (Adıyaman) and Kızıldağ (Hatay) ophiolites, observed in the south (Fig. 1) [16, 17, 20, 21, 22, 18, 19, 23, 24, 25, 26, 4]. The study area is placed in the area among Sivrice

### Article History:

Received: 2020/06/05

Accepted: 2020/11/08

Online: 2020/12/31

**Correspondence to:** Nusret Nurlu,  
Cukurova University, Geological  
Engineering, 01330, Balcalı, Adana, Turkey  
E-Mail: nusretnurlu@gmail.com  
Phone: +90 322 338 70 81  
Fax: +90 322 338 70 81

and Baskil (Elazığ) regions. The outcrops of the rocks forming the Kömürhan ophiolite and related metamorphic sole rocks which are the main subject of this paper start from the Kömürhan Bridge and continue to the west of Sivrice town (Elazığ), mainly along the Malatya-Elazığ highway (Fig. 1b).

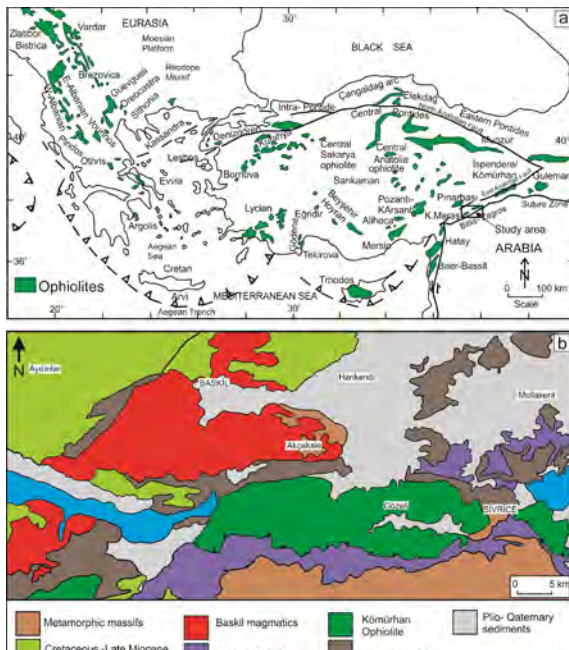


**Figure 1.** a) Neo-Tethyan ophiolites in the eastern Mediterranean region (from [27, 23]). b) Simplified geological map of the Kömürhan ophiolite (Malatya-Elazığ region), simplified from [28].

The whole-rock geochemistry, geochronology, and petrology of Kömürhan ophiolite and are properly described [23, 29]. However, a detailed examination of mineral chemistry, petrography and field relations of metamorphic sole rocks of Kömürhan ophiolite is yet reported. The principal objectives of this paper are to: (a) yield mineral chemistry of the metamorphic sole rocks; (b) report the geodynamic setting, protolith and geothermobarometric development of metamorphic sole rocks and also mineral data; and (c) summarise the geodynamic environment of the Kömürhan ophiolite during the development of the Southeast Anatolian Suture Zone of the Neo-Tethyan oceanic region within the eastern Mediterranean tectonic roof.

## GEOLOGICAL SETTING

The ophiolitic unit is observed in an area of approximately 135-140 km<sup>2</sup> [23, 29]. The Kömürhan ophiolite is located on the Middle Eocene-aged Maden Complex south of the Kömürhan Bridge, with an overlapping contact relationship outside of the study area. It is unconformably overlain by the late Paleocene-early Eocene Seske formation. The Kömürhan ophiolite is also cut by the Upper Cretaceous

aged Baskil granitoid, which provides wide dispersions in the region [23, 29]. This intrusive contact relationship has been developed synthetically in places (Fig. 2–3). The mineral chemistry data of clinopyroxenes are various and yields a filtered appearance of the contents of the protolith from which the clinopyroxene crystallized, lending it the prospective to give insight into the geodynamic environment of metamorphic sole rocks of Kömürhan ophiolite. Metamorphic sole rocks are observed in the Kömürhan Bridge and Karakaya Hill in a fairly narrow area, approximately 250–280 meters thick. The examined metamorphic sole rocks consist of a reverse zoned metamorphic slice that varies from green-schist facies to amphibolite facies. Although the unit is observed directly on the basis of ultramafic cumulates, due to the effectiveness of tectonism, the normal stratigraphic sequence is distorted as a result of occasional tilting [23, 29]. The examined rocks belonging to the metamorphic sole rocks are mainly represented by amphibolite, plagioclase-amphibolite schist, plagioclase-clinopyroxene-amphibole schist, and epidote-plagioclase amphibole schist and especially schist type metamorphic rocks are remarkable because they have a macroscopically distinct schistosity and present alterations colours in shades of green (Fig. 3).

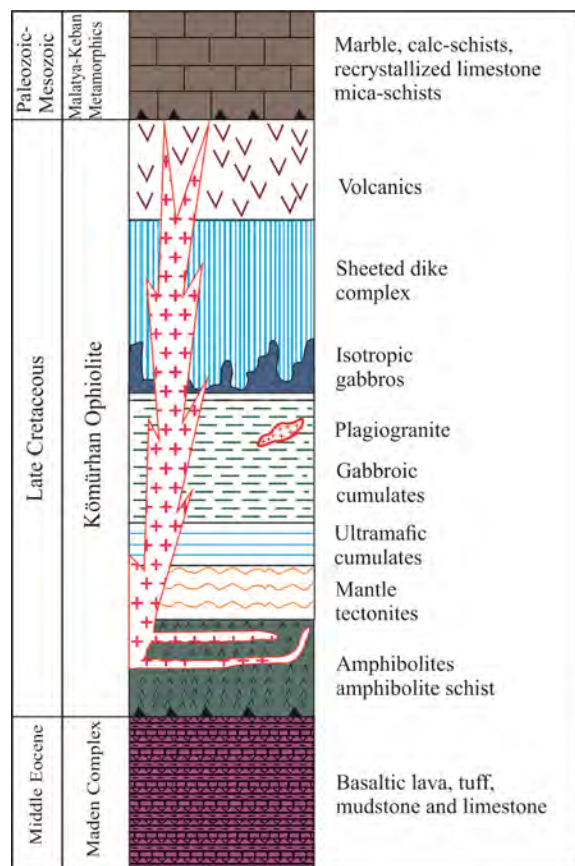


**Figure 2.** Synthetic log of the Kömürhan ophiolite (from [23, 29])





**Figure 3.** Field photographs of the metamorphic sole rocks and serpentinites of Kömürhan ophiolite. (a) A tectonic relation with the amphibolites and serpentinites in the Kömürhan ophiolite. (b) General view of amphibolites of metamorphic sole rocks of Kömürhan ophiolite. (c) Plagioclase amphibole schist (d) Field observation of the amphibole schist.

## MATERIAL AND METHODS

### Petrographical analyses

The metamorphic sole and mafic dike rock types were initially examined in thin section handling an optical microscope (ca. 115 thin sections) and conducted the sampling of rocks suitable for petrological analysis.

### Electron microprobe analyses

Thin sections (about 30 microns thick) for four samples were prepared by the EAS Thin Section Laboratory at the Department of Earth and Atmospheric Sciences (EAS) at the University of Alberta. Major element compositions of minerals and phase relationships were studied by electron microprobe at the EAS at the University of Alberta (Canada). The operating conditions were; 40 degrees take off angle, accelerating voltage 20 kV, beam current 20 nA, and beam diameter <1 micron (fully focused), except on the zeolite points that were run separately with a 10-micron diameter beam. The K $\alpha$  X-ray lines of 13 elements were measured using the following diffraction crystals: PET (pentaerythritol) – P, K, Ca, Ti, V, Cr; TAP (thallium hydrogen phthalate) – Na, Mg, Al, Si; LIF (lithium fluoride) – Mn, Fe, Ni. Total count times of 30 seconds were used for both emission peaks and background positions for all elements except Na, for which 60 seconds was used. Interference corrections were applied to V for interference by Ti, and to Cr for interference by V, and to Mn for interference by Cr [24]. Intensity data were reduced according to [25] and the choice of mineral standards varied with the mineral analysed. Oxygen was calculated by stoichiometry and included in the data reduction.

Representative data are shown in Tables 1–4. Detailed mineral chemistry analyses of 35 points on clinopyroxene, plagioclase, titanite and amphibole minerals were carried out on 2 samples from the rocks belonging to the metamorphic sole observed in the Kömürhan ophiolite (Table 1–4).

## PETROGRAPHY AND MINERALOGY

Amphibolites have a darker green alteration surface, are generally massive and are observed to be more strength compared to schist type rocks. Detailed petrographic properties reported as a result of thin section determination studies on metamorphic sole rocks compiled in the study area are given below. The amphibolites in the study region are represented by plagioclase, hornblende, epidote, titanite and  $\pm$  zircon  $\pm$  opaque minerals such as magnetite. These rocks present generally nematoblastic and granoblastic textures and are commonly dark green coloured. Calcite, prehnite, and quartz are mainly seen in the vein of the amphibolite type rocks. Feldspars are commonly represented by plagioclases and these minerals present various degrees of alteration. Though, non-altered plagioclases showing polysynthetic twinning have been seen.

Pyroxenes are represented by diopsides and they have been seen as relicts in most of the amphibolites. The plagioclase-amphibolite schists present nematoblastic texture and consist of green hornblende (50-55 vol%), plagioclase (30–35 vol%) and rare quartz, opaque minerals (Fig. 4a). The epidote-plagioclase amphibole schist present epidote (7–8 vol%), plagioclase (30–35 vol%) and hornblende (50–55 vol%) and has nematoblastic texture. Serpentinized wherlites are described as rocks holding olivine (45-55 vol%), serpentinite (20–25 vol%), and clinopyroxene (20–25 vol%). A

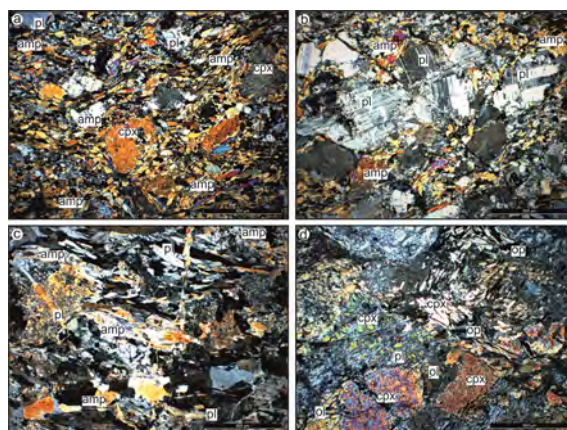


**Figure 4.** (a) Nematoblastic, granoblastic textures in the amphibolite. (b) Plagioclase porphyroblast in the schists. (c) Nematoblastic texture in the plagioclase-amphibole schist. (d) serpentinized wherlite presenting granular and mesh textures (abbreviations: cpx, clinopyroxene; pl, plagioclase; amp, amphibole; ol, olivine).

**Table 1.** Composition of the amphibole from the metamorphic sole rocks of K m rhan ophiolite.

Sample	KMP-1	KMP-2	KMP-3	KMP-4	KMP-5	KMP-6	KMP-7	KMP-8	KMP-9	KMP-10	KMP-11
SiO <sub>2</sub>	53.05	54.63	54.84	53.74	54.74	54.57	54.62	54.86	54.54	53.73	54.02
TiO <sub>2</sub>	0.48	0.04	0.04	0.34	0.06	0.05	0.06	0.00	0.06	0.06	0.05
Al <sub>2</sub> O <sub>3</sub>	2.55	0.44	0.73	1.75	0.86	0.83	0.84	0.69	0.73	0.80	0.54
Cr <sub>2</sub> O <sub>3</sub>	0.19	0.00	0.06	0.20	0.07	0.00	0.03	0.00	0.04	0.10	0.04
FeO	4.84	4.85	4.46	4.36	4.44	5.02	4.99	4.43	4.63	4.84	4.91
MnO	0.17	0.19	0.17	0.19	0.18	0.21	0.20	0.18	0.21	0.18	0.19
MgO	14.78	15.34	15.35	15.15	15.48	14.97	14.95	15.41	15.07	15.12	15.20
CaO	23.37	24.72	24.63	24.26	24.66	24.54	24.49	24.83	24.66	24.57	24.69
Na <sub>2</sub> O	0.37	0.15	0.24	0.27	0.21	0.20	0.24	0.23	0.20	0.24	0.17
K <sub>2</sub> O	0.00	0.00	0.00	0.00	0.00	0.00	0.00	0.00	0.00	0.00	0.00
A	7.02	5.14	4.95	5.84	5.09	5.65	5.59	4.89	5.16	5.40	5.28
C	23.37	24.72	24.63	24.26	24.66	24.54	24.49	24.83	24.66	24.57	24.69
F	19.79	20.38	19.98	19.70	20.10	20.20	20.14	20.02	19.91	20.14	20.30
TOTAL	99.82	100.41	100.54	100.31	100.73	100.40	100.43	100.68	100.16	99.66	99.82
Si	1.95	2.00	2.01	1.97	2.00	2.00	2.00	2.00	2.01	1.98	1.99
Ti	0.01	0.00	0.00	0.01	0.00	0.00	0.00	0.00	0.00	0.00	0.00
Al	0.11	0.02	0.03	0.08	0.04	0.04	0.04	0.03	0.03	0.03	0.02
Fe <sup>+3</sup>	0.00	0.00	0.00	0.00	0.00	0.00	0.00	0.00	0.00	0.01	0.00
Cr <sup>+3</sup>	0.01	0.00	0.00	0.01	0.00	0.00	0.00	0.00	0.00	0.00	0.00
Fe <sup>+2</sup>	0.15	0.15	0.14	0.13	0.14	0.15	0.15	0.14	0.14	0.14	0.15
Mn	0.01	0.01	0.01	0.01	0.01	0.01	0.01	0.01	0.01	0.01	0.01
Mg	0.81	0.84	0.84	0.83	0.84	0.82	0.82	0.84	0.83	0.83	0.84
Ca	0.92	0.97	0.96	0.95	0.96	0.97	0.96	0.97	0.97	0.97	0.98
Na	0.03	0.01	0.02	0.02	0.01	0.01	0.02	0.02	0.01	0.02	0.01
K	0.00	0.00	0.00	0.00	0.00	0.00	0.00	0.00	0.00	0.00	0.00
H	0.00	0.00	0.00	0.00	0.00	0.00	0.00	0.00	0.00	0.00	0.00
TOTAL	4.00	4.00	4.00	4.00	4.00	4.00	4.00	4.00	4.00	4.00	4.00
Wo	48.98	49.59	49.79	49.77	49.65	49.79	49.79	49.93	50.08	49.96	49.71
En	43.10	42.82	43.17	43.25	43.37	42.26	42.29	43.12	42.58	42.78	42.58
Fs	7.92	7.59	7.04	6.98	6.98	7.95	7.92	6.95	7.34	7.26	7.72
Total	100.00	100.00	100.00	100.00	100.00	100.00	100.00	100.00	100.00	100.00	100.00

Number of ions on the basis of six (O). \*Total Fe is expressed as FeO.

few orthopyroxenes are rarely seen (Fig. 4d) and these rocks are presenting granular and mesh textures. The plagioclase-clinopyroxene-amphibole schist displays prominent foliation because of the preferred orientation of plagioclase (10–15 vol %), pyroxene (25–30 vol %), amphibole (40–45 vol %). The plagioclases are immensely altered to sericite and saussurite and these rocks also have accessory minerals such as apatite and zircon.

## MINERAL CHEMISTRY

The EMPA (electron microprobe analyses) data for significant pyroxenes, amphiboles, biotites, and titanites

from metamorphic sole rocks of K m rhan ophiolites are given in Table 1-4. Formulae have been calculated on the basis of six (O) and twelve cations (including Na, K, Ca and H). In point of quadrilateral components, the clinopyroxene contents are  $Wo_{48.9-49.7}Fs_{6.95-7.95}En_{42.3-43.4}$  in plagioclase-clinopyroxene amphibole schist. The Mg# of the clinopyroxenes are ranging from 0.846 to 0.861 (Table 2). Based on the Fe-Ca-Mg discrimination diagram of Morimoto (1989), the examined pyroxenes are fall in a distinct tight group on the Ca-rich limit of the diopside subfield (Fig. 5a). [32] suggested a set of basic discrimination diagrams in order to recognize the possible geodynamic environment of paleo-basalt on the basis of the mineral chemistry of clinopyroxenes. A series of diag-

**Table 2.** Composition of the pyroxene from the metamorphic sole rocks of K m rhan ophiolite.

Sample	KMP-1	KMP-2	KMP-3	KMP-4	KMP-5	KMP-6	KMP-7	KMP-8	KMP-9
SiO <sub>2</sub>	50.95	49.4	50.76	51.19	49.32	50.01	52.65	50.45	49.51
TiO <sub>2</sub>	0.39	0.34	0.32	0.32	0.52	0.35	0.23	0.37	0.47
ZnO	0	0	0	0	0	0	0	0	0
Al <sub>2</sub> O <sub>3</sub>	6.82	8.4	7.22	6.93	8.46	7.72	5.53	7.82	7.66
Cr <sub>2</sub> O <sub>3</sub>	0.04	0.41	0.28	0.19	0.25	0.23	0.23	0.03	0.06
FeO	8.23	8.09	7.77	7.69	8.22	8.13	7.04	8.08	8.16
NiO	0.03	0.04	0.03	0	0.02	0.04	0.02	0	0.03
MnO	0.15	0.18	0.16	0.17	0.16	0.17	0.14	0.15	0.15
MgO	16.6	16.08	16.56	16.99	16.19	16.24	17.62	16.49	16.42
CaO	12.62	12.65	12.68	12.73	12.63	12.7	12.9	13	12.61
Na <sub>2</sub> O	1.03	1.17	1	1	1.32	1.08	0.7	1.08	1.19
K <sub>2</sub> O	0.01	0.02	0.01	0.01	0.02	0.01	0.01	0.02	0.01
TOTAL	96.87	96.77	96.82	97.24	97.11	96.67	97.09	97.53	96.28
Species	Mg-Hbl	Mg-Hbl	Mg-Hbl	Mg-Hbl	Mg-Hbl	Mg-Hbl	Act	Mg-Hbl	Mg-Hbl
T (ideally 8 apfu)									
Si	7.277	7.081	7.248	7.268	7.052	7.17	7.452	7.173	7.131
Al	0.723	0.919	0.752	0.732	0.948	0.83	0.548	0.827	0.869
T subtotal	8	8	8	8	8	8	8	8	8
C (ideally 5 apfu)									
Ti	0.042	0.037	0.034	0.034	0.056	0.038	0.024	0.04	0.051
Al	0.425	0.5	0.463	0.427	0.477	0.474	0.375	0.483	0.431
Cr	0.005	0.046	0.032	0.021	0.028	0.026	0.026	0.003	0.007
Fe <sup>3+</sup>	0.038	0.054	0.019	0.042	0.059	0.032			0.066
Ni	0.003	0.005	0.003		0.002	0.005	0.002		0.003
Mn <sup>2+</sup>	0.007	0.006	0.014	0.009	0.003	0.012	0.017	0.018	
Fe <sup>2+</sup>	0.945	0.916	0.909	0.871	0.924	0.943	0.833	0.961	0.916
Mg	3.535	3.436	3.525	3.596	3.451	3.471	3.718	3.495	3.525
C subtotal	5	5	4.999	5	5	5.001	4.995	5	4.999
B (ideally 2 apfu)									
Mn <sup>2+</sup>	0.011	0.015	0.005	0.012	0.017	0.009			0.018
Ca	1.931	1.943	1.94	1.936	1.935	1.951	1.956	1.98	1.946
Na	0.058	0.042	0.055	0.052	0.049	0.04	0.044	0.02	0.035
B subtotal	2	2	2	2	2.001	2	2	2	1.999
A (from 0 to 1 apfu)									
Na	0.227	0.283	0.222	0.224	0.317	0.26	0.149	0.278	0.297
K	0.002	0.004	0.002	0.002	0.004	0.002	0.002	0.004	0.002
A subtotal	0.229	0.287	0.224	0.226	0.321	0.262	0.151	0.282	0.299
O (non-W)	22	22	22	22	22	22	22	22	22
W (ideally 2 apfu)									
OH	2	2	2	2	2	2	2	2	2
W subtotal	2	2	2	2	2	2	2	2	2
Sum T,C,B,A	15.229	15.287	15.223	15.226	15.322	15.263	15.146	15.282	15.297
Altot	1.148	1.419	1.215	1.159	1.425	1.304	0.923	1.31	1.3
P	2.19	2.97	2.37	2.22	2.99	2.62	1.65	2.64	2.61

**Table 3.** Composition of the pyroxene from the metamorphic sole rocks of Kömürhan ophiolite (continued).

Temperature based on Ti (Otten, 1984) - warning: semi empirical; best used to determine magmatic versus secondary compositions									
T (C) Ti-hbl	779.269	758.510	759.258	770.487	781.608	757.842	759.364	744.855	780.186
	9748	7585	3878	1664	1973	6965	0939	5743	0399

Number of ions on the basis of 23 oxygens. Total Fe is expressed as FeO\*.

**Table 3.** Composition of the plagioclase from the metamorphic sole rocks of Kömürhan ophiolite.

Sample	KMF-1	KMF-2	KMF-3	KMF-4	KMF-5	KMF-6	KMF-7	KMF-8	KMF-9	KMF-10	KMF-11	KMF-12
SiO <sub>2</sub>	31.42	48.96	49.22	41.66	45.64	48.95	46.66	47.92	48.99	46.09	67.01	49.2
Al <sub>2</sub> O <sub>3</sub>	1.27	32.96	32.86	33.78	34.4	33.45	34.92	33.96	33.18	35.14	20.56	32.53
TiO <sub>2</sub>	37.44	0	0	0	0	0	0	0	0	0	0	0
FeO	0.46	0.03	0.02	0.34	0.06	0.04	0.08	0.03	0.03	0.06	0.07	0.02
MnO	0.03	0	0	0	0	0	0	0	0	0.02	0	0
MgO	0.41	0	0	0.02	0	0	0	0	0	0	0	0.02
CaO	27.76	15.12	14.97	22.74	18.31	15.31	17.19	16.16	15.18	18.13	0.79	14.55
Na <sub>2</sub> O	0	2.85	2.94	0.56	1.36	2.74	1.69	2.41	2.83	1.49	11.07	3.16
K <sub>2</sub> O	0.01	0	0.01	0.02	0	0.01	0	0	0	0	0.01	0
TOTAL	98.96	99.95	100.07	99.13	99.79	100.55	100.58	100.53	100.22	100.95	99.51	99.48
Cations												
Si	1.71	2.23	2.24	1.94	2.10	2.22	2.13	2.18	2.23	2.10	2.95	2.25
Al <sup>IV</sup>	1.29	0.77	0.76	1.06	0.90	0.78	0.87	0.82	0.77	0.90	0.05	0.75
Al <sup>VI</sup>	-1.21	1.01	1.01	0.80	0.97	1.01	1.01	1.00	1.01	0.98	1.02	1.00
Ti	1.53	0.00	0.00	0.00	0.00	0.00	0.00	0.00	0.00	0.00	0.00	0.00
Fe <sup>2+</sup>	0.02	0.00	0.00	0.01	0.00	0.00	0.00	0.00	0.00	0.00	0.00	0.00
Mn	0.00	0.00	0.00	0.00	0.00	0.00	0.00	0.00	0.00	0.00	0.00	0.00
Mg	0.03	0.00	0.00	0.00	0.00	0.00	0.00	0.00	0.00	0.00	0.00	0.00
Ca	1.62	0.74	0.73	1.14	0.90	0.74	0.84	0.79	0.74	0.88	0.04	0.71
Na	0.00	0.25	0.26	0.05	0.12	0.24	0.15	0.21	0.25	0.13	0.94	0.28
K	0.00	0.00	0.00	0.00	0.00	0.00	0.00	0.00	0.00	0.00	0.00	0.00
Total	5.00	5.00	5.00	5.00	5.00	5.00	5.00	5.00	5.00	5.00	5.00	5.00
Or	0.04	0.00	0.06	0.10	0.00	0.06	0.00	0.00	0.00	0.00	0.06	0.00
Ab	0.00	25.43	26.21	4.26	11.85	24.45	15.10	21.25	25.23	12.95	96.15	28.21
An	99.96	74.57	73.74	95.64	88.15	75.49	84.90	78.75	74.77	87.05	3.79	71.79

Number of ions the basis of 8 oxygens. Total Fe is expressed as FeO\*.

rams were proposed to discriminate orogenic from non-orogenic suites (Ca versus Ti+Cr), subalkali from alkaline basalts (Ti versus Ca + Na), and tholeiitic orogenic from calc-alkaline orogenic suites (Ti versus Al) (Figs. 5b–d). Based on these useful discrimination diagrams, it can be seen that the analysed pyroxene samples are all plotted in the field of orogenic suite (Fig. 5b). These clinopyroxenes are also expressly alkaline basalts (Fig. 5c). The examined pyroxenes with tholeiitic compositions lie certainly in the orogenic subfield (Fig. 5d). Based on [32] discrimination diagrams, metamorphic sole seen to be orogenic attitude together with an intense tholeiitic characteristic. Electron microprobe analysis compositions show that almost all feldspars are bytownite (An<sub>71-88</sub>) in amphibolite,

while rare feldspar samples are anorthite (An<sub>96-99</sub>) and also an example is albite (An<sub>4</sub>) (Fig. 6a) (Table 3). Hornblende is the dominant component in the metamorphic sole rocks of Kömürhan ophiolite, in particular, those from the south–eastern district of Kömürhan ophiolite. Mineralogically heterogeneous crystals presenting varying colours from field to field inside individual crystal have been avoided for EPMA. The characteristic magnesian–hornblende is described by SiO<sub>2</sub>=49.32–52.65%, Al<sub>2</sub>O<sub>3</sub>=5.53–8.46%, TiO<sub>2</sub>=0.23–0.52%, MgO=16.08–17.62%, FeO=7.04–8.23%, K<sub>2</sub>O=0.01–0.02% and overall the examined amphiboles are presenting a magnesian character together with a limited range of Mg number (Mg<sup>#</sup>=Mg/(Mg + Fe<sup>2+</sup>)) are ranging from 78 to 82 and of a

**Table 4.** Composition of the titanite from the metamorphic sole rocks of K m rhan ophiolite

Sample	KMT-1	KMT-2	KMT-3
SiO <sub>2</sub>	30.88	30.84	30.86
TiO <sub>2</sub>	37.14	37.61	38.25
Al <sub>2</sub> O <sub>3</sub>	1.65	1.31	1.03
Cr <sub>2</sub> O <sub>3</sub>	0.12	0.11	0.16
FeO	0.42	0.42	0.38
MnO	0.05	0.05	0.03
MgO	0.06	0.00	0.02
CaO	27.83	27.91	27.86
Na <sub>2</sub> O	0.00	0.00	0.00
K <sub>2</sub> O	0.00	0.00	0.00
TOTAL	98.16	98.28	98.61
Notes	titanite	titanite	titanite
Si	2.03	2.03	2.03
Ti	1.84	1.86	1.89
Zn	0.00	0.00	0.00
Al	0.13	0.10	0.08
Cr	0.01	0.01	0.01
Fe	0.02	0.02	0.02
Ni	0.00	0.00	0.00
Mn	0.00	0.00	0.00
Mg	0.01	0.00	0.00
Ca	1.96	1.97	1.96
Na	0.00	0.00	0.00
K	0.00	0.00	0.00
O	9.94	9.95	9.97
Cations	6.00	6.00	6.00

calcic affinity ( $[(Na + Ca)B > 1$  and  $[Na]B < 0.5$ ). According to discrimination diagrams of [33], examined amphiboles from sole rocks of K m rhan ophiolite can be chemically defined as magnesio–hornblende (Fig. 6b).

Seeing that whole metamorphic sole rocks examined are extensively mafic in character, their mineral assemblages have been ideally indicated by the ACF discrimination diagram (Fig. 7a) which is suggested by [34]. The studied amphibolite facies of metamorphic sole rocks mostly plotted in the diopside and hornblende zone of mafic rocks. [35] reported the semi-quantitative geobarometer to state the pressure evolution of hornblendes from the metamorphic rocks. The calculated pressures were less than 0.5 GPa. The estimated pressure for the examined rocks, calculated from the contents of the Al<sup>IV</sup> versus Na<sup>M4</sup> a.p.f.u. numbers from hornblendes, was 2-5 kbar (Fig. 7b). The pattern of Al<sup>IV</sup>/Ti ratios from the examined amphiboles Al<sup>IV</sup> versus Ti diagram presents that the participation of the contamination and magma mixing role in the geodynamic evolution of the

analyzed rocks (Fig. 7c). Hornblendes from metamorphic and igneous processes have been categorized by Al<sup>VI</sup> vs. Al<sup>IV</sup> diagram [36]. The examined hornblendes from the studied rocks are metamorphic origin, derived by the metamorphic process (Fig. 7d).

## DISCUSSION

The best observed stratigraphic–tectonomagmatic units of Southeast Turkey in the Cretaceous have been (i) op-

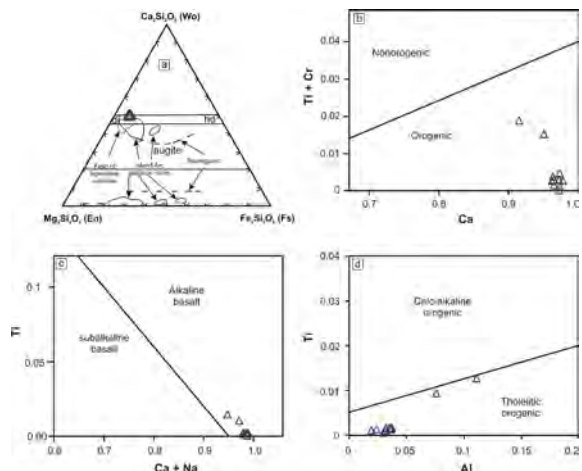


**Figure 5.** (a) Clinopyroxene major element compositions. (b) Plot of Ti + Cr versus Ca proposes that the metamorphic sole rocks from orogenic composition. Nonorogenic, orogenic, subalkaline, alkaline, calcalkaline and tholeiitic subfields are after [32].

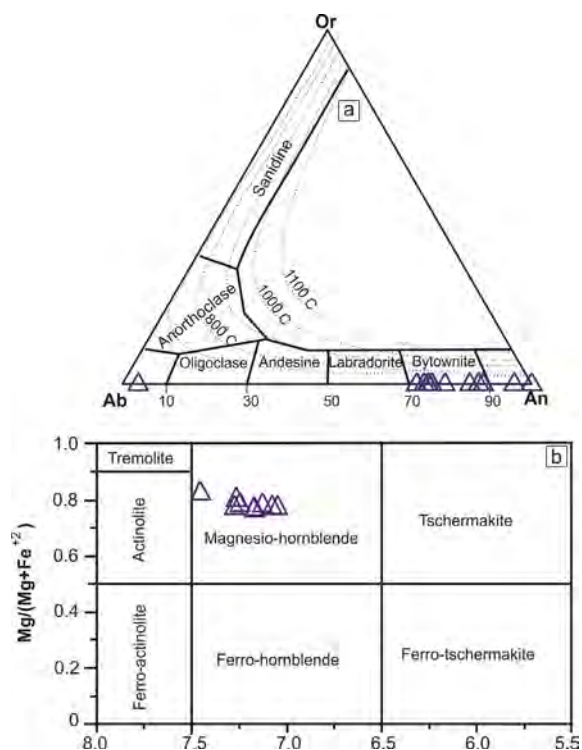


**Figure 6.** (a) Or-Ab-An discrimination diagram for feldspar (after Leake and Woolley Arps 1997) b) Amphibole discrimination diagram for  $(Na+K)A < 0.5$  (a) and  $(Na + K)A > 0.5$  (b) (after [33]).

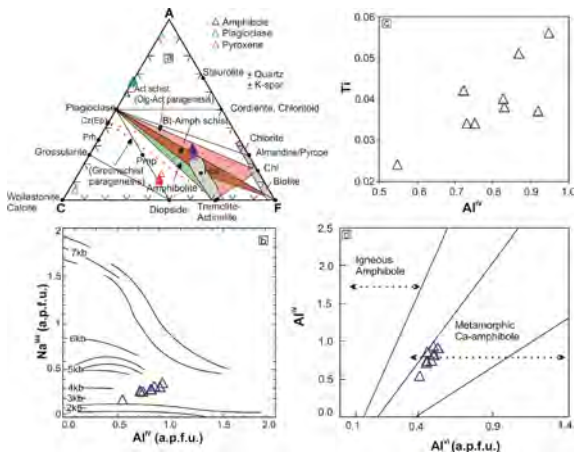


**Figure 7.** (a) Mineral assemblages of the amphiboles from Kömürhan ophiolite are shown in the ACF diagram (Best 1982). A = Al<sub>2</sub>O<sub>3</sub> + Fe<sub>2</sub>O<sub>3</sub> ± (Na<sub>2</sub>O + K<sub>2</sub>O); C = CaO - 3,3 P<sub>2</sub>O<sub>5</sub>; F = FeO + MgO + MnO. (b) Comparison of Na<sup>M4</sup> and Al<sup>IV</sup> positions for amphibole from Metamorphic sole rocks of the Kömürhan ophiolite (after [29]). The mineral chemistry data of the amphiboles from the Kömürhan ophiolite: (c) Al<sup>IV</sup> versus Al<sup>VI</sup> diagrams (after Fleet and Barnett, 1978); (d) Plot of amphibole data on Ti versus Al<sup>IV</sup> diagram (after [33]).

hiolites (e.g. İspendere, Guleman, Kömürhan Göksun), (ii) metamorphic massifs (e.g. Keban, Malatya metamorphics), (iii) granitic bodies (e.g. Baskil granitoid) and volcanic arcs (e.g. Elazığ–Yüksekova magmatics). The SAOB geodynamic evolution included onward relative movement of the nappes which contain both ophiolitic and metamorphic massifs, towards the Arabian platform throughout from Late Cretaceous to Miocene time interval [37, 16, 17, 38, 47]. Malatya–Keban metamorphics is a unit with low-grade metamorphism that rarely contains metaconglomerate, together with marble, schist, slate, and black phyllites [39,17]. Sheeted dykes and isotropic gabbros of Kömürhan ophiolite are tholeiitic in character (Nb/Y=0.2–0.06), and rare earth element (REE) spider and tectonomagmatic discrimination diagrams suggest that these rocks are formed in a supra-subduction zone geodynamic setting [23, 29]. Rızaoğlu et al. (2006) also reported that the metamorphic sole rocks of the Kömürhan ophiolite present tholeiitic in character (Nb/Y=0.07–0.33) and Rare earth element (REE)–spider diagram and tectonomagmatic discrimination diagrams indicate that these rocks have an island arc character. The Kömürhan ophiolite was formed in the Late Cretaceous (~ 90 My) between the Arabian platform in the south and the Taurus platform in the north, on a supra-subduction zone tectonic setting in the southern branch of Neotethys [23, 29]. Clinopyroxenes in the metamorphic sole rocks are of affinity because these mafic minerals are constantly resisting in retrogressive metamorphism and such other mafic minerals are converted to epidote and/or chlorite-type secondary minerals. Many researchers developed several discrimination/variation diagrams for clinopyroxenes based on their major and minor element compositions [40, 32, 41]. These diagrams allow researchers

to evaluate the origin of metamorphic sole rocks, together with the aim of defining the geodynamic setting of Kömürhan ophiolite. Rızaoğlu et al. (2006) reported that volcanics mainly basaltic of the Kömürhan ophiolite present tholeiitic in nature depend on their Nb/Y ratios (0.5–0.02). These basaltic volcanics are thought to be protolith of metamorphic sole rocks, which are the main subject of research. The hornblende structural formulae have been conducted on the basis of the ACES2013 Excel spreadsheet [36], whereas Inverse thermobarometry has been calculated by using the basis of the Ti in–hornblende and amphibole–plagioclase compositions [43, 44]. Whole hornblende compositions, presented in Table 1. have been calculated by operating the Excel spreadsheet for the Al–in–hornblende geobarometry [45] and also Hbl–Pl thermobarometry; the calculation equation is  $0.5 + (0.331 \times \text{Altot}) + [0.995 \times (\text{Altot} \times \text{Altot})]$  [45, 46]. ISOPLOT 4.15 Excel add–in has been used for the inverse geothermobarometry [46] and the data provided by this method have been used for weighted average calculations of the P–T status. For examined hornblendes from the metamorphic sole rocks the inverse geothermobarometry models given a weighted average value of  $2.48 \pm 0.33$  kbar (95 % conf., MSWD = 0.71, probability= 0.68). For magnesio–hornblendes from the metamorphic rocks, the temperatures are ranging from  $744.9 \pm 40$  °C to  $781.0 \pm 40$  °C with a weighted mean value of  $766.0 \pm 26$  °C (95 % conf., MSWD = 0.102, probability= 0.999).

## CONCLUSION

From the outcomes of this analysis and the subsequent discussion, the following conclusions were drawn.

- The metamorphic sole rocks of Kömürhan ophiolite are composed of four main lithologies; amphibolite (Pl+Mg–Hbl+Ttn±Ap) plagioclase–amphibole schist (Pl+Mg–Hbl+Cpx+Ttn±Zrn±Ap), plagioclase–clinopyroxene–amphibole schist (Pl+Di+Mg–Hbl+Ttn±Ap), and epidote–plagioclase amphibole schist (Ep+Pl+Mg–Hbl+Ttn±Ap±Qtz±Zrn).
- The metamorphic sole rocks occurred as a result of the metamorphism of the island–arc tholeiite (IAT) type mafic rocks which separated from the upper section of the subducted ophiolitic crust and then dipped under the plate.
- The examined amphiboles in the metamorphic sole rocks of Kömürhan ophiolite experienced calculated temperatures of 744–781 °C throughout the metamorphism with a weighted average value of  $766.0 \pm 26$  °C as well as pressures of 1.65–2.99

kbar with a weighted mean value of  $2.48 \pm 0.33$  kb at an approximate depth of 8 km.

- The new petrographic, detailed mineral chemistry analyses, together with geochemical interpretations, and geothermobarometry estimates from the amphibole schist–amphibolites of K m rhan ophiolite, suggest that these rocks occurred on a subducted slab during the ophiolite formations in a Supra-subduction zone geodynamic setting.

## ACKNOWLEDGEMENT

The author would like to thank Dr. Andrew Locock for performing mineral chemistry analyses and The author is also indebted to the anonymous reviewers and the Editor for their constructive comments and suggestions, which greatly helped to improve the manuscript. Funding information: Financial supports from the  ukurova University Research Foundation (Project No: FBA- 2021-13093).

## References

1. Williams H. and Smyth W.R. Metamorphic aureoles beneath ophiolite suites and Alpine peridotites: Tectonic implications with west Newfoundland examples. *Am. J. Sci.* 273, (1973) 594–621.
2. Coleman R.G. Tectonic setting for ophiolite obduction in Oman. *J. Geophys. Res.* 86, (1981) 2497–2508.
3. Searle M.P. and Cox J. Subduction zone metamorphism during formation and emplacement of the Semail ophiolite in the Oman Mountains. *Geol. Mag.* 139, 3, (2002) 241–255.
4. Nurlu, N. U–Pb zircon geochronology and geochemistry of the metamorphic sole rocks of the Meydan m lange, South-East Turkey: Implications for ophiolite emplacement and protolith, *GEOLOGICA CARPATHICA*, 71, 2, (2020) 183–205.
5. Al-Riyami K., Robertson A., Dixon J. and Xenophontos C. Origin and emplacement of the Late Cretaceous Baer–Bassit ophiolite and its metamorphic sole in NW Syria. *Lithos* 65, 1, (2002) 225–260.
6.  elik  .F. Detailed geochemistry and K–Ar geochronology of the metamorphic sole rocks and their mafic dykes from the Mersin Ophiolite, Southern Turkey: *Turk. J. Earth Sci.* 17, (2008) 685–708.
7. Sayit, K., Bedi, Y., Tekin, U.K., G nc ođlu, M.C., Okuyucu, C. Middle Triassic backarcbasalts from the blocks in the Mersin M lange, southern Turkey: implications for the geodynamic evolution of the Northern Neotethys. *Lithos* 268, (2017) 102–113.
8. Nurlu, N. Petrology and LA–ICP–MS zircon geochronology for Late Cretaceous felsic dikes and intermediate volcanic rocks hosted in Mersin ophiolite, South Turkey and its implications. *Geosci J* (2020). <https://doi.org/10.1007/s12303-020-0020-0>.
9. Guilmette, C., Smit, M.A., van Hinsbergen, D.J.J., G rer, D., Corfu, F., Charette, B., Maffione, M., Rabeau, O., and Savard, D. Forced subduction initiation recorded in the sole and crust of the Semail Ophiolite of Oman: *Nature Geoscience*, v. 11, p. (2018) 688–695, <https://doi.org/10.1038/s41561-018-0209-2>.
10. Kim, S., Jang, Y., Kwon, S., Samuel, O. V., Kim, S.W., Park, S., Santosh, M., Kokkalas, S. Petro-tectonic evolution of metamorphic sole of the Semail ophiolite, UAE, *Godwana Research*, 86 v, (2020) p. 203–221.
11. Howard, D. P. Unravelling ophiolite emplacement history with microfossils - the Baer-Bassit ophiolite of NW Syria. Doctoral thesis, UCL (University College London). (2006) p. 1–232.
12. Chan, G. H., Malpas, J., Xenophontos, C., Lo, C. H. Timing of subduction zone metamorphism during the formation and emplacement of Troodos and Baer–Bassit ophiolites: insights from 40Ar–39Ar geochronology. *Geol. Mag.* 144 (5), 2007, pp. 797–810.
13. Lytwyn J.N and Casey J.F. The geochemistry of post kinematic mafic dyke swarms and subophiolitic metabasites, Pozanti–Karsanti ophiolite, Turkey: Evidence for ridge subduction. *Geol. Soc. Am. Bull.* 107, (1995) 830–850.
14. Gnos E., and Peters T. K–Ar ages of the metamorphic sole of the Semail ophiolite: implications for cooling history. *Contrib. Mineral. Petrol.* 113, (1993) 325–332.
15.  eng r A.M.C. and Yılmaz Y. Tethyan evolution of Turkey: A plate tectonic approach. *Tectonophysics* 75, (1981) 181–241.
16. Yılmaz, Y. New evidence and model on the evolution of the southeast Anatolian orogen. *Geological Society of America Bulletin*, 105, (1993) 251–271.
17. Yılmaz Y., Yiđitbaş E. and Gen  Ş.C. Ophiolitic and Metamorphic Assemblages of Southeast Anatolia and their Significance in the Geological Evolution of the Orogenic Belt. *Tectonics* 12, (1993) 1280–1297.
18. Robertson, A. H. F., Usta mer, T., Parlak, O.,  nl gen , U. C., Tasli, K. and Inan, N. The Berit transect of the Tauride thrust belt, S. Turkey: Late Cretaceous–Early Cenozoic accretionary/ collisional processes related to closure of the Southern Neotethys. *Journal of Asian Earth Sciences*. (2006)
19. Robertson A.H. F., Parlak O., Rizaođlu T.,  nl gen   ., Inan N., Tasli K. and Usta mer T. Tectonic evolution of the South Tethyan ocean: evidence from the Eastern Taurus Mountains (Elazıđ region, SE Turkey). *Geol. Soc. London, Spec. Publ.* 272, (2007) 231–270.
20. Yazgan E. and Chessex R. Geology and Tectonic Evolution of the South–eastern Taurides in the Region of Malatya. *Turk. Assoc. Petrol. Geol.* 3, (1991) 1–42.
21. Bađcı U., Parlak O. and H ck V. Whole-Rock Mineral Chemistry of Cumulates from the Kızıladađ (Hatay) Ophiolite (Turkey): Clues for Multiple Magma Generation During Crustal Accretion in the Southern Neotethyan Ocean. *Mineral. Mag.* 69, 1, (2005) 53–76.
22. Beyarslan M. and Bing l A.F. Petrology of a suprasubduction zone ophiolite (Elazıđ, Turkey). *Canad. J. Earth Sci.* 37, (2000) 1411–24.
23. Rizaođlu, T., Parlak, O., H ck, V., İřler, F. Nature and significance of Late Cretaceous ophiolitic rocks and its relation to the Baskil granitoid in Elazıđ region, SE Turkey. In *Tectonic Development of the Eastern Mediterranean*, Robertson, A.H.F., Mountrakis, D. (eds). Geological Society, London, Special Publication, 260: (2006) 327–350.
24. Parlak O., Rizaođlu T., Bađcı U., Karaođlan F. and H ck V. Tectonic significance of the geochemistry and petrology of ophiolites in southeast Anatolia, Turkey. *Tectonophysics* 473, (2009) 173–187.
25. Nurlu N. Geochemistry and Tectonic Significance of the Tectonomagmatic Units in the Helete (Kahramanmarař) Region. PhD Thesis,  ukurova University Intitute of Natural and Applied Sciences, (2016) 1–281. (in Turkish with English abstract).
26. Nurlu N., Parlak O., Robertson A.H.F. and Quadt A. Implications of Late Cretaceous U–Pb zircon ages of granitic intrusions cutting ophiolitic and volcanogenic rocks for the assembly of the Tauride allochton in SE Anatolia (Helete area, Kahramanmarař Region, SE Turkey). *Int. J. Earth Sci.* 105, (2016) 283–314.
27. Robertson A.H.F. Overview of the genesis and emplacement of Mesozoic ophiolites in the eastern Mediterranean Tethyan region.

- Lithos 65, (2002) 1-67.
28. MTA (General Directorate of Mineral Research and Exploration). 1:500.000 scaled 513 Geological Maps of Turkey (Adana map section), Ankara-Turkey. (2002) (in Turkish with 514 English abstract) <http://www.mta.gov.tr/eng/maps/geological-500000> .
  29. Rızaoğlu, T. Petrography and Geochemistry of the Tectonomagmatic Units Cropping Out Between Baskil and Sivrice (Elazığ), PhD Thesis, Çukurova University Institute of Natural and Applied Sciences, (2006) 1-259. (in Turkish with English abstract).
  30. Donovan J.J., Snyder D.A and Rivers M.L. An Improved Interference Correction for Trace Element Analysis. *Microbeam Analysis 2*, (1993) 23-28.
  31. Armstrong J.T. Quantitative analysis of silicates and oxide minerals: Comparison of Monte-Carlo, ZAF and Phi-Rho-Z procedures. In: Newbury D.E. (Ed.): *Microbeam Analysis*. San Francisco Press, (1988) 239-246.
  32. Leterrier, J., Maury, R., Thono, P., Girard, D., and Marchal, M. Clinopyroxene composition as a method of identification of the magmatic affinities of paleovolcanic series: *Earth and Planetary Science Letters*, v. 59, p. (1982) 139-154.
  33. Leake B.E., Woolley A.R., Arps C.E.S., Birch W.D., Gilbert M.C., Grice J.D., Hawthorne F.C., Kato A., Kisch H.J., Krivovichev V.G., Linthout K., Laird J., Mandarino J.A., Maresch W.V., Nickel E.H., Rock N.M.S., Schumacher J.C., Smith D.C., Stephenson N.C.N., Ungaretti L., Whittaker E.J.W. and Youzhi G., Nomenclature of amphiboles; Report of the Subcomm. on Amphiboles Intern. Miner. Ass., Commiss. New Minerals and Mineral Names. *Am. Mineral.*, 82: (1997) 1019-1037.
  34. Best M. G. *Igneous and metamorphic petrology*. Freeman, San Francisco, USA, (1982) 1-458.
  35. Brown E.H. The crossite content of ca-amphibole as a guide to pressure of metamorphism. *J. Petrol.* 18, (1977) 53-72. <https://doi.org/10.1093/petrology/18.1.53>
  36. Fleet, M.E., Barnett, R.L. Partitioning in calciferous amphiboles from the Froot Mine, Sudbury, Ontario. *Can. Mineral.* 16, (1978) 527-532.
  37. Yildirim, M. and Yilmaz, Y. Güneydogu Anadolu orojenik kuşağının ekaylı zonu. *Bulletin of Turkish Association of Petroleum Geologists*, 3, (1991) 57-73. (in Turkish with English abstract).
  38. Robertson, A. H. F., Ustaömer, T., Parlak, O., Ünlügenç, U. C., Tasli, K. and İnan, N. The Berit transect of the Tauride thrust belt, S. Turkey: Late Cretaceous-Early Cenozoic accretionary/ collisional processes related to closure of the Southern Neotethys. *Journal of Asian Earth Sciences*. (2006)
  39. Turan, M., Ve Bingöl, A. F. Kovancılar-Baskil (Elazığ) Arası Bölgenin Tektono-stratigrafik Özellikleri. *Ahmet Acar Jeoloji Sempozyumu, Bildiriler, Çukurova Üniversitesi, Adana, (1991) 213-227.* (in Turkish with English abstract).
  40. Nisbet, E., and Pearce, J. Clinopyroxene composition in mafic lavas from different tectonic settings: Contributions to Mineralogy and Petrology, v. 63, p. (1977) 149-160.
  41. Beccalova, L., Macciotta, G., Piccardo, G.B., and Zeda, O. Clinopyroxene composition of ophiolite basalts as petrogenic indicator: *Chemical Geology*, v. 77, p. (1989) 165-182
  42. Locock A.J. 2014: An Excel spreadsheet to classify chemical analyses of amphiboles following the IMA 2012 recommendations. *Comput. Geosci.* 62, 1-11.
  43. Johnson M.C. and Rutherford M.J. Experimental calibration of the aluminum in hornblende geobarometer with application to long valley caldera (California) Volcanic Rocks. *Geology* 17, (1989) 837-841.
  44. Holland T. and Blundy J. Non-ideal interactions in calcic amphiboles and their bearing on amphibole-plagioclase thermometry. *Contrib. Miner. Petrol.* 116, (1994) 433-447.
  45. Anderson J.L., Barth A.P., Wooden J.L. and Mazdab F. Thermometers and thermobarometers in granitic systems. *Rev. Mineral. Geochem.* 69, 1, (2008) 121-142.
  46. Ludwig K.R. *User's Manual for Isoplot 3.00: A Geochronological Toolkit for Microsoft Excel*. Special Publication/Berkeley Geochronology Center (2003) 74.
  47. Nurlu N. U-Pb zircon geochronology and geochemistry of the metamorphic sole rocks of the Meydan mélangé, South-East Turkey: Implications for ophiolite emplacement and protolith. *Geologica Carpathica*, 71, 2, (2020) 183-205.
  48. Akıncı A. C., Robertson A. H. F., Ünlügenç U. C. Late Cretaceous-Cenozoic subduction-collision history of the Southern Neotethys: new evidence from the Çağlayanerit area, SE Turkey. *International Journal of Earth Sciences* 105, (2016) 315-337



# Quantum Mechanical Calculation of Molybdenum and Tungsten Influence on the CrM-oxide Catalyst Acidity

Oyegoke Toyese<sup>1</sup> , Fadimatu N. Dabai<sup>1</sup> , Adamu Uzairur<sup>2</sup>  and Baba El-Yakubu Jibril<sup>1</sup> 

<sup>1</sup>Ahmadu Bello University, Department of Chemical Engineering, Zaria, Nigeria

<sup>2</sup>Ahmadu Bello University, Department of Chemistry, Zaria, Nigeria

## ABSTRACT

Semi-empirical calculations were employed to understand the effects of introducing promoters such as molybdenum (Mo) and tungsten (W) on chromium (III) oxide catalyst for the dehydrogenation of propane into propylene. For this purpose, we investigated CrM-oxide (M = Cr, Mo, and W) catalysts. In this study, the Lewis acidity of the catalyst was examined using Lewis acidity parameters (Ac), including ammonia and pyridine adsorption energy. The results obtained from this study of overall acidity across all sites of the catalysts studied reveal Mo-modified catalyst as the one with the least acidity while the W-modified catalyst was found to have shown the highest acidity signifies that the introduction of Mo would reduce acidity while W accelerates it. The finding, therefore, confirms tungsten (W) to be more influential and would be more promising when compared to molybdenum (Mo) due to the better avenue that is offered by W for the promotion of electron exchange and its higher acidity(s). The suitability of some molecular descriptors for acidity prediction as a potential alternative to the current use of adsorption energies of the probes was also reported.

### Keywords:

Molecular descriptor; Metallic oxide; Semi-empirical calculation; Chromium oxide; Lewis acidity; Molecular probe.

## INTRODUCTION

Propylene is one of the feedstocks in the petrochemical industries. It is commonly used as a precursor to producing important intermediates and products, such as isopropanol, polypropylene, propylene oxide, epichlorohydrin, and acrylonitrile [1, 2]. Several researchers have investigated the challenges encountered in propylene production which includes searching ways of increasing catalyst selectivity for propylene and decreasing catalyst deactivations. In addressing this challenge, a density functional theory (DFT) calculation was employed by Yan et al. [3] to propose a radical mechanism for propane dehydrogenation over  $\text{Ga}_2\text{O}_3$  (100) where H abstraction by O(2) site was identified as a low energy barrier step. Ming et al. [4] employed DFT calculations to show that the introduction of tin into platinum catalyst lowers the energy barrier for propylene desorption and simultaneously increases the activation energy for propylene dehydrogenation, which has a positive effect on the selectivity of propylene production. Lauri et al. [5] also made related findings for the use of Pt-Sn catalyst, which lowered the coking rate while weakening the binding of propylene. Timothy [6] confirmed

that PtGa alloy has superior catalytic properties than Sn-Ga alloy and similar properties to those deduced for Pt-Sn alloy as reported by Lauri et al. [5]. Stephanie et al. [7] found that an increase in hydrogen pressure lowers the coverage of deeply dehydrogenated coke precursors on the surface. Other similar findings have been reported in the literature [8, 9, 10, 11].

Recently, Oyegoke et al. [12] computationally showed that the chromium sites are highly acidic and reactive compared to the oxygen sites, identifying chromium sites as the leading active site in the promotion of propane dehydrogenation into propylene over  $\text{Cr}_2\text{O}_3$  catalyst. Previous works such as Gascón et al. [13] have identified that the  $\text{Cr}_2\text{O}_3$  catalyst in its pure form shows low catalyst selectivity for desired products and rapidly deactivates.

The search has shown that no work has investigated the role of foreign materials like molybdenum (Mo) and tungsten (W) in influencing the Lewis acidity of a catalyst site and how the material influences the performance of the  $\text{Cr}_2\text{O}_3$  catalyst. Therefore, in this current

### Article History:

Received: 2020/06/18

Accepted: 2020/11/02

Online: 2020/12/31

Correspondence to: Oyegoke Toyese,  
Ahmadu Bello University, Chemical  
Engineering, Zaria, NIGERIA  
E-Mail: oyegoketoyese@gmail.com  
Phone: +234 703 047 91 06

study, an approximation of the parameterized method 3 (PM3) of the semi-empirical theory was used to study the influence of foreign materials on the acidity of the chromium (III) oxide catalyst in a dehydrogenation process, using ammonia and pyridine (computationally) as molecular probes for the evaluation of the Lewis acidity of the sites. The suitability of some molecular descriptors as a potential substitute for using the probe's adsorption energies in the measurement of Lewis acidity (Ac) was evaluated. Its progress should reduce the time, cost, and efforts used in the evaluation of Ac.

## THEORY

In molecular modeling, the molecular descriptors are diagrammatically presented in Fig. 1 establishing the relationship that exist among them. The electron affinity (EA) commonly defined as the capability of a ligand/catalyst/adsorbent to accept precisely one electron from a donor [14], which is known to be computed by chemists in the form:

$$EA \approx -ELUMO \quad (1)$$

The ionization energies (IE) known to be the energy required to remove electrons from the outermost shell is mathematically expressed in equation (2) in line with the report of Bendjeddou et al. [15].

$$IE \approx -EHOMO \quad (2)$$

The electronegativity (EN) of species can be mathematically expressed as:

$$EN, \chi = \frac{(IE+EA)}{2} \approx -\left(\frac{ELUMO + EHOMO}{2}\right) \quad (3)$$

The chemical potential (CP) of species was defined to be the negative form of electron negativity (EN), and in line with the report of Bendjeddou et al. [15], it can be mathematically expressed as:

$$CP, \mu = -\frac{\partial E}{\partial N} \approx -\chi \quad (4)$$

Chemical hardness (CH) of the structure/site is a molecular descriptor that defines structural stability and reactivity. It is expressed in the form [14, 15]:

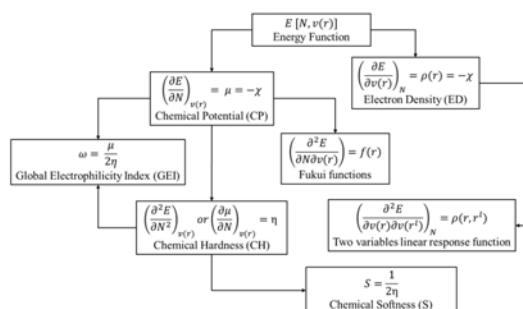


Figure 1. Molecular Descriptors employed in Molecular Modelling.

$$CH, \eta = \left(\frac{\partial^2 E}{\partial N^2}\right) = \left(\frac{\partial \mu}{\partial N}\right) \approx \left(\frac{IE - EA}{2}\right) \quad (5a)$$

$$CH, \eta \approx \left(\frac{ELUMO - EHOMO}{2}\right) \quad (5b)$$

Although, according to Luis et al. [16], some works tend to neglect the term  $\frac{1}{2}$ , and when this is done, it approximates what is known as energy bandgap, E-gap.

Softness (S), known as the reciprocal of hardness often defined as the property of molecules that measure the degree of chemical reactivity of a given species [14, 16]. It usually is in the form:

$$S = \frac{1}{2\eta} \quad (6)$$

Global Electrophilicity Index (GEI) is a measure of the ability of a molecule to take up electrons [17, 18] and can be expressed in equation (5). It can also be said to be the tendency of an electrophile to acquire an extra amount of electron density, given by  $\mu$ , and the resistance of a molecule to exchange electron density with the environment, given by Domingo et al. [19].

$$GEI, \omega \equiv \frac{\mu^2}{2\eta} \text{ or } \frac{\chi^2}{2\eta} \quad (7)$$

Likewise, this parameter,  $\omega$  is called the "electrophilicity index" and is considered to be a measure of electrophilic power, just as, in classical electrostatics, power is  $\frac{V^2}{R}$ , and  $\mu$  and  $\eta$  serve the purpose of potential (V) and resistance (R), respectively [18, 19, 20].

## COMPUTATIONAL BACKGROUND

In this study, the computations were carried out with the use of the Semi-empirical Parameterized Model 3 (PM3) calculation method in the Spartan 18 software package and ran on an HP 15 Pavilion Notebook (Intel Core i3 Processor @ 1.8 GHz and 6 GB RAM). This study involves the use of Spartan 18 in modeling and running all the molecular simulations while Microsoft Excel was used to aid both the mathematical and statistical analysis carried out. The molecular structures of the species involved in this study were sketched with the ACD/ChemSketch 11.

### Choice of cluster structures

The molecular structures employed in representing chromium (III) oxide catalyst clusters or slabs were adopted from Compere et al. [21] and was found to be in line with the clusters reported in other studies [22, 23, 24, 25, 26, 27] while that of the probes and reactant was built to be in line with the molecular structure present in PubChem

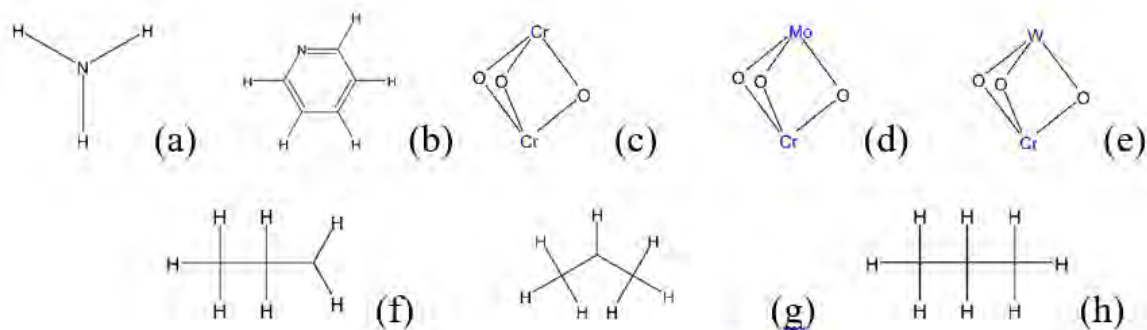


**Figure 2.** Molecular structure of molecular probes (a-b), unmodified catalyst cluster (c), modified catalyst cluster (d-e), Isopropyl species (f-g), propane (h).

online database. Besides, the modified surface of the catalyst (or modified form of the catalyst cluster) was built through the substitution of one chromium (III) oxide cluster with different metals such as molybdenum (Mo) and tungsten (W) to yield two modified catalyst clusters with names, Mo-modified, and W-modified, catalyst respectively. Fig. 2 pictorially displays the molecular structures employed in this study.

### Ground-state geometrical optimizations

The catalyst, reactant, and molecular probe structures were built and minimized using the molecular mechanics (MMFF) method to remove strain energy to improve accuracy according to previous studies [28]. After this, the geometry optimizations and computations were carried out for the respective structures involved in this study using a PM3 method at the ground state. Infrared (IR) frequency, orbital, and energies calculations were carried out on all optimized structures, and the absence of any imaginary frequencies confirmed that each optimized structure was located at a minimum on its IR spectra plot. All computations are made with SCF tolerance of  $10^{-9}$ . The PM3 basis set was employed because literature confirms it is one of the best for computations that involve transition metals, such as chromium [28, 29].

### Molecular descriptors and adsorption energy computation

The heat of formation for the adsorbed species, catalyst slab, and catalyst slab with adsorbed species was calculated. The Infra-Red spectra, molecules' energies (E), and molecular parameters were evaluated from the computational approach employed, and the chemical hardness (CH), electronegativity (EN), chemical potential (CP), energy bandgap (E-gap), and global electrophilicity index (GEI) were calculated using Equation (1-7) [28]. Adsorption energies were calculated using the equation (6), which was in line with the literature [28, 30, 15, 31, 32]:

$$E_{ads} = E_{pq} - E_p - E_q \quad (8)$$

where  $E_{ads}$  is adsorption energy,  $E_p$  is the total energy of adsorbate (p),  $E_q$  is the total energy of free cluster or catalyst slab (q), and  $E_{pq}$  is the total energy of adsorbed cluster or catalyst slab with adsorbate (pq).

### Lewis acidity evaluation

The Lewis acidity of different catalyst sites was evaluated using ammonia as a molecular probe. The sites' Lewis acidity was evaluated or rated using the adsorption energies calculated for the ammonia adsorption across the catalyst sites using the equation (8). The Lewis acidity of the catalyst sites was equally measured with the use of pyridine adsorption energies. This study approach was found to be in line with the method employed in the literature [33, 34, 12] in the measurement of Lewis acidity, which was taken to be a direct function of the probe adsorption energies across the sites. After this, the correlation that existed with the use of ammonia and pyridine was examined.

### Acidity-reactivity correlation analysis

Molecular descriptors computed were correlated with Lewis acidity (Ac) of the catalyst, and their relationship with Ac of the catalyst site was evaluated using spearman's correlation analysis. The effects of different metals (or promoters) on the catalyst metallic sites' Lewis acidity were evaluated.

## RESULTS AND DISCUSSION

### Catalysts, Probe, Reactant, and Adsorption Species' Geometrical Optimization

The molecular properties computed from the geometry optimization of the probes, propane, and adsorption species are presented in Table 1 and Fig. 3 for the catalysts.

**Table 1.** Molecular Properties of the Probes, Catalysts, Isopropyl(s), and Propane.

Name	Formula	ELUMO (eV)	EHOMO (eV)	E (eV)	E <sub>Gap</sub> (eV)	CH, $\eta$ (eV)	EN, $\chi$ (eV)	CP, $\mu$ (eV)	GEI, $\omega$ (eV)
Ammonia	H <sub>3</sub> N	3.33	-9.70	-0.13	13.03	6.51	3.18	-3.18	0.39
Pyridine	C <sub>5</sub> H <sub>5</sub> N	-0.01	-10.10	1.32	10.09	5.05	5.05	-5.05	1.26
Propyl-1	C <sub>3</sub> H <sub>7</sub>	3.22	-9.51	0.45	12.73	6.36	3.15	-3.15	0.39
Propyl-2	C <sub>3</sub> H <sub>7</sub>	3.22	-8.91	0.09	12.13	6.06	2.85	-2.85	0.33
Hydrogen	H <sub>2</sub>	0.00	-13.07	2.26	13.07	6.54	6.54	-6.54	1.63
Propane	C <sub>3</sub> H <sub>8</sub>	3.71	-11.51	-1.02	15.22	7.61	3.90	-3.90	0.50

These results presented include the highest occupied molecular orbital energy (EHOMO), lowest unoccupied molecular orbital energy (ELUMO), ionization energy (IE), electron affinity (EA), chemical hardness (CH), electronegativity (EN), bandgap (E-Gap), and others. The energy bandgap (E-Gap) is known to be the absolute difference between the EHOMO and LUMO energies of any structure [15]. However, the optimized structures' geometry is presented in Table A6 in the Supplementary Information of this report.

Table 1 shows that propane has the most significant energy gap (15.22 eV), while pyridine has the shortest energy gap (10.09 eV), which implies that pyridine (molecular probe) would be the most reactive and least stable while propane will be the least reactive and most stable materials. From the CrM-oxide surfaces, this study also identified that the unmodified surface of the chromium (III) oxide showed the shortest energy band gap (11.83 eV). In comparison, the surface-modified with molybdenum showed the most significant energy band gap (13.58 eV) in Fig. 3 (Table A1 in Supplementary Information). This result indicates that the presence of the molybdenum and tungsten increases the stability of the catalyst surface. In other words, it can be said that molybdenum and tungsten are harder molecules compared to unmodified Cr<sub>2</sub>O<sub>3</sub> structures [15].

In the result of electronegativity (EN) presented in Fig. 3 (Table A1 in Supplementary Information), it was observed

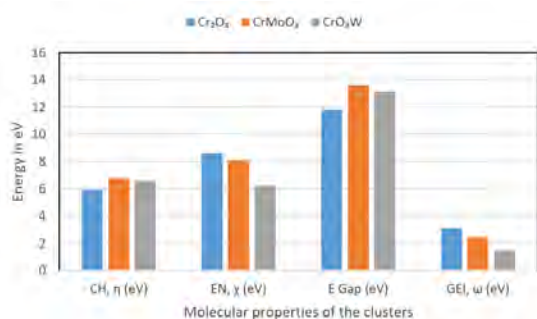


**Figure 3.** Molecular Properties of the Catalysts (Note: E Gap = Band Gap, CH = Chemical Hardness, EN = Electronegativity, GEI = Global Electrophilicity Index).

that chromium (III) oxide has the highest electron affinity (8.60 eV) while isopropyl showed the least electronegativity (2.85-3.15 eV). These findings imply that the chromium (III) oxide has a high ability to accept electrons, while isopropyl shows the least potential for electron reception. It further shows that the presence of tungsten and molybdenum decreases the EN of Cr<sub>2</sub>O<sub>3</sub> catalyst, which agreed with David [35] showing that tungsten (W) and molybdenum (Mo) displayed a relative lower EN compared to chromium (Cr).

Similarly, it was observed that unmodified chromium (III) oxide has the highest LUMO energy (-2.68 eV), while propane has the lowest LUMO energy (3.71 eV). These findings imply that unmodified chromium (III) oxide possesses a high ability to attract electrons to its surface while propane possesses the least electron attraction ability. This result shows that the unmodified chromium (III) oxide is most likely to accept electrons from the adsorbates like propane and propylene during the binding process. It is evident from its results obtained as 3.12 eV for the global Electrophilicity Index (GEI), which shows that unmodified chromium (III) oxide is highly reactive and good electrophile due to its high GEI value [18].

The chemical hardness (CH) results in Table 1, and Fig. 3 shows that pyridine has the lowest IE (5.05 eV), while propane has the highest chemical hardness (7.61 eV), indicating that propane has the highest resistance towards the deformation of its electron cloud of atoms. It further shows that the presence of tungsten and molybdenum increases the chemical hardness of Cr<sub>2</sub>O<sub>3</sub> catalyst (as shown in Fig. 3), which agreed with the literature [35] showing that tungsten (W) and molybdenum (Mo) displayed a relatively higher chemical hardness compared to chromium (Cr). Similarly, it was observed that isopropyl species has the highest HOMO energy (-9.51 eV to -8.91 eV) while molybdenum modified chromium (III) oxide surface has the lowest HOMO energy (-14.89 eV). This finding indicates that pyridine would quickly release electrons compared to other species and surfaces modified with metals like tungsten and molybdenum, which will not quickly release electrons for a reaction process [36].

**Table 2.** Lewis acidity of Cr<sub>2</sub>O<sub>3</sub> using Ammonia probe.

Site	ELUMO (eV)	EHOMO (eV)	E (eV)	Ac_Cr <sub>2</sub> O <sub>3</sub>	CH, η (eV)	EN, χ (eV)	CP, μ (eV)	GEI, ω (eV)
Cr	4.56	-4.33	-8.01	-7.00	4.45	-0.11	0.11	0.00
O	8.70	0.66	-4.17	-3.16	3.41	-4.68	4.68	1.45

**Table 3.** Lewis acidity of CrMoO<sub>3</sub> using Ammonia probe.

Site	ELUMO (eV)	EHOMO (eV)	E (eV)	Ac_CrMoO <sub>3</sub>	CH, η (eV)	EN, χ (eV)	CP, μ (eV)	GEI, ω (eV)
Cr	3.98	-5.89	-2.31	-1.45	4.94	0.96	-0.96	0.05
Mo	4.54	-6.88	-7.99	-7.13	5.71	1.17	-1.17	0.06
O	10.41	-0.50	-5.44	-4.58	5.46	-4.96	4.96	1.02

**Table 3.** Lewis acidity of CrWO<sub>3</sub> using Ammonia probe.

Site	ELUMO (eV)	EHOMO (eV)	E (eV)	Ac_CrWO <sub>3</sub>	CH, η (eV)	EN, χ (eV)	CP, μ (eV)	GEI, ω (eV)
Cr	4.96	-5.03	-14.26	-11.87	5.00	0.04	-0.04	0.00
W	4.28	-2.10	-11.48	-9.09	3.19	-1.09	1.09	0.09
O	9.50	-0.30	-5.82	-6.02	4.65	-4.60	4.60	1.01

### Lewis Acidity Evaluation of CrM-Oxide Catalyst Site

Here, the different potential sites on both unmodified and modified chromium (III) oxide surfaces were evaluated for acidity using the adsorption energies (Eads). This study evaluated the use of pyridine, and ammonia adsorption energy was employed. In contrast, the use of other molecular descriptors such as LUMO energy, electronegativity (EN), chemical hardness (CH), and global Electrophilicity index (GEI) as potential Lewis acidity descriptors were evaluated. The method employed in the Lewis acidity computation is in line with that employed in past works [33, 37, 12].

#### Adsorption of Ammonia on CrM-Oxide Surface

The ammonia adsorption energies tagged 'Ac\_Cr<sub>2</sub>O<sub>3</sub>, Ac\_CrMoO<sub>3</sub>, and Ac\_CrWO<sub>3</sub>' for the respective sites are presented in Table 2-4. The evaluation of the result identifies that the chromium (Cr) site on the unmodified chromium (III) oxide showed the highest Lewis acidity while the oxygen (O) site was found to be the lowest Lewis acidity. The findings agreed with the literature [38, 39], which identified Cr as the most active site.

This deduction indicates that oxygen (O) is the most basic Lewis site, while chromium (Cr) is the most acidic Lewis site on unmodified chromium (III) oxide surface. According to Michorczyk et al. [40, 39], this implies that Cr, which is unsaturated, would be more unstable and be more active

for adsorption of propane, unlike the oxygen sites, which agree with the finding of Gascón et al. [13] that confirms the Cr site to be active.

CrM-oxide surface with chromium site is substituted with molybdenum; the finding from the results presented in Table 3 shows that the Lewis acidity trend of the sites on the surface is molybdenum (Mo) > oxygen (O) > chromium (Cr). This finding indicates that the chromium (Cr) site would be the most basic Lewis site, while molybdenum (Mo) would be the most acidic Lewis site.

Further study of Table 4 shows that the chromium (Cr) site is the most acidic Lewis site while oxygen (O) shows the least acidic Lewis site on the surface modified with substitution of chromium with tungsten (W). It implies that the oxygen (O) site is the most basic Lewis site.

The overall assessment of the different catalyst Lewis acidity shows that CrWO<sub>3</sub> (-11.87 eV) > CrMoO<sub>3</sub> (-7.13 eV) > Cr<sub>2</sub>O<sub>3</sub> (-7.00 eV) in their increasing order of acidity. This deduction finds an agreement with the reports of Bailey et al. [41] and Chen et al. [42], which indicates that tungsten is more promising when compared to Mo-modified Cr<sub>2</sub>O<sub>3</sub> due to the high Lewis acidity of W-modified Cr<sub>2</sub>O<sub>3</sub>.

#### Adsorption of Pyridine on CrM-Oxide Surfaces

Here, this study's findings on the evaluation of Lewis acidity of the catalyst sites using pyridine as the molecular probe are presented in Table 5.

**Table 5.** Lewis acidity of Cr<sub>2</sub>O<sub>3</sub> using Pyridine probe.

Site	ELUMO (eV)	EHOMO (eV)	E (eV)	Ac_Cr <sub>2</sub> O <sub>3</sub>	CH, η (eV)	EN, χ (eV)	CP, μ (eV)	GEI, ω (eV)
Cr	1.94	-5.54	-6.62	-7.06	3.74	1.80	-1.80	0.22
O	8.28	1.38	-3.68	-4.12	3.45	-4.83	4.83	1.69

**Table 6.** Lewis acidity of CrMoO<sub>3</sub> using Pyridine probe.

Site	ELUMO (eV)	EHOMO (eV)	E (eV)	Ac_CrMoO <sub>3</sub>	CH, η (eV)	EN, χ (eV)	CP, μ (eV)	GEI, ω (eV)
Cr	4.46	-2.25	-2.66	-3.25	3.35	-1.11	1.11	0.09
Mo	2.08	-6.83	-6.64	-7.23	4.46	2.38	-2.38	0.32
O	5.05	-0.86	-3.76	-4.35	2.95	-2.09	2.09	0.37

**Table 7.** Lewis acidity of CrWO<sub>3</sub> using Pyridine probe.

Site	ELUMO (eV)	EHOMO (eV)	E (eV)	Ac_CrWO <sub>3</sub>	CH, η (eV)	EN, χ (eV)	CP, μ (eV)	GEI, ω (eV)
Cr	2.05	-5.32	-12.23	-11.29	3.69	1.63	-1.63	0.18
W	3.14	-3.97	-10.72	-9.78	3.55	0.42	-0.42	0.01
O	5.34	-1.14	-10.02	-9.08	3.24	-2.10	2.10	0.34

A trend similar to the one deduced from the use of ammonia as the probe was observed showing that the chromium (Cr) site on the unmodified chromium (III) oxide showed its high Lewis acidity (pyridine adsorption energy) while the oxygen (O) site was found to be the lowest Lewis acidity. This result indicates that oxygen (O) is the most basic Lewis site, while chromium (Cr) is the most acidic Lewis site on unmodified chromium (III) oxide surface. This deduction implies that pyridine adsorption energy studies confirm the Cr site as the most acidic and active site, in agreement with Michorczyk et al. [40] report.

The finding on the CrM-oxide surface with chromium site is substituted with molybdenum presented in Table 6 shows that the chromium (Cr) site would be the most basic Lewis site. In contrast, molybdenum (Mo) would be the most acidic Lewis site when the pyridine probe is employed, which was found to agree with the initial deductions made for the use of ammonia as the molecular probe.

Table 7 showed that the chromium (Cr) site is the most acidic Lewis site, while oxygen (O) shows the least acidic Lewis site on the surface modified with substitution of chromium with tungsten (W). It indicates that the oxygen (O) site is the most basic Lewis site. These findings agree with the deductions made from the use of ammonia as molecular probes.

The trend of the catalyst Lewis acidity observed for CrWO<sub>3</sub>, CrMoO<sub>3</sub>, and Cr<sub>2</sub>O<sub>3</sub> was found to show a similar order with that obtained when ammonia was used as pyri-

dine. Likewise, the deductions agree with the literature [41, 42], which indicates that tungsten would perform better than Mo-modified Cr<sub>2</sub>O<sub>3</sub> due to the high Lewis acidity of W-modified Cr<sub>2</sub>O<sub>3</sub> surface.

### Correlation of Catalyst Lewis Acidity & Molecular Descriptors

This analysis tends to evaluate the correlation of Lewis acidity measured in terms of ammonia and pyridine adsorption energy presented in Table A2-A4 of the Supplementary Information, including results showing the ammonia and pyridine probe Lewis acidity relationship with other molecular descriptors such as ELUMO, EHOMO, CH, EN, CP, and GEI as potential Lewis acidity descriptors using the results presented in Table 2 – 7.

The correlation analysis results for the chromium site shows a correlation coefficient of +1.00 for the relation between ammonia and pyridine Lewis acidity of chromium site,  $r(aAc\_Cr / pAc\_Cr)$  evaluated in Table A2 of the Supplementary Information. The findings obtained from the analysis reveals that there exists a good and direct relationship in the use of ammonia or pyridine as a molecular probe for the assessment of Lewis acidity, which was found to agree with the literature [32, 12], which made the similar deduction that shows a unity of result output in the use of ammonia and pyridine in the measurement of Lewis acidity. The results equally show that there is a good relationship for GEI (-0.95), CP (-0.99), EN (-0.99), E (+1.00), EHOMO (-0.90), and ELUMO (-0.89) except for CH (-0.53) that shows the

fair correlation for the deductions made from the used ammonia and pyridine for the chromium site evaluation.

Furthermore, it was identified that a good relationship thus exists for all the molecular descriptors aforementioned except for aCH (-0.02) with Lewis acidity deduced via the use of ammonia as a molecular probe. Nevertheless, when pyridine was employed, all molecular descriptors showed a good correlation or relationship with the Lewis acidity as well except for the ammonia HOMO energy (-0.49) and aCH (-0.12) that shows a weak correlation as  $r$  is -0.4 (as shown in Table A2). Findings from the study of results presented in Table A2 of the Supplementary Information identifies GEI, CP, EN, and ELUMO descriptors as better potential substitutes for the use of probe adsorption energies for the study of Lewis acidity.

In the study of substituted metal or introduced metal sites, the correlation analysis result presented in Table A3 of the Supplementary Information shows a correlation coefficient of +1.00 for the relationship between ammonia and pyridine Lewis acidity of chromium site,  $r$  (aAc\_M / pAc\_M). The results imply that the Lewis acidity evaluation with the use of ammonia positively agrees well with that deduced with the use of pyridine. These findings are similar to the reports of Liu et al. [34] and Oyegoke et al. [12], which made a similar deduction that shows a unity of result outputs in using ammonia and pyridine for the measurement of Lewis acidity. Moreover, analogous correlations were also obtained for all other descriptors except for GEI (-0.51) and ELUMO (-1.00), which shows a negative correlation (where GEI correlation was found below).

Also, all molecular descriptors were found to agree with Lewis acidity evaluated via the use of ammonia except for pyridine ionization energy, i.e., pCH (+0.54). However, when pyridine is used as a molecular probe, only ammonia aCH was found to show a fair relationship with the Lewis acidity with a correlation coefficient of  $r = +0.62$ , unlike others that showed a better correlation. The findings indicate that chemical hardness (CH) would be a weak substitute for molecular probe adsorption energy as a molecular descriptor to measure Lewis acidity.

The correlation assessment results for Lewis acidity presented in Table A4 of the Supplementary Information indicate that the  $r$  (aAc\_O / pAc\_O) is +0.90, which signifies that there is a good and positive agreement between the use of ammonia and pyridine as a molecular probe in the evaluation of oxygen site Lewis acidity. Moreover, the ELUMO (-0.89), EHOMO (+0.96), CH (-0.98), and GEI (+1.00) showed a good correlation, while CP (-0.32) and EN (-0.32) showed a weak correlation for the outcomes obtained from the use of ammonia and pyridine comparison. Further study of

the parameters shows that all molecular descriptors show a good relationship with the Lewis acidity measured with the use of ammonia except for aEN (-0.20), aCP (+0.20), aELUMO (-0.46), and pCH (+0.42), which indicates a weak correlation with the Lewis acidity. ELUMOs ( $p = +0.47$ ,  $a = 0.00$ ), aHOMO (+0.39), and aCH (-0.16) showed a weak correlation when pyridine was employed to evaluate the Lewis acidity of the oxygen sites. The findings imply that the use of ELUMOs, aHOMO, CHs, aEN, and aCP as potential molecular descriptors would result in a poor prediction for oxygen sites.

A positive and good correlation was identified for aEN, aGEI, and pELUMO, while aELUMO, pEN, and pGEI showed a negative and good correlation from the results (Table A2 in Supplementary Information) for Cr-Site. In the correlation analysis of M-site presented in Table A3 of the Supplementary Information, aGEI and pELUMO was found to show a good and positive correlation with Lewis acidity. In contrast, aELUMO was found to be the only good and negative correlation for Lewis acidity across M-site. A good and positive correlation was found for aELUMO and pEN, while a negative correlation was found for GEIs and pELUMO with Lewis acidity at O-site.

The correlation analysis of all the molecular descriptors reveals GEIs, pCP, pEN, and pEHOMO correlate well with the Lewis acidity evaluated at all the sites using ammonia, pyridine, and ammonia, respectively. This finding confirms the pyridine-based descriptors such as GEI, CP, EN, and EHOMO as proper molecular acidity descriptors. At the same time, GEI was the only ammonia-based descriptor that could only serve as an alternative or substitute for molecular probe adsorption energy to measure catalyst site Lewis acidity.

The nature of the relationship between catalyst surfaces molecular descriptors such as ELUMO, EHOMO, E Gap, CH, EN, CP, and GEI in Fig. 4 (Table A1 of the Supplementary Information) and Lewis acidity of the catalyst sites (such as Cr, M, and O in Table 2-7) are presented in Table A5 of the Supplementary Information. Findings from this study shows that the correlation coefficient average of the

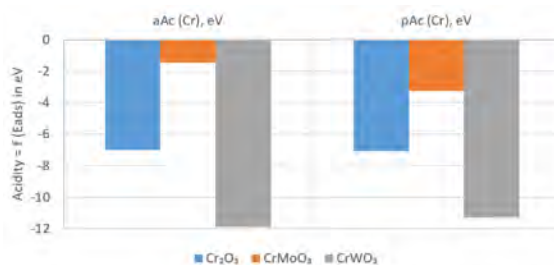


**Figure 4.** Result of Chromium (Cr) Site Acidity on the CrM-Oxide Catalyst Surface.

molecular descriptors goes in the trend of CH (-0.23) < E Gap (-0.23) < ELUMO (-0.81) < GEI (+0.82) < CP (-0.90) < EN (+0.90) < EHOMO (-0.92). This result indicates that EN and E Gap correlate poorly while other catalyst surface descriptors such as ELUMO, GEI, CP, EN, and EHOMO correlate well, but only EHOMO correlates best with the Lewis acidity of different catalyst sites. Therefore, this study identifies that GEI, ELUMO, EHOMO, CP, and EN would suitably describe the intensity of catalyst surface Lewis acidity without the use of molecular probe adsorption energy. However, EHOMO describes it best as it is displayed in Table A5 of the Supplementary Information. This finding was contrary to Jupp et al. [43], which present that GEI would be the best Lewis acidity descriptor.

### Assessment of Introduced Metals (M) Effect on CrM-oxide Catalyst Acidity

#### Effect of introducing metal (M) on the Cr-site Lewis acidity on the CrM-oxide

Here, the chromium site on a surface modified with tungsten was the most acidic with -11.29 to -11.87 eV adsorption energy, while the molybdenum modified surface showed a lower acidic site with adsorption energy -1.45 to -3.63 eV as shown in Fig. 4.

The order of the chromium site acidity was in the following order:  $\text{CrWO}_3 > \text{Cr}_2\text{O}_3 > \text{CrMoO}_3$ . This finding reveals that molybdenum on the chromium (III) oxide surface reduces the chromium site acidity while tungsten increases.

#### Effect of introduced metal (M) on the M-site Lewis acidity on the CrM-oxide surface

Fig. 5 shows that for the different metal sites (molybdenum and tungsten), the molybdenum modified surface showed a higher acidity (with adsorption energy of -7.13 to -7.23 eV) compared to the unmodified  $\text{Cr}_2\text{O}_3$  surface. In comparison, the tungsten modified surface was found to be the most acidity site (with adsorption energy of -9.09 to -9.78 eV). The order of the introduced or different metal site Lewis acidity was identified to be in the trend

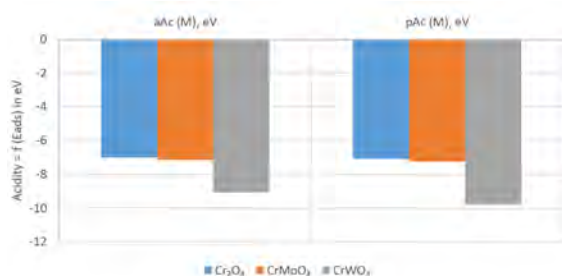


**Figure 5.** Result of Foreign Metal (M) Site Acidity on the CrM-Oxide Catalyst Surface.

of  $\text{CrWO}_3 > \text{CrMoO}_3 > \text{Cr}_2\text{O}_3$ .

This study shows that both molybdenum and tungsten metal sites exhibit a higher Lewis acidity than their respective chromium sites, signifying that the metals' presence increases the Lewis acidity of the catalyst surface for better exchange of electrons.

### Effect of introduced metal (M) on the O-site Lewis acidity on the CrM-oxide surface

In the evaluation of the Lewis acidity across the oxygen sites on different catalyst clusters, CrM-oxide (where M = Cr, Mo, and W metals), the results collected presented in Fig. 6 shows that oxygen sites found on surface modified with tungsten exhibits the highest Lewis acidity with an adsorption energy of -6.060 to -9.08 eV while the oxygen sites on the unmodified surface exhibit the least Lewis acidity with an adsorption energy of -3.16 to -4.12 eV.

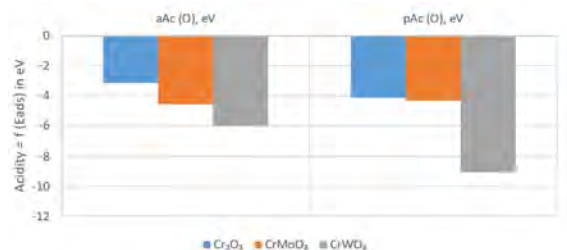


**Figure 6.** Result of Oxygen (O) Site Acidity on the CrM-Oxide Catalyst Surface.

However, the oxygen sites' Lewis acidity was in the trend:  $\text{CrWO}_3 > \text{CrMoO}_3 > \text{Cr}_2\text{O}_3$ . This trend order shows that the presence of Mo and W in the modified catalyst surface results in an increase in the Lewis Acidity of oxygen site on the catalyst's respective surfaces.

## CONCLUSION

With the use of the parameterized method 3 (PM3) of the semi-empirical theory, this work was able to investigate the influence of molybdenum (Mo) and tungsten (W) on the acidity of the chromium (III) oxide catalyst, using ammonia and pyridine (computationally) as molecular probes for the assessment of the catalyst sites' Lewis acidity. The suitability of some molecular descriptors for Lewis acidity prediction was also investigated as a potential alternative to the current use of probes' adsorption energies.

This study's findings indicate that introducing the Mo and W on chromium (III) oxide catalyst increases its stability due to the broad energy bandgap identified for the foreign metals' presence. Likewise, the presence of the foreign metals (Mo and W) was found to have increased the  $\text{Cr}_2\text{O}_3$



catalyst chemical hardness (CH) while, on the other side, resulting in a decrease in electronegativity (EN) of Cr<sub>2</sub>O<sub>3</sub> catalyst, which would aid in preventing the production of undesired products and cokes when used in dehydrogenation process. Among the adsorbates considered in this study, pyridine (molecular probe) was found to be the most reactive and least stable, while propane was found to be the least reactive and most stable materials.

The evaluation of the catalyst Lewis acidity with the use of ammonia (as the molecular probe) reveals that chromium (Cr) is the most acidic site across on the catalyst surfaces when compared to its oxygen (O) site. Although introducing foreign metals like Mo and W on it indicates that the catalyst surfaces modified with molybdenum (Mo) would suppress the catalyst's acidity. At the same time, tungsten (W) would accelerate the acidity, indicating that the introduction of Mo reduces the acidity while W increases it. The study further identifies that these findings were in line with that made from the use of pyridine.

Moreover, the chromium site acidity order reveals that the presence of molybdenum on the Cr<sub>2</sub>O<sub>3</sub> surface reduces the chromium site acidity while tungsten increases it, unlike the oxygen acidity that increases in the presence of either Mo or W. The acidity of introduced (or foreign) metal sites was identified to be more acidic relative to unmodified Cr<sub>2</sub>O<sub>3</sub>, which increases the total catalyst acidity for better exchange of electrons due to their higher Lewis acidity(s) when compared to their respective chromium sites on their modified surfaces. This finding shows that tungsten would be more promising when compared to Mo-modified Cr<sub>2</sub>O<sub>3</sub> due to the high Lewis acidity of W-modified Cr<sub>2</sub>O<sub>3</sub> for the dehydrogenation process.

## ACKNOWLEDGMENT

The authors wish to thank the management of the Chemical Engineering Department of ABU Zaria for their constant interest and valuable advice in this project. Also, the first author wishes to acknowledge the financial support of the PTDF that made my program a success.

## ABBREVIATION

aAc	Ammonia-based Lewis acidity of ...
pAc	Pyridine-based Lewis acidity of ...
CP	Chemical potential, $\mu$
CH	Chemical hardness, $\eta$
Cr	Chromium Site

DFT	Density functional theory
E	Total energies of the structures
EA	Electron affinity
Eads	Adsorption energy
E-gap	Bandgap
EHOMO	The energy of HOMO orbital
ELUMO	The energy of LUMO orbital
EN	Electronegativity, $\chi$
Ep	The total energy of adsorbate (p)
Epq	The total energy of the catalyst slab with adsorbate (pq)
Eq	The total energy of the free cluster or catalyst slab (q) or E-surface
H	Hydrogen atom
HOMO	Highest occupied molecular orbital
IE	Ionization energy
GEI	Global electrophilicity index, $\omega$
IR	Infrared spectra
L	The bond length in angstrom
LUMO	Lowest unoccupied molecular orbital
M	Foreign metal introduced metal or promoter sites
MMFF	Molecular mechanics force field
Mo	Molybdenum atom
P1	Propyl-1
P2	Propyl-2
PM3	Parameterized method three approximation of semi-empirical theory
r	Correlation coefficient

r (aAc) The correlation coefficient of ammonia-based Lewis acidity (aAc) to ...

r (pAc) The correlation coefficient of pyridine-based Lewis acidity (pAc) to ...

W Tungsten atom

## References

- Budavari S. Propylene. The Merck Index, 12th ed., New Jersey: Merck & Co., 1996, p. 1348-1349.
- Ren Y, Zhang F, Hua W, Yue Y, Gao Z. "ZnO supported on high silica HZSM-5 as new catalysts for dehydrogenation of propane to propene in the presence of CO<sub>2</sub>," *Catalysis Today*, 2009; 148(3-4): 316-322.
- Yan L, Zhen H, Jing L, Kang-Nian F. "Periodic Density Functional Theory Study of Propane Dehydrogenation over Perfect Ga<sub>2</sub>O<sub>3</sub> (100)," *Surface, J. Phys. Chem. C*, 2008, 112(51):20382-20392.
- Ming L, Yi A, Xing G, Zhi J, De C. "First-Principles Calculations of Propane Dehydrogenation over PtSn Catalysts," *ACS Catalysis*, 2012, 2(6):1247-1258.
- Lauri N, Karoliina H. "Selectivity in Propene Dehydrogenation on Pt and Pt<sub>3</sub>Sn Surfaces from First Principles," *ACS Catalysis*, 2013, 3(1):3026-3030.
- Timothy H. "Computational study of the catalytic dehydrogenation of propane on Pt and Pt<sub>3</sub>Ga catalysts," *Doctoral Thesis*, 2015.
- Stephanie S, Maarten K, Vladimir V, Evgeniy A, Marie-Françoise R, Guy B. "The Positive Role of Hydrogen on the Dehydrogenation of Propane on Pt (111)," *ACS Catalysis*, 2017, 7(11): 7495-7508.
- Biloen P, Dautzenberg F, Sachtler W. "Catalytic dehydrogenation of propane to propene over platinum and platinum-gold alloys," *Journal of Catalysis*, 1977, 50(1): 77-86.
- Benco L, Bucko T, Hafner J. "Dehydrogenation of propane over ZnMOR. Static and dynamic reaction energy diagram," *Journal of catalysis*, 2011, 277(1): 104-116.
- Li H, Yue Y, Miao C, Xie Z, Hua W, Gao Z. "Dehydrogenation of ethylbenzene and propane over Ga<sub>2</sub>O<sub>3</sub>-ZrO<sub>2</sub> catalysts in the presence of CO<sub>2</sub>," *Catalysis Communications*, 2007, 8(9): 1317-1322.
- Ming-Lei Y, Yi-An Z, Chen F, Zhi-Jun S, De C, Xing-Gui Z. "DFT study of propane dehydrogenation on Pt catalyst: effects of step sites," *Physical Chemistry, Chemical Physics*, 2011, 13(1): 3257-3267.
- Oyegoke T, Dabai FN, Uzairu A, Jibril BY. "Insight from the Study of Acidity and Reactivity of Cr<sub>2</sub>O<sub>3</sub> Catalyst in Propane Dehydrogenation: A Computational Approach," *Bayero Journal of Pure and Applied Sciences*, 2018, 11(1): 178-184.
- Gascón J, Téllez C, Herguido J, Menéndez M. "Propane dehydrogenation over a Cr<sub>2</sub>O<sub>3</sub>/Al<sub>2</sub>O<sub>3</sub> catalyst: transient kinetic modeling of propene and coke formation," *Applied Catalysis A: General*, 2003, 248(1-2): 105-116.
- Parthasarathi R, Subramanian V, Royb D, Chattaraj P. "Electrophilicity index as a possible descriptor of biological activity," *Bioorganic & Medicinal Chemistry*, 2004, 12(1): 5533-5543.
- Bendjedou A, Abbas T, Gouasmia AK, Villemin D. "Molecular structure, HOMO-LUMO, MEP, and Fukui function analysis of some TTF donor substituted molecules using DFT (B3LYP) calculations," *Int Res J Pure Appl Chem*, 2016, 12(1):1-9.
- Parr R, Szentpály L, Liu S. "Electrophilicity Index," *J. Am. Chem. Soc.*, 1999, 121(1): 1922-1924.
- Pratim K, Utpal S, Debesh R. "Electrophilicity Index," *Chemical Review*, 2006, 106(1): 2065-2091.
- Domingo L, Ríos-Gutiérrez M, Pérez P. "Applications of the Conceptual Density Functional Theory Indices to Organic Chemistry Reactivity," *Molecules*, 2016, 21(748): 1-22.
- Robert G, La'szlo V, Shubin L. "Electrophilicity Index," *J. Am. Chem. Soc.*, 1999, 121(1): 1922-1924.
- Compere C, Costa D, Jolly LH, Maugerc E, Giessner-Prettre C. "Modeling of the adsorption on Cr<sub>2</sub>O<sub>3</sub> clusters of small molecules and ions present in seawater. A preliminary non-empirical study," *New J. of Chem*, 2000, 24(12): 993-998.
- Yanbiao W, Xinxin G, Jinla W. "Comparative DFT Study of Structure and Magnetism of TM<sub>n</sub>Om (TM = Sc - Mn, n = 1 - 2, m = 1 - 6) Clusters," *Physical Chemistry Chemical Physics*, 2010, 12(1): 2471-2477.
- Veliash S, Xiang K, Pandey R, Recio J, Newsam J. "Density Functional Study of Chromium Oxide Clusters: Structures, Bonding, Vibrations, and Stability," *J. Phys. Chem. B*, 1997, 102(1): 1126-1135.
- Garrain PA, Costa D, Marcus P. "Biomaterial- biomolecule interaction: DFT-D study of glycine adsorption on Cr<sub>2</sub>O<sub>3</sub>," *The Journal of Physical Chemistry C*, 2010, 115(3): 719-727.
- Shah EV, Roy DR. "Magnetic switching in Cr<sub>x</sub> (x= 2-8) and its oxide cluster series," *Journal of Magnetism and Magnetic Materials*, 2018, 451: 32-37.
- Dzade N, Roldan A, de Leeuw N. "A density functional theory study of the adsorption of benzene on hematite (α-Fe<sub>2</sub>O<sub>3</sub>) surfaces," *Minerals*, 2014, 4(1): 89-115.
- Lau KC, Kandalam AK, Costales A, Pandey R. "Equilibrium geometry and electron detachment energies of anionic Cr<sub>2</sub>O<sub>4</sub>, Cr<sub>2</sub>O<sub>5</sub>, and Cr<sub>2</sub>O<sub>6</sub> clusters," *Chemical physics letters*, 2004, 393(1-3): 112-117.
- Warren J. *A Guide to Molecular Mechanics and Quantum Chemical Calculations*, Irvine, CA: Wavefunction, 2003.
- Warren H, Sean O. *Spartan 16 for Windows, Macintosh and Linux: User Guide and Tutorial*, CA: Wavefunction, 2017, pp. 435-518.
- Maldonado F, Stashans A. "DFT modeling of benzoyl peroxide adsorption on α-Cr<sub>2</sub>O<sub>3</sub> (0001) surface," *Surface Review and Letters*, 2016, 23(5): 1650037.
- Guo-Liang D, Zhen-Hua L, Jing L, Wen-Ning W, Kang-Nian F. "Deep Oxidation in the Oxidative Dehydrogenation Reaction of Propane over V<sub>2</sub>O<sub>5</sub>(001): Periodic DFT Study," *The Journal of Physical Chemistry C*, 2012, 116(1): 807-817.
- Satyajit D, Nand K, Plaban J, Ramesh C. "DFT Insight on Oxygen Adsorbed Pt Trimer Cluster (Pt<sub>3</sub>) for CO Oxidation," *Computational and Theoretical Chemistry*, 2017, 1114(1): 1-7.
- Liu C, Li G., Emiel E, Hensen J, Pidko E. "Relationship between acidity and catalytic reactivity of faujasite zeolite: A periodic DFT study," *Journal of Catalysis*, 2016, 344(1): 570-577.
- Liu C, Tranca I, van Santen RA, Hensen RJ, Pidko EA. "Scaling relations for acidity and reactivity of zeolites," *The Journal of Physical Chemistry C*, 2017, 121(42): 23520-23530.
- David R. "CRC Handbook of Chemistry and Physics, 84th Edition," in Section 10, Atomic, Molecular, and Optical Physics; Ionization Potentials of Atoms and Atomic Ions, 84th ed., Boca Raton, Florida: CRC Press., 2003, pp. (10-178)-(10-179).
- Fukui K., "Role of frontier orbitals in chemical reactions," *Science*, 1982, 218(4574): 747-754.
- Lillehaug S., "A Theoretical Study of Cr/oxide Catalysts for Dehydrogenation of Short Alkanes," *The University of Bergen, Department of Chemistry*, 2006.
- Lugo HJ, Lunsford JH. "The dehydrogenation of ethane over chromium catalysts," *Journal of Catalysis*, 1985, 91(1): 155-166.
- Michorczyk P, Ogonowski J, Kuśtrowski P, Chmielarz L. "Chromium oxide supported on MCM-41 as a highly active and

- selective catalyst for dehydrogenation of propane with CO<sub>2</sub>,” Applied Catalysis A: General, 2008, 349(1-2): 62-69.
39. Michorczyk P, Ogonowski J, Zeńczak K. “Activity of chromium oxide deposited on different silica supports in the dehydrogenation of propane with CO<sub>2</sub>—a comparative study,” Journal of Molecular Catalysis A: Chemical, 2011, 349(1-2): 1-12.
  40. Bailey BC, Schrock RR, Kundu S, Goldman AS, Huang Z, Brookhart M. “Evaluation of Molybdenum and Tungsten Metathesis Catalysts for Homogeneous Tandem Alkane Metathesis,” Organometallics, 2009, 28(1): 355-360.
  41. Chen K, Bell AT, Iglesia E., “Kinetics and Mechanism of Oxidative Dehydrogenation of Propane on Vanadium, Molybdenum, and Tungsten Oxides,” Journal of Physical Chemistry B, 2000, 104(1): 1292-1299.
  42. Jupp A, Johnstone T, Stephan D. “The Global Electrophilicity Index as a Metric for Lewis Acidity,” Dalton Transactions, 2018, 45(1): 1-7.
  43. Yun Y, Araujo JR, Melaet G, Baek J, Archanjo BS, Oh M, Alivisatos AP, Somorjai GA. “Activation of Tungsten Oxide for Propane Dehydrogenation and Its High Catalytic Activity and Selectivity,” Catalysis Letters, 2017, 147(3): 622–632.
  44. Salamanca-Guzmán M, Licea-Fonseca YE, Echavarría-Isaza A, Faro A, Palacio-Santos LA. “Oxidative dehydrogenation of propane with cobalt, tungsten and molybdenum based materials,” Revista Facultad de Ingeniería Universidad de Antioquia, 2017, 84(1): 97-104.

## APPENDIX

**Table A1.** Molecular Properties of the Catalysts.

Name	Formula	ELUMO (eV)	EHOMO (eV)	E (eV)	E <sub>Gap</sub> , (eV)	CH, η (eV)	EN, χ (eV)	CP, μ (eV)	GEI, ω (eV)
Chromia	Cr <sub>2</sub> O <sub>3</sub>	-2.68	-14.51	-0.88	11.83	5.92	8.60	-8.60	3.12
Mo-Chromia	CrMoO <sub>3</sub>	-1.31	-14.89	-0.73	13.58	6.79	8.10	-8.10	2.42
W-Chromia	CrWO <sub>3</sub>	0.37	-12.80	-2.26	13.17	6.59	6.22	-6.22	1.47

**Table A2.** Correlation of Cr-Site Lewis Acidity Results.

	αELUMO (eV)	αEHOMO (eV)	αAc <sub>Cr</sub>	aCH, η (eV)	aEN, χ (eV)	aCP, μ (eV)	aGEI, ω (eV)	pELUMO (eV)	pEHOMO (eV)	pAc <sub>Cr</sub>	pCH, η (eV)	pEN, χ (eV)	pCP, μ (eV)	pGEI, ω (eV)
αELUMO (eV)	1.00													
αEHOMO (eV)	0.58	1.00												
αAc <sub>Cr</sub>	-1.00	-0.57	1.00											
aCH, η (eV)	0.01	-0.81	-0.02	1.00										
aEN, χ (eV)	-0.82	-0.94	0.81	0.57	1.00									
aCP, μ (eV)	0.82	0.94	-0.81	-0.57	-1.00	1.00								
aGEI, ω (eV)	-0.90	-0.87	0.90	0.42	0.99	-0.99	1.00							
pELUMO (eV)	-0.89	-0.89	0.88	0.46	0.99	-0.99	1.00	1.00						
pEHOMO (eV)	-0.88	-0.90	0.87	0.48	0.99	-0.99	1.00	1.00	1.00					
pAc <sub>Cr</sub>	-0.99	-0.49	1.00	-0.12	0.75	-0.75	0.85	0.79	0.82	1.00				
pCH, η (eV)	0.85	0.92	-0.84	-0.53	-1.00	1.00	-0.99	0.83	-1.00	-0.78	1.00			
pEN, χ (eV)	0.88	0.90	-0.87	-0.47	-0.99	0.99	-1.00	-1.00	-1.00	-0.82	1.00	1.00		
pCP, μ (eV)	-0.88	-0.90	0.87	0.47	0.99	-0.99	1.00	-1.00	1.00	0.82	-1.00	-1.00	1.00	
pGEI, ω (eV)	0.73	0.98	-0.72	-0.67	-0.99	0.99	-0.95	-0.96	-0.97	-0.65	0.98	0.97	-0.97	1.00

**Table A3.** Correlation of M-Site Lewis Acidity Results.

	<i>aELUMO</i> (eV)	<i>aEHOMO</i> (eV)	<i>aAc_M</i>	<i>aCH</i> , $\eta$ (eV)	<i>aEN</i> , $\chi$ (eV)	<i>aCP</i> , $\mu$ (eV)	<i>aGEI</i> , $\omega$ (eV)	<i>pELUMO</i> (eV)	<i>pEHOMO</i> (eV)	<i>pAc_M</i>	<i>pCH</i> , $\eta$ (eV)	<i>pEN</i> , $\chi$ (eV)	<i>pCP</i> , $\mu$ (eV)	<i>pGEI</i> , $\omega$ (eV)
<i>aELUMO</i> (eV)	1.00													
<i>aEHOMO</i> (eV)	-0.79	1.00												
<i>aAc_Cr</i>	1.00	-0.78	1.00											
<i>aCH</i> , $\eta$ (eV)	0.81	-1.00	0.80	1.00										
<i>aEN</i> , $\chi$ (eV)	0.77	-1.00	0.75	1.00	1.00									
<i>aCP</i> , $\mu$ (eV)	-0.77	1.00	-0.75	-1.00	-1.00	1.00								
<i>aGEI</i> , $\omega$ (eV)	-0.83	0.32	-0.84	-0.35	-0.28	0.28	1.00							
<i>pELUMO</i> (eV)	-1.00	0.80	-1.00	-0.82	-0.78	0.78	0.82	1.00						
<i>pEHOMO</i> (eV)	-0.83	1.00	-0.82	-1.00	-0.99	0.99	0.38	0.84	1.00					
<i>pAc_Cr</i>	1.00	-0.83	1.00	0.85	0.81	-0.81	-0.79	-1.00	-0.87	1.00				
<i>pCH</i> , $\eta$ (eV)	0.56	-0.95	0.54	0.94	0.96	-0.96	-0.01	-0.58	-0.93	0.62	1.00			
<i>pEN</i> , $\chi$ (eV)	0.92	-0.97	0.90	0.98	0.96	-0.96	-0.54	-0.92	-0.98	0.94	0.85	1.00		
<i>pCP</i> , $\mu$ (eV)	-0.92	0.97	-0.90	-0.98	-0.96	0.96	0.54	0.92	0.98	-0.94	-0.85	-1.00	1.00	
<i>pGEI</i> , $\omega$ (eV)	0.90	-0.98	0.89	0.98	0.97	-0.97	-0.51	-0.91	-0.99	0.93	0.86	1.00	-1.00	1.00

**Table A4.** Correlation of O-Site Lewis Acidity Results.

	<i>aELUMO</i> (eV)	<i>aEHOMO</i> (eV)	<i>aAc_O</i>	<i>aCH</i> , $\eta$ (eV)	<i>aEN</i> , $\chi$ (eV)	<i>aCP</i> , $\mu$ (eV)	<i>aGEI</i> , $\omega$ (eV)	<i>pELUMO</i> (eV)	<i>pEHOMO</i> (eV)	<i>pAc_O</i>	<i>pCH</i> , $\eta$ (eV)	<i>pEN</i> , $\chi$ (eV)	<i>pCP</i> , $\mu$ (eV)	<i>pGEI</i> , $\omega$ (eV)
<i>aELUMO</i> (eV)	1.00													
<i>aEHOMO</i> (eV)	-0.92	1.00												
<i>aAc_Cr</i>	-0.46	0.77	1.00											
<i>aCH</i> , $\eta$ (eV)	0.99	-0.97	-0.60	1.00										
<i>aEN</i> , $\chi$ (eV)	-0.77	0.47	-0.20	-0.66	1.00									
<i>aCP</i> , $\mu$ (eV)	0.77	-0.47	0.20	0.66	-1.00	1.00								
<i>aGEI</i> , $\omega$ (eV)	-0.84	0.98	0.87	-0.91	0.30	-0.30	1.00							
<i>pELUMO</i> (eV)	-0.89	1.00	0.82	-0.95	0.39	-0.39	1.00	1.00						
<i>pEHOMO</i> (eV)	-0.79	0.96	0.91	-0.88	0.22	-0.22	1.00	0.98	1.00					
<i>pAc_Cr</i>	0.00	0.39	0.89	-0.16	-0.63	0.63	0.55	0.47	0.62	1.00				
<i>pCH</i> , $\eta$ (eV)	-1.00	0.90	0.42	-0.98	0.81	-0.81	0.80	0.86	0.75	-0.05	1.00			
<i>pEN</i> , $\chi$ (eV)	0.85	-0.99	-0.86	0.92	-0.32	0.32	-1.00	-1.00	-0.99	-0.53	-0.82	1.00		
<i>pCP</i> , $\mu$ (eV)	-0.85	0.99	0.86	-0.92	0.32	-0.32	1.00	1.00	0.99	0.53	0.82	-1.00	1.00	
<i>pGEI</i> , $\omega$ (eV)	-0.84	0.98	0.87	-0.91	0.30	-0.30	1.00	1.00	1.00	0.55	0.80	-1.00	1.00	1.00

**Table A5.** Correlation of Lewis Acidity and Catalyst Surfaces' Molecular Descriptors.

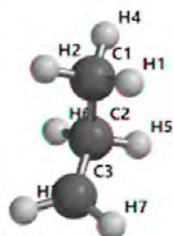
	ELUMO (eV)	EHOMO (eV)	CH, $\eta$ (eV)	EN, $\chi$ (eV)	CP, $\mu$ (eV)	GEI, $\omega$ (eV)	E <sub>Gap</sub> (eV)	aAc_Cr	aAc_M	aAc_O	pAc_Cr	pAc_M	pAc_O
ELUMO (eV)	1.00												
EHOMO (eV)	0.80	1.00											
CH, $\eta$ (eV)	0.69	0.13	1.00										
EN, $\chi$ (eV)	-0.97	-0.93	-0.48	1.00									
CP, $\mu$ (eV)	0.97	0.93	0.48	-1.00	1.00								
GEI, $\omega$ (eV)	-1.00	-0.82	-0.67	0.97	-0.97	1.00							
E <sub>Gap</sub> (eV)	0.69	0.13	1.00	-0.48	0.48	-0.67	1.00						
aAc_Cr	-0.50	-0.91	0.28	0.71	-0.71	0.52	0.29	1.00					
aAc_M	-0.95	-0.95	-0.44	1.00	-1.00	0.96	-0.43	0.74	1.00				
aAc_O	-1.00	-0.77	-0.73	0.95	-0.95	1.00	-0.73	0.45	0.93	1.00			
pAc_Cr	-0.57	-0.95	0.19	0.77	-0.77	0.60	0.19	1.00	0.80	0.53	1.00		
pAc_M	-0.92	-0.97	-0.35	0.99	-0.99	0.93	-0.35	0.80	1.00	0.89	0.85	1.00	
pAc_O	-0.91	-0.98	-0.34	0.99	-0.99	0.92	-0.33	0.81	0.99	0.89	0.86	1.00	1.00
Average of Ac(s)	-0.81	-0.92	-0.23	0.90	-0.90	0.82	-0.23	-	-	-	-	-	-

**Table A6.** The Geometry of Different Structures Optimized by the PM3 method.

## Molecular probe and other small molecules



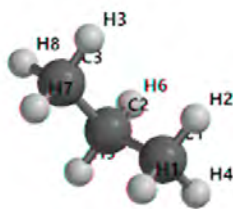
Ammonia



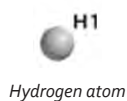
Propane



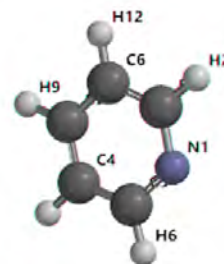
Propyl-2



Propyl-1



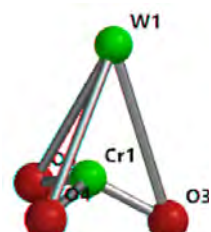
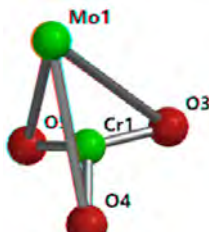
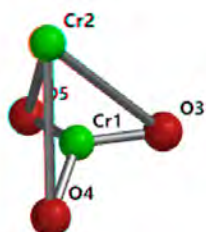
Hydrogen atom



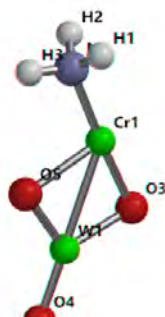
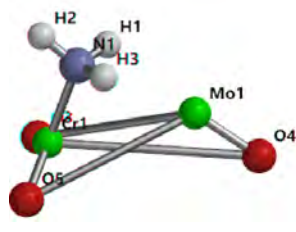
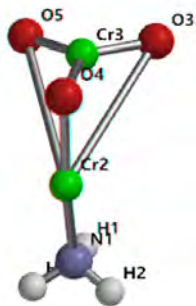
Pyridine

**Table A6.** The Geometry of Different Structures Optimized by the PM3 method (continued).

*Catalyst clusters*

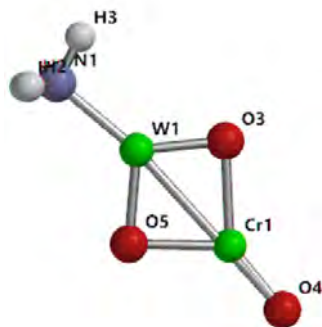
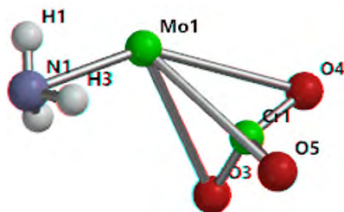


*Adsorption of ammonia probe on chromium, Cr-sites*



*Adsorption of ammonia probe on modified M-sites (M = W, Mo)*

Unmodified one, M = Cr, remaining unchanged



*Adsorption of ammonia probe on oxygen, O-sites*

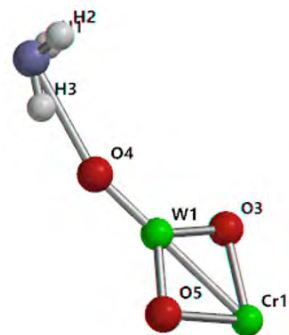
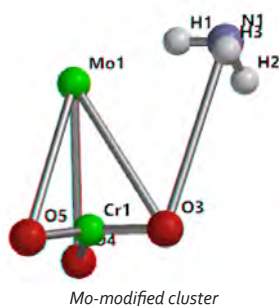
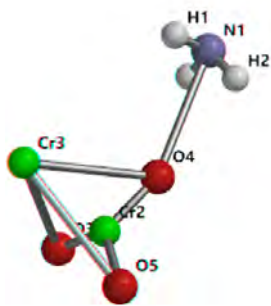
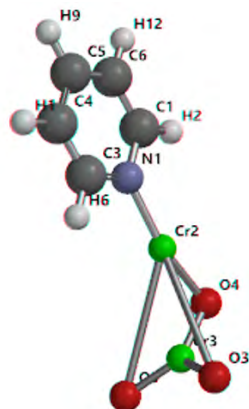
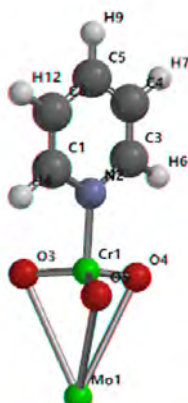


**Table A6.** The Geometry of Different Structures Optimized by the PM3 method (continued).

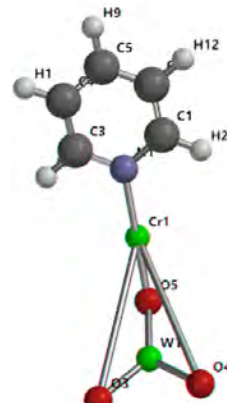
*Adsorption of pyridine probe on chromium, Cr-sites*



*Unmodified cluster*

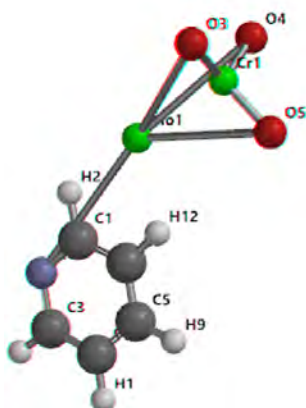


*Mo-modified cluster*

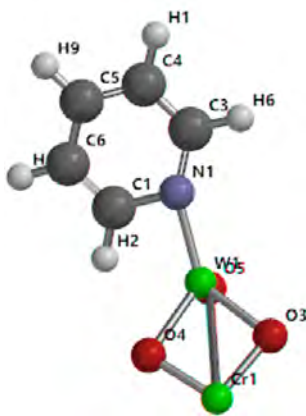


*W-modified cluster*

*Adsorption of pyridine probe on modified M-sites (M = W, Mo)*



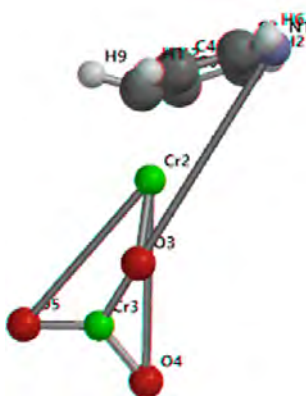
*M = Mo-site*



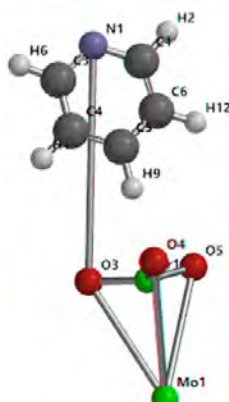
*M = W-site*

*Unmodified one, M=Cr, remaining unchanged*

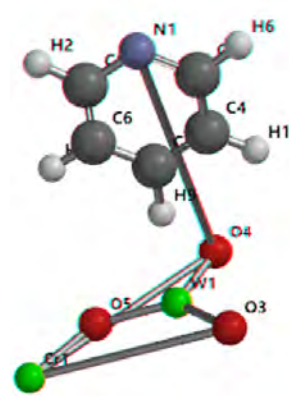
*Adsorption of pyridine probe on oxygen, O-sites*



*Mo-modified cluster*



*Mo-modified cluster*



*Mo-modified cluster*





# Performance Evaluation of Empirical Path Loss Models for a Linear Wireless Sensor Network Deployment in Suburban and Rural Environments

Yaser Dalveren<sup>1</sup> and Ali Kara<sup>2</sup>

<sup>1</sup>Atilim University, Department of Avionics, Ankara, Turkey

<sup>2</sup>Atilim University, Department of Electrical and Electronics Engineering, Ankara, Turkey

## ABSTRACT

This article presents a preliminary propagation study on the accuracy of empirical path loss models for efficient planning and deployment of a linear wireless sensor network (LWSN) based on long range (LoRa) enabled sensor nodes in suburban and rural environments. Real-world deployment of such network requires accurate path loss modelling to estimate the network coverage and performance. Although several models have been studied in the literature to predict the path loss for LoRa links, the assessment of empirical path loss models within the context of low-height peer to peer configured system has not been provided yet. Therefore, this study aims at providing a performance evaluation of well-known empirical path loss models including the Log-distance, Okumura, Hata, and COST-231 Hata model in a peer to peer configured system where the sensor nodes are deployed at the same low heights. To this end, firstly, measurement campaigns are carried out in suburban and rural environments by utilizing LoRa enabled sensor nodes operating at 868 MHz band. The measured received signal strength values are then compared with the predicted values to assess the prediction accuracy of the models. The results achieved from this study show that the Okumura model has higher accuracy.

### Keywords:

Propagation models; LoRa; Path loss; Suburban; Rural.

## INTRODUCTION

In the past few years, Wireless Sensor Networks (WSNs) have been evolving in many different aspects such as agricultural, industrial, and surveillance. In order to collect sensor data, the wireless nodes are deployed in an area with a specific network topology. Although there are various network topologies to deploy WSNs, the geographic conditions of the given area and the purpose of the application have still vital importance to decide the structure of network topology. Especially, when linear structures like pipelines, railways, roads or tunnels need to be monitored, WSN are formed as linear network topology which is known as linear-WSN (LWSN) [1].

In a typical LWSN, the sensor nodes are communicated within a hierarchical order. The hierarchical structure requires the single-hop communication model between the transmitting and receiving nodes. Generally, for an outdoor deployment, the communication range between these nodes is desired to be kept as high as possible. For this reason, it is necessary to use proper

radio transceiver that enables long-range communication distances. During the last years, the LoRa (Long Range) which is one of the low-power wide-area networks (LPWAN) technologies operating in the license-free ISM frequency band technology offers important advantages in communication range [2]. Its efficiency has been experimentally proven by various studies [3-12]. Recently, it has been also adapted to several LWSN-based applications [13-15].

On the other hand, real-world deployment of LWSNs requires an accurate prediction of network coverage and performance. In this context, a great understanding of the propagation impairments that affect the propagation links is strictly needed for designing such networks. One of the impairments adversely affecting the links is already known as path loss which describes the variation in the received signal power based on the distance between the receiving and transmitting nodes. Path loss also depends on the area or environment where the network is deployed. In this context, the environ-

### Article History:

Received: 2020/07/10

Accepted: 2020/11/16

Online: 2020/12/31

Correspondence to: Yaser Dalveren, Atilim University, Avionics, 06830, Ankara, TURKEY

E-Mail: yaser.dalveren@atilim.edu.tr

Phone: +90 312 586 83 20

mental conditions (terrain profile or topography) in terms of buildings, mountains, and hills that directly impact on path loss must be taken into account. Therefore, real-world deployment of LSWNs require accurate path loss modelling to estimate the network coverage.

Even though there are several path loss models that can be applicable to outdoor links for various bands, there has been no specific model to predict the path loss for LoRa links until now. However, many empirical path loss models have been studied in the literature, most of which consider the urban environment [8-10, 16-20]. Only few studies have evaluated empirical path loss models for suburban and/or rural environments [8, 9, 19, 20]. It is worth noting that these studies are based on base station/gateway to mobile terminal configuration where the transmitter is deployed higher than the receivers. As far as we know, the assessment of well-known empirical path loss models within the context of low-height peer to peer configured system for LoRa links has not been provided yet.

This study presents preliminary propagation study for accurate deployment of a LWSN-based monitoring system proposed in [15]. The main purpose is to provide performance evaluation of well-known empirical path loss models, namely the Log-distance, Okumura, Hata, and COST-231 Hata model in a low-height peer to peer configured system. In this context, the predicted received signal strength indicator (RSSI) values are compared with the propagation measurements carried out in suburban and rural areas at 868 MHz using LoRa enabled sensor nodes in order to evaluate the prediction accuracy of the models. The comparison results show that the Okumura model has higher prediction accuracy when compared to other models. Thus, to the best of our knowledge, this is the first study in the literature that provides the assessment of well-known empirical path loss models within the context of low-height peer to peer configured system for LoRa links. Besides, it is believed that the initial results achieved from in this study offer useful insights for efficient planning and deployment of LWSNs

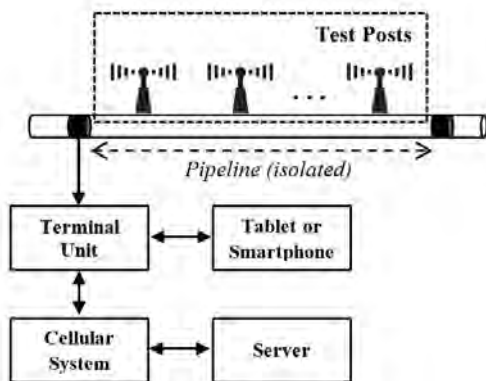


Figure 1. The LWSN-based Monitoring System [15].

based on LoRa enabled sensor nodes or transceivers in suburban and rural environments such as [15].

The article is organized as follows. In the following section, LWSN-based monitoring system is overviewed. The details about the field measurements are then presented in Section 3. Next, the path loss models investigated under this study are described in Section 4. In Section 5, the comparison results are provided and discussed. Conclusions are given in the last section.

## RELATED WORK

The LWSN-based system in [15] is proposed as an alternative to traditional cathodic protection (CP) monitoring of oil and natural gas pipeline systems. Contrary to traditional CP monitoring systems, as a novelty, the proposed system is designed to be used in extreme environments (deep valleys, deserts, etc.) where the communication infrastructure is limited or unavailable. The main structure of the system is illustrated in Fig. 1. As shown in the figure, the system consists test posts (TPs), each of which have a sensor node connected to the measurement unit. Here, low-bit sensor nodes with low-antenna height are used to provide bidirectional links. In this way, each TP is able to transmit the collected data through the neighbour TPs in a sequence.

In this system, the sensor nodes typically include LoRa module to achieve the maximum reasonable communication range. Evidently, a large-scale deployment of this system requires accurate characterization of the propagation channel. As mentioned previously, most of the existing works on the performance of LoRa coverage use the gateways/transmitters located much higher than the mobile terminals/receivers. However, when the system architecture shown in Fig. 1 is concerned, it is necessary to provide accurate models for peer to peer configuration where the transmitter and the receiver are located at the same low heights. Otherwise, inaccurate models will result in poor decision making during large-scale deployment of the LWSN system. Accordingly, for an accurate deployment of the given sensor network, the effects of the distance between the sensor nodes and the environmental conditions on the LoRa links in suburban and rural environments should be examined.

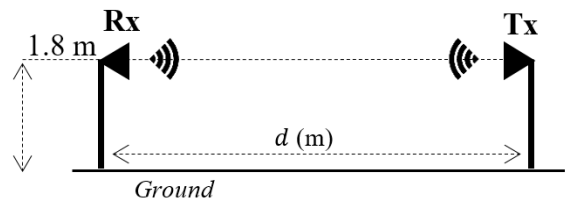


Figure 2. Link configuration of the measurement campaign.

## MEASUREMENT SETUP

In order to evaluate the accuracy of the well-known empirical path loss models for suburban and urban environments, a set of propagation measurements are taken by the LoRa enabled sensor nodes. Fig. 2 shows the conceptual overview of the measurement setup.

The measurement setup consists of a transmitter node (Tx) and a receiver node (Rx). For receiving purposes, the sensor node shown in Fig. 3 is used. It comprises a microstrip antenna with 1 dBi gain [21] and a LoRa (SX1276) module which is stacked on Arduino Mega board. For transmitting purposes, the sensor node which is designed to be used in the LWSN-based system discussed in the previous section is used (Fig. 4). It comprises a LoRa module, two directive antennas, and a RF splitter for coupling the LoRa output to the antenna ports. In fact, it is designed to use two directive antennas placed back-to-back to provide bidirectional links in a real deployment. However, for this study, one of the ports of the Tx was disabled by connecting a standard flat antenna to provide peer to peer configuration. An iden-

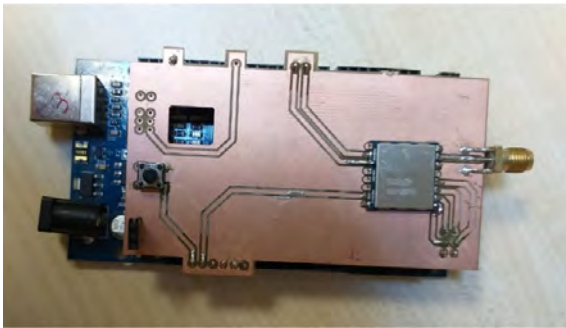


Figure 3. The receiver node (Rx) used for path loss measurements.

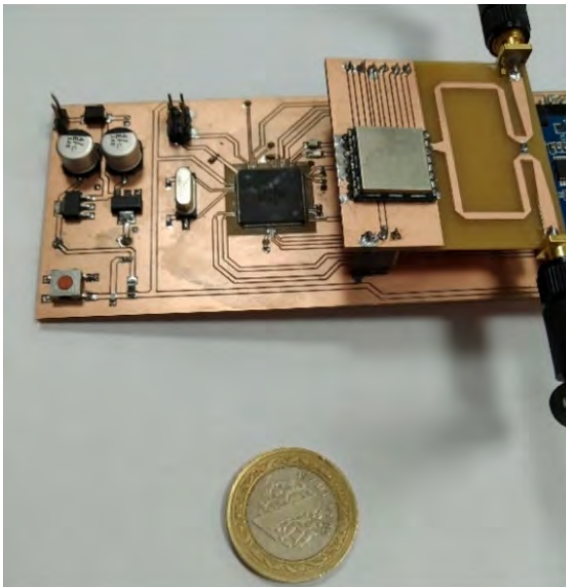


Figure 4. The transmitter node (Tx) used for path loss measurements.

Table 1. LoRa settings and the configurations used for the Tx and Rx.

Parameters for the Measurements	
Spreading factor	7
Bandwidth	125 kHz
Coding rate	4/5
Output power	17 dB
Center frequency	868 MHz
Payload length	8 bytes
Preamble	6 symbols

tical antenna used in the Rx was then connected to the other port of the Tx. By means of 1 m SMA cable, the microstrip antennas of the nodes were then mounted on the top of the stands with equal heights above the ground (1.8 m). On the other hand, the LoRa settings and the configurations used for the Tx and the Rx are listed in Table 1.

The measurements were performed in suburban and rural environments around the Atilim University campus located in Incek, Ankara (Turkey). The suburban environment is composed of a combination of trees, weeds, and buildings with about 4 m, 10 cm, and 7 m heights as shown in Fig. 5 (a). The rural environment is mainly composed of weeds with 10 cm height (Fig. 5 (b)).

During the measurements, the Tx was fixed at a laboratory of the Atilim University, and the Rx was moved by following a specific path over the measurement points. The propagation environments considered for the measurements is non line-of-sight (NLOS) because of no direct visibility between the Tx and Rx in the measurement points. The separation distance between the Tx and the Rx ( $d$ ) varied in the range of 0.5–5 km. At the measurement points, the Tx was configured to send 100 packets. The measurements were repeated five times to remove local propagation (multipath) effects. In total, over 40 measurements were taken at 8 measurement points in each environment. Mean RSSI values



Figure 5. (a) Suburban environment, (b) Rural environment.

were then calculated using the recorded measurements. For LoRa (SX1276), it is useful to note that the RSSI is a measure of the incoming signal power at RF input port ( $P_r$ , in dBm) where the signal power (RssiValue) can be expressed as [22]

$$RssiValue = -2 \cdot P_r + \beta \quad (1)$$

where  $\beta$  is the RSSI offset (in dB). The effective signal strength (in dBm) is then obtained as follows

$$RSSI = \frac{-RssiValue}{2} \quad (2)$$

Besides, in order to evaluate the signal strength of the received packet, the following expression is also used

$$Packet\ Strength(dBm) = -157 + RSSI_{packet} \quad (3)$$

where  $RSSI_{packet}$  is an averaged of RSSIs.

Moreover, Packet Reception Ratio (PRR), which is the proportion of the number of packets successfully received to the packets transmitted in total, were calculated at each measurement point where the targeted packet reception rate (PRR) is around 95% for the low bit rate LWSN system in [15].

## PATH LOSS MODELS

To get a deeper insight of wireless channel characterization, an analysis of the propagation in terms of received power is required. Typically, the received power ( $P_r$ , in dBm) can be calculated as [23]

$$P_r = P_t + G_r + G_t - L_p \quad (4)$$

where  $P_t$  is transmitted power (in dBm),  $G_r$  and  $G_t$  are the antenna gains respectively of the receiver and transmitter (in dB), and  $L_p$  is the path loss (in dB) which is an attenuation that is caused by the range between the receiver and the transmitter as well as the characteristics of the environment. As the  $L_p$  significantly affects the propagation links, it needs to be predicted for an accurate design of the networks.

In the following, the empirical path loss models for rural and suburban links that can be used in the frequency band dedicated to LoRa in Europe (868 MHz) are presented.

### Log-distance Model

As it is widely known, the propagation channels based on theoretical or measurement indicate that the average  $P_r$  tends to decrease logarithmically with distance. This can be expressed by [24]

$$L_p(d) = L_p(d_0) + 10n \log\left(\frac{d}{d_0}\right) + X_\sigma, \quad (5)$$

where  $L_p(d)$  is the path loss (in dB) for a transmitter-receiver separation distance  $d$  (in meters),  $L_p(d_0)$  is the reference path loss (in dB) calculated using the free space

path loss formulation at a given reference distance  $d_0$  (in meters),  $n$  is the path loss exponent which varies based on the propagation environment,  $X_\sigma$  is the shadowing effect that is a zero-mean Gaussian random variable with standard deviation  $\sigma$  (in dB).

### Okumura Model

The Okumura model, which is one of the most used models in radio propagation, is applicable for the frequency range between 150 MHz and 1920 MHz and the distances between 1 km and 100 km. To determine the  $L_p$ , firstly, the free space path loss between the measurement points is determined. Then, the value of the median attenuation relative to free space and correction factors are added. It can be expressed as [25]

$$L_p = L_f + A_\mu - G(h_t) - G(h_r) - G_A \quad (6)$$

where  $L_f$  is the free space path loss,  $A_\mu$  is the median attenuation relative to free space,  $G(h_t)$  is the transmitter or base station antenna height gain factor,  $G(h_r)$  is the receiver or mobile antenna height gain factor, and  $G_A$  is the gain that varies according to the environment. The values of  $A_\mu$  and  $G_A$  can be reached from the Okumura's empirical plots [24, 25]. The  $G(h_t)$  and  $G(h_r)$  can be calculated from the following expressions

$$G(h_t) = 20 \log\left(\frac{h_t}{300}\right) \text{ for } 1000 \text{ m} > h_t > 30 \text{ m}, \quad (7)$$

$$G(h_r) = 10 \log\left(\frac{h_r}{3}\right) \text{ for } h_r \leq 3 \text{ m}, \quad (8)$$

$$G(h_r) = 20 \log\left(\frac{h_r}{3}\right) \text{ for } 10 \text{ m} > h_r > 3 \text{ m}. \quad (9)$$

### Hata Model

The Hata model is another widely used model to predict path loss in radio propagation. It formulates the Okumura's empirical plots for various parameters. It is applicable for the frequency range between 150 MHz and 1500 MHz and the distances between 1 km and 20 km. This model is presented to calculate the  $L_p$  in urban environments, however, it incorporates path loss factors and correction factor for the applications in suburban and rural environments. The path loss in urban environments ( $L_{p,urban}$ ) is expressed as [26]

$$L_{p,urban} = 69.55 + 26.16 \log f_c - 13.82 \log h_t - \alpha_{h_r} + (44.9 - 6.55 \log h_t) \log d \quad (10)$$

where  $f_c$  is the frequency (in MHz),  $h_t$  is the transmitter or base station antenna height ranging from 30 m to 200 m,  $h_r$  is the receiver or mobile antenna height ranging from 1 m to 10 m,  $d$  is defined in (5), and  $\alpha_{h_r}$  is the correction factor for the receiver antenna height (in dB). It is given

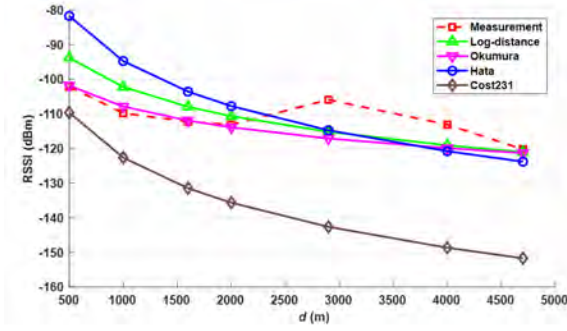


Figure 6. Comparison of the measured and simulated data (rural).

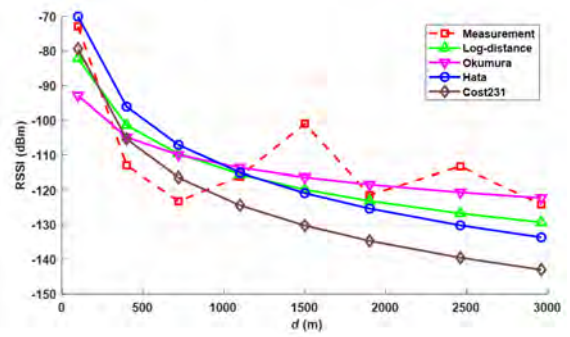


Figure 7. Comparison of the measured and simulated data (suburban).

for a small to medium sized city by

$$\alpha_{h_r} = (1.1 \log f_c - 0.7) h_r - (1.56 \log f_c - 0.8). \quad (11)$$

Then, the path loss in a suburban environment is obtained by

$$L_{p,suburban} = L_{p,urban} - 2[\log(f_c / 28)]^2 - 5.4, \quad (12)$$

and the path loss in a rural environment is obtained by

$$L_{p,rural} = L_{p,urban} - 4.78 \log f_c^2 + 18.33 \log f_c - 40.98. \quad (13)$$

### COST-231 Model

This model is developed as an extended version of the Hata model which is designed to be used in the frequency band ranging from 500 MHz to 2000 MHz. It is widely used to predict path loss due to its simplicity. The model can be expressed as follows [27]

$$L_p = 46.3 + 33.9 \log f_c - 13.82 \log h_t - \alpha_{h_r} + (44.9 - 6.55 \log h_t) \log d + C_m \quad (14)$$

where the parameters  $f_c$ ,  $h_t$ ,  $h_r$ ,  $\alpha_{h_r}$ , and  $d$  are defined in (10) while the correction factor ( $C_m$ ) is defined as 0 dB for suburban or rural environments.

## RESULTS AND ANALYSIS

In order to assess the prediction accuracy of the empirical path loss models under this study, the RSSI measurements are compared with the simulation data obtained using the models. Fig. 6 and Fig. 7 show comparison between the measured and the models in rural and suburban link, respectively. Table 2 and Table 3 also present the corresponding values. It should be noted that the path loss exponent  $n$  is determined as 6 dB while the parameter  $X_\sigma$  is determined as 2.8 and 3.2 for rural and suburban

Table 2. Mean values of the RSSI measurement and the simulation data in rural link (dBm).

Method	Distance (m)						
	500	1000	1600	2000	2900	4000	4700
Measurement	-102.1	-109.8	-112.2	-113.1	-105.9	-113.1	-120.2
Log-distance model	-93.8	-102.2	-107.9	-110.6	-115.2	-119.1	-121
Okumura model	-101.8	-107.9	-111.9	-113.9	-117.1	-119.9	-121.3
Hata model	-81.71	-94.7	-103.5	-107.7	-114.7	-120.7	-123.8
COST-231 Hata model	-109.6	-122.6	-131.4	-135.6	-142.6	-148.6	-151.7

Table 3. Mean values of the RSSI measurement and the simulation data in suburban link (dBm).

Method	Distance (m)							
	100	400	720	1100	1500	1900	2460	2960
Measurement	-72.9	-113	-123.2	-116.1	-101	-121.4	-113.3	-124.1
Log-distance model	-82.2	-101.5	-109.6	-115.5	-119.8	-123.1	-126.7	-129.3
Okumura model	-92.8	-104.9	-110	-113.7	-116.4	-118.4	-120.7	-122.3
Hata model	-70	-96.1	-107.1	-115.1	-120.9	-125.3	-130.2	-133.6
COST-231 Hata model	-79.4	-105.4	-116.5	-124.4	-130.2	-134.7	-139.5	-142.9

link, respectively [24]. Besides, for the COST-231 Hata model, the parameter  $C_m$  is defined as 0 dB for both rural and suburban link [24, 27]. Moreover, for the Okumura model, the parameter  $A_\mu$  is defined as 19 dB while the parameter  $G_A$  is defined as 26.5 dB and 21.5 dB for rural and suburban link, respectively [24, 25].

At first glance, as can be seen from the results achieved for the rural link, the measured RSSI values agree well with the Log-distance and Okumura model simulation, and mostly agree with the Hata model simulation. However, the predicted values by the COST-231 Hata differ from the RSSI values. In rural link, it is worth noting that the PRR substantially reduced beyond the measurement point at 4.7 km (above 95%). Beyond that point, as the percentage of losses dramatically increased, it is determined as the maximum achievable communication distance.

On the other hand, the results achieved for the suburban link show that the predicted values obtained by the Log-distance, Okumura, and Hata model relatively agree with the RSSI values while the predicted values obtained by the COST-231 Hata model again differ from the RSSI values. Here, based on the PRRs, the maximum achievable distance is also found to be 2.7 km for suburban link.

The prediction errors of the path loss models are also calculated to evaluate their performance in detail. To do this, the error statistics such as the mean absolute error ( $\Delta_e$ ), the standard deviation of the prediction error ( $\sigma_e$ ), and the mean prediction error ( $\mu_e$ ) are used [16]. The metric  $\mu_e$  can be calculated by

$$\mu_e = \frac{1}{N} \sum_{i=1}^N \Delta_{RSSI} \tag{15}$$

where  $N$  denotes the number of samples, and  $\Delta_{RSSI}$  is the difference between the predicted data ( $RSSI_p$ ) and measured data ( $RSSI_m$ ) which can be obtained by

$$\Delta_{RSSI} = RSSI_p - RSSI_m. \tag{16}$$

The metric  $\Delta_e$  and  $\sigma_e$  can be then calculated by

$$\Delta_e = \frac{1}{N} \sum_{i=1}^N |\Delta_{RSSI}|, \tag{17}$$

and

$$\sigma_e = \sqrt{\frac{1}{N} \sum_{i=1}^N (\Delta_{RSSI} - \Delta_e)^2}. \tag{18}$$

Thus, the prediction errors of the models are listed in Table 4 and Table 5 for rural and suburban link, respectively. Here, a negative or positive value of the  $\mu_e$  metric indicates that the model underestimates or overestimates the received signal power. Moreover,  $\Delta_e$  corresponds to the prediction accuracy of the models. In this context, the small value of  $\Delta_e$  indicates that the model has higher prediction accuracy.

**Table 4.** Prediction errors of the models (rural).

Error Metric	Log-distance	Okumura	Hata	COST-231 Hata
$\mu_e$	0,9	-2,5	4,2	-23,7
$\Delta_e$	5,5	3,2	9,9	23,7
$\sigma_e$	7,7	7,2	12	48,5

**Table 5.** Prediction errors of the models (suburban).

Error Metric	Log-distance	Okumura	Hata	COST-231 Hata
$\mu_e$	-2,9	-1,7	-1,8	-11
$\Delta_e$	9,3	8,9	10,9	14,6
$\sigma_e$	16,1	15,1	18	28,6

Based on the results listed in Table 4, it is clear that the Log-distance and Hata model overestimate the received signal power in rural link while other models underestimate the received signal power. It is also evident that the Okumura model has higher prediction accuracy when compared to other models ( $\Delta_e = 3,2$ ,  $\sigma_e = 7,2$ ). According to the results provided in Table 5, all path loss models underestimate the received signal power in suburban link. For this case, however, the Okumura, Log-distance and Hata model behave similarly and achieve similar prediction accuracy when considering  $\Delta_e$  and  $\sigma_e$ . Yet, the Okumura model seems to have relatively higher prediction accuracy ( $\Delta_e = 8,9$ ,  $\sigma_e = 15,1$ ) than the other models. On the other hand, one of the important factors that highly affect the performance of the COST-231 Hata model is the parameter  $C_m$ . Although it is defined as 0 dB for both suburban and open (rural) environments in many sources in the literature, it may have lower values when the rural environment conditions are considered. However, this requires more experimental study and comprehensive analysis.

In order to assess the prediction accuracies of the models in more detail, the Cumulative Distribution Function (CDF) for a Gaussian (in dB) distribution function of  $|\Delta_{RSSI}|$  for all models in rural and suburban link are represented in Fig. 8 and Fig. 9, respectively. From the figures, it is clear that the COST-231 Hata model has the worst prediction accuracy in both rural and suburban link. From Fig. 8, on the other hand, it can be observed that the Okumura model achieves the best prediction accuracy where it manages to achieve 38% of the points that have an error under 5 dBm while the Log-distance the Hata model achieve 33% and 12% of the points, respectively. As shown in Fig. 9, the accuracy of the models is significantly reduced where the Okumura model only manages to achieve 17% of the points that have an error under 5 dBm while the Log-distance the Hata model achieve 10% and 16% of the points, respectively. Thus, although the Okumura model has slightly better prediction

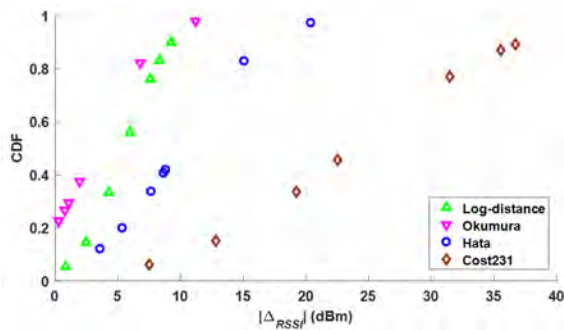


Figure 8. CDF of  $|\Delta_{RSSI}|$  for all models (rural).

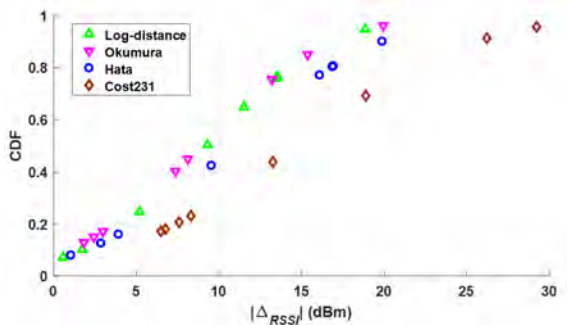


Figure 9. CDF of  $|\Delta_{RSSI}|$  for all models (suburban).

accuracy than the Hata model, it is still necessary to enrich the number of measurements in order to achieve certain performance results in suburban link. This, in fact, constitutes a part of future works as discussed in the following section.

## CONCLUSION AND FUTURE WORK

In this work, an assessment of well-known empirical path loss models (the Log-distance, Okumura, Hata, and COST-231 Hata model) within a context of low-height peer to peer configured system for LoRa links in suburban and rural environments is provided. The accuracy of path loss models is evaluated by comparing the predicted RSSI values with the measurements conducted at 868 MHz in suburban and rural environments around the Atilim University campus, Ankara. The results show that the Okumura model provides higher prediction accuracy while the COST-231 Hata model has lower accuracy in both suburban and rural environments.

This study constitutes as a preliminary propagation study of an ongoing project on the development of LWSN-based CP monitoring of oil and natural gas pipeline systems. Obviously, the number of the collected data from the measurements is relatively insufficient to provide an exact result especially in suburban links. For this reason, in the near future, the current work is expected to be enhanced by increasing the data size with more field tests and measurements. Particularly, the path loss effects of LWSN under

development will be characterized by conducting measurement campaigns using LoRa enabled sensor nodes at different heights from the ground (in the range of 0.25 m to 2 m) in various types of environments. But still, we believe that even this initial study would offer useful insights for many researchers who work on the planning and deployment of LWSNs based on LoRa enabled sensor nodes in suburban and rural environments.

## References

- Jawhar I, Mohamed N, Agrawal DP. Linear wireless sensor networks: Classification and applications. *Journal of Network and Computer Applications* 34(5) (2011) 1671–1682. doi: 10.1016/j.jnca.2011.05.006.
- Centenaro M, Vangelista L, Zanella A, Zorzi M. Long-range communications in unlicensed bands: The rising stars in the IoT and smart city scenarios. *IEEE Wireless Communications* 23(5) (2016) 60–67. doi: 10.1109/MWC.2016.7721743.
- Neumann P, Montavont J, Noël T. Indoor deployment of lowpower wide area networks (LPWAN): A LoRaWAN case study. Paper presented at the IEEE 12th International Conference on Wireless and Mobile Computing, Networking and Communications (WiMob), New York, 1–8, 2016. doi: 10.1109/WiMOB.2016.7763213.
- Petajajarvi J, Mikhaylov K, Yasmin R, Hamalainen M, Iinatti J. Evaluation of LoRa LPWAN technology for indoor remote health and wellbeing monitoring. *International Journal of Wireless Information Networks* 24(2) (2017) 153–165. doi: s10776-017-0341-8.
- Gregora L, Vojtech L, Neruda M. Indoor signal propagation of LoRa technology. Paper presented at the 17th International Conference on Mechatronics - Mechatronika (ME), Prague, 1–4, 2016.
- Nolan KE, Guibene W, Kelly MY. An evaluation of low power wide area network technologies for the Internet of Things. Paper presented at the International Wireless Communications and Mobile Computing Conference (IWCMC), Paphos, 439–444, 2016. doi: 10.1109/IWCMC.2016.7577098.
- Petric T, Goessens M, Nuaymi L, Toutain L, Pelov A. Measurements, performance and analysis of LoRa FABIAN, a realworld implementation of LPWAN. Paper presented at the IEEE 27th Annual International Symposium on Personal, Indoor, and Mobile Radio Communications (PIMRC), Valencia, 1–7, 2016. doi: 10.1109/PIMRC.2016.7794569.
- Petajajarvi J, Mikhaylov K, Roivainen A, Hanninen T, Pettissalo M. On the coverage of LPWANs: Range evaluation and channel attenuation model for LoRa technology. Paper presented at the 14th International Conference on ITS Telecommunications (ITST), Copenhagen, 55–59, 2015. doi: 10.1109/ITST.2015.7377400.
- Lauridsen M, Nguyen H, Vejlggaard B, Kovacs IZ, Mogensen P, Sorensen M. Coverage comparison of GPRS, NB-IoT, LoRa, and SigFox in a 7800 km<sup>2</sup> area. Paper presented at the IEEE 85th Vehicular Technology Conference (VTC Spring), Sydney, 1–5, 2017. doi: 10.1109/VTCSpring.2017.8108182.
- Sanchez-Iborra R, Sanchez-Gomez J, Ballesta-Vinas J, Cano MD, Skarmeta AF. Performance evaluation of LoRa considering scenario conditions. *Sensors* 18(3) (2018) 772. doi:10.3390/s18030772.
- Iova O, Murphy AL, Picco GP, Ghio L, Molteni D. LoRa from the city to the mountains: Exploration of hardware and environmental factors. Paper presented at the 2017 International Conference on Embedded Wireless Systems and Networks, Sweden, 317–322, 2017.
- Del Campo G, Gomez I, Calatrava S, Martinez R, Santamaria A.

- Power distribution monitoring using LoRa: Coverage analysis in suburban areas. Paper presented at the 2018 International Conference on Embedded Wireless Systems and Networks, Madrid, 233–238, 2018.
13. Abrardo A, Pozzebon A. A Multi-hop LoRa linear sensor network for the monitoring of underground environments: The case of the medieval aqueducts in Siena, Italy. *Sensors* 19 (2019) 402. doi: 10.3390/s19020402.
  14. Abrardo A, Fort A, Landi E, Mugnaini M, Panzardi E, Pozzebon A. Black powder flow monitoring in pipelines by means of multi-hop LoRa networks. Paper presented at the II Workshop on Metrology for Industry 4.0 and IoT (MetroInd4.0&IoT), Naples, Italy, 312-316, 2019. doi: 10.1109/METROI4.2019.8792890.
  15. Kara A, Imran MAA, Karadag K. Linear wireless sensor networks for cathodic protection monitoring of pipelines. Paper presented at the IEEE International Conference on Mechatronics, Robotics and Systems Engineering, Bali, 233–236, 2019. doi:10.1109/MORSE48060.2019.8998664.
  16. Harinda E, Hosseinzadeh S, Larijani H, Gibson RM. Comparative performance analysis of empirical propagation models for LoRaWAN 868MHz in an urban scenario. Paper presented at the IEEE 5th World Forum on Internet of Things (WF-IoT), Limerick, Ireland, 154–159, 2019. doi: 10.1109/WF-IoT.2019.8767245.
  17. Jörke P, Böcker S, Liedmann F, Wietfeld C. Urban channel models for smart city IoT-networks based on empirical measurements of LoRa-links at 433 and 868 MHz. Paper presented at the IEEE 28th Annual International Symposium on Personal, Indoor, and Mobile Radio Communications (PIMRC), Montreal, 1–6, 2017. doi: 10.1109/PIMRC.2017.8292708.
  18. Paredes M, Bertoldo S, Carosso L, Lucianaz C, Marchetta E, Allegretti M, Savi P. Propagation measurements for a LoRa network in an urban environment. *Journal of Electromagnetic Waves and Applications* 33(15) (2019) 2022–2036. doi: 10.1080/09205071.2019.1661287.
  19. Linka H, Michael R, Aliuy OG, Jonas K. Path loss models for low-power wide-area networks: Experimental results using LoRa. Paper presented at the VDE ITG-Fachbericht Mobilkommunikation, Osnabruck, Germany, 1–5, 2018.
  20. El Chall R, Lahoud S, El Helou M. LoRaWAN network: Radio propagation models and performance evaluation in various environments in Lebanon. *IEEE Internet of Things Journal* 6(2) (2019) 2366–2378. doi: 10.1109/JIOT.2019.2906838.
  21. Yilmaz VS, Bilgin G, Aydin E, Kara A. Miniaturised antenna at sub-GHz band for industrial remote controllers. *IET Microwaves, Antennas & Propagation* 13(9) (2019) 1408–1413. doi: 10.1049/iet-map.2018.5886.
  22. SEMTECH LoRa SX1276 Datasheet. Available online (last accessed on 12.11.2020): <https://www.semtech.com/products/wireless-rf/lora-transceivers/sx1276>.
  23. Bertoni HL. *Radio Propagation for Modern Wireless Systems*, Prentice-Hall, London, 2000.
  24. Rappaport TS. *Wireless Communications: Principles and Practice*, Prentice-Hall, Upper Saddle River, New Jersey, 2009.
  25. Okumura T, Ohmori E, Fukuda K. Field strength and its variability in VHF and UHF land mobile service. *Review Electrical Communication Laboratory* 16(9-10) (1968) 825–873.
  26. Hata, M. Empirical formula for propagation loss in land mobile radio services. *IEEE Transactions on Vehicular Technology* 29(3) (1980) 317–325. doi: 10.1109/T-VT.1980.23859.
  27. COST Action 231. *Digital mobile radio towards future generation systems, final report*. European Communities (1999) EUR 18957.



# Investigation of Bond Strength Between GFRP Wrapped Steel Reinforcement and Concrete with Pullout Test

Bogachan Basaran<sup>1</sup>  Erkan Turkmen Donmez<sup>2</sup> 

<sup>1</sup>Amasya University, Department of Construction, Amasya, Turkey

<sup>2</sup>Amasya University, Department of Design, Amasya, Turkey

## ABSTRACT

The bond behavior of glass fiber reinforced plastic (GFRP) wrapped deformed steel reinforcements having corrosion resistant with concrete is one of the important factors affecting the flexural performance and ductility of structural member exposed to bending. However, the number of studies on the bond of these reinforcements with concrete is insufficient due to not existing so much investigation on this issue. In this study, resin-impregnated glass fibers were wrapped on deformed steel reinforcements and new composite reinforcements of three diameters were produced, and these composite reinforcements bond with concrete were examined by pullout test. In addition, the bond of these composite reinforcements was compared with the bond of unwrapped deformed steel reinforcement. In this context, a total of 18 pullout tests were conducted in the study. As a result of the study, it is observed that maximum bond strength of FRP wrapped deformed steel reinforcements being not applied surface deformation (ribs, wound, sand coated etc.) ranged from 0.41 times to 0.64 times according to unwrapped steel reinforcements. In addition, it has been observed that the GFRP wrapped steel reinforcements maintain their bond strength up to high slipping values after reached the maximum bond strength values, compared to unwrapped deformed steel reinforcements.

**Keywords:** Bond strength, Hybrid FRP reinforcement, Bond of reinforcement, GFRP reinforcement, Composite rebar, Technical textiles, Glass fiber.

## Article History:

Received: 2020/08/21

Accepted: 2020/11/28

Online: 2020/12/31

**Correspondence to:** Boğaçhan Başaran,  
E-mail: bogachan.basaran@amasya.edu.tr;  
Phone: +90 358 211 5042;  
Fax: +90 358 218 0104.

## INTRODUCTION

Due to the corrosion of steel in reinforced concrete structures over time, the use of corrosion-resistant glass fiber reinforced polymer (GFRP) reinforcements as reinforcing bars in concrete has become increasingly common in recent years. Production costs are decreasing due to the widespread use of GFRP and their usage areas are increasing. However, since GFRP reinforcements have low shear and compressive strength (310–482 MPa) compared to tensile strengths (450–1600 MPa), FRP reinforcement usage as reinforcement bars in concrete is limited. For this reason, GFRP reinforcements are generally used as tension bars or stirrups in flexural members like such as beams and slabs. In addition, GFRP reinforcements reduce the ductility of structural members and cause them to have a brittle structural behavior due to their brittle stress-strain behavior (rupture strain 1.2–5% and linear behavior until rupture) compared to steel reinforcement (1–3).

Researchers have developed two different methods to overcome the disadvantages of GFRP and steel materials used in the structural member compared to each other. One of these methods is to use both FRP reinforcements and steel reinforcements independently from each other in the same structural member. In this method, it is aimed to reduce the displacement problems that occur under the usage load of FRP reinforced beams depending on the use of steel reinforcement (4–6). Another method is to produce new composite reinforcements by combining different types of materials (7–15). Composite reinforcements produced by this method are generally of two types. One of them can be in the form of wrapping / braiding / pultruded GFRP around a deformed / plain steel core. Other one can be on the basis of the use of distributed steel wires in the GFRP reinforcement. The production purposes of these reinforcements can be listed as follows; to protect the steel from corrosion by covering around the steel with FRP; to increase the low elasticity modulus of GFRP (35–60

GPa) by using steel in reinforcement; to eliminate the brittle stress-strain behavior of GFRP; to reduce the cost of GFRP.

As it is known, bond behavior between reinforcement and concrete affects significantly the flexural capacity and ductility of the structural members and can determine the energy absorbing capacity of the structural members. Determine the bond strength between the reinforcement bars and concrete is affected by many factors like type of reinforcement, reinforcement surface properties, reinforcement diameter, reinforcement embedment length, concrete compressive strength, etc. For this reason, it has been observed that the bond strength of GFRP reinforcements with concrete varies between 0.34 and 1.28 times the bond strength of steel reinforcements (16). However, since the number of studies conducted in the literature on these reinforcements is very limited, the number of resources related to bond between concrete and GFRP+steel reinforcement is very low. Ju, et al. (17), produced composite reinforcements by braiding glass fiber impregnated with vinyl ester on ribbed steel reinforcements. In addition, on these reinforcements have been applied various surface deformations (rib spacing, sand-coated shape). In the study, the effect of surface deformation properties of these reinforcements on bond behavior was investigated with 30 pullout tests. As a result of the study, it was observed that the bond strength of the completely sanded reinforcements had the highest bond strength (approximately 90.5% of the steel reinforcement, 20 MPa). Saikia et al. (18) produced composite reinforcements by helically wrapping the epoxy impregnated glass fiber strands on the plain steel core. The bond strength is 3.3 MPa as a result of the pullout test. In addition, it was stated that the beams constructed by using these reinforcements had collapsed due to lack of bond in beams.

In this study, new composite reinforcement have been produced by wrapped resin-impregnated glass fibers on the deformed steel reinforcement with the filament winding method. Wrapped reinforcements produced with this production method have much higher ductility (approximately 3 times higher) unlike the hybrid reinforcements produced in previous studies (17,18) (strain values at maximum stress approximately 1.5%). For this reason, the bond behavior of composite (steel+GFRP) reinforcements with this high ductility has not been studied before. Therefore, the bond behavior of these reinforcements should be examined. In the study, the effect of the reinforcement diameter and the GFRP ratio on the bond strengths and behaviors of the produced reinforcements with concrete were investigated with nine pullout tests. In addition, bond behaviors of concrete with unwrapped deformed steel reinforcement (8, 10 and 12 mm) composed of the core part in GFRP wrapped reinforcement were investigated with nine pullout tests. As a result

of the study, the bond behaviors of the two reinforcement types were compared.

## EXPERIMENTAL STUDY

### Production of GFRP Wrapped Steel Reinforcements

Within the scope of the study, filament winding method was used to produce glass reinforced plastic (GFRP) wrapped steel reinforcements (Fig. 1). This method is generally used in composite pipe production (19–21). The production of reinforcements was carried out in three stages. In the first stage, 0.9 mm diameter glass fiber were passed through the epoxy resin bath and epoxy was absorbed into the glass fiber. In the second stage, epoxy-impregnated glass fibers are winding on deformed steel reinforcements of various diameters (8, 10 and 12 mm) rotating at a constant speed, at an angle of 30 degrees to increase the reinforcement ductility in two layers. In the third stage, steel reinforcements wrapped GFRP were cured after 2 hours of 80 ° C and then cured again for 2 hours at 120 ° C.

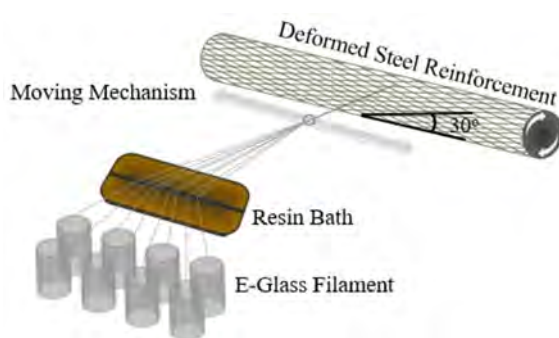


Figure 1. Production of GFRP wrapped steel reinforcements



Figure 2. Production of completed reinforcement

**Table 1.** Physical and mechanical properties of fibers and resin.

	E-Glass fiber	Epoxy
Filament tex (g/1000 m)	2501	-
Filament diameter (μm)	17.8	-
Density (g/cm <sup>3</sup> )	2.6	1.18
Tensile strength (MPa)	3300-3900	61
Tensile elongation (%)	4.5-4.9	2
Modulus of elasticity (GPa)	78-80	3.64

The physical and mechanical properties of glass fibers and epoxy resin, which are the materials that make up the FRP wrapped ribbed steel reinforcement, are shown in Table 1 and the reinforcements produced are shown in Fig. 2. The values of glass fibers and epoxy resin have been obtained from the manufacturer's catalog data.

**Mechanical and Physical Properties of Reinforcements**

In order to determine the tensile properties of the reinforcements produced by wrapping two layers of GFRP with a thickness of 0.9 mm on the 8, 10 and 12 mm deformed steel reinforcement used in the study and the steel properties of the steel reinforcement, a total of 18 tensile tests were performed. Tensile tests of steel reinforcement have been done according to EN ISO 15630-1 (22) and EN ISO 6892-1 (23) standards. Tensile tests of GFRP wrapped steel reinforcement were carried out by making caps similar to the tensile caps specified in ASTM D 7205 (24). The physical and mechanical properties of the reinforcements are presented in Table 2. In Table 2,  $D_{steel}$  is the outer diameter of the ribbed steel reinforcement (mm);  $D$  is the outer diameter of GFRP wrapped deformed steel reinforcement (mm);  $n=A_{GFRP}/A$  is the ratio of the GFRP cross-sectional area to the entire reinforcement in the GFRP wrapped deformed steel reinforcement.  $\sigma_{yield,0.2\%}$  is the average yield strength of the reinforcement, corresponding to 0.2% elongation percentage from the origin in the stress strain diagram (MPa);  $\sigma_{ultimate}$  is the average maximum tensile strength of the reinforcement (MPa);  $\epsilon_{max}$  is the strain that corresponds to the ultimate stress (%);  $E_{0.2\%}$  is the slope of the line drawn from origin onto the stress value corresponding to the percent elongation of 0.2% in the stress strain diagram (GPa). In the determination of the reinforcement yield stress in the stress-strain diagrams of the hybrid reinforcement, the 0.2% offset method was not used, since the hybrid reinforcement exhibits a parabolic behavior up to the yield zone (the beginning of the 2nd linear line) (Fig. 3). While determining the yield stresses of the reinforcement, instead of this method, the stress values corresponding to the 0.2% strain value from the origin (because of the reinforcement yielding at the end of the parabolic curve) has been used.

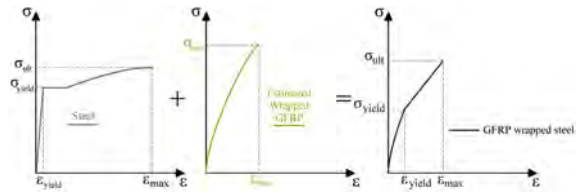


**Figure 3.** Stress-strain diagrams of reinforcements.

**Table 2.** Physical and mechanical properties of reinforcements.

Reinforcement type	$D_{steel}$ (mm)	$D$ (mm)	$n$	$\sigma_{yield,0.2\%}$ (MPa)	$\sigma_{ultimate}$ (MPa)	$\epsilon_{max}$ (%)	$E_{0.2\%}$ (GPa)
Steel	8.17	-	-	465	735	12.76	222
Steel	10.16	-	-	426	667	12.12	190
Steel	12.28	-	-	440	673	16.88	212
GFRP+ Steel	8.17	11.77	0.52	226	478	4.88	113
GFRP+ Steel	10.16	13.76	0.45	241	541	5.78	120
GFRP+ Steel	12.28	15.88	0.40	242	528	6.44	121

**Mechanical and Physical Properties of Concrete**

C25 / 30 class concrete having maximum aggregate diameter of 16 mm is used in the pullout test samples. In addition, CEM I 42.5N and Water/Cement ratio of 0.60 were used as cement type in the concrete mixture. Mixture calculations of concrete were made according to TS 802 (25). The materials and their proportions that compose of the concrete mixture are presented in Table 3. In order to determine the concrete compressive strengths, six concrete mixtures prepared in size of 150x150x150 mm<sup>3</sup>. The 28-day cube concrete compressive strength tests of the samples taken were determined as 30.96 MPa by performing according to TS-EN 12390-3 (26) standard.

**Table 3.** Mixing ratios of 1 m<sup>3</sup> of concrete (kg/m<sup>3</sup>)

Coarse aggregate (5-15 mm)	Fine aggregate (0-5 mm)	Water (kg)	Cement (kg)	Density (kg/m <sup>3</sup> )
550	1300	180	300	2330

**Preparation and Method for Reinforcement Pullout Tests**

While preparing the pull-out test samples, the reinforcements in all samples were adjusted so that the embedment length in the concrete is  $5\Phi$  ( $L$ ) according to codes ACI 440.3R-12 (27) and ASTM D7913 (28). Thick bands were used to adjust the concrete embedment lengths of the reinforcements. After the prepared reinforcements were centered on 150x150x150 mm<sup>3</sup> concrete molds with specially made steel apparatus, the concrete mixtures prepared were casted into the molds. In this way, a total of 9 GFRP wrapped reinforcement pullout test samples were prepared, 3 of each test sample (Fig. 4). In addition, 9 unwrapped steel reinforcement pullout test samples were prepared to compare the bond of FRP wrapped steel re-

**Table 4.** Pullout test samples.

Pullout Test Sample	$D_{steel}$ (mm)	$D$ (mm)	$n$	$L$ (mm)
S8	8.17	-	-	40.85
S10	10.16	-	-	50.80
S12	12.28	-	-	61.40
GFRP+S8	8.17	11.77	0.52	58.85
GFRP+S10	10.16	13.76	0.45	68.80
GFRP+S12	12.28	15.88	0.40	79.40

inforcement samples and unwrapped steel reinforcement samples. The prepared experiment samples are presented in Table 4.

After the experiment samples, which were taken out of the mold at the end of 2 days, were kept under laboratory conditions for at least 28 days, pullout tests were carried out. In the experiments, the heads of the universal testing machine (UTM) with a capacity of 600kN was rearranged for pullout experiments and the test speed of the machine was adjusted to be 2 mm per minute. During the experiments, in order to measure the amount of slipping of the reinforcement from the concrete, two pieces of 0.01 mm precision linear potentiometers were attached to the loading end of the test samples. In addition, during the experiments, voltage changes in both the potentiometers and the load cell of the UTM were recorded with a 16bit high resolution data acquisition system. The image of the test setup and test samples is presented in Fig. 5.

### Determination of Bond Strength

The reinforcement tensile force values obtained for each pullout sample were converted into bond force values using Eq. (1). Eq. (3) is calculated from the tensile force coming to the reinforcement and bond force equation

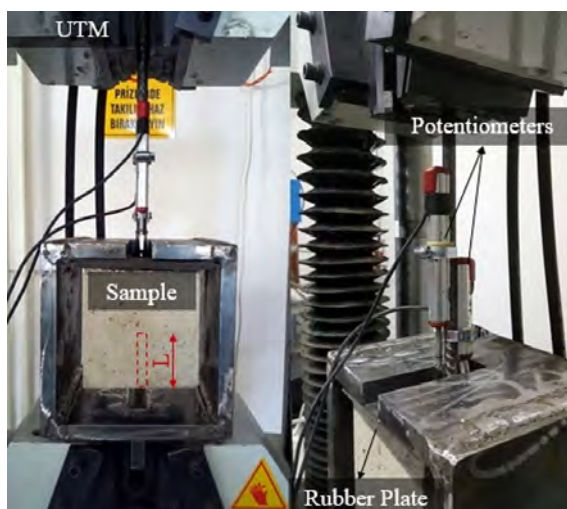


**Figure 5.** The experimental setup

between reinforcement and concrete. In Eq. (3), it is assumed that bond strength are spread homogeneously over the length of bond. Equation 3 is also used in determining the FRP reinforcement-concrete bond strength (28).

$$F_{tensile} = F_{bond} \tag{1}$$

$$F_{tensile} = \pi DLu \tag{2}$$

$$u = \frac{F_{tensile}}{\pi DL} \tag{3}$$

Where,  $F_{tensile}$  is the pullout force to the reinforcement (N);  $F_{bond}$  is the bond force between reinforcement and concrete (N);  $D$  is outer diameter of reinforcement (mm);  $L$  is bond length (mm);  $u$  is bond strength between concrete and reinforcement (MPa).

### TEST RESULTS

In this study, 18 pullout tests were carried out to examine the bond between GFRP wrapped steel reinforcement and the unwrapped steel reinforcement with concrete. The pullout test results are presented in Table 5.

**Table 4.** Pullout test samples.

Test Sample	$D$ (mm)	$L$ (mm)	$F_{max}$ (N)	$U_{max}$ (MPa)	$U_{average}$ (MPa)	Failure Mode
S8-1	8.17	40.9	25007	23.85	-	Pullout
S8-2	8.17	40.9	27912	26.62	25.10	Pullout
S8-3	8.17	40.9	26043	24.84	-	Pullout
S10-1	10.16	50.8	32992	20.35	-	Pullout
S10-2	10.16	50.8	38827	23.95	22.51	Pullout
S10-3	10.16	50.8	37681	23.24	-	Pullout
S12-1	12.28	61.4	48080	20.30	-	Pullout
S12-2	12.28	61.4	48894	20.64	20.74	Pullout
S12-3	12.28	61.4	50438	21.29	-	Splitting
GFRP+S8-1	11.77	58.9	23814	10.94	-	Pullout
GFRP+S8-2	11.77	58.9	21088	9.69	10.37	Pullout
GFRP+S8-3	11.77	58.9	22786	10.47	-	Pullout
GFRP+S10-1	13.76	68.8	29061	9.77	-	Pullout
GFRP+S10-2	13.76	68.8	32553	10.95	10.84	Pullout
GFRP+S10-3	13.76	68.8	35066	11.79	-	Pullout
GFRP+S12-1	15.88	79.4	55567	14.03	-	Splitting
GFRP+S12-2	15.88	79.4	53333	13.46	13.26	Splitting
GFRP+S12-3	15.88	79.4	48659	12.28	-	Pullout

Various error modes can occur during pullout tests (reinforcement failure, pull-out failure, concrete splitting failure, concrete cone failure) (29-30). In this study, generally,

pullout and splitting failures were observed. However, due to the short embedment length of the reinforcement ( $5\Phi$ ) in the concrete, the number of experiments that resulted in pullout failure was observed are considerably higher than the number of experiments that resulted in splitting failure mode. General pullout samples of GFRP wrapped reinforcement and deformed steel reinforcement that resulted in pullout failure mode are presented in Figures 6.a and 6.b, respectively. No visible deformation was observed on the surfaces of GFRP wrapped reinforcements pullout from concrete. The experiments that resulted in the splitting of concrete were generally seen in samples with large reinforcement diameters. The reason is that may be the high bond forces. As the bond force carried by mechanical locking increases, the radial forces occurring perpendicular to the reinforcement axis increase and therefore the concrete is split by exceeding the tensile strength of the concrete. Some of the test samples that resulted in splitting failure mode are presented in Fig. 6.c-e.

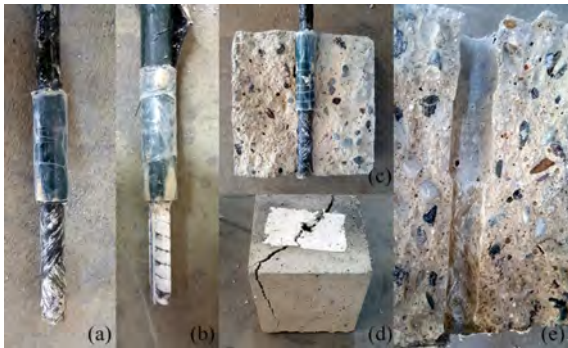


Figure 6. Samples of collapse after the experiments

The average bond strength of reinforcements produced by wrapping GFRP on 8 mm diameter deformed steel reinforcements are 0.41 times the average bond strength of 8 mm diameter unwrapped steel reinforcements. This ratio is 0.48 for 10 mm reinforcement and 0.64 for 12 mm reinforcement (Fig. 7). However, although GFRP wrapped deformed reinforcements are not subjected to any surface deformation (rib, groove, sand coated, etc.), bond strength values with concrete are quite satisfactory. As it can be seen from Fig. 7, steel reinforcement diameter increases while reinforcement bond strength decreases. However, bond strength increases in FRP wrapped reinforcements.



Figure 7. Comparison of average bond strength of reinforcements

In Fig.8, the relationship between the bond strength of the reinforcement with concrete and the GFRP section ratio in the reinforcement section is shown. There is a very high correlation between these two factors, such as 0.94. As can be seen from Fig.8, as the GFRP section ratio in the reinforcement increases, the bond strength between the reinforcement and the concrete decreases.

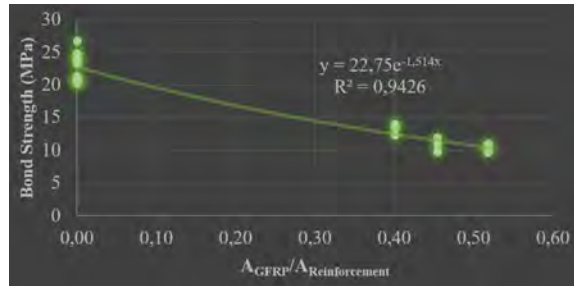


Figure 8. Relationship between bond strength and GFRP cross-sectional area

The bond strength-slip curves obtained as a result of pullout tests are presented in Figs. 9, 10 and 11 for both GFRP wrapped and unwrapped deformed steel reinforcements. When the bond strength-slip curves of the reinforcements are examined and it is seen that all GFRP wrapped reinforcements have lower bond stiffness (the slope of the linear line drawn from the origin to the stress value up to point where curve begins) compared to the steel reinforcements. However, the slip values corresponding to the maximum bond strength values of GFRP wrapped reinforcements are very similar to those of steel reinforcements. The difference between the bond stiffness of the reinforcements resulted from the low maximum bond strength of the GFRP wrapped reinforcements compared to the deformed steel reinforcements. In addition, it was observed that bond stiffness decreased with increasing GFRP cross-sectional area. This situation is thought to be caused by the increase in the crushing amount of the GFRP wrapping due to the increase in the GFRP cross section area in the reinforcement.

When the slipping behaviors of the reinforcements after the maximum bond strength are examined, the bond strength values of deformed steel reinforcements have decreased rapidly due to the fact that the ribs of the steel reinforcement shear the concrete suddenly. However, compared to steel reinforcements, GFRP wrapped reinforcements have preserved bond strength values to long slip values by the effect of friction forces. This is thought to be due to the fact that the reinforcement surface is gradually crushed by concrete due to its low rigidity and hardness compared to steel reinforcement. However, it is not clear whether the bond strength values of the reinforcement after the maximum bond strength values are affected by the GFRP cross-sectional area in the reinforcement.

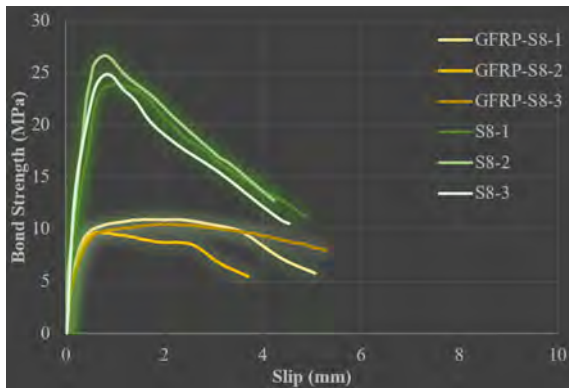


Figure 9. Bond strength-slip curves of 8 mm reinforcements

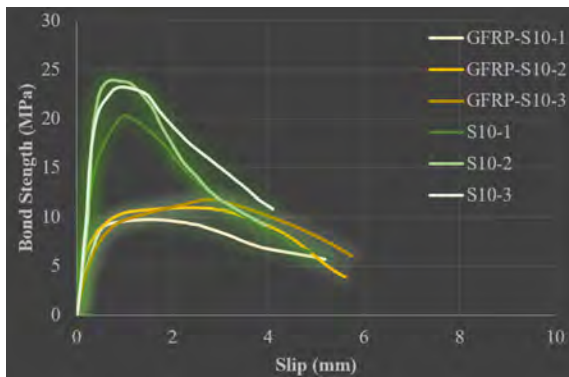


Figure 10. Bond strength-slip curves of 10 mm reinforcements

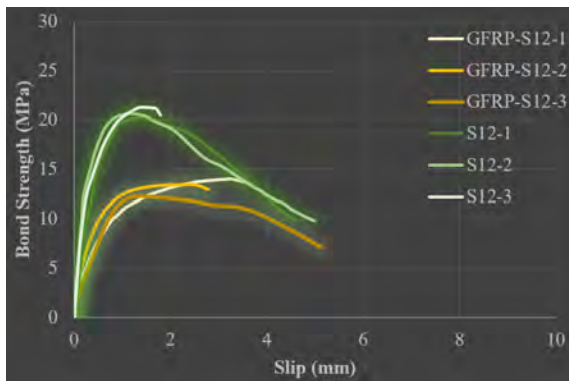


Figure 11. Bond strength-slip curves of 12 mm reinforcements

## CONCLUSIONS

In this study, the bond behaviors of glass fiber reinforced plastic (GFRP) wrapped steel reinforcements of various diameters produced by filament winding method have been investigated by pullout tests. In addition, bond behavior of deformed steel reinforcements used in making GFRP wrapped reinforcement was also tested under the same experimental conditions. Within the scope of the study, a total of 18 pullout tests were carried out using reinforcements of various diameters embedded in C25 class 150x150x150 mm<sup>3</sup> concretes with embedment length of

5Φ. The main observed developments in the study can be summarized as follows:

- Maximum bond strength of GFRP wrapped deformed steel reinforcements ranged from 0.41 times to 0.64 times the maximum bond strength of steel reinforcement. Although no surface deformation (ribs, grooves, windings, sandblasting, etc.) is applied to the surfaces of GFRP wrapped reinforcements, bond strength of composite reinforcement was seen higher than expected. If surface deformation processes are applied to composite reinforcement, bond strength values can be much more improved.

- Unlike deformed steel reinforcements, bond strength has increased as the reinforcement diameter increases in GFRP wrapped reinforcement. However, this increase was inversely related to the GFRP cross section ratio in GFRP wrapped reinforcements. In addition, due to the increase of the GFRP cross-sectional area in the GFRP-wrapped reinforcements, the crushing amount of the GFRP wrapped increases and it has been observed that it has a bond reducing effect.

- The slipping values corresponding to the approximate maximum bond strength of GFRP wrapped reinforcements are similar to those of steel reinforcements.

- Unlike steel reinforcements, bond did not drop suddenly after maximum bond strength in GFRP wrapped reinforcements. Relatively compared to steel reinforcement samples, GFRP wrapped reinforcements maintained their bond strength values up to large slip values.

- At the end of the experiments, due to the short embedment lengths, pullout failure was observed. No visible deformation was observed on the reinforcement surfaces of all samples with GFRP wrapped reinforcement.

As a result, considering that the bond strength values of FRP rebars are in a wide range of 0.34 to 1.28 times the bond strength values of steel rebars, it is thought that additional studies are needed to expand the scope of experimental and statistical studies to determine the bond strength of FRP wrapped reinforcements.

## ACKNOWLEDGEMENT

The study was supported by Amasya University Scientific Research Project Coordination Unit under the project number FMB-BAP 19-0429. This support is gratefully acknowledged. The experiments were conducted in the Structural Material Laboratory of the Technical Sciences Vocational School, Amasya University.

## References

1. ACI 440.1R-15 Guide for the Design and Construction of Structural Concrete Reinforced with Fiber-Reinforced Polymer (FRP) Bars. American Concrete Institute (ACI). MI, USA, 2015.
2. ACI 440R-96 State-of-the-Art Report on Fiber Reinforced Plastic (FRP) Reinforcement for Concrete Structures. American Concrete Institute (ACI). MI, USA, 2002.
3. fib bulletin 40 FRP Reinforcement in RC structures. International Federation for Structural Concrete (fib). Lausanne, Switzerland, 2007.
4. El Refai A, Abed F, Al-Rahmani A. Structural performance and serviceability of concrete beams reinforced with hybrid (GFRP and steel) bars. *Construction and Building Materials* 96 (2015) 518-29.
5. Lau D, Pam HJ. Experimental study of hybrid FRP reinforced concrete beams. *Engineering Structures* 32 (12) (2010) 3857-65.
6. Gemi L, Madenci E, Özkılıç YO. Çelik, Cam FRP ve Hibrit Donatılı Betonarme Kirişlerin Eğilme Performansının İncelenmesi. *Düzce Üniversitesi Bilim ve Teknoloji Dergisi* 30:8 (2020) 1470-83.
7. Ju M, Lee S, Park C. Response of Glass Fiber Reinforced Polymer (GFRP)-Steel Hybrid Reinforcing Bar in Uniaxial Tension. *International Journal of Concrete Structures and Materials* 11 (2017) 677-86.
8. Correia L, Cunha F, Mota C, Figueiredo R, Nunes JP. Pseudo-Ductile Braided Composite Rods (BCRs) Produced by Braiding. In: ECCM17 – 17th European Conference on Composite Materials. Munich, Germany, 2016.
9. Seo D-W, Park K-T, You Y-J, Lee S-Y. Experimental Investigation for Tensile Performance of GFRP-Steel Hybridized Rebar. *Advances in Materials Science and Engineering* 2016 (2016) 1-12.
10. Seo D-W, Park K-T, You Y-J, Hwang J-H. Evaluation for Tensile Performance of Recently Developed FRP Hybrid Bars. *International Journal of Emerging Technology and Advanced Engineering* 4(6) (2014) 631-7.
11. Wu G, Sun ZY, Wu ZS, Luo YB. Mechanical Properties of Steel-FRP Composite Bars (SFCBs) and Performance of SFCB Reinforced Concrete Structures. *Advances in Structural Engineering* 15(4) (2012) 625-35.
12. Behnam BR. Reliability model for ductile hybrid FRP rebar using randomly dispersed chopped fibers. Wayne State University, Detroit, Michigan, 2012.
13. Etman EE-S. Innovative Hybrid Reinforcement for Flexural Members. *Journal of Composites for Construction* 15(1) (2011) 2-8.
14. Cheung MMS, Tsang TKC. Behaviour of Concrete Beams Reinforced with Hybrid FRP Composite Rebar. *Advances in Structural Engineering* 13(1) (2010) 81-93.
15. Cui Y, Cheung MMS, Noruziaan B, Lee S, Tao J. Development of ductile composite reinforcement bars for concrete structures. *Materials and Structures* 41(9) (2008) 1509-18.
16. Basaran B, Kalkan I. Investigation on variables affecting bond strength between FRP reinforcing bar and concrete by modified hinged beam tests. *Composite Structures* 242 (2020) 112185.
17. Ju M, Park G, Lee S, Park C. Bond performance of GFRP and deformed steel hybrid bar with sand coating to concrete. *Journal of Reinforced Plastics and Composites* 36(6) (2017) 464-75.
18. Saikia B, Thomas J, Ramaswamy A, Rao KSN. Performance of hybrid rebars as longitudinal reinforcement in normal strength concrete. *Materials and Structures* 38 (284) (2005) 857-64.
19. Gemi L, Köklü U, Yazman Ş, Morkavuk S. The effects of stacking sequence on drilling machinability of filament wound hybrid composite pipes: Part-1 mechanical characterization and drilling tests. *Composites Part B: Engineering* 186 (2020) 107787.
20. Gemi L, Köroğlu MA, Ashour A. Experimental study on compressive behavior and failure analysis of composite concrete confined by glass/epoxy  $\pm 55^\circ$  filament wound pipes. *Composite Structures* 187 (2018) 157-68.
21. Peters ST. *Composite Filament Winding*. ASM International, 2011.
22. EN ISO 15630-1:2010 Steel for the reinforcement and prestressing of concrete – Test methods – Part 1: Reinforcing bars, wire rod and wire (ISO 15630-1:2010). European Committee for Standardization. 2010.
23. EN ISO 6892-1:2016 Metallic materials – Tensile testing – Part 1: Method of test at room temperature (ISO 6892-1:2016). European Committee for Standardization. 2016.
24. ASTM D7205/D7205M-06 Standard Test Method for Tensile Properties of Fiber Reinforced Polymer Matrix Composite Bars. ASTM International. USA, 2016.
25. TS 802 Beton Karışım Tasarımı Hesap Esasları. Türk Standartları Enstitüsü (TSE). Ankara, 2016.
26. EN 12390-3:2009 Testing hardened concrete – Part 3: Compressive strength of test specimens. European Committee for Standardization. 2009.
27. ACI 440.3R-12 Guide Test Methods for Fiber-Reinforced Polymer (FRP) Composites for Reinforcing or Strengthening Concrete and Masonry Structures. American Concrete Institute (ACI). MI, USA, 2012.
28. ASTM D7913 / D7913M – 14. Standard Test Method for Bond Strength of Fiber-Reinforced Polymer Matrix Composite Bars to Concrete by Pullout Testing. ASTM International. 2014.
29. ACI 355.1R-91 State-of-The-Art Report on Anchorage to Concrete. American Concrete Institute (ACI). 1991.
30. Müsevitoğlu A, Arslan MH, Aksoylu C, Özkılıç A. Experimental and analytical investigation of chemical anchors's behaviour under axial tensile. *Measurement* 158 (2020) 107689.





# Selective Removal of Penicillin G from Environmental Water Samples by Using Molecularly Imprinted Membranes

Meshude Akbulut Soylemez 

Hacettepe University, Department of Chemistry, Ankara, Turkey

## ABSTRACT

Penicillin G imprinted membranes were prepared by utilizing UV induced in-situ polymerization. The characterization of membranes was conducted by using ATR-FTIR, XPS, SEM and AFM. The binding properties of imprinted membranes were evaluated against concentration and time. The binding capacity of the membranes was tested for real water samples. The size of the binding cavities of membranes was determined by using PALS. The specific selectivity of the membranes was investigated by using similar  $\beta$ -lactams, penicillin V and amoxicillin. The specific binding of the membranes was determined as 3.27  $\mu\text{g/g}$  for penicillin G while this value was obtained as 0.83 and 0.51  $\mu\text{g/g}$  for penicillin V and amoxicillin, respectively. The binding capacity of the membrane was determined as 5.03  $\mu\text{g.g}^{-1}$  for ultra pure water while this value was obtained as 4.01  $\mu\text{g.g}^{-1}$  and  $\sim 3.50 \mu\text{g.g}^{-1}$  for tap water and natural water samples from different sources, respectively.

### Keywords:

Membrane; Molecularly imprinted polymer; Penicillin G.

## INTRODUCTION

Since its discovery, penicillin G has been useful for the treatment of infectious diseases in humans and animals. This compound is one of the most widely used drugs among antibiotics. Unfortunately, there is a continuous release of antibiotics due to the widespread and overuses of this family of the drug in some certain places such as hospitals and farms. Release of antibiotics to environmental waters is a crucial problem for human health. The residues of antibiotics were detected in industrial and municipal wastewater, and also surface and groundwater samples [1-4]. The residues of antibiotics in environmental waters may cause the development of antibiotic resistance [5]. The recognition and removal of the antibiotics from environmental water are necessary to protect public health by using easy, compatible, cheap and reliable materials.

There are several sensing and recognition systems for Penicillin G prepared by utilizing molecularly imprinting method [6-8]. Most of them are related by detecting of antibiotics from complex matrices such as food and food derivatives like milk, chicken, etc. [8, 9]. The production methods includes synthesis of nanoparticles by emulsion polymerization [9], surface imprinting onto various support materials like magnetic nanoparticles [10] or non-woven fabrics [11]. Unfortunately,

the number of researches on the removal of Penicillin G is not many. Molecularly imprinted polymers are functional materials prepared by polymerizing functional monomers and a crosslinking agent around a template molecule. Removing the template molecule from the network provides recognition sites that can accurately fit the template molecule concerning its affinity, size and shape. In this study, Penicillin G imprinted membranes were prepared by utilizing UV induced polymerization method for removal of the template molecule Penicillin G from real water samples. Photopolymerization is a good alternative to thermal polymerization by providing polymerization and crosslinking at room temperature. It is possible to say that the synthesis at room temperature is an important factor to get molecularly imprinted polymers with high specific selectivity depending on the stability of pre-polymerization complexes [10].

## EXPERIMENTAL

### Materials

Penicillin G, penicillin V, amoxicillin, methacrylic acid (MAA), ethylene glycol dimethacrylate (EGDMA), dimethylformamide (DMF), methanol, acetic acid and benzophenone were purchased from Sigma-

### Article History:

Received: 2020/08/21

Accepted: 2020/11/21

Online: 2020/12/31

Correspondence to: Meshude Akbulut Soylemez, Hacettepe University, Chemistry, 06800, Beytepe, Ankara, Turkey  
E-Mail: meshude@hacettepe.edu.tr

Aldrich (Milwaukee, USA). All the reagents and solvents were used as received without any further purification step.

### Preparation of Penicillin G imprinted membranes

Penicillin G (0.503 mmol) was dissolved in 2 mL DMF and then 2.01 mmol MAA was added into the solution. The solution had been kept overnight at 4 °C. EGDMA (5.00 mmol) and 8 mL of DMF were added. The ratio of MAA to penicillin G was kept as 4:1 [11]. The formation of pre-polymerization complex between template and functional monomers and the synthesis of penicillin G imprinted membranes were illustrated in Fig. S1. Finally, 20.0 mg of benzophenone was added. The solution was purged with nitrogen and then placed between two identical silanized glass slides which separated by a rubber O-ring. The solution filled glass slides was placed into a zip-lock plastic bag under a nitrogen blanket. The polymerization was carried out by using a Philips type HB 171/A self-tanning UV lamp, adapted with four fluorescent tubes of Philips CLEO 15 W UVA. The irradiation time was kept as 90 min. The distance from the glass slides to the UV lamp was held as 10 cm. Subsequently, Penicillin G imprinted membranes (MIM) were carefully removed from the surface of the glass slides. The template molecule and unpolymerised monomers were washed out of the membranes with a mixture of acetic acid/methanol/water (1/5/1, by volume) until no Penicillin G was detected through a UV spectrometer. The non-imprinted membranes (NIM) was prepared using the same technique except for the addition of penicillin G.

### Characterization of membranes

ATR-FTIR, XPS, SEM and AFM were used in the chemical and physical characterisation of membranes. The size of the recognition sites in the membranes was investigated by employing positron annihilation lifetime spectrometer (PALS) to analyze the effect of the presence of the template molecule.

The FTIR experiments were performed using Thermo Nicolet iS10 Thermo Nicolet iS10 model spectrometer in attenuated total reflection (ATR) mode. Spectra were recorded by accumulating 32 scans with a resolution of 4 cm<sup>-1</sup>.

Experiments with X-ray photoelectron spectroscopy (XPS) were carried out using a Thermo spectrometer with a monochromated Al K  $\alpha$  X-ray source. Survey and core scans were reported with a pass energy of 30 eV and 200 eV, respectively. All analyzes were performed at a take-off angle of 90°. Elemental composition of the surface of the membranes was examined with a 400  $\mu$ m X-ray spot size and binding energy ranged from 0-1000 eV.

SEM membrane images were taken using an FEI Quanta 200FEG instrument with an accelerating voltage of 2.00 kV. Until screening, samples had been sputter-coated with gold.

Bruker Nanoscope 9 atomic force microscopy (AFM) was employed in tapping mode to make the morphological investigation of the membranes.

PALS experiments were performed using a standard system with detectors whose scintillators are plastic. The position of the detectors was face-to-face. The positron source was <sup>22</sup>Na with an activity of 11  $\mu$ Ci, in the form of dried NaCl solution between two thin Kapton foils with glued together. The instrument time resolution was 258 ps (FWHM). The source was placed between two identical membranes in a typical 'sandwich' configuration. Each spectrum was saved in the air at room temperature every 3 h for a total count of 3 $\times$ 10<sup>6</sup>. The sum of 5 spectra was used to produce 1.5 $\times$ 10<sup>7</sup> counts. The spectra obtained were examined using the program LT [12].

### Investigation of binding properties of membranes

Batch binding experiments were performed to determine the binding capacity of imprinted and non-imprinted membranes. The membranes were incubated in 2 mL Penicillin G solutions with a various concentration in the range of 0.5-50 ppm. The concentration of Penicillin G before and after incubation was analyzed by employing a UV-vis Varian Cary100 spectrophotometer at a maximum absorption wavelength of 216 nm [11]. The number of repetition of the analyses was three. The binding behaviour of membranes was analysed by using adsorption isotherms. The adsorbed amount of penicillin G ( $q_e$ ) was determined by using the following equation:

$$q_e = \frac{C_i - C_f}{W} \times V \quad (1)$$

where  $C_i$  and  $C_f$  are the initial and equilibrium concentrations of template molecule, penicillin G ( $\mu$ mol/L), respectively,  $V$  is the volume of solution (L),  $W$  is mass of the dry membrane (g).

The kinetic behaviour of adsorption was investigated by incubation for various periods in 3 ppm Penicillin G solution.

The reusability of the membranes was investigated by an adsorption-desorption cycle which was repeated 7 times. The concentration of Penicillin G was 3 ppm and the incubation time was 20 min. After each adsorption step, the membrane was washed as described before and then the incubation was repeated.

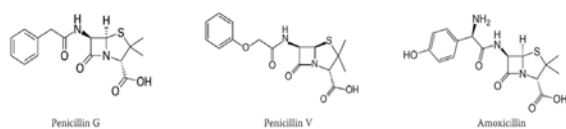


**Figure 1.** Chemical structures of antibiotics.

The specific selectivity of imprinted membranes was investigated by incubation in the presence of similar compounds, Penicillin V and amoxicillin (Fig. 1). The concentrations of antibiotics were kept as 3 ppm and the incubation time was 20 min.

The binding performance of the membranes was investigated in real water samples collected from Pazar Creek (in Ankara) and Kızılırmak (in İskilip/Çorum region). And the binding performance of the membranes was also tested in tap water. Water samples were firstly filtered by using a 0.25  $\mu\text{m}$  Nylon filter and stored at +4 °C until analysis. Before experiments 3 ppm Penicillin G was spiked into the water samples. The incubation time was kept as 20 min. All the experiments were repeated three times.

## RESULTS AND DISCUSSION

### Chemical characterization of membranes

As can be seen in Fig. 2 the structural characterization of imprinted and non-imprinted membranes was carried out by ATR-FTIR spectroscopy. The peak at  $1721\text{ cm}^{-1}$  is attributed to stretching of C=O groups of methacrylic acid and EGDMA. The stretching vibration of  $\text{sp}^3$  hybridized C-H bonds can be seen at  $2943\text{ cm}^{-1}$  while the bending vibration of the same group is at  $1454\text{ cm}^{-1}$ . The peak at  $1140\text{ cm}^{-1}$  corresponds to the stretching of C-O groups in dialkyl ethers [13]. All the peaks can confirm the chemical structure of poly(ethylene glycol dimethacrylate-co-methacrylic acid). Unfortunately, it is not possible to see any evidence of the presence of the template molecule due to its trace amount in the polymeric network by using FTIR. However, the presence of the template molecule can be proven by using more sensitive instrumental analysis methods such as XPS. XPS is a useful tool which provides detailed information about the chemical composition of the surfaces after modification for the approximately 10 nm depth from the surface.

Therefore, the surface elemental composition of membranes was investigated by employing XPS. The survey scans of MIM and NIM can be seen in Fig 3. The chemical compositions of the imprinted and non-imprinted membranes show similarities for C1s (285 eV) and O1s (532 eV) peaks with an exception of the N1s peak at 400 eV for MIM [14]. The appearance of N1s peak proves the presence of the template in the crosslinked polymer.

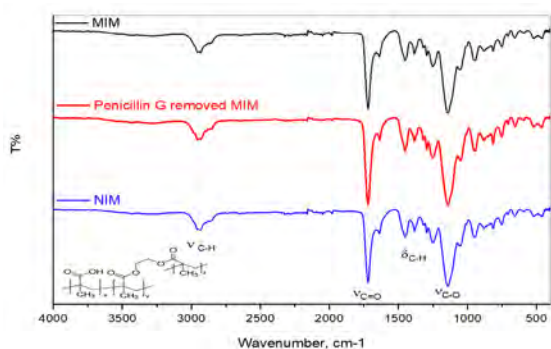


**Figure 2.** FTIR spectra of the imprinted membrane (MIM), template removed imprinted membrane and non-imprinted membrane (NIM).

The C1s core level spectra of MIM, penicillin G removed MIM and NIM can be seen in Fig 4. The common and the major component for all is the C-C and C-H peak which is detected at 284. eV. The component at 286.0 eV is attributed to the C-O [15]. The highest binding energy value (~288.3 eV) can be ascribed to C=O groups of copolymeric matrix [14]. There is one more component in MIM spectrum at 287.4 eV which corresponds to C-N type carbon atoms in amide (399.9 eV) and lactam groups (400.2 eV) of penicillin G (Fig. S2) [15]. This is a direct evidence of the presence of the template molecule in the imprinted membrane. It can be said that the procedure for the removal of template molecule is sufficient as can be noticed with the disappearance of C-N in the spectrum of penicillin G removed MIM. The binding ability of the MIM was also investigated by XPS analysis. The C-N peak at 287.4 eV appears again for the penicillin G removed MIM after penicillin G incubation in 3 ppm for 20 min.

### Physical and morphological characterization of membranes

The presence of the template molecule in the imprinted polymers can cause various morphological differences [16]. The difference in the morphological structures of the surfaces of NIM and MIM can be seen from SEM

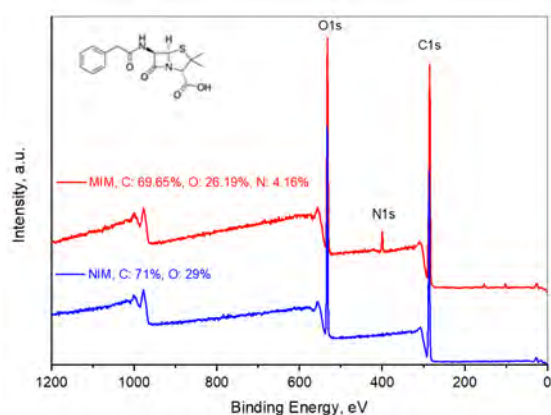


**Figure 3.** Survey scans of penicillin G imprinted (MIM) and non-imprinted membranes (NIM) and the chemical structure of penicillin G.

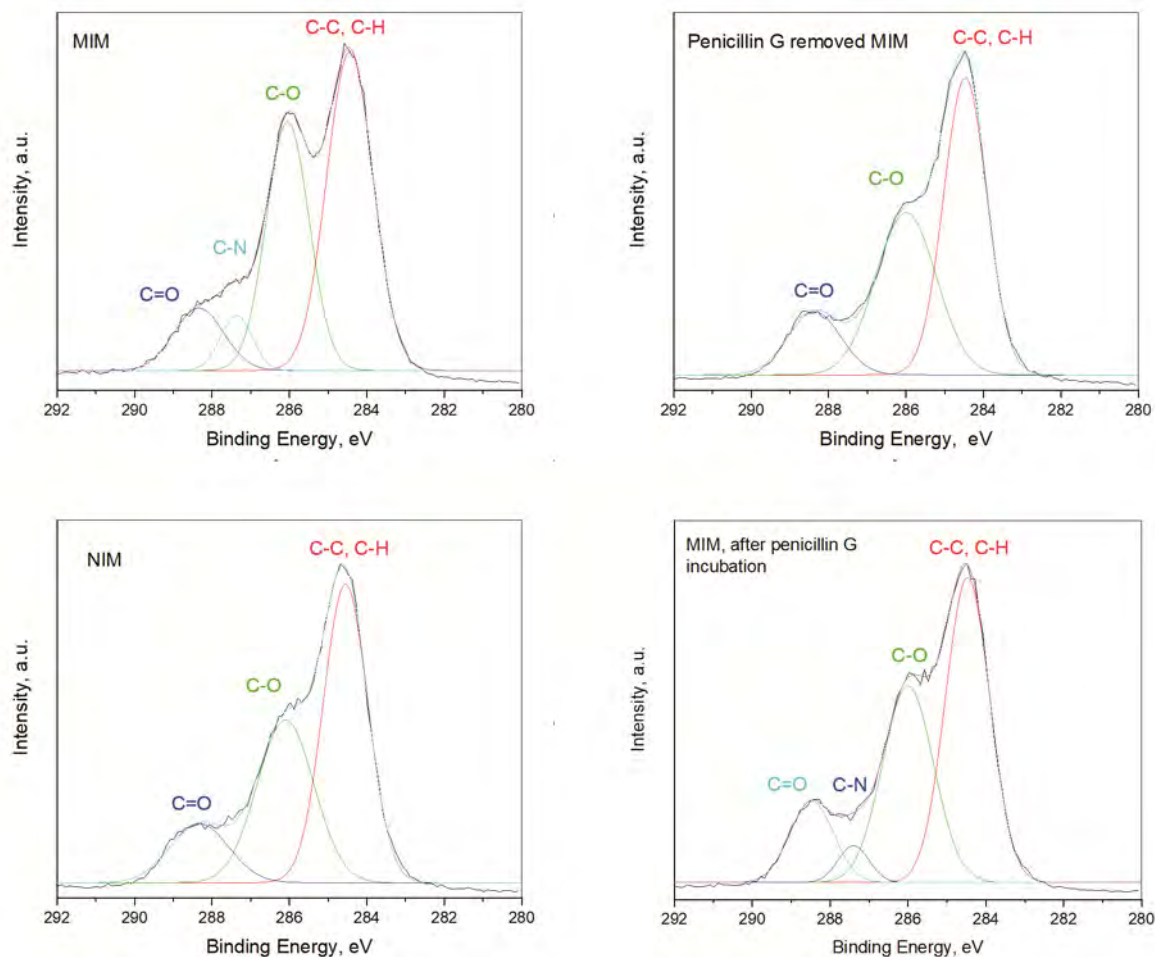


**Figure 4.** C1s spectra of penicillin G imprinted membranes (MIM), penicillin G free imprinted membranes by washing with a solution of acetic acid:methanol:water, non-imprinted membranes (NIM) and penicillin G free imprinted membranes after incubation in 3 ppm penicillin G solution for 20 min.

images (Fig. 5). The interaction between the monomer and the template can cause more porosity and roughness on the surface of the membranes [17].

The roughness of the surfaces of the membranes was also investigated by employing AFM (Fig 6). The value of Rq is determined as 234 and 98 for MIM and NIM, respectively. The roughness of the surface of MIM provides higher binding capacity for penicillin G due to the increasing in surface area and permeability of the membranes that provides to

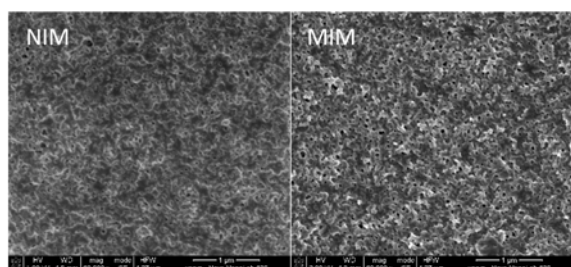


**Figure 5.** SEM images of NIM and MIM.

enhance in the possibility of the interaction between MIM and penicillin G [18].

The size of the free volume holes in the membranes was investigated by employing PALS. It is an absolute and highly sensitive method which provides detailed and certain information on the size and size distribution of free volume holes in polymeric structures [19, 20] and defects in metals [21]. The selectivity of the molecularly imprinted polymers can be controlled mainly by two factors: 1) chemical affinity of the recognition sites and 2) binding cavity size and size

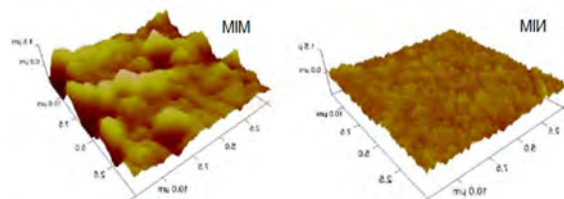


**Figure 6.** AFM images of non-imprinted (NIM) and imprinted membranes (MIM).

distribution [13]. The second factor gains more importance when the binding of compounds with a similar molecular size is considered. Therefore, it is important to have information about the size of the binding cavities of imprinted polymers. In previous work from our laboratory, the average diameter of the free volume holes of imprinted polymers of penicillin G prepared by grafting on the non-woven fabric was determined as 0.570 nm while this value was obtained as 0.469 nm for non-imprinted polymer grafts [13]. In this study, the diameter of the free volume holes in MIM was obtained as  $0.558 \pm 0.003$  nm that matches to previously obtained data. The pore size of the NIM ( $0.434 \pm 0.002$  nm) was also similar to the previous data for the control polymer. The obtained data also correlates to the molecular diameter of the penicillin G which was reported as 0.500 nm by Wu and coworkers [22].

## Investigation of the binding properties of membranes

### Adsorption isotherms

To examine the binding characteristics of the membranes binding isotherms were constructed. Adsorption isotherms are created by using the equilibrium concentration of an analyte onto an adsorbent ( $q_e$ ) and the concentration of the analyte in the solution ( $c_e$ ) with which it is in contact. This relationship is explained by using several equations. The most common models used to investigate the binding behaviours of the molecularly imprinted polymers are Langmuir, Bi-Langmuir and Freundlich isotherms (Table S1) [23]. The binding isotherms Langmuir and Freundlich were used to determine the binding

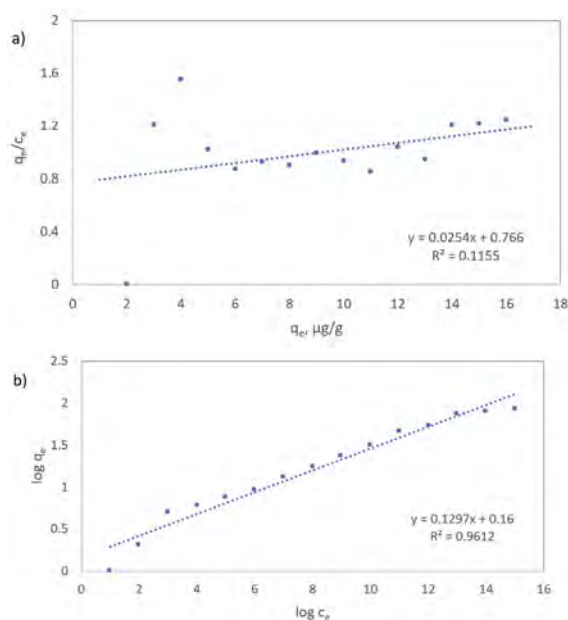


**Figure 7.** a) Langmuir and b) Freundlich isotherms for molecularly imprinted membranes (MIM).

efficiency of the membranes (Fig. 7). As it is apparent the binding behaviour of MIM fits Freundlich model with an  $R^2$  value of 0.96. Heterogeneous binding models are more suitable to evaluate the binding behaviours of imprinted polymers due to their heterogeneous nature of the recognition sites [23]. The heterogeneity index,  $n$  which varies in the range of 0-1 was determined as 0.13. The value of  $n$  shows an increase with an increase in homogeneity of the system and it equals to the 1 for an ideal homogeneous system [24]. As can be noticed the MIM prepared by conventional free radical polymerization method has a heterogeneous nature due to the polymerization method [25].

### Kinetics of adsorption of penicillin G imprinted membranes

The kinetic evaluation of the adsorption is important as the type of the adsorption gives information about the nature of the binding. The adsorption rate-limiting step can be managed by diffusing the template to the adsorbent surface, or by the chemical interaction between the template and the adsorbent. Generally, the binding in molecularly imprinted polymers is controlled by chemical affinity between template and host. The kinetics of adsorption was evaluated by using Lagergren's first-order rate equation and pseudo-second-order rate equation (Table S2). The kinetic behaviour of the prepared membranes matches the pseudo-second-order kinetic model with an  $R^2$  value of 0.99 (Fig. 8), which suggests that the rate-determining step of penicillin G adsorption is regulated by the chemical affinity of penicillin G to MIM [16, 26].

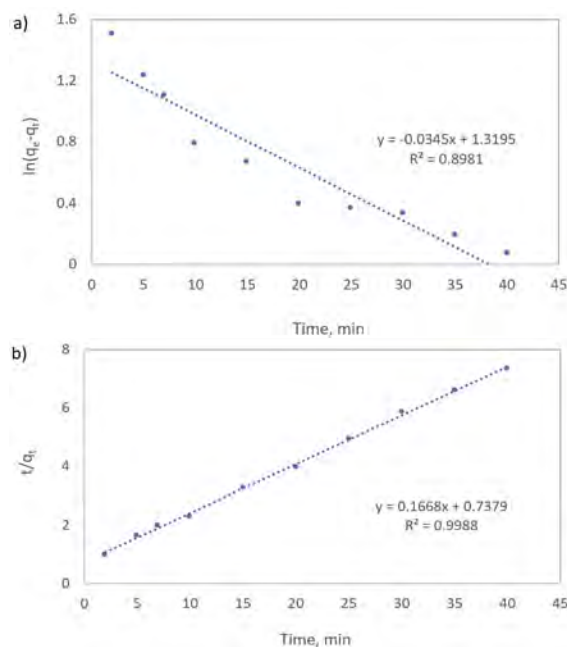


**Figure 8.** Curves of (a) first-order and (b) pseudo-second-order kinetic models (incubation concentration of penicillin G was 3 ppm,  $n=3$ ).

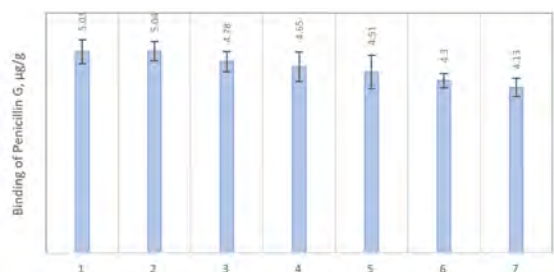


**Figure 9.** Binding of penicillin G which was determined by using the same imprinted membrane after each adsorption for seven cycles (incubation concentration of penicillin G= 3 ppm, incubation time= 20 min, n= 3).

### Reusability of the membranes

The reusability of the membranes was investigated by repeating the adsorption-desorption cycle 7 times (Fig. 9). After each binding step, the removal of the template molecule was achieved by solvent extraction which was described previously. The performances of the imprinted membranes did not show a significant decrease upon repeated use. The crosslinked imprinted membranes can be used for many times without a significant binding capability loss.

### The binding capability of imprinted and non-imprinted membranes

As is evident from Fig. 10 the adsorption capacity of MIM is greater than the binding capacity of NIM. The morphological differences and the data about the size of the recognition sites support the higher binding capability of the MIM. The roughness of the surfaces of the MIM enhances the chemical interaction between penicillin G and the imprinted membranes. It can be assumed that the rise in surface area due to the roughness makes the availability of the binding sites easier [18]. Non-imprinted membranes (NIM) were produced without the addition of the template molecule using the same procedure. The absence of a template molecule produces smoother surface due to the lack of any specific chemical interaction [16].

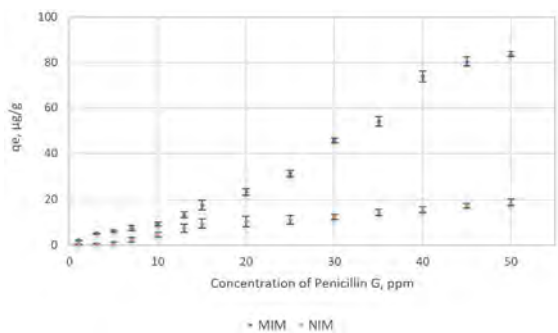


**Figure 10.** The adsorption capacity of imprinted (MIM) and non-imprinted membranes (NIM) (n= 3, incubation time 20 min).

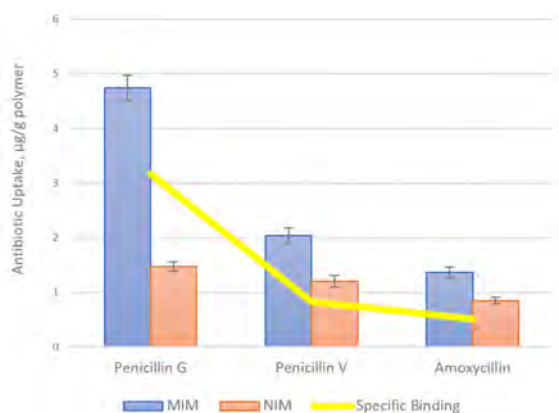


**Figure 11.** Selectivity of penicillin G imprinted (MIM) and non-imprinted membranes (NIM) against penicillin V and amoxicillin (concentration of each antibiotic= 3ppm, incubation time=20 min, n=3).

It still has a porous structure because of the presence of a porogen solvent.

### Specific selectivity of membranes

Specific selectivity of the membranes was investigated by using structurally similar  $\beta$ -lactam antibiotics such as amoxicillin and penicillin V (Fig. 11). The concentration of the antibiotics was kept as 3 ppm for 20 min incubation. The specific binding (SB) value is a criterion to investigate the specific selectivity of the imprinted polymers against the target molecule. SB is determined by subtracting of the binding onto non-imprinted polymers due to the non-specific interactions from the binding of imprinted polymers. Thus, the obtained binding data is the result of the specific interaction between the template and adsorbent [27]. SB of the MIM was determined as 3.27  $\mu\text{g/g}$  polymer for penicillin G while this value obtained as 0.83 and 0.51  $\mu\text{g/g}$  polymer for penicillin V and amoxicillin, respectively. Because of the complete complement of the binding sites in terms of shape, size and unique interaction between the template molecule penicillin G and the imprinted membrane, the highest SB value was obtained for the template molecule [11].

The selectivity ( $k$ ) and relative selectivity coefficients ( $k'$ ) were determined by using equations summarized in Table S3. The selectivity coefficient ( $k$ ) is used to investigate the degree of selectivity of molecularly imprinted and non-imprinted polymers towards the target molecule. The selectivity of the MIM for penicillin G is 2.33 and 3.48 times higher than the selectivity towards penicillin V and amoxy-cillin, respectively (Table S4). The relative selectivity coefficients were determined as 1.38 and 1.46 for penicillin V and amoxicillin, respectively. The data prove that the specific selectivity of MIM is higher than the NIM as expected due to the formation of binding sites by templating of penicillin G.

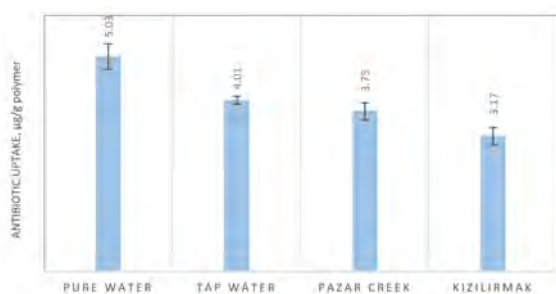


**Figure 12.** Binding performance of the imprinted membranes in real water samples.

### Investigation of the binding capacity in real samples

To analyze the binding capabilities of the imprinted membranes in real samples tap water and natural surface water samples from different regions were used. As it is apparent in Fig. 12 the binding capacities of the MIM decreases due to the complexity of the real samples [16]. The binding capacity of the MIM was determined as 4.01  $\mu\text{g}\cdot\text{g}^{-1}$  for tap water and  $\sim 3.50 \mu\text{g}\cdot\text{g}^{-1}$  for natural surface waters which contains 3 ppm spiked penicillin G, respectively. It is possible to say that the imprinted membranes can be useful to remove penicillin G from real water samples.

### CONCLUSION

Penicillin G imprinted membranes were produced by UV induced in-situ polymerization of methacrylic acid in the presence of a crosslinking agent. The detailed structural and physical characterization of the membranes was carried out using various methods of spectroscopy and microscopy. XPS was used to prove the existence of the template inside the imprinted membranes. The change in morphology of the membranes was investigated by SEM and AFM. The interaction of the template molecule and the network results in the roughness of the imprinted membrane surface. The size of the free volume holes of the imprinted membranes was investigated by PALS. The kinetic behaviour of the imprinted membranes supports the presence of the chemical affinity between penicillin G and the membranes. The binding capability of the membranes was investigated for real water samples. The binding capacity was determined as approximately 3.50  $\mu\text{g}\cdot\text{g}^{-1}$ . As a result, the prepared membranes can be useful to remove penicillin G from natural surface water samples. The use of the molecularly imprinted membranes as a filtration material for the selective removal of penicillin G from environmental water sources can be considered as the main novelty of this work.

### ACKNOWLEDGEMENT

I would like to thank Prof. Dr. Olgun Güven for his continuing support and encouragement throughout my studies.

### References

- Junker T, Alexy R, Knacker T, Kümmerer K. Biodegradability of 14C-Labeled antibiotics in a modified laboratory scale sewage treatment plant at environmentally relevant concentrations. *Environmental Science & Technology* 40 (2006) 318-324.
- Giger W, Alder AC, Golet E, Kohler HPE, McArdell CS, Molnar E, Siegrist H, Suter MJF. Occurrence and fate of antibiotics as trace contaminants in wastewaters, sewage sludges, and surface waters. *Chimia* 57 (2003) 485-491.
- Kolpin D, Furlong ET, Meyer MT, Thurman EM, Zaugg SD, Barber LB, Buxton HT. Pharmaceuticals, hormones, and other organic waste water contaminants in U.S. streams, 1999-2000: A national reconnaissance. *Environmental Science & Technology* 36 (2002) 1202-1211.
- Golet EM, Strehler A, Alder AC, Giger W. Determination of fluoroquinolone antibacterial agents in sewage sludge and sludge-treated soil using accelerated solvent extraction followed by solid-phase extraction. *Analytical Chemistry* 74 (2002) 5455-5462.
- Palmer AC, Angelino E, Kishony R. Chemical decay of an antibiotic inverts selection for resistance. *Nature Chemical Biology* 6 (2010) 105-107.
- Karaseva N, Ermolaeva T, Mizaikoff B. Piezoelectric sensors using molecularly imprinted nanospheres for the detection of antibiotics. *Sensors and Actuators B: Chemical* 225 (2016) 199-208.
- Jalili R, Khataee A, Rashidi M-R, Razmjou A. Detection of penicillin G residues in milk based on dual-emission carbon dots and molecularly imprinted polymers. *Food Chemistry* 314 (2020) 126172.
- Kwon D, Yoo H, Lee H, Jeon S. Colorimetric detection of penicillin G in milk using antibody-functionalized dendritic platinum nanoparticles. *Sensors and Actuators B* 255 (2018) 552-556.
- Weber P, Riegger BR, Niedergall K, Tovar GEM, Bach M, Gauglitz G. Nano-MIP based sensor for penicillin G: Sensitive layer and analytical validation. *Sensors and Actuators B* 267 (2018) 26-33.
- Pupin RR, Foguel MV, Gonçalves LM, Sotomayor MPT, Magnetic molecularly imprinted polymers obtained by photopolymerization for selective recognition of penicillin G. *Journal applied polymer science* 137 (2020) 48496.
- Söylemez MA, Güven O. Preparation and detailed structural characterization of Penicillin G imprinted polymers by PALS and XPS. *Radiation Physics and Chemistry* 159 (2019) 174-180.
- Kansy J. Microcomputer program for analysis of positron annihilation lifetime spectra. *Nuclear Instruments and Methods in Physics Research Section A* 374 (1996) 235-244.
- Li H, Hu J, Wang C, Wang X. Removal of amoxicillin in aqueous solution by a novel chicken feather carbon: kinetic and equilibrium studies. *Water Air Soil Pollution* 228 (2017) 201.
- Tsai H-J, Su Y-Y, Tseng C-C, Hsu W-K. Selective modification of aligned carbon nanotubes by N<sub>2</sub> plasma and their diode behavior. *RSC Advance* 8 (2018) 10680-10685.
- Söylemez MA, Güven O. Radiation induced in-situ synthesis of

- membranes for removal of 2,4-dichlorophenoxy acetic acid from real water samples. *Radiation Physics and Chemistry* 171 (2020) 108708.
16. Mkhize DS, Nyoni H, Quinn LP, Mamba BB, Msagati TA. Molecularly imprinted membranes (MIMs) for selective removal of polychlorinated biphenyls (PCBs) in environmental waters: fabrication and characterization. *Environmental Science and Pollution Research* 24 (2017) 11694–11707.
  17. Yoshimi Y, Namayama S, Piletsky SA. Changes in the porosity and permeability of a molecularly imprinted membrane induced by the adsorption of a trace quantity of template. *The Open Analytical Chemistry Journal* 7 (2013) 22–29.
  18. Li FY, Li Y, Chung TS, Chen H, Jean YC, Kawi S. Development and positron annihilation spectroscopy (PAS) characterization of polyamide imide (PAI)–polyethersulfone (PES) based defect-free dual-layer hollow fiber membranes with an ultrathin dense-selective layer for gas separation. *Journal of Membrane Science* 378 (2011) 541.
  19. Awad S, Chen HM, Grady BP, Paul A, Ford WT, Lee LJ, Jean YC. Positron annihilation spectroscopy of polystyrene filled with carbon nanomaterials. *Macromolecules* 45 (2012) 933.
  20. *Positron Annihilation in Semiconductors: Defect Studies*, Reinhard Krause-Rehberg, Hartmut S. Leipner, page: 1-2, C Springer-Verlag Berlin Heidelberg, 1999, Printed in Germany.
  21. Wu X-B, Fan K-Q, Wang Q-H, Yang K-Q. C-terminus mutations of *Acremonium chrysogenum* deacetoxy/deacetylcephalosporin C synthase with improved activity toward penicillin analogs. *FEMS Microbiology Letters* 246 (2005) 103–110.
  22. Umpleby RJ, Baxter SC, Chen Y, Shah RN, Shimizu KD. Characterization of molecularly imprinted polymers with the Langmuir-Freundlich isotherm. *Analytical Chemistry* 73 (2001) 4584–4591.
  23. Rampey AM, Umpleby II RJ, Rushton GT, Iseman JC, Shah RN, Shimizu KD. Characterization of the imprint effect and the influence of imprinting conditions on affinity, capacity, and heterogeneity in molecularly imprinted polymers using the Freundlich isotherm-affinity distributions analysis. *Analytical Chemistry* 76 (2004) 1123–1133.
  24. Söylemez MA, Barsbay M, Güven O. Preparation of well-defined erythromycin imprinted non-woven fabrics via radiation-induced RAFT-mediated grafting. *Radiation Physics and Chemistry* 142 (2018) 77–81.
  25. Sajini T, Gigimol MG, Mathew B. Kinetic and thermodynamic studies of molecularly imprinted polymers for the selective adsorption and specific enantiomeric recognition of D-mandelic acid. *Journal of Polymer Research* 26 (2019) 88.
  26. Lakshmi D, Akbulut M, Ivanova-Mitseva PK, Whitcombe MJ, Piletska EV, Karim K, Güven O, Piletsky SA. Computational design and preparation of MIPs for atrazine recognition on a conjugated polymercoated microtitre plate. *Industrial & Engineering Chemistry Research* 52 (2013) 13910–13916.
  27. Ansell RJ, Mosbach K. Magnetic molecularly imprinted polymer beads for drug radioligand binding assay. *Analyst* 123 (1998) 1611–1616.

## APPENDIX

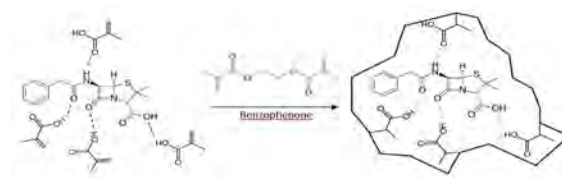


**Figure S1.** Synthesis of penicillin G imprinted polymers by employing methacrylic acid and ethylene glycol dimethacrylate as functional monomer and crosslinking agent, respectively.

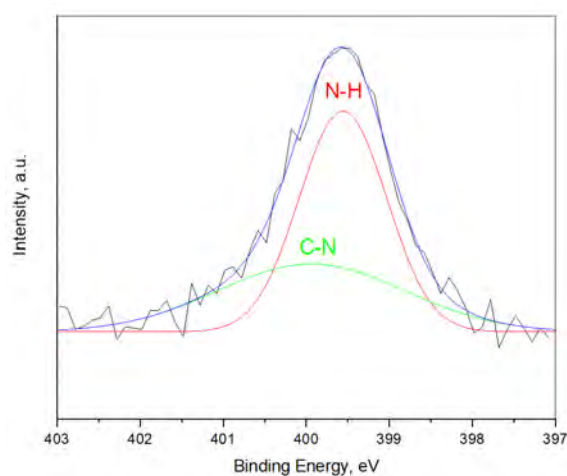


**Figure S2.** N1s spectrum of penicillin G imprinted membrane (MIM).

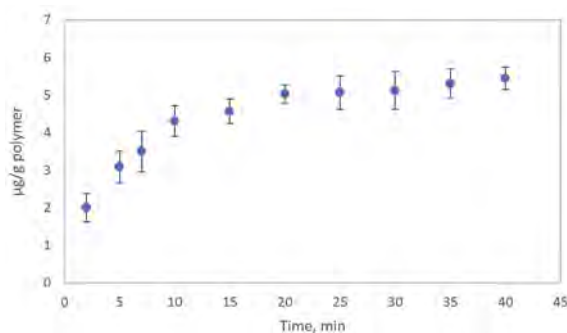


**Figure S3.** The binding capacity of the penicillin G imprinted membranes vs time.



**Table S1.** Adsorption isotherm models and related parameters.

Isotherm Model	Equation	Parameter
Langmuir	$q_e = \frac{NKc_e}{1 + Kc_e}$	$q_e$ , bound concentration of analyte on imprinted membrane $c_e$ , free concentration of analyte in solution $N$ , number of binding sites $K$ , binding constant
Scatchard Equation	$\frac{q_e}{c_e} = KN - Kq_e$	
Freundlich	$q_e = k_f c_e^n$	$k_f$ , adsorption constant $n$ , heterogeneity index

Lagergren's first-order rate equation and pseudo second-order rate equation [1] were employed to evaluate the kinetics of the binding by using the equations which summarized in Table S2. The binding capacity of the membranes changes with time as apparent in Fig. S3.

**Table S2.** Kinetic models and related parameters.

Kinetic Model	Equation	Parameter
Pseudo-First Order Kinetic Model	$\ln(q_e - q_t) = \ln(q_e) - k_1 t$	$q_e$ , amount of the analyte adsorbed at equilibrium $q_t$ , amount of the analyte adsorbed at time $t$ $t$ , time
Pseudo-Second Order Kinetic Model	$\frac{t}{q_t} = \left( \frac{1}{k_2 q_e^2} \right) + \left( \frac{1}{q_e} \right) t$	$k_1$ , pseudo-first order rate constant $k_2$ , pseudo-second order rate constant

Periasamy K, Namasvayam C. Process development for removal and recovery of cadmium from waste water by a low cost adsorbent: adsorption rate and equilibrium studies. *Ind. Eng. Chem. Res.* 1994, 33, 317–320.

**Table S3.** Equations and related parameters for dissociation constant ( $K_d$ ), selectivity ( $k$ ) and relative selectivity coefficient ( $k'$ ).

	Equation	Parameter
Dissociation Constant ( $K_d$ )	$K_d = \frac{(C_0 - C_f)}{C_f} x \frac{V}{m}$	$C_0$ Initial concentration of dye $C_f$ Final concentration of dye $V$ volume of the solution $M$ mass of the dry polymer
Selectivity Coefficient ( $k$ )	$k = \frac{K_{d\text{Penicillin G}}}{K_{d\text{Antibiotic}}}$	$k_{MIM}$ Selectivity coefficient of imprinted membrane $k_{NIM}$ Selectivity coefficient of non-imprinted membrane
Relative Selectivity Coefficient ( $k'$ )	$k' = \frac{k_{MIM}}{k_{NIM}}$	

**Table S4.** Dissociation constant ( $K_d$ ) and selectivity ( $k$ ) and relative selectivity coefficient ( $k'$ ).

	$K_{d,MIM}$	$K_{d,NIM}$	$k_{MIM}$	$k_{NIM}$	$k'$
Penicillin G	4.75	2.04	-	-	-
Penicillin V	2.04	1.20	2.33	1.69	1.38
Amoxicillin	1.36	0.85	3.48	2.39	1.46



# Boron Doped TiO<sub>2</sub> For The Photodegradation of 4-nitrophenol: Optimization of The Doping Parameters

Nazli Turkten<sup>1</sup>, Dila Kaya<sup>2</sup> and Zekiye Cinar<sup>3</sup>

<sup>1</sup>Kirsehir Ahi Evran University, Department of Chemistry, Kirsehir, Turkey

<sup>2</sup>Istanbul Medeniyet University, Department of Chemistry, Istanbul, Turkey

<sup>3</sup>Yildiz Technical University, Department of Chemistry, Istanbul, Turkey

## ABSTRACT

In this work we prepared boron doped TiO<sub>2</sub> (B-TiO<sub>2</sub>) photocatalysts and evaluated their photocatalytic activity for the degradation of our model organic pollutant, 4-nitrophenol (4-NP). The photocatalysts were prepared using wet impregnation method with different calcination times, calcination temperatures and dopant amounts in order to determine the optimum parameters. The degradation of the pollutant was carried out in a specially designed degradation chamber and characterized by UV-Vis spectrophotometry. The degradation kinetics were evaluated with pseudo-first order kinetics by comparing rate constants and half-lives of various photocatalytic reactions. It was found that the highest removal rate was obtained for 0.50 % boron doping with calcination at 450°C for 3 hours. The results showed that TiO<sub>2</sub> could be doped with boron, which is in abundance in our country, and used for the photocatalytic degradation of a toxic pollutant in water. The promising results for the organic matter removal could pave the way for further studies of environmental applications.

### Keywords:

Boron doped TiO<sub>2</sub>; Photocatalysis; 4-Nitrophenol; Pseudo first order kinetics; Doping parameters.

## INTRODUCTION

With diminishing resources for drinkable water in the world, wastewater treatment is more relevant than ever today. There are a number of physical, chemical, electrochemical and biological treatment methods [1-5] to remove harmful pollutants from aqueous systems. One of these methods is photocatalysis which is one of the advanced oxidation processes (AOPs) and basically includes the use of a photocatalyst for the mineralization of the pollutant into harmless small molecules such as CO<sub>2</sub> and H<sub>2</sub>O [6, 7]. This is made possible by oxidation with reactive oxidizing radicals produced from the combined use of a photocatalyst and an appropriate light source.

Heterogeneous photocatalysis is an economically feasible choice among AOPs since it has low operational costs and it is possible to work at ambient conditions without the need of other chemicals [8]. The most widely researched and utilized photocatalyst is TiO<sub>2</sub> which is a semiconductor with a band gap energy of approximately 3.2 eV [9, 10]. Due to this band gap energy, photocatalytic degradation using TiO<sub>2</sub> is performed under ultraviolet (UV) light which has the corresponding energy to initiate the excitation and transfer of an electron from the valence band to the conduction band

of TiO<sub>2</sub>, leaving behind a positively charged hole. The formation of these electron-hole (e<sup>-</sup> / h<sup>+</sup>) pairs leads to the subsequent oxidation of adsorbed organic matter on TiO<sub>2</sub> surface through the generation of reactive oxidizing species such as HO<sub>2</sub>•, HO• and O<sub>2</sub>•<sup>-</sup> [11, 12].

There is a variety of approaches and strategies such as surface modification [13, 14], doping with another element [15, 16] or synthesizing composite materials [17, 18] to enhance the activity of TiO<sub>2</sub> under solar light or to obtain a more powerful photocatalyst. We have found through our previous research that doping with metals [19, 20], non-metals [21] or co-doping [16, 22] could influence the photocatalytic activity of TiO<sub>2</sub> for the degradation of a variety of pollutants. In this work, we have used boron as the dopant and obtained B-TiO<sub>2</sub> which has previously been utilized as a catalyst [23-25]. It is known that doping with transition metals narrows the band-gap of TiO<sub>2</sub>, making it more efficient under solar light and reduces the recombination rate of electron-hole (e<sup>-</sup> / h<sup>+</sup>) pairs [26].

Boron deposits in Turkey are estimated to be 948 million tons according to 2017 report of Turkish National Boron Research Institute, which constitutes 73% of

### Article History:

Received: 2020/09/01

Accepted: 2020/11/08

Online: 2020/12/31

Correspondence to: Dila Kaya, Istanbul Medeniyet University, Chemistry, 34700, Istanbul, Turkey  
E-Mail: dila.kaya@medeniyet.edu.tr  
Phone: +90 216 280 33 33

the world's boron reserves [27]. Because of its natural abundance in various mineral forms in Turkey, we chose boron as the dopant. We have used boric acid ( $H_3BO_3$ ) as the boron source for doping. Boric acid also finds use in a myriad of areas from glass industry to detergents, nuclear reactors, and medicine.

Phenols and their derivatives are pollutants that are known to cause toxicity in wastewaters. Especially nitrophenols that are highly toxic are released in water as effluents of numerous industries [28]. One of these compounds is 4-nitrophenol (4-NP) which has a maximum allowed concentration of 20 ppb in water [6]. We have chosen 4-NP as the pollutant to be studied because of its environmental relevance and toxicity.

In this work, we prepared B-doped  $TiO_2$  photocatalysts by altering the experimental conditions. Successful doping was shown by SEM-EDX measurements. The photocatalytic activity of the catalysts were determined from the heterogeneous photocatalytic degradation of 4-NP. We have investigated the effects of calcination time, calcination temperature and dopant amount in order to find the most promising photocatalyst in terms of activity. We used pseudo-first order kinetic model to obtain and compared rate constant values of the photocatalytic reactions. We also studied the removal percentages of the pollutant for assessing the photocatalytic efficiencies of the newly prepared B- $TiO_2$  photocatalysts. We compared our results with the photocatalytic removal of 4-NP by bare  $TiO_2$ .

## MATERIAL AND METHODS

We used Evonik P25  $TiO_2$  as the precursor to be doped. Evonik P25 is a mixture of anatase (79%) and rutile phases (21%). The doping procedure was achieved using the well-established wet impregnation method. Boric acid ( $H_3BO_3$ ) was used as the dopant source. It was obtained from Merck and used without further purification. All the solutions were prepared with distilled water.

### Preparation of Doped Photocatalysts

Boron doped photocatalysts were obtained via wet-impregnation method where  $TiO_2$  is impregnated with the dopant solution, which in our case was boric acid. Briefly, we mixed 10 g  $TiO_2$  with 15 mL aqueous boric acid solution at different concentrations and stirred at room temperature for 1 hour. Dopant concentration was varied between 0.25 – 1.00% wt. Obtained photocatalysts were then washed with distilled water and dried for 24 hours at 373 K. After the drying process, the samples were calcined at 350, 450 and 550°C for predetermined amounts of time. In order to achieve a narrow size distribution

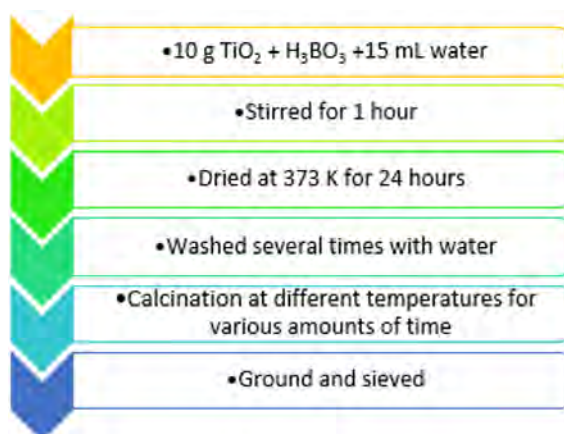


Figure 1. Preparation steps for the B-doped photocatalysts

of the particles, the calcined photocatalysts were ground and sieved from a 32 Micron sieve. The complete preparation process is summarized in Figure 1.

The abbreviations for the obtained photocatalysts stand for their preparation conditions. For example, 0.25-450-3 B- $TiO_2$  stands for the photocatalyst that has 0.25% wt. boron and was calcined at 450°C for 3 hours. All photocatalysts were named accordingly and presented in Table 1.

Table 1. RBoron Dose(% wt.), Calcination Times and Temperatures for the Preparation of Doped Photocatalysts.

Photocatalyst	Boron Dose (%wt.), Calcination Temperature and Time
0.25-B-450-3	0.25% B, 450°C, 3hr
0.50-B-450-3	0.50% B, 450°C, 3hr
0.75-B-450-3	0.75% B, 450°C, 3hr
1.00-B-450-3	1.00% B, 450°C, 3hr
0.50-B-450-1	0.50% B, 450°C, 1hr
0.50-B-450-5	0.50% B, 450°C, 5hr
0.50-B-350-1	0.50% B, 350°C, 1hr
0.50-B-350-3	0.50% B, 350°C, 3hr
0.50-B-350-5	0.50% B, 350°C, 5hr
0.50-B-550-1	0.50% B, 550°C, 1hr
0.50-B-550-3	0.50% B, 550°C, 3hr
0.50-B-550-5	0.50% B, 550°C, 5hr

### Characterization of Photocatalysts

In order to show that the wet impregnation of  $TiO_2$  with boron was indeed achieved successfully, we have used scanning electron microscopy with energy dispersive X-Ray analysis (SEM-EDX). The analysis was carried on a FEI-Philips XL30 instrument equipped with EDAX unit operating at 5 kV. Photocatalyst powders were supported on carbon tape prior to analysis.

## Photocatalytic Degradation Experiments

In order to assess the photocatalytic capabilities of the B-TiO<sub>2</sub> samples, we have investigated the degradation reaction of 4-NP under UV-A light in a specially designed reactor. The reactions were carried out in a double-jacketed pyrex photoreactor. Five 8-watt black fluorescent lights were used as the light source. The reactor was connected to a water bath to utilize constant temperature at 25°C. 600 mL solution containing 4-NP ( $1.0 \times 10^{-4}$  mol/L) with 0.2 g/100 mL B-TiO<sub>2</sub> photocatalyst was suspended in an ultrasonic bath for 30 minutes in dark in order to reach adsorption equilibrium. The solution was then introduced to the photocatalytic reactor and mechanically stirred through the reaction. The photocatalytic experiments were carried out at the natural pH of the solutions without pH adjustment. 10 mL samples were collected at predetermined time intervals and were immediately filtered through 0.45 μm Millipore HA (cellulose acetate) filters to separate TiO<sub>2</sub> from the solution. Absorbance values of the samples at λ = 317 nm were determined with a Perkin Elmer LS 55 UV-Visible spectrophotometer, and the concentrations of the solutions were calculated from calibration curves.

Photocatalytic efficiencies were compared using removal percentages of 4-NP with B-TiO<sub>2</sub> photocatalysts. These were calculated from Eq.1 where C<sub>0</sub> is the initial 4-NP concentration and C is 4-NP concentration at time t.

$$\text{Removal \%} = \left( \frac{C_0 - C}{C_0} \right) \times 100 \quad (1)$$

Experiments in identical conditions were also carried out for bare Evonik P25 TiO<sub>2</sub> for comparison purposes.

### Kinetic Calculations

The degradation was estimated to follow pseudo-first order kinetics as was the case in our previous works [16, 29]. The degradation rate constant was obtained from Eq. 2 where C<sub>0</sub> is the initial concentration (mol/L), C is the concentration (mol/L) after time (t) (mins) of the degradation reaction, and k is the first-order rate constant:

$$\ln \left( \frac{C}{C_0} \right) = kt \quad (2)$$

## RESULTS AND DISCUSSION

### Effect of Dopant Amount

Photocatalysts were prepared using different amounts of dopant and their efficiencies on 4-NP degradation were investigated. With this purpose, 0.25, 0.50, 0.75 and 1.00

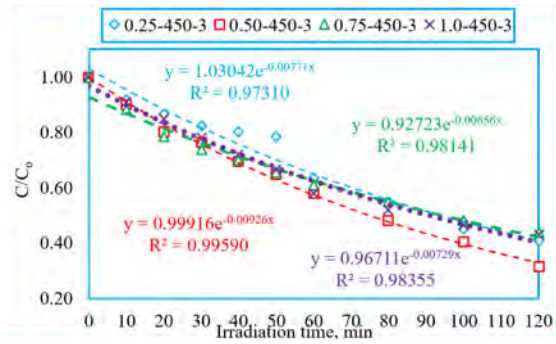


Figure 2. PC/C<sub>0</sub> – t plots for photocatalysts with different dopant amounts

% wt. boric acid was used as dopant and 3 hours of calcination at 450°C was performed. Degradation reaction was continued for 120 mins and C/C<sub>0</sub> values were plotted against time in Fig.2.

Kinetic data was modeled by pseudo first-order reaction kinetics and rate constants (k, min<sup>-1</sup>), as well as half-lives (t<sub>1/2</sub>, min) were calculated from Fig. 2 using Eq. 2 and listed in Table 2. Removal % values were calculated according to Eq. 1 and also presented in Table 2.

It can be seen that the photocatalytic degradation rate of 4-NP increased and then decreased and it was found that among the studied range, 0.50 % wt. showed the best result in terms of degradation with 68.47% removal. Photocatalytic degradation rate constant was also found to be highest for 0.50-450-3 which consequently yielded the lowest half-life. A similar behavior was observed for selenium doping of TiO<sub>2</sub> by Gurkan et. al. [30] which was attributed to two conflicting effects of doping. Enhanced photocatalytic activity is caused by the energy levels generated by the dopant ion, which acts as an electron or a hole trap. Also, the reaction rate is directly proportional to the absorption of photons, which again is increased by doping. But if the dopant concentration is high (i.e. higher than 0.50% wt.), increase in the recombination rate of the charge carriers is observed because of the decreased average distance between trap sites. We continued our experiments with 0.50% wt. dopant as the optimum amount since it provided the highest photocatalytic activity of the studied photocatalysts.

Table 2. Effect of dopant amount of B- TiO<sub>2</sub> photocatalysts for the degradation of 4-NP

Photocatalyst	Removal (%)	k (10 <sup>-3</sup> .min <sup>-1</sup> )	t <sub>1/2</sub> (min)
0.25-450-3	59.02	7.71	89.90
0.50-450-3	68.47	9.26	74.85
0.75-450-3	56.13	6.56	105.66
1.0-450-3	56.99	7.29	95.08

## Effects of Calcination Time and Temperature

In order to investigate the effects of calcination properties on the photocatalytic activities of the photocatalysts, we used three different calcination times and three temperature values. Studied calcination times and temperatures were 1, 3 and 5 hours, and 350, 450 and 550°C, respectively. The removal % value for each photocatalyst was calculated and given in Fig. 3.



**Figure 3.** Removal % values for photocatalysts with different calcination times and temperatures.

When Fig. 3 is taken into account, we can conclude that highest removal percentages were obtained with photocatalysts prepared by 3 hours calcination time for every temperature value. This finding suggests that the optimum calcination time is 3 hours. For a better comparison, we also give the dependence of removal % values to calcination temperatures in Fig. 4.

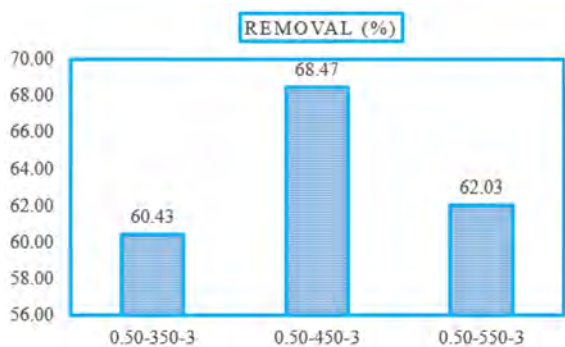


**Figure 4.** Dependence of removal % values for photocatalysts with different calcination temperatures.

We can conclude that out of the studied calcination temperature values, photocatalyst prepared at 450°C had the highest photocatalytic efficiency for the degradation of 4-NP. The exact ranking was 450°C > 550°C > 350°C with 68.47%, 62.03% and 60.43%, respectively.

The kinetic parameters of the photocatalytic degradation reactions were also calculated and given in Table 3 for each photocatalyst prepared by different calcination times and temperatures.

**Table 3.** Effect of dopant amount of B- TiO<sub>2</sub> photocatalysts for the degradation of 4-NP

Photocatalyst	Removal (%)	k (10 <sup>-3</sup> .min <sup>-1</sup> )	t <sub>1/2</sub> (min)
0.50-450-1	58.61	7.44	93.16
0.50-450-3	68.47	9.26	74.85
0.50-450-5	62.37	7.82	88.64
0.50-350-1	56.56	7.48	92.67
0.50-350-3	60.43	7.60	91.20
0.50-350-5	57.94	7.20	96.27
0.50-550-1	55.68	6.57	105.50
0.50-550-3	62.03	8.20	84.53
0.50-550-5	59.10	7.69	90.14

Table 3 shows that once again 0.50-450-3 yields the best photocatalysis efficiency for the degradation of 4-NP. The obtained rate constant for this photocatalyst was 9.26x10<sup>-3</sup> min<sup>-1</sup>, which is higher than all other prepared photocatalysts. t<sub>1/2</sub> value suggests that the degradation of half of the initial 4-NP concentration takes approximately 75 mins where it could be as high as 105.50 mins, which is the case for 0.50-550-1.

Taking into consideration the removal % values, rate constants and half-lives, we have concluded that calcination at 450°C for 3 hours yields the most efficient boron doped photocatalyst for the degradation of 4-NP. Calcination temperature and times could alter the crystallographic properties of TiO<sub>2</sub> [31]. It is known that with increased calcination times, the particle size also increases [32], which could be the reason for lower photocatalytic efficiency obtained for 550°C. This increase in size is attributed to the fact that calcination at high temperatures or for long periods cause the doped ions to be desorbed [22]. The increase in the photocatalytic activity when calcination temperature is increased from 350°C to 450°C, can be caused by the greater formation of hydroxyl radicals per unit surface area [33]. We could conclude that calcination at 450°C for three hours yields the highest radical formation and smallest crystal size than other studied values.

## Comparison of Doped and Bare TiO<sub>2</sub> Efficiencies

We have also compared the photocatalytic efficiencies of doped and bare TiO<sub>2</sub> under UV light in order to reveal the effect of doping with boron. The results of photodegradation of 4-NP with doped (0.50-450-3) and bare P25 TiO<sub>2</sub> under identical experimental conditions of photocatalyst amount, 4-NP concentration and irradiation time are given in Fig. 5.

When the removal rates were compared, 0.50-450-3 was found to be more efficient with a removal rate of 68.47

% than TiO<sub>2</sub> with 64.40 %. Kinetic parameters of reaction rate and half-life were also improved by doping. Rate constant and half-life values were 7.29 10<sup>-3</sup> min<sup>-1</sup> and 95.08 min for bare TiO<sub>2</sub> while they were found to be 7.82 10<sup>-3</sup> min<sup>-1</sup> and 88.64 min for 0.50-450-3. Although the difference may not seem significant, one should keep in mind that the main purpose of doping is to make TiO<sub>2</sub> more efficient under sunlight. The results of solar photocatalysis could show a more enhanced activity for B-doped samples since there is no direct correlation between the visible light activity and the photocatalytic activity [30]. But at this time, solar photodegradation is beyond the scope of our study and we could conclude that doping with boron enhances the photodegradation efficiency under UV light.

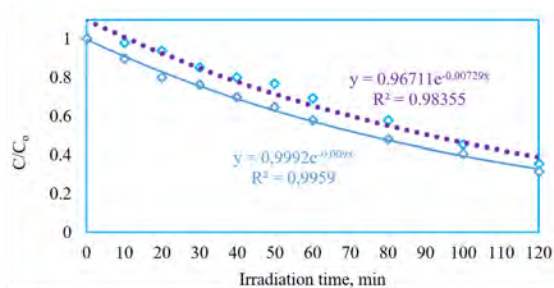


**Figure 5.**  $C/C_0 - t$  plots for bare (purple) and doped (blue) photocatalysts (P25 and 0.50-450-3, respectively.)

### Morphology of the Photocatalysts

In this section we have compared the morphologies of doped and bare photocatalysts and shown that doping has indeed taken place, using elemental analysis. SEM images and EDX spectra of B-doped TiO<sub>2</sub> (0.50-450-3) and bare TiO<sub>2</sub> are given in Fig. 6.

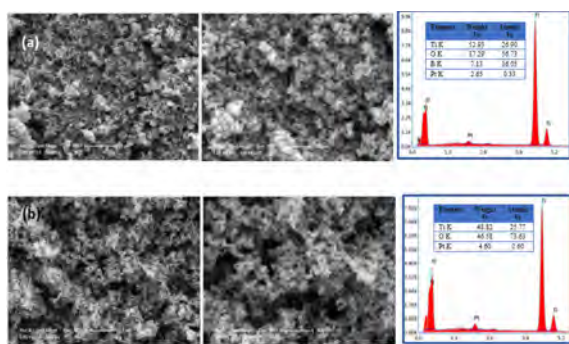


**Figure 6.** SEM images (left) x 50000, (right) x 100000 and elemental analysis (a) B-doped TiO<sub>2</sub>, (b) bare TiO<sub>2</sub>.

The SEM images of both B-doped TiO<sub>2</sub> (450-5-3 TiO<sub>2</sub>) and bare TiO<sub>2</sub> consist of almost spherical particles with an average particle size of ~20 nm. Because of the doping effect of TiO<sub>2</sub>, B-doped TiO<sub>2</sub> nanoparticles show a slight aggregation and the particle size is increased. The EDX spectra that are used to analyze the elemental composition of the photocatalysts demonstrate that the main components are Ti and O elements for both of the photocatalysts, as expected.

No impurities are observed in EDX spectra. The presence of boron in the EDX spectrum of B-doped TiO<sub>2</sub> confirms the doping procedure is successfully achieved.

### CONCLUSION

Here, we investigated the heterogeneous photocatalytic degradation reaction of 4-NP, using the newly prepared, boron doped TiO<sub>2</sub> photocatalysts. We prepared these photocatalysts using the well-established wet-impregnation technique and evaluated the effects of doping conditions on the photocatalytic activities of B-TiO<sub>2</sub> catalysts. The doping was proven by SEM-EDX results. Optimization of dopant amount, calcination times and temperatures were performed. The photocatalytic activity and performance of the B-TiO<sub>2</sub> photocatalysts were evaluated in terms of removal percentage of 4-NP and also rate constants obtained from pseudo-first order kinetics model. The optimum amount of dopant was found to be 0.50% wt which yielded the best result in terms of pollutant removal. Highest removal of 4-NP was 68.47 % which was achieved by calcination of the photocatalyst at 450°C, 3 hours. Photocatalysis was performed with both doped catalyst, 0.50-450-3 and bare TiO<sub>2</sub> in order to show the effect of doping. The results indicated that the 4-NP removal as well as kinetic parameters were improved after doping. The findings of this work showed that TiO<sub>2</sub> could be doped with boron and used for the photocatalytic degradation of a toxic pollutant in water. In a time when water treatment is more relevant than ever, we think this work could provide a valuable insight for preparing photocatalysts by doping with an element that is in abundance in Turkey. Solar efficiency of boron-doped photocatalysts could be studied in the future, which would be promising for commercial applications.

### References

1. Chen G. Electrochemical technologies in wastewater treatment. Separation and Purification Technology 38 (2004) 11-41.
2. Choi KJ, Kim SG, Kim CW, Kim SH. Effects of activated carbon types and service life on removal of endocrine disrupting chemicals: amitrol, nonylphenol, and bisphenol-A. Chemosphere 58 (2005) 1535-1545.
3. Ahn D-H, Chang W-S, Yoon T-I. Dyestuff wastewater treatment using chemical oxidation, physical adsorption and fixed bed biofilm process. Process biochemistry 34 (1999) 429-439.
4. Rice RG. Applications of ozone for industrial wastewater treatment—a review. Ozone: science & engineering 18 (1996) 477-515.
5. Korzeniewska E, Harnisz M. Relationship between modification of activated sludge wastewater treatment and changes in antibiotic resistance of bacteria. Science of the Total Environment 639 (2018) 304-315.
6. San N, Hatipoğlu A, Koçtürk G, Çınar Z. Photocatalytic degradation of 4-nitrophenol in aqueous TiO<sub>2</sub> suspensions: Theoretical prediction of the intermediates. Journal of Photochemistry and

- Photobiology A: Chemistry 146 (2002) 189-197.
7. Jenny Schneider DB, Jinhua Ye, Gianluca Li Puma, Dionysios D Dionysiou, Photocatalysis: Fundamentals and Perspectives. 2016, London, UK: Royal Society of Chemistry.
  8. Pelaez M, Nolan NT, Pillai SC, Seery MK, Falaras P, Kontos AG, Dunlop PSM, Hamilton JWJ, Byrne JA, O'Shea K, Entezari MH, Dionysiou DD. A Review on the Visible Light Active Titanium Dioxide Photocatalysts for Environmental Applications. *Applied Catalysis B: Environmental* 125 (2012) 331-349.
  9. Nakata K, Fujishima A. TiO<sub>2</sub> photocatalysis: Design and applications. *Journal of Photochemistry and Photobiology C: Photochemistry Reviews* 13 (2012) 169-189.
  10. Henderson MA. A surface science perspective on TiO<sub>2</sub> photocatalysis. *Surface Science Reports* 66 (2011) 185-297.
  11. Etacheri V, Di Valentin C, Schneider J, Bahnemann D, Pillai SC. Visible-light activation of TiO<sub>2</sub> photocatalysts: Advances in theory and experiments. *Journal of Photochemistry and Photobiology C: Photochemistry Reviews* 25 (2015) 1-29.
  12. Bora LV, Mewada RK. Visible/solar light active photocatalysts for organic effluent treatment: Fundamentals, mechanisms and parametric review. *Renewable and Sustainable Energy Reviews* 76 (2017) 1393-1421.
  13. Kaya D, San N. Heterogeneous Photocatalytic Degradation of 4-Nitrophenol via TiO<sub>2</sub>, Surface-Modified with Salicylic Acid. *FRESENIUS ENVIRONMENTAL BULLETIN* 26 (2017) 4953-4962.
  14. Low J, Cheng B, Yu J. Surface modification and enhanced photocatalytic CO<sub>2</sub> reduction performance of TiO<sub>2</sub>: a review. *Applied Surface Science* 392 (2017) 658-686.
  15. Guayaquil-Sosa J, Serrano-Rosales B, Valadés-Pelayo P, De Lasa H. Photocatalytic hydrogen production using mesoporous TiO<sub>2</sub> doped with Pt. *Applied Catalysis B: Environmental* 211 (2017) 337-348.
  16. Birben NC, Uyguner-Demirel CS, Sen-Kavurmaci S, Gurkan YY, Turkten N, Cinar Z, Bekbolet M. Comparative evaluation of anion doped photocatalysts on the mineralization and decolorization of natural organic matter. *Catalysis Today* 240, Part A (2015) 125-131.
  17. Yüce E, Mert EH, Krajnc P, Parin FN, San N, Kaya D, Yıldırım H. Photocatalytic Activity of Titania/Polydicyclopentadiene PolyHIPE Composites. *Macromolecular Materials and Engineering* 302 (2017) 1700091.
  18. Li J, Liu Y, Li H, Chen C. Fabrication of g-C<sub>3</sub>N<sub>4</sub>/TiO<sub>2</sub> composite photocatalyst with extended absorption wavelength range and enhanced photocatalytic performance. *Journal of Photochemistry and Photobiology A: Chemistry* 317 (2016) 151-160.
  19. Birben NC, Uyguner-Demirel CS, Kavurmaci SS, Gürkan YY, Turkten N, Cinar Z, Bekbolet M. Application of Fe-doped TiO<sub>2</sub> specimens for the solar photocatalytic degradation of humic acid. *Catalysis Today* 281 (2017) 78-84.
  20. Turkten N, Cinar Z, Tomruk A, Bekbolet M. Copper-doped TiO<sub>2</sub> photocatalysts: application to drinking water by humic matter degradation. *Environmental science and pollution research international* (2019).
  21. Gurkan YY, Turkten N, Hatipoglu A, Cinar Z. Photocatalytic degradation of cefazolin over N-doped TiO<sub>2</sub> under UV and sunlight irradiation: Prediction of the reaction paths via conceptual DFT. *Chemical Engineering Journal* 184 (2012) 113-124.
  22. Gurkan Y, Kasapbasi E, Turkten N, Cinar Z. Influence of Se/N Codoping on the Structural, Optical, Electronic and Photocatalytic Properties of TiO<sub>2</sub>. *Molecules* 22 (2017) 414.
  23. Wang Y, Jia K, Pan Q, Xu Y, Liu Q, Cui G, Guo X, Sun X. Boron-doped TiO<sub>2</sub> for efficient electrocatalytic N<sub>2</sub> fixation to NH<sub>3</sub> at ambient conditions. *ACS Sustainable Chemistry & Engineering* 7 (2018) 117-122.
  24. Wang W-K, Chen J-J, Gao M, Huang Y-X, Zhang X, Yu H-Q. Photocatalytic degradation of atrazine by boron-doped TiO<sub>2</sub> with a tunable rutile/anatase ratio. *Applied Catalysis B: Environmental* 195 (2016) 69-76.
  25. Quiñones DH, Rey A, Álvarez PM, Beltrán FJ, Li Puma G. Boron doped TiO<sub>2</sub> catalysts for photocatalytic ozonation of aqueous mixtures of common pesticides: Diuron, o-phenylphenol, MCPA and terbuthylazine. *Applied Catalysis B: Environmental* 178 (2015) 74-81.
  26. Khan R, Kim SW, Kim T-J, Nam C-M. Comparative study of the photocatalytic performance of boron-iron Co-doped and boron-doped TiO<sub>2</sub> nanoparticles. *Materials Chemistry and Physics* 112 (2008) 167-172.
  27. <https://www.boren.gov.tr/pages/reserves/103>. [cited 2020 August].
  28. Ahmed S, Rasul MG, Martens WN, Brown R, Hashib MA. Heterogeneous Photocatalytic Degradation of Phenols in Wastewater: A Review on Current Status and Developments. *Desalination* 261 (2010) 3-18.
  29. San N, Hatipoglu A, Koçtürk G, Çınar Z. Prediction of primary intermediates and the photodegradation kinetics of 3-aminophenol in aqueous TiO<sub>2</sub> suspensions. *Journal of Photochemistry and Photobiology A: Chemistry* 139 (2001) 225-232.
  30. Gurkan YY, Kasapbasi E, Cinar Z. Enhanced solar photocatalytic activity of TiO<sub>2</sub> by selenium(IV) ion-doping: Characterization and DFT modeling of the surface. *Chemical Engineering Journal* 214 (2013) 34-44.
  31. Choi H, Antoniou MG, Pelaez M, de la Cruz AA, Shoemaker JA, Dionysiou DD. Mesoporous Nitrogen-Doped TiO<sub>2</sub> for the Photocatalytic Destruction of the Cyanobacterial Toxin Microcystin-LR under Visible Light Irradiation. *Environmental Science & Technology* 41 (2007) 7530-7535.
  32. Chen Y-F, Lee C-Y, Yeng M-Y, Chiu H-T. The effect of calcination temperature on the crystallinity of TiO<sub>2</sub> nanopowders. *Journal of Crystal Growth* 247 (2003) 363-370.
  33. Xiao Q, Ouyang L. Photocatalytic activity and hydroxyl radical formation of carbon-doped TiO<sub>2</sub> nanocrystalline: Effect of calcination temperature. *Chemical Engineering Journal* 148 (2009) 248-253.



# Preparation, Characterization and Evaluation of Some New Amides as Antimicrobial Agents

Sukriye Cakmak and Aysel Veyisoglu<sup>1</sup>

Sinop University, Department of Medical Services and Techniques, Sinop, Turkey

## ABSTRACT

The some new amide derivatives 1(a-c) and, 2d were synthesized by the two-step N-acylation of 4-nitroaniline or heterocyclic amine derivatives with acyl chlorides. All of the products were determined using <sup>13</sup>C NMR, <sup>1</sup>H NMR, FT-IR spectroscopies and elemental analysis. Antimicrobial activities of the molecules were evaluated against various bacterial and fungal species. The results show that the some new compounds exhibit good antibacterial and antifungal activities.

### Keywords:

Amides; Secondary amides; N-acylation, Antimicrobial activity; Characterization.

## INTRODUCTION

Amides are an important class of organic compounds in which a carbonyl group is connected to a nitrogen atom. These compounds and those similar possess various excellent biological activities including antibacterial, antifungal [1-6], antioxidant [7-11], insecticide [12], anticonvulsant, analgesic, and anti-tumor agents [13-17].

As is known, amide formation does not occur spontaneously at room temperature and for this reason, it is necessary to pre-activated the carboxylic acids such as acid chlorides. For this purpose, the corresponding amides were synthesized the pre-activation the carboxyl group using thionyl chloride and then, in the presence of triethylamine (TEA) the interaction of those activation products with amine derivatives. The obtained compounds were characterized using <sup>13</sup>C NMR, <sup>1</sup>H NMR, FT-IR spectroscopies and elemental analysis. Antimicrobial activities of the synthesized compounds were evaluated against various bacterial and fungal species. These target molecules were tested for their antibacterial and antifungal activities using serial dilution technique. As a result, compounds 1b and 2d showed good antibacterial and antifungal activities.

## MATERIAL AND METHODS

### Measurement and Reagent

All chemicals were purchased from Sigma-Aldrich, Merck or ABCR and directly used without further purification other than commercial thionyl chloride.

### Article History:

Received: 2020/10/20

Accepted: 2020/11/17

Online: 2020/12/31

**Correspondence to:** Sukriye Cakmak,  
Sinop University, Medical Services and  
Techniques, 57000, Sinop, Turkey  
E-Mail: scakmak@sinop.edu.tr Phone:  
+90 368 27157 57-Ext: 34 10 Fax: +90  
368 27157 58

It was twice distilled; colorless product of high purity was obtained (b.p. 77 °C/760 mmHg). Melting points were determined using Stuart SMP 30 apparatus. The FT-IR spectra were obtained on Bruker Vertex 80V spectrometer. The <sup>1</sup>H NMR and <sup>13</sup>C NMR spectra were recorded a Bruker/Biospin 400 MHz spectrometer instrument using CDCl<sub>3</sub> as solvent and TMS as internal standard. The elemental analyses were carried out on a Costech, ECS 4010 elemental analyser.

### Preparation of new amide compounds 1(a-c) and 2d

The newly amide compounds 1(a-c) and 2d were prepared as a result of the two-step reaction shown in Fig. 1. In the firstly step, activation step, the acid chloride intermediate was formed by the interaction of thionyl chloride and carboxylic acid by the procedure as previously described in the literature [18]. In the second step, the acylation step: Heterocyclic amine or 4-nitroaniline derivatives (12 mmol) was dissolved in THF (6 mL) and triethylamine (8 mmol) was added dropwise. Then, to mixture was added dropwise (14 mmol) of 3-acetoxy-2-methylbenzoyl chloride or 2-thiophene carbonyl chloride in 8 mL of THF at room temperature [19]. After this mixture was allowed to stir for 14 hours at room temperature, the resulting white salt precipitate was filtered and washed several times with water. The filtrate was then precipitated with water and the obtained the white crude product was recrystallized from acetonitrile.

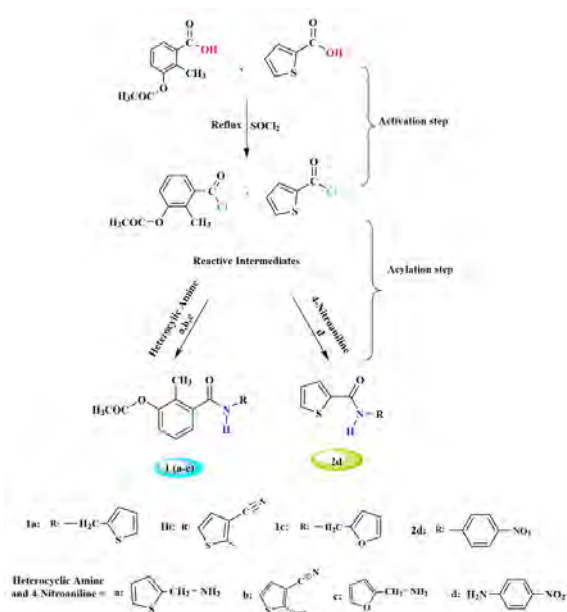


**Figure 1.** General synthesis of compounds 1(a-c) and 2d

### Antimicrobial activity

Four new synthesized molecules were exhibited antimicrobial activities against the following eight microorganisms including Gram-staining-positive (*Bacillus subtilis* ATCC 6633; *Staphylococcus aureus* ATCC 25923; *Enterococcus faecalis* ATCC 29212), Gram-staining-negative (*Escherichia coli* ATCC 25922; *Klebsiella pneumoniae* ATCC 70060; *Pseudomonas aeruginosa* ATCC 27853) bacteria and fungi (*Aspergillus niger* ATCC 16404; *Candida albicans* ATCC 1023). Antimicrobial activities were performed using the microdilution method (MIC) [20] by the broth microdilution method carried out in 96-well microplates. Synthesized compounds were dissolved in DMSO at the appropriate concentration. The cultures

**Table 2.** The results for elemental analysis of prepared compounds (1a-1c) and 2d

Compound	Calculated				Experimental			
	N %	C %	H %	S %	N %	C %	H %	S %
1a	4.84	62.22	5.18	11.06	4.74	62.71	5.06	10.75
1b	9.32	59.94	3.99	10.65	8.74	60.45	3.88	10.13
1c	5.12	65.87	5.49	-	5.01	66.07	4.87	-
2d	11.28	53.18	3.22	12.89	10.84	53.33	2.89	12.11

were obtained from nutrient broth for all the bacterial strains after 24 h of incubation at 28 °C. Fungi were maintained in nutrient broth after incubation for 24 h at 37 °C. Bacterial and fungi cells were homogenized in nutrient broth. The turbidity of bacterial and fungi suspensions was set at a concentration of approximately 106 cells/ml. Only inoculated broth was used as controls. 100 µL sus-

pension of each microorganism and 100 µL suspension of compound tested were added into the wells. The microplate with no growth of microorganism was recorded to represent the MIC enounced in µg/mL. Amoxicillin and Tetracycline were used as the reference standard for antibacterial activity while Ketoconazole was used as the reference standard for antifungal activity, the MIC value were showed in Table 5.

## RESULTS AND DISCUSSION

### Physical characteristics

The some physical, chemical properties, and elemental analysis results of the newly synthesized molecules are given in Tables 1 and 2.

**Table 1.** The physical, chemical properties of prepared molecules (1a-1c) and 2d

Code	Structure)	Melting point (°C)	Yield (%)
1a		123-126	62
1b		109-111	51
1c		96-98	58
2d		207-210	63

### IR Spectra

The infrared spectrum of compound 1a displayed a significant vibrational band at 3271 cm<sup>-1</sup> for the presence of a seconder amide. The absorption for an amide carbonyl (-NHC=O) was observed at 1637 cm<sup>-1</sup> while an absorption for the carbonyl of ester was observed at 1751 cm<sup>-1</sup>.

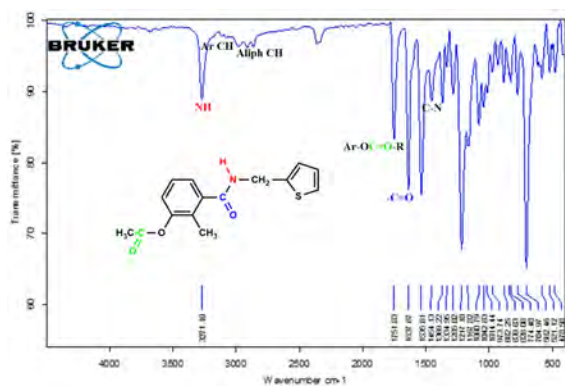


**Figure 2.** FT-IR spectrum of compound 1a

Due to resonance the aromatic ring with oxygen atom, the strong C=O stretching vibration of ester carbonyl is ( $\sim 1740\text{ cm}^{-1}$ ) higher than normal stretching vibration of ester carbonyl. The other remarkable band at around  $1454\text{ cm}^{-1}$  belongs to C-N stretching vibration as shown in Fig. 2. In addition, important IR absorptions of the synthesized molecules are given in the Table 3. These spectral data are consistent with similar structures given in the literature [21, 22].

### NMR Spectra

In the  $^1\text{H}$  NMR spectra of molecule 1a there are two singlets at 2.26 ppm (s, Ar- $\text{CH}_3$ ) and 2.34 ppm (s,  $-\text{OCOCH}_3$ ) belong to the methyl protons on the benzene ring and methyl protons bound to ester carbonyl respectively. The characteristic NH peak for amides was observed as a singlet at 6.27 ppm (s,  $-\text{NHC}=\text{O}$ ). The methylene protons in the structure of compound 1a interacted with the amide proton and were observed as a doublet at 4.79 ppm. The signals of the phenyl ring protons (H1-H3) appeared at between 7.25-6.97 ppm. Of phenyl ring protons, the H2 proton coupled to the H3 proton show a doublet and gives a triplet by coupling the H1 and the H3 as being 7.28 ppm. The signals of the thiophene protons resonated in slightly lower up-field compared to the phenyl protons. These thiophene protons, labeled as H4, H5, and H6, showed two doublets and a triple signals observed in the range of 7.11-6.95 ppm (Fig. 3). These values obtained are in

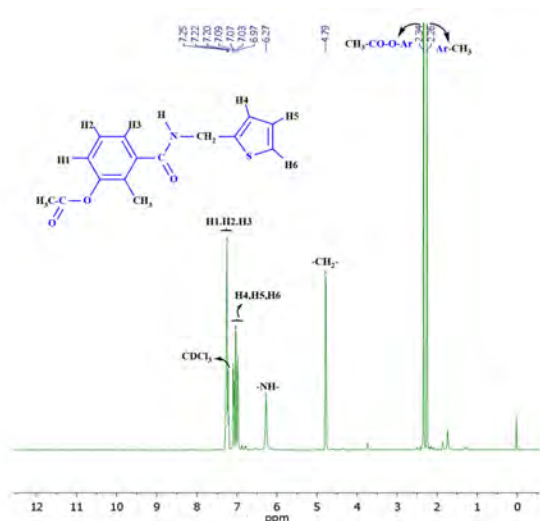


**Figure 3.**  $^1\text{H}$  NMR spectrum of compound 1a in  $\text{CDCl}_3$

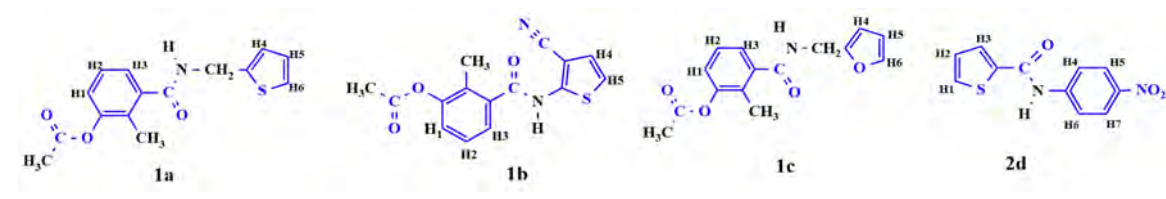
consistent with similar compounds in the literature [21]. In the Table 4 are illustrated the chemical shift values of the other compounds.

### $^{13}\text{C}$ NMR Spectra

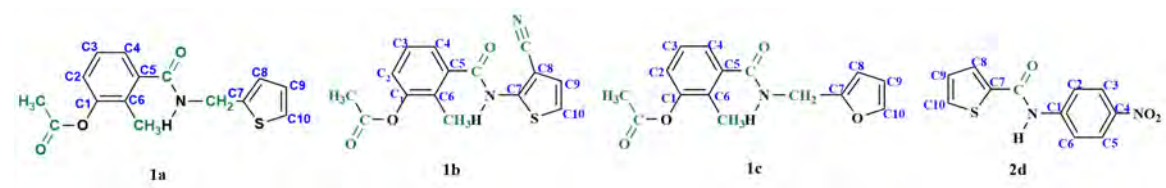
The  $^{13}\text{C}$  NMR spectrum of compound 1a recorded in  $\text{CDCl}_3$  showed 15 different carbon signals. Two of these signals belong to ester carbonyl carbon and amide carbonyl carbon, was observed at 169.3 ppm and 168.9 ppm, respectively. The phenyl ring carbons (C1-C6) were detected at 149.7, 124.4, 126.1, 123.8, 138.1 and 128.6 ppm respectively. The carbons (C7-C10) belonging to the thiophene ring were resonated at 140.5, 127.0, 126.6 and 125.4 ppm, respectively. While the methyl carbon atom attached to the ester carbonyl group was observed at 20.7 ppm, the other methyl carbon atom attached to the phenyl ring resonated at 12.9 ppm (Fig. 4) The methylene carbon atom ( $-\text{CH}_2-$ ) was observed at 38.7 ppm. These chemical shift values are compatible with the literature and confirm the formation of the target molecule [21]. The carbon chemical shifts values of other synthesized molecules are illustrated in the Table 5.

**Table 3.** Important IR bands of synthesis compounds ( $\text{cm}^{-1}$ )

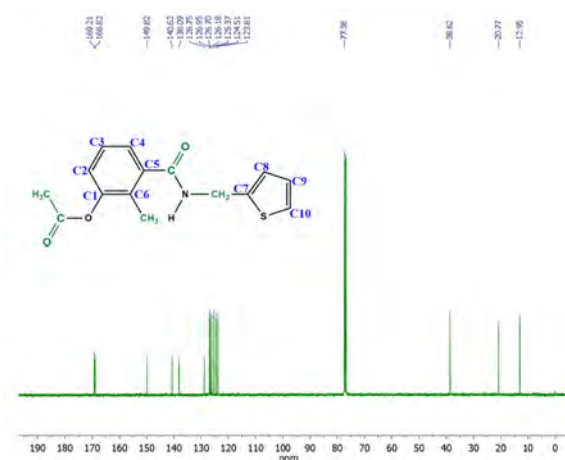
Comp.	-NH	Ar CH	Aliph CH	Amide C=O	Ester C=O	C-N	Ar-C≡N	Ar-NO <sub>2</sub>	
								N=O (Asym. Stretch)	N=O (Sym. Stretch)
1a	3271	3070-3040	2970-2845	1637	1751	1454	-	-	-
1b	3244	3113-3081	2981-2934	1755	1787	1457	2229	-	-
1c	3264	3075-3012	2978-2907	1644	1744	1441	-	-	-
2d	3358	3138-3106	-	1641	-	1412	-	1538 (Asym.) 1322 (Sym.)	852

**Table 4.**  $^1\text{H}$  NMR spectral values of the synthesized molecules ( $\delta$ , ppm, in  $\text{CDCl}_3$ )


Comp	H1	H2	H3	N-H	H4	H5	H6	H7	-CH2-	-COCH3	A r - CH3
1a	7.24-7.20 (d)	7.28-7.20 (t)	7.28-7.24 (d)	6.27 (s)	7.11-7.07 (d)	7.11-6.95 (t)	7.02-6.95 (d)	-	4.78-4.77 (d)	2.34 (s)	2.26 (s)
1b	7.30-7.28 (d)	7.36-7.31 (t)	7.38-7.36 (d)	8.92 (s)	7.95-7.93 (d)	7.96-7.94 (d)	-	-	-	2.52 (s)	2.35 (s)
1c	7.24-7.22 (d)	7.28-7.24 (t)	7.39-7.35 (d)	6.12 (s)	6.36-6.31 (d)	7.10-7.08 (d)	7.24-7.22 (d)	-	4.64-4.62 (d)	2.35 (s)	2.25 (s)
2d	7.45-7.43 (d)	7.28-7.20 (m)	8.29-8.27 (d)	7.90 (s)	7.67-7.65 (d)	7.86-7.84 (d)	7.77-7.76 (d)	8.01-7.77 (d)	-	-	-

**Table 5.**  $^{13}\text{C}$  NMR spectral data for the synthesized compounds ( $\delta$ , ppm, in  $\text{CDCl}_3$ )


Comp	C1	C2	C3	C4	C5	C6	C=O - Ester	C=O - Amide	C7	C8	C9	C10	-CH2-	C O - CH3	A r - CH3	R
1a	149.7	124.4	126.1	123.8	138.1	128.6	169.3	168.2	140.5	126.6	127.0	125.4	38.7	20.7	12.9	-
1b	150.3	126.4	127.7	125.7	134.6	129.6	169.0	162.1	134.6	118.6	129.0	125.4	-	20.9	13.3	124.0
1c	150.8	124.5	126.7	123.7	138.1	128.7	169.2	168.8	149.8	110.5	107.6	142.3	36.8	20.7	12.9	-
2d	136.0	119.3	125.1	135.2	125.1	119.3	-	156.6	132.0	128.1	128.4	129.3	-	-	-	-

**Figure 4.**  $^{13}\text{C}$  NMR spectrum of compound 1a in  $\text{CDCl}_3$ 

### Antimicrobial activities

The four newly synthesized molecules were tested in vitro for antimicrobial activity against three Gram-staining-positive, three Gram-staining-negative bacterial strains

and two fungi strains. While 1a and 1c compounds did not show antimicrobial activity, 2d and 1b compounds showed antimicrobial activity (Table 6). The MIC values of 2d and 1b were determined between the dose of 500–1000  $\mu\text{g}/\text{mL}$  and 125–500  $\mu\text{g}/\text{mL}$ , respectively, against Gram-positive, Gram-negative bacteria and fungus species. The 2d and 1b compounds showed better antimicrobial activity against *S. aureus*, *E. faecalis*, *K. pneumoniae* and *P. aeruginosa* than the Amoxicillin standard.

### CONCLUSION

In this article, four new amide molecules (1a-1c) and 1d were successfully prepared by two-step synthesis reactions consisting of activation and acylation steps. The structural analysis of the obtained molecules was made using FT-IR,  $^1\text{H}$  NMR,  $^{13}\text{C}$  NMR, spectroscopy and elemental analyses techniques. All of the target molecules were screened for their antibacterial and antifungal activities using serial dilution technique. As a result, among tested compounds 1b and 2d were exhibited good anti-

**Table 6.** The minimum inhibition concentrations (MIC's) of the tested molecules

Sample	Minimum inhibition concentration ( $\mu\text{g/mL}$ )							
	Gram-staining-positive			Gram-staining-negative			Fungi	
	B. subtilis	S. aureus	E. faecalis	E. coli	K. pneumoniae	P. aeruginosa	A.niger	C. albicans
1a	-	-	-	-	-	-	-	-
1b	125	125	125	125	125	125	125	500
1c	-	-	-	-	-	-	-	-
2d	500	500	500	500	500	500	1000	1000
Amoxicillin	<2	>1000	>1000	32	>1000	>1000	NT	NT
Tetracycline	<2	8	8	<2	8	4	NT	NT
Ketoconazole	NT	NT	NT	NT	NT	NT	1	2

NT: not tested

microbial activity. This antimicrobial activity can be the directly related to the nature of the substituents on the ring of compounds 1b and 2d.

### References

- Aftab K, Aslam K, Kousar S, Nadeem, MJUH. Synthesis, characterization and biological evaluation of tryptamine based benzamide derivatives. *Pakistan Journal of Pharmaceutical Sciences* 29 (2) (2016) 423–428.
- Aytemir MD, Hider RC, Erol DD, Özalp M, Ekizoğlu, M. Synthesis of new antimicrobial agents; amide derivatives of pyranones and pyridinones. *Turk Journal of Chemistry* 27 (2003) 445–452.
- Kabara JJ, Conley AJ, Truant, JP. Relationship of chemical structure and antimicrobial activity of alkyl amides and amines. *Antimicrobial Agents and Chemotherapy* 2(6) (1972) 492–498.
- Gore, RP. Synthesis, characterization and antimicrobial activity of N'-(substituted phenyl)-2-(1H-azol-1-yl) acetamides. *Der Pharma Chemica* 6(6) (2014) 35–38.
- Kushwaha N, Saini RK, Kushwaha, SK. Synthesis of some amide derivatives and their biological activity. *International Journal of ChemTech Research* 3(1) (2011) 203–209.
- Wu J, Kang S, Luo L, Shi Q, Ma J, Yin J, Song B, Hu D, Yang, S. Synthesis and antifungal activities of novel nicotinamide derivatives containing 1,3,4-Oxadiazole. *Chemistry Central Journal* 7 (2013) 64.
- Panyatip P, Johns NP, Priprem A, Nakagawa K, Puthongking, P. Effect of N-amide substitution on antioxidative activities of melatonin derivatives. *Scientia Pharmaceutica* 3 (2020) 88.
- Saedia M, Golia F, Mahdavia M, Dehghanb G, Faramarzic MA, Foroumadia A, Shafieea, A. Synthesis and biological investigation of some novel sulfonamide and amide derivatives containing coumarin moieties. *Iranian Journal of Pharmaceutical Research* 13(3) (2014) 881–892.
- Marinova E, Georgiev L, Totseva I, Seizova K, Milkova, T. Antioxidant activity and mechanism of action of some synthesised phenolic acid amides of aromatic amines. *Czech Journal of Food Sciences* 31(1) (2013) 5–13.
- Malki F, Touati A, Moulay, S. Comparative study of antioxidant activity of some amides. *Journal of Analytical & Pharmaceutical Research* 5(3) (2017) 00143.
- Bhat M, Belagali S, Shastry PR, Rai, VR. Synthesis, characterization, and biological study of phenylalanine amide derivatives. *Monatshefte für Chemie* 147 (2002) 2002–2008.
- Batista-Pereira LG, Castral TC, da Silva MTM, Amaral BR, Fernandes JB, Vieira PC, da Silva MFGF, Corre, AG. Insecticidal Activity of Synthetic Amides on Spodoptera frugiperda. *Zeitschrift für Naturforschung C* 61(3-4), (2006) 196–202.
- Desai AD, Chikhaliya, KH. Synthesis and studies of 1-[2-(Aryl Amino-2-Oxo Ethyl) amino]-4-(N-Methyl Piperazino)-benzene derivatives. *E-Journal of Chemistry* 2(1) (2005) 15–20.
- da Silva Carrara V, Cunha-Júnior EF, Torres-Santos EC, Corrêa AG, Monteiro JL, Demarchi IG, Campana Lonardoni MV, Garcia Cortez, DA. Antileishmanial activity of amides from piper amalago and synthetic analogs. *Revista Brasileira de Farmacognosia Brazilian Journal of Pharmacognosy* 23(3) (2013) 447–454.
- Ballard TE, Wang X, Olekhovich I, Koerner T, Seymour C, Hoffman PS, Macdonald, TL. Biological activity of modified and exchanged 2-amino-5-nitrothiazole amide analogues of nitazoxanide. *Bioorganic & Medicinal Chemistry Letters* 20 (2010) 3537–3539.
- Jafar NNA, SadiqMajeed, N. Microwave assisted synthesis of amide derivatives of the drug ciprofloxacin and screening the biological properties. *International Journal of ChemTech Research* 9(7) (2016) 387–395.
- Graul A, Castaner, J. *Drugs of the Future* 22 (1997) 956–968.
- Jung ME, Abrecht, S. Improved synthesis of 3-substituted 7-methoxybenzofurans. Useful intermediates for the preparation of morphine analogs of organic chemistry. *Journal of Organic Chemistry* 53(2) (1988) 423–425.
- Mazik M, Bläser D, Boese, R. Hydrogen-bonding motifs in the crystals of secondary diamides with 2-amino-6-methyl- and 2,6-diaminopyridine subunits. *Tetrahedron* 55(44) (1999) 12771–12782.
- Schwalbe R, Steele-moore L, Goodwin, A. Antimicrobial Susceptibility Testing Protocols. (2007) 430.
- Cakmak S, Kütük H, Odabaşoğlu M, Yakan H, Büyükgüngör, O. Spectroscopic properties and preparation of some 2,3 dimethoxybenzamide derivatives. *Letters in Organic Chemistry* 13(3) (2016) 181-194.
- Kırca BK, Cakmak S, Kütük H, Odabasoglu M, Büyükgüngör, O. Synthesis and characterization of 3-acetoxy-2-methyl-N-(phenyl)benzamide and 3-acetoxy-2-methyl-N-(4-methylphenyl)benzamide. *Journal of Molecular Structure* 1151 (2018) 191-197.

# APPENDIX

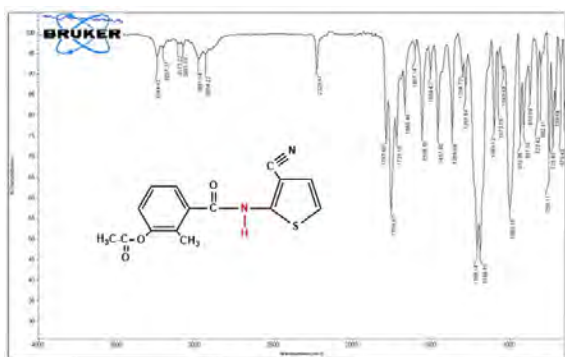


Figure S1. FT-IR spectrum of compound 1b

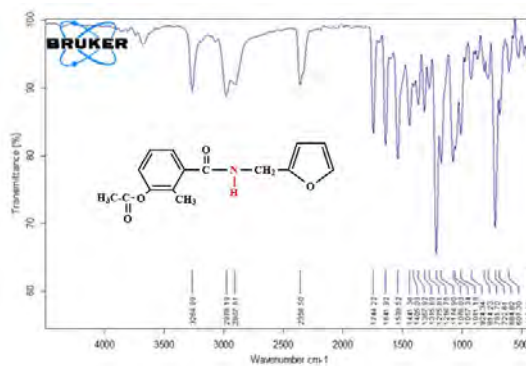


Figure S4. FT-IR spectrum of compound 1c

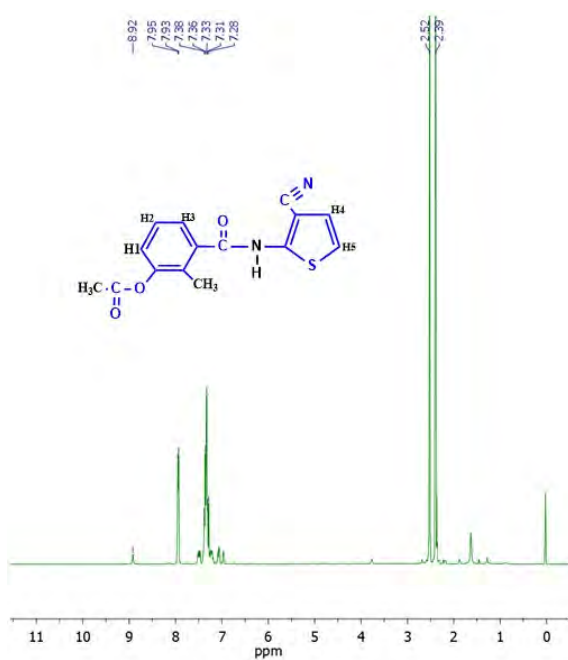


Figure S2. <sup>1</sup>H NMR spectrum of compound 1b in CDCl<sub>3</sub>

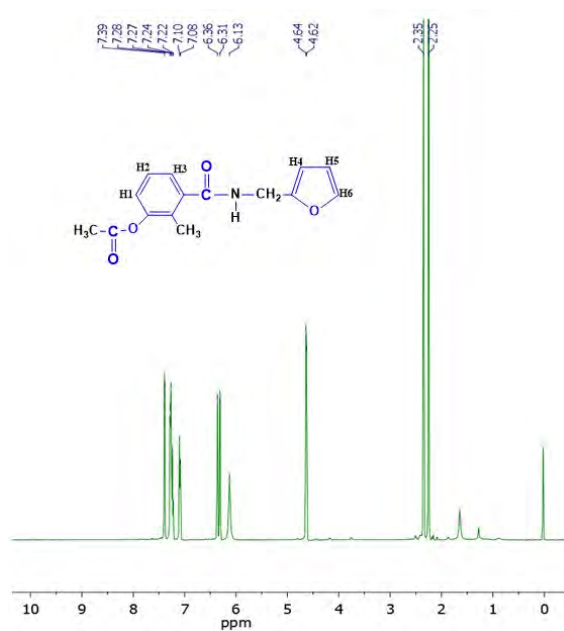


Figure S5. <sup>1</sup>H NMR spectrum of compound 1c in CDCl<sub>3</sub>

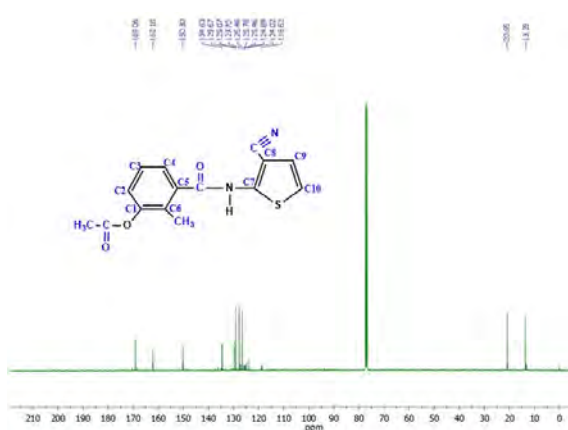


Figure S3. <sup>13</sup>C NMR spectrum of compound 1b in CDCl<sub>3</sub>

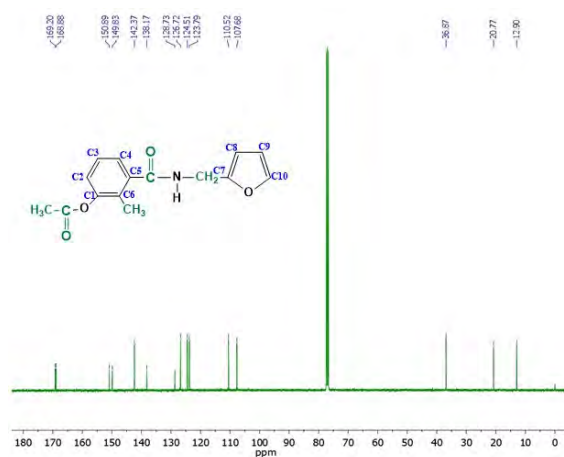


Figure S6. <sup>13</sup>C NMR spectrum of compound 1c in CDCl<sub>3</sub>

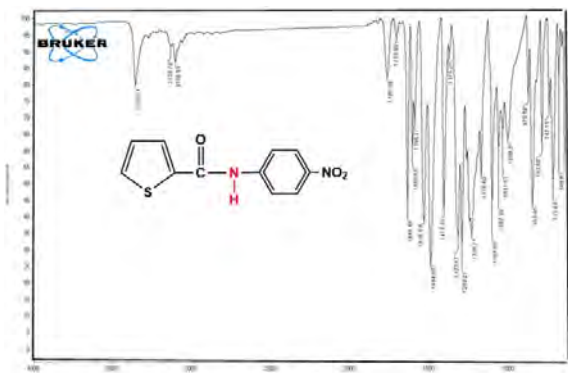


Figure S7. FT-IR spectrum of compound 2d



Figure S8. <sup>1</sup>H NMR spectrum of compound 2d in CDCl<sub>3</sub>

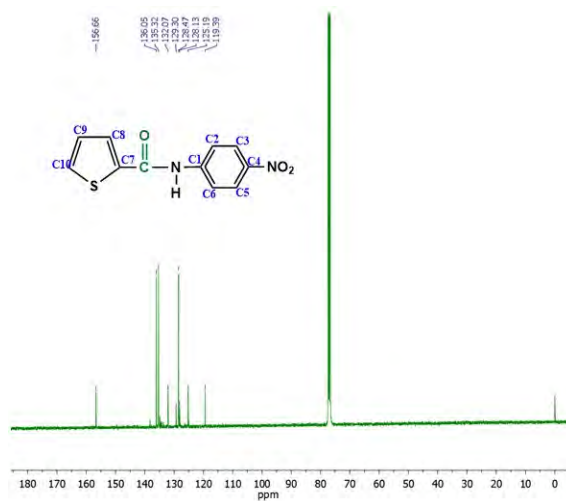


Figure S9. <sup>13</sup>C NMR spectrum of compound 2d in CDCl<sub>3</sub>

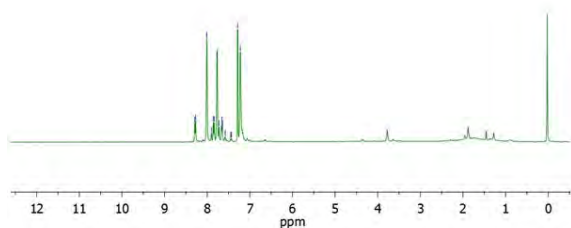
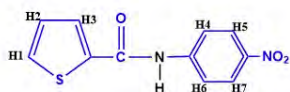


Figure S8. <sup>1</sup>H NMR spectrum of compound 2d in CDCl<sub>3</sub>





## Wintering Bird Diversity and Population Sizes at Obruk Dam Lake (Corum) in Turkey

Kadir Ulusoy<sup>1</sup> and Safak Bulut<sup>1</sup>

Hittit University, Department of Molecular Biology and Genetics, Corum, Turkey

### ABSTRACT

In this study, species diversity of waterbirds, which are the indicator species of wetland quality were investigated at Obruk Dam Lake in Turkey, which was built in 1996 and started to operate in 2009. Obruk Dam built on River Kızılırmak within Çorum province has created a new habitat for waterbird with a lake surface area of 50 km<sup>2</sup>. As a result of the studies, 21 waterbird species belonging to 6 orders were identified. According to the results of the mid-winter waterbird census revealed in 2018 and 2019, 26.975 and 13.158 individuals of waterbirds were counted in Obruk Dam Lake respectively and it has been proved that the Obruk Dam Lake forms a new terrain especially for birds. Although the census for the year 2020 could not be done completely due to adverse conditions, short observations in 2020 show that the Obruk Dam Lake continues to be used intensively by waterbirds. During the research, intensive and off season hunting activities were observed in the field. In this context, studies have been initiated to keep the censuses continuous in order to monitor the status of the new wetland formed by the Obruk Dam Lake and the waterbirds which are using this wetland.

#### Keywords:

Benefits of dams; Wetlands; Biodiversity; Bird Census; Waterbirds.

### INTRODUCTION

Wetlands are ecosystems with a high biodiversity that allow their inhabiting species to carry out their basic vital activities such as feeding, sheltering and breeding [1]. Identification of wetlands cannot be easily achieved due to variations in the occurrence of birds and vegetation, variable water regimes and ranging from inlands to marine waters [2]. Although the definition of wetlands may vary, the most widely accepted definition in the world is the one included in the RAMSAR Convention [3]. According to international Ramsar Convention wetlands are defined as "...areas of marsh, fen, peatland or water, whether natural or artificial, permanent or temporary, with water that is static or flowing, fresh, brackish or salt, including areas of marine water the depth of which at low tide does not exceed six meters..." and waterbird is defined as "...birds ecologically dependent on wetlands..." [4].

Different types of wetlands increase the ecosystem diversity, and in return, species using these wetlands increase biological and genetic diversity [5, 6]. Although wetlands are important hotspots for the conservation of biodiversity, they cover less than 2% of the continental surface on earth and continue to shrink [7]. Changes in

land use such as urbanization and conversion to agricultural land due to population growth causes wetland decreasing in proportion to the increase in human population [8]. Turkey has a significant amount of wetlands compared to continental Europe. Although wetlands that exist in Turkey are known to be important for breeding and wintering bird species, information about the populations of bird species using these areas are limited [9]. Waterbirds are considered as indicators of wetland quality and restoration as parameters of local biodiversity, and many ecologists think that birds are one of the visible indicators of total productivity of biotic systems [2].

Mid-Winter Waterbird Census (MWWC) is one of the main methods used for long term monitoring of the changes in wetlands, as well as detecting changes in waterbird populations. MWWC was made at 1967 in Turkey for the first time and with the participation of national and international institutions and non-governmental organizations 34th was in 2018, 35th MWWC was made in 2019 [10].

Dam constructions change the environment by creating an artificial lake area on rivers, which may af-

#### Article History:

Received: 2020/11/01

Accepted: 2020/12/20

Online: 2020/12/31

**Correspondence to:** Kadir Ulusoy, Hittit University, Department of Molecular Biology and Genetics, 19030, Corum, Turkey  
E-Mail: kadirulusoy@hitit.edu.tr  
Phone: +90 364 227 7001  
Fax: +90 364 227 7005

fect the biota present in the area before the construction. Waterbird populations vary under the influence of different factors such as water quality in dam lakes, depth of water, vegetation structure around the lake area, fishing, and water sports [11]. Dam lakes and ponds can create different alternative habitats for waterbird, as well as respond to the different ecological needs of different species thus increasing the diversity of species in the area [12]. Research results in Karkamış Dam Lake showed that the new wetland ecosystem created by the dam construction has significantly increased the biodiversity in the area. Censuses on waterbird resulted in the count of 118,434 individuals in 2005, and 73,964 individuals in 2007. After these results, the newly formed wetland ecosystem was included to the "Important Bird Areas of Turkey, 2004 update" [13, 14].

Obruk Dam Lake, the study area, was put into operation in 2009 with a 50.21 km<sup>2</sup> maximum lake area [15] forming a new wetland ecosystem. During the field visits in Obruk Dam Lake, it was determined that the area was started to be used by waterbirds and the purpose of this study is to identify these waterbird species.

## MATERIAL and METHOD

### Study Area

Obruk Dam Lake is located on Kızılırmak River, covering an area of approximately 50 km long in the southwest-northeast direction, with respect to the flow direction of the river (Fig. 1). The dam is surrounded by the districts of İskilip, Oğuzlar and Dodurga in northwest and the districts of Laçın and Çorum (Center) in southeast. The closest settlement area to the dam shore is the Oğuzlar district, which is on average 2.5 km away. The Çorum-Çankırı D180 highway passes over the dam by a bridge from the upstream part of the dam, and the road that provides access to the Oğuzlar district passes through the downstream part.

The general vegetation structure consists of deciduous forests and sparse larch forests. In the vicinity of the lake, dry farming, fruit production and greenhouse cultivation



**Figure 1.** Satellite Image of Point Transect Locations on the Google Earth image.

are carried out as well these, irrigated agriculture by dam water exists. It was also observed that cattle and ovine breeding were carried out in the surrounding villages. There are reeds densely in the lake area between Kumçelteği, Karlık and Tozluburun villages in the southeast of the bridge that passes over the lake. Although the lake shores are generally bare due to anthropogenic effect, there are partly reeds in the regions where the seasonal flowing streams reach the lake. In Obruk Dam, commercial fishing is allowed with a hunting quota determined by the cooperative. During the field trips, we also witnessed illegal waterbird hunting.

### Waterbird Census

Canon EOS 7D Mark II DSLR digital camera, Canon 100/400 mm L and 400 mm L lenses, Nikon Aculon 10x42 binoculars, Nikon 20-60x50 field scope, DJI Phantom 4 Pro drone, and mechanical counters were used during censuses. In the field studies, bird species are identified according to Heinzel et al [16] and Porter et al [17]. Observed bird species together with the census results were recorded in the field notebook. Bird Censuses were made in 2018 and 2019, in January. In January 2020 a short monitoring and census was done to check the current status of study area because of bad weather conditions, low visibility, difficulties to access to the observation points by reason of muddy roads, and continuously movements of waterbirds due to hunting activities. Depending on these reasons census in 2020 was done from only 3 vantage points and condition of wetland was observed.

Field studies were done by using point transect method [18, 19]. Line transect method was carried out by boat on the lake in order to determine the locations where waterbird colonies are used extensively, and the point transects were made out from 8 vantage points (Fig. 1). The satellite image of the locations where the point transects made are shown in Fig. 1 and their coordinates are shown in Table 1. A total of 8 vantage points were decided due to both of topographic structure of the lake shore and vantage points' view of field. The length of lake area using by waterbirds are approximately 13 km long and the widest area of lake is about 3 km long. Because of these situations, we used the points that have the characteristics of having a wide view of the lake area, the clear viewing angles of the shores and existence of waterbird colonies at the vantage points we chose. During the vantage points were determined, the viewing angle of each point and the area to be observed from each point were predetermined, and necessary precautions were taken to prevent the census results from being adversely affected by possible duplicate counts. We have counted waterbirds one by one using mechanical counter and field scope from right to left in view from vantage points. Waterbirds that moves in the opposite of the counting direction were included to

**Table 1.** UTM Coordinates of Point Transect Locations

Location No	East	North
	36T	
1	631893	4498132
2	629901	4496954
3	629541	4494626
4	630824	4495309
5	636208	4499195
6	637408	4498491
7	635293	4500302
8	637151	4500306

census; in order to prevent recounting of waterbirds flying or changing location, individuals which changed their place in the direction of counting were not included in the results.

Entire observation areas and the waterbird colonies in the observation areas were photographed by a DSLR camera with a 400 mm lens mounted before censuses at predetermined locations. The images were combined with Adobe Photoshop CS3 Extended PC software to create a panoramic view of the observation areas, and the "count tool" in the same PC software was used for carrying out the waterbird censuses.

## RESULTS

The waterbird census results are given in Table 2. *Aythya ferina* (Common pochard) is listed as "VU=Vulnerable", *Numenius arquata* (Eurasian curlew) and *Turdus iliacus* (Redwing) are listed as "NT=Near Threatened"; and remaining 18 waterbird species are listed as "LC=Least Concern" according to the IUCN (International Union for Conservation of Nature) RedList [20]. In terms of Bern Convention (Convention on the Conservation of European Wildlife and Natural Habitats) 6 species are listed in Appendix II (Strictly protected fauna species), 15 species are listed in Appendix III (Protected fauna species) [21].

14 waterbird species from 6 orders were identified in Obruk Dam Lake in 2018 winter season and from these species 26.975 individuals were counted with the most common species *Fulica atra* (Eurasian coot) with 23.772 individuals. It was followed by *Anas platyrhynchos* (Mallard) with 1.151 individuals and *Tadorna tadorna* (Ruddy shelduck) with 761 individuals, respectively.

In the winter season of 2019, 13.158 individuals from 19 waterbird species were counted, and the most common species was *Fulica atra*, represented with 10.655 individuals. Census results show that *F. atra* was followed by *Anas platyrhynchos* (Mallard) with 1,101 individuals and *Anas*

*crecca* (Eurasian teal) with 601 individuals. The census results for January 2019 are given in Table 2.

As a result of the field study conducted in January 2020, a total of 11.597 waterbirds were counted in the study area, and the most observed species were *Fulica atra* with 10.101 individuals and *Anas platyrhynchos* with 1.062 individuals, respectively. During the short observations, 7 waterbird species were identified belonging to 6 orders. These results also are shown in Table 2.

Two different areas were detected that mostly preferred by waterbirds in Obruk Dam Lake. One of these locations is the shallow part of the area, stretching from the shores of Salur and Karaburun villages to the vicinity of the Kızılırmak Bridge, reaching a depth of about 5 meters and covering an area of approximately 30 km<sup>2</sup>. The second location is the reed-bed, which extends from the shores of Tozluburun village to the shores of Kumçelteği village, where the lake area starts.

In the observations, we found that Eurasian coot, Mallard, and Great crested grebe formed colonies together, away from the shores. Cormorant species were usually observed roosting in the submerged tree branches or floating around these trees. Ruddy shelduck usually prefers bare fender areas on the opposite shore of Yalakçay village. Heron species (Great egret, Little egret and Gray heron) were observed roosting on the whole lake shore rather than a specific area.

Our monitoring studies showed that waterbirds do not choose locations like the shores of settlements by the lake and the coastal areas where human activities such as angling, picnic and boat docks regions. There is Kızılırmak Bridge on the D-180 highway which provides transportation between İskilip and Çorum on the lake and divides dam lake into two parts and waterbirds do not use bridge and areas near bridge because of disturbance.

## DISCUSSION

Although, dams built on rivers are damaging the existing ecosystem, they can also provide significant benefits for the ecosystem in case of appropriate physical conditions [11, 13]. This research aimed to determine the waterbird species wintering in Obruk Dam Lake. In Turkey, MWWC was started in 1967, and censuses are still being conducted annually under the leadership of the General Directorate of Nature Conservation and National Parks (DKMP) [10]. In Obruk Dam Lake, which started to operate in 2009, the first waterbird census was made by Erciyas Yavuz and Kartal (2012) [22]. After the first census, a census was made in the following year by Erciyas Yavuz and İsfendiyaroğlu [23], and no other mid-winter

**Table 1.** Winter Waterbird Census Results of 2018 and 2019 and short observation results of 2020

Common Name	Scientific Name	2018	2019	2020
Eurasian coot	<i>Fulica atra</i>	23,772	10,655	10,101
Mallard	<i>Anas platyrhynchos</i>	1,151	1,101	1,062
Ruddy shelduck	<i>Tadorna ferruginea</i>	761	52	48
Great cormorant	<i>Phalacrocorax carbo</i>	558	112	126
Black-headed gull	<i>Chroicocephalus ridibundus</i>	184	205	63
Great egret	<i>Ardea alba</i>	104	51	12
Little egret	<i>Egretta garzetta</i>	93	1	-
Little grebe	<i>Tachybaptus ruficollis</i>	84	165	-
Eurasian teal	<i>Anas crecca</i>	57	601	-
Yellow-legged gull	<i>Larus michalensis</i>	55	-	-
Northern shoveler	<i>Anas clypeata</i>	39	-	-
Green sandpiper	<i>Tringa ochropus</i>	28	-	-
Grey heron	<i>Ardea cinerea</i>	23	14	-
Great crested grebe	<i>Podiceps cristatus</i>	19	132	185
Common redshank	<i>Tringa totanus</i>	-	20	-
Red-crested pochard	<i>Netta rufina</i>	-	16	-
Common pochard	<i>Aythya ferina</i>	-	9	-
Common greenshank	<i>Tringa nebularia</i>	-	8	-
Common shelduck	<i>Tadorna tadorna</i>	-	2	-
Eurasian curlew	<i>Numenius arquata</i>	-	2	-
Tufted duck	<i>Aythya fuligula</i>	-	2	-
Unidentified waterbird		47	10-	-
TOTAL		26,975	13,158	11,597

waterbird census was conducted in Obruk Dam Lake until 2018. Results of censuses compared with Mid-Winter Waterbird Census (MWWC) results made by DKMP, it is seen that Obruk Dam Lake is the 13th location from 153 different locations with 26975 waterbirds wintering in 2018 in the ranking of highest number of waterbird counted locations list [3].

According to the results of MWWC in 2019, among 154 different locations with the highest number of waterbird counts, Obruk Dam Lake ranked the 24th with 13.158 individuals [10]. These results clearly show the status of Obruk Dam Lake among the sites hosting the highest waterbird populations in Turkey. This newly formed wetland, created by Obruk Dam Lake, which hosted 26.975 individuals in 2018 and 13.158 in 2019, is an important wintering location for waterbird species in Turkey, as reflected by the census results.

Obruk dam, which is built on Kızılırmak, as a reservoir type has created a new habitat especially for water birds, as in the case of Karkamış dam, as a result of observations made with. The Karkamış dam, built in 2000, has been an area visited by more than 20,000 waterbirds on average, alt-

hough there are differences in numbers every year. In the studies carried out, 110 bird species were identified in the Karkamış dam [13]. Obruk dam formed a new habitat especially for waterbirds following the impoundment of the dam, as in the example of Karkamış dam, and 59 different bird species and 22 different water bird species can be observed.

As a result of the studies carried out in Karaçomak and Beyler dams built in Kastamonu neighbouring province of Çorum, 23 waterbird species from 11 families belonging to 6 orders in total were identified. 17 species belonging to 6 orders in Karaçomak dam and 22 species belonging to 6 orders observed in Beyler dam [24]. When Obruk dam is compared with Karaçomak dam built between 1968-1973 and Beyler dam built in 1993, it is seen that the variety of species and the number of individuals are higher in Obruk dam. These results support that Obruk dam creates a new wetland and a new habitat for water birds.

In Eber and Köyceğiz lakes which are important wetlands of Turkey, 59 waterbird species belonging to 14 orders and 38 waterbird species belonging to 12 orders have been identified respectively [25]. Obruk dam contains 22 waterbird species belonging to 6 orders and approximately half of

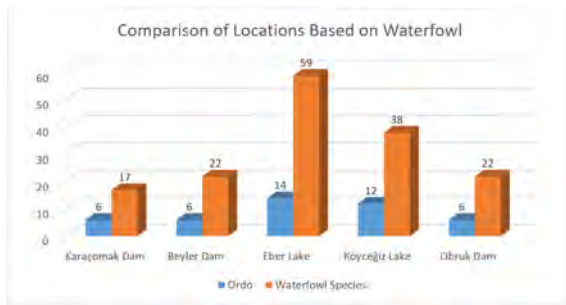


**Figure 2.** Comparison of Locations based on waterbird species

the species diversity in these areas (Fig. 2).

Intense and illegal hunting is thought to have a higher negative effect on waterbird, reflecting on the behaviour of populations as an avoidance to use the area. Precautions to be taken on this issue have been identified and negotiations have been initiated with the relevant authorities and actions have been started to reduce illegal hunting in the future times. Studies have been started to determine the water quality and water quality will be monitored according to the results to be obtained and if necessary, actions will be planned and implemented which are essential. Results of short observation and limited census in January 2020 shows that Obruk Dam lake wetland is still being used intensely by waterbird actually. The partial increase in the number of individuals proves that the Obruk Dam Lake is a new habitat especially for waterbird and indicates the necessity of monitoring its condition in the coming years.

## CONCLUSION

As a result of the censuses made in 2018 and 2019, as well as the short monitoring carried out in 2020, waterbird species diversity and the number of individuals hosted by the Obruk Dam Lake show that a new wetland has been formed in the Çorum Province. With the construction of Obruk Dam, this wetland has increased the biodiversity of the region, creating new habitats where bird species that did not previously use the area can perform activities such as wintering and feeding.

Our studies in Obruk Dam Lake are important as they provide data about the status of waterbird species in the area for the first time. In this context, mid-winter waterbird censuses will be repeated every year and the relationship between waterbird species and Obruk Dam Lake will be revealed more clearly and precisely.

## ACKNOWLEDGEMENT

This study is the thesis of Kadir Ulusoy which was supported by Hitit University Scientific Research Projects Coordination Unit (FEF19001.17.007). In addition, we would like to thank the graduate student Mujde Fistik for

her contributions during the census and Biologist Deniz Candas for her support during the writing of the article.

## References

- Süllü N. "Konya-Ereğli Akgöl'ün avifaunası" PhD Thesis, Selçuk Üniversitesi institute of science, 2006.
- Weller MW. Wetland birds: habitat resources and conservation implications. Cambridge University Press, Cambridge, 1999.
- DKMP, "Kış Ortası Su Kuşu Sayımları 2018", Ankara, 2018.
- Ramsar Convention Secretariat, 2013. The Ramsar Convention Manual: a guide to the Convention on Wetlands (Ramsar, Iran, 1971), 6th ed. Ramsar Convention Secretariat, Gland, Switzerland.
- Tırlı A, Baylan E. Wetland management in Turkey: Problems, achievements and perspectives. African Journal of Agricultural Research, c. 4, sy 11, (2009) 1106–1119.
- Keten A, Arslangündoğdu Z, Selmi E. Düzce-Efteni Gölü Kuş Türleri. Düzce Üniversitesi Orman Fakültesi Ormancılık Dergisi, c. 8, sy 1 (2012) 10–18.
- Cruz T, Lima J, Luís A, Azeiteiro UM. Avifauna conservation and disturbance ecology in a coastal freshwater lagoon. Environmental monitoring and assessment, c. 190, sy 10 (2018) 592.
- Czech HA, Parsons KC. Agricultural wetlands and waterbirds: a review. Waterbirds (2002) 56–65.
- Perktaş U, Albayrak AB, Ayaş Z. The evaluation of some key wetlands for waterfowl in central Anatolia, Turkey, in: Hanson AR, Kerekes JJ (Eds.). Limnology and Aquatic Birds: Abstracts and Selected Papers from the Fourth Conference of Societas Internationalis Limnologiae (SIL) Aquatic Birds Working Group. Paper presented at Fourth Conference of Societas Internationalis Limnologiae (SIL) Aquatic Birds Working Group, Sackville, New Brunswick, Canada, 3–7 August. Springer. Netherlands, pp. 166, 2006.
- DKMP, "Kış Ortası Su Kuşu Sayımları 2019", Ankara, 2019.
- Mori Y, Kawanishi S, Sodhi NS, Yamagishi S. The relationship between waterfowl assemblage and environmental properties in dam lakes in central Japan: implications for dam management practice. Ecology and Civil Engineering, c. 3, sy 1, (2000) 103–112.
- Halil S. Oğurlu İ. Ertuğrul ET. Karacaören I baraj gölünün kuş faunası. Mehmet Akif Ersoy Üniversitesi Fen Bilimleri Enstitüsü Dergisi, c. 9, sy 1 (2018) 22–28.
- Sönmez ME, Kılıç Z. Benefits Of Dams For The Ecosystem: The Sample Of Karkamış Dam (Turkey), in: Gâstescu P, Marszelewski W, Breţcan P. (Eds.). 2nd International Conference - Water resources and wetlands Conference Proceedings. Paper presented at 2nd International Conference - Water resources and wetlands, Tulcea (Romania), 11-13 September. Romanian Limnogeographical Association, Dâmboviţa, pp. 432-438, 2014.
- Kılıç DT, Eken G. Türkiye'nin Önemli Kuş Alanları 2004 Güncellemesi, Doğa Derneği, Ankara, 2004.
- Limak, "Obruk Barajı ve HES". 2009. <http://www.limak.com.tr/sectorler/insaat/projeler/tamamlanan-tum-projeler/barajlar/obruk-barajı-ve-hes> (access date: August, 22, 2020).
- Heinzel H, Fitter R, Parslow J, Boyla A. Türkiye'nin ve Avrupa'nın kuşları: Kuzey Afrika ve Ortadoğu dahil, Doğal Hayatı Koruma Derneği, İstanbul, 2002.
- Porter RF, Christensen S, Schiermacker-Hansen P. Türkiye ve Ortadoğu'nun Kuşları, Uzerler Matbaası, Ankara, 2009.
- Bibby CJ, Burgess ND, Hill DA, Mustoe S. Bird census techniques. Elsevier, 2000.
- Gregory RD, Gibbons DW, Donald PF. Bird census and survey

- techniques, in: Sutherland WJ, Newton I, Green R (Eds.). Bird ecology and conservation, Oxford University Press, Oxford, pp. 17-56, 2004.
20. IUCN. "The IUCN Red List of Threatened Species". Version 2020-3. <https://www.iucnredlist.org>. Downloaded on [28.12.2020]
  21. Bern Convention, (1979): Bern Convention: Convention on the Conservation of European Wildlife and Natural Habitats, 19/09/1979 <https://www.coe.int/en/web/conventions/full-list/-/conventions/treaty/104> (06/01/2020)
  22. Erciyas Yavuz K, Kartal E. Türkiye Kış Ortası Su Kuşu Sayımları 2011. Ondokuz Mayıs Üniversitesi Yayınları, Samsun, 2012.
  23. Erciyas Yavuz K, İsfendiyaroğlu S. 2012 Türkiye Kış Ortası Su Kuşu Sayımları. Doğa Derneği, İzmir, 2013.
  24. Uğış A, Akkuzu E, Evcin Ö. Kastamonu Yöresi Beyler ve Karaçomak Barajı Gölü Sucul Kuşları. Kastamonu Univ., Journal of Forestry Faculty 16 (2016) (2): 447-462.
  25. Saygılı F, Yiğit N, Bulut Ş. The spatial and temporal distributions of waterbirds in Lakes Akşehir-Eber and Lake Köyceğiz in western Anatolia, Turkey-a comparative analysis. Turkish Journal of Zoology 35 (2011) 467-480.